THÈSE

En vue de l'obtention du

DOCTORAT DE L'UNIVERSITÉ DE TOULOUSE

Délivré par :

Institut National Polytechnique de Toulouse (Toulouse INP)

Discipline ou spécialité :

Energétique et Transferts

Présentée et soutenue par :

M. JAVIER CRESPO ANADON

le jeudi 12 janvier 2023

Titre :

Simulation à grandes échelles de l'allumage des moteurs d'avion dans des conditions d'exploitation pertinentes et application à la technologie de la combustion giratoire

---

Ecole doctorale :

Mécanique, Energétique, Génie civil, Procédés (MEGeP)

Unité de recherche :

Centre Européen de Recherche et Formation Avancées en Calcul Scientifique (CERFACS)

Directeurs de Thèse :

MME BÉNÉDICTE CUENOT

MME ELEONORE RIBER

Rapporteurs :

M. ANDREAS KEMPF, University Duisburg-Essen

M. DENIS VEYNANTE, CENTRALESUPELEC GIF SUR YVETTE

Membres du jury :

M. MARC BELLENOUE, ENSMA POITIERS, Président

M. JAMES R. DAWSON, NORWEGIAN UNI OF SCE AND TECHN TRONDHEIM, Membre

MME BÉNÉDICTE CUENOT, CERFACS, Membre

MME ELEONORE RIBER, CERFACS, Membre

M. STÉPHANE RICHARD, GROUPE SAFRAN, Invité

2

Abstract

SAFRAN Helicopter Engines has recently developed the spinning combustion technology in which the burnt gases from one injector travel tangentially along the combustor annulus towards the neighboring injectors. Compared to a conventional design, this arrangement modifies the ignition process, which is a critical phase for aeroengines. In addition to that, few ignition studies in literature feature actual aeronautical igniters. This thesis aims to numerically reproduce the kernel formation and flame propagation at conditions occurring in spinning combustion engines fitted with aeronautical igniters at relevant operating conditions. For this objective, the in-house code AVBP has been used together with models for the energy addition from the igniter, semi-detailed chemistry and a recent version of the thickened flame model using a generic sensor and a static and dynamic formulation for the subgrid chemistry-turbulence closure term. The results have been compared to experiments from partner laboratories and show that the Large-Eddy Simulation calculations are able to reproduce the kernel formation and propagation in spinning combustion technology engines. An average error of 10% in the time for complete chamber ignition was obtained when using a dynamic formulation of the subgrid chemistry-turbulence closure term. As a conclusion, this thesis gives further support to the use of LES as a tool for the design of combustion chamber systems in aircraft engines, in particular in novel configurations such as the spinning combustion technology.

Résumé

SAFRAN Helicopter Engines a récemment développé la technologie de combustion

4

giratoire dans laquelle les gaz brûlés d'un injecteur se déplacent tangentiellement le long de l'anneau de la chambre de combustion vers les injecteurs voisins. Par rapport à une conception classique, cet arrangement modifie le processus d'allumage, qui est une phase critique pour les moteurs d'avion. De plus, peu d'études sur l'allumage dans la littérature présentent des allumeurs aéronautiques réels. Cette thèse a pour but de reproduire numériquement la formation du noyau et la propagation de la flamme aux conditions rencontrées dans les moteurs à combustion giratoire équipés d'allumeurs aéronautiques aux conditions de fonctionnement réelles. Pour cet objectif, le code AVBP a été utilisé avec des modèles pour l'addition d'énergie de l'allumeur, une chimie semi-détaillée et une version récente du modèle de flamme épaissie utilisant un senseur générique et une formulation statique et dynamique pour le terme d'interaction chimie-turbulence de sous-maille. Les résultats ont été comparés aux expériences des laboratoires partenaires et montrent que les calculs de la simulation à grande échelle sont capables de reproduire la formation et la propagation du noyau dans les moteurs à technologie de combustion giratoire. Une erreur moyenne de 10% dans le temps pour l'allumage complet de la chambre a été obtenue en utilisant une formulation dynamique du terme de chimie-turbulence de sous-maille. En conclusion, cette thèse apporte un soutien supplémentaire à l'utilisation de la simulation à grande échelles comme outil pour la conception des systèmes de chambres de combustion dans les moteurs d'avion, en particulier pour les nouvelles configurations telles que la technologie de combustion giratoire.

Contents

List of Figures

11

12

13

14

15

17

19

20

23

24

25

26

List of Tables

List of Acronyms

Acronym	Meaning
ARC	Analytically Reduced Chemistry
CFD	Computational Fluid Dynamics
CFL	Courant-Friedrichs-Lewy
DNS	Direct Numerical Simulation
DRG	Directed Relation Graph method
DRGEP	DRG with Error Propagation
EE	Euler-Euler
ED	Energy Deposition
EL	Euler-Lagrange
FAR	Fuel-air ratio
GRC	Globally Reduced Chemistry
LES	Large Eddy Simulation
LP	Leading Point
LW	Lax-Wendroff
MIE	Minimum Ignition Energy
NSCBC	Navier-Stokes Characteristic Boundary Conditions
NTNU	Norges Teknisk-Naturvitenskapelige Universitet
PDF	Probability Density Function
PIV	Particle Image Velocimetry
PLIF	Planar Laser-Induced Fluorescence
PVC	Precessing Vortex Core
QSS	Quasi-Steady State
QSSA	QSS Approximation
RANS	Reynolds Averaged Navier-Stokes
RMS	Root-Mean-Square
SCT	Spinning combustion technology
SMD	Sauter mean diameter
TF	Thickened Flame
TFLES	Thickened Flame model for LES
TTGC	Two-step Taylor-Galerkin scheme version C

Non-dimensional numbers

Non-dimensional number	Meaning
B_M	Spalding number for mass transfer
B_T	Spalding number for heat transfer
Da	Damköhler number
Le	Lewis number
Nu	Nusselt number
Pr	Prandtl number
Pr_t	Turbulent Prandtl number
Re	Reynolds number
Re_t	Turbulent Reynolds number
Re_p	Particle Reynolds number
Sc	Schmidt number
Sh	Sherwood number
St	Stokes number
TI	Takeno Index

Subscripts and superscripts

Index	Meaning
F	Index of a fuel quantity
g	Index of a gaseous phase quantity
glob	Index of a quantity at global equivalence ratio
l	Index of a liquid phase quantity
O	Index of an oxidiser quantity
p	Index of a particle quantity
stoch	Index of a quantity at stoichiometric equivalence ratio
tot	Superscript of a total (gas + liquid) quantity

Chapter 1

Industrial Context

Contents

1.1   Motivation

A great challenge in aeronautical combustors consists in ensuring ignition at all flight conditions, in particular at high altitude where low temperature and pressure make ignition more difficult. Safran HE has recently developed the spinning combustion technology (SCT) depicted in Fig. 1-1. It consists in injecting the airflow and the fuel tangentially into the combustor. In this way, the hot gases produced by the flame attached to one injector are directed towards the next injector along the combustor annulus, eventually creating a unique flame ring which expands across the full combustor.

The spinning combustion technology has been embedded in the Arrano engine de-
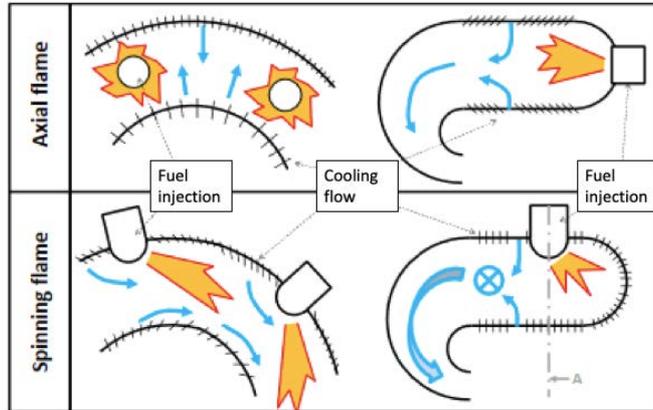
Figure 1-1: Spinning combustion technology (SCT) adapted from [121]

veloped by Safran Helicopter Engines, which features a shaft power between 1100 and 1300 horsepower and is targeted to medium-size helicopters (4 to 6 ton helicopters). An image of the Arrano engine is shown in Fig. 1-2.
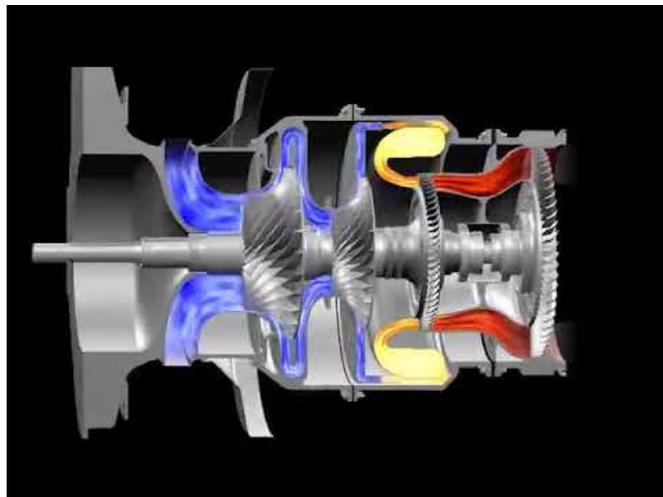
Figure 1-2: Arrano engine (Courtesy of Safran Helicopter Engines)

This technology has several advantages, among which it offers better light-around capability, which can be beneficial for future hybrid-electric systems, greater temperature homogeneity at the combustor exit, and reduced mass and cost.

Hybridization could represent up to a 20% reduction in fuel consumption [1]. One

of the possible configurations for hybrid-electric engines, named "Eco-mode" by Safran consists in using only one of the gas turbines during phases where a reduced power is needed (e.g. cruising), while using all the engines where maximum power is required (e.g. take-off or manoeuvering). For this reason, it is necessary to be able to re-ignite the other engine in a short time if needed. This feature will be introduced in the Airbus Helicopters RACER demonstrator.

Ensuring relight at cruise conditions is a safety-critical requirement for engine certification. The temperature at cruise conditions can reach several tens of degrees Celsius below zero, which inhibits the evaporation of the liquid fuel in the combustor. In addition to that, other combustor constraints such as pollutants reduction can lead to combustor designs which pose additional difficulties for relight at altitude.

Despite recent insights gained into ignition in conventional aeroengine designs [36, 68, 82], specific work is required for SCT, which introduces new mechanisms. In fact, due to the novelty of the SCT, not all ignition mechanisms are fully understood from an academic point of view and the effect of different parameters (engine geometry, air/fuel velocity, mixture...) on ignition are still not fully explored. A comprehensive understanding of ignition processes in SCT would open new innovation perspectives and allow improving the already impressive light-around performances of SCT, with possible extension to ultra-lean combustion or extreme altitude re-ignition.

Although there exists several ignition systems for engines (e.g. radio-frequency, laser, etc. [20]), most modern devices rely on igniters which generate an electrical discharge. Figure 1-3 contains a comparison of a conventional spark plug used mainly in automotive applications and a surface-discharge used mainly in aeronautical applications.

Surface discharge igniters are composed by coaxial electrodes: the high voltage electrode is the center electrode and the cylinder wall is the mass electrode. A high energy discharge is produced at the surface of the spark plug as shown in Fig. 1-4.

CONVENTIONAL PLUG   SURFACE-GAP PLUG

TERMINAL STUD

CERAMIC INSULATOR

CENTER ELECTRODE

SILLMENT SEALS

SHELL

GASKET

FIRING GAP

GROUND ELECTRODE

X-ray view of conventional and surface-gap plug
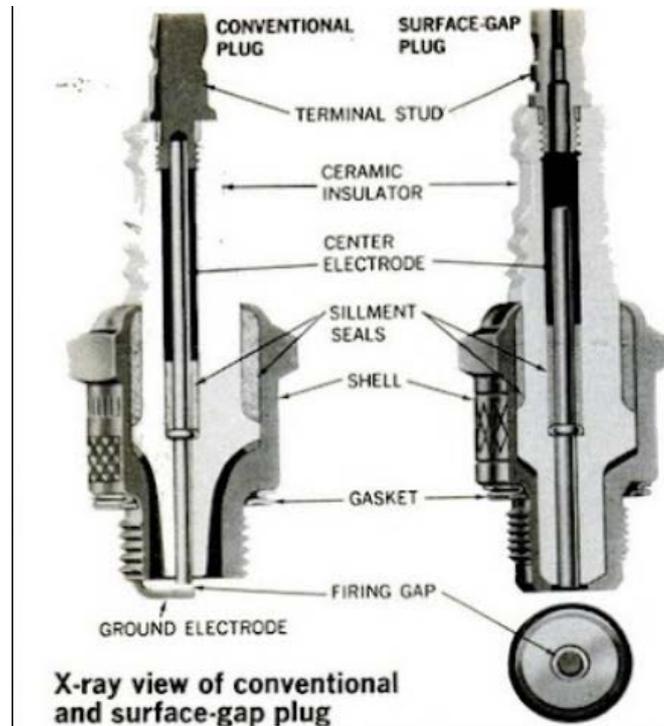
Figure 1-3: Comparison of a conventional spark plug used mainly in automotive applications (Left) and surface-discharge igniters used mainly in aeronautical applications (Right) [2]

Some advantages of surface dischargers are easier cooling and less accumulation of cokes deposits. Figure 1-5 contains a sketch showing the location of the igniter inside the combustor.

Surface dischargers are characterized by a relatively short deposition time ($< 1ms$) and higher energy ($\approx 1J$) than its automotive counterparts. The discharge at the surface generates a kernel of hot gases which is ejected away from the igniter surface.

1.2   Role of Numerical Simulation

As mentioned in the previous section, ensuring relight at high altitude remains a challenge for engine manufacturers and the number of dimensions of the design space
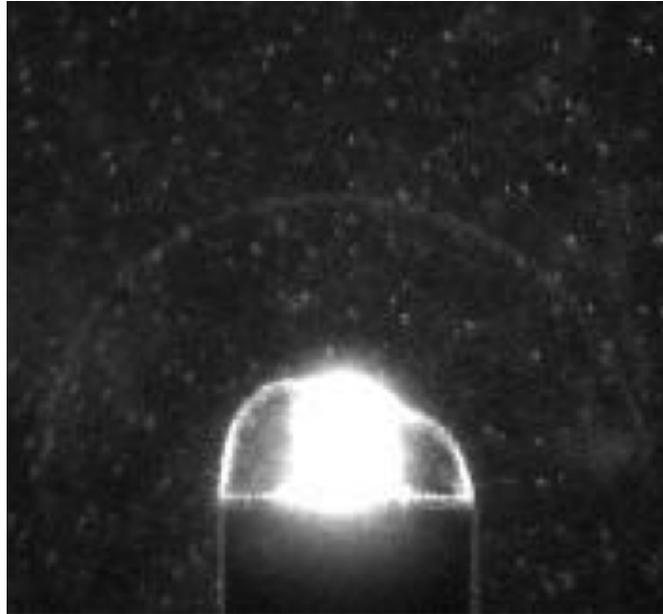
Figure 1-4: Surface discharge a few instants after start [20]
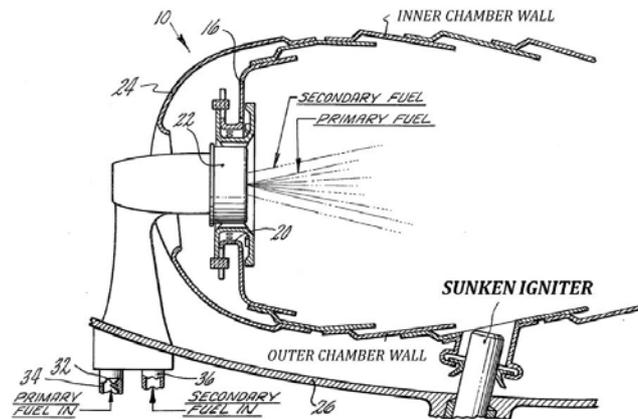
Figure 1-5: Location of a surface discharge igniter ("Sunken igniter") inside the combustor [123]

is high. Furthermore, the study of engine relight needs to cover at least three distinct phases: the formation of a flame kernel from a spark, the growth of the said flame kernel to ignite one injector and the flame propagation between injectors. Due to the complex shapes of combustors and the complexity of chemical effects, this process cannot be studied accurately using simplified analytical methods. In addition to that,

the large number of dimensions of the combustor design makes experimental testing unaffordable for the whole range of possibilities. On the other hand, computational fluid dynamics and, in particular, Large Eddy Simulations (LES) are able to capture most of the relevant physical phenomena at a reduced cost. Previous studies [23,36,68] have shown relative success in predicting the ignition dynamics in lab-scale engine-like annular combustors using both gaseous and liquid fuels. However, However, these works do not use aeroengine-type igniters but simple pin-pin low energy ignition systems. In addition, there is no current available studies covering the effects of a strong swirling motion occurring in the spinning combustion technology.

1.3   Organization of this Thesis

The work in this thesis covers the development and validation of a high-energy ignition model and the study of ignition and flame propagation in a new configuration characterized by a strong swirl flow. First, a review on the physics of ignition is introduced in chapter 2. Chapter 3 contains a description of theoretical and numerical aspects of combustion. Chapter 4 and chapter 5 cover the equations for the gaseous and disperse phases. A discussion of several methods to describe the formation of a kernel from the igniter spark is made in chapter 6. Following to that, the chosen ignition model is applied to an actual high-energy low-duration aeronautical igniter in an experiment consisting of a cylindrical chamber which represents the cross-flow conditions occurring in helicopter engines equipped with SCT. Following to that, a direct numerical simulation is presented which shows a detailed study of the ignition in a spray of droplets in chapter 7. Lastly, ignition is analyzed in a laboratory experiment which features the same levels of swirling flow encountered in engines equipped with spinning combustion technology in chapter 8. In all cases, a semi-detailed chemistry description is used by means of the analytically reduced chemistry approach. In addition to that, several subgrid models for describing the turbulence-chemistry inter-

action are tested [31,32] and a new sensor to study turbulence-chemistry interaction [117] is employed.

Chapter 2

Literature Review

Contents

This chapter contains a literature review on the process of ignition. It is divided into the different phases: spark, kernel formation, flame growing beyond the integral length scale, burner ignition and inter-burner propagation. Due to the novelty of spinning combustion technology, both conventional designs and challenges introduced by this new technology are discussed. The chapter ends with a review on the available modelling techniques for introducing detailed chemistry in numerical calculations.

2.1   Spark

The sparking phase, in which an electric current is established between the igniter electrodes, can be divided into 3 phases: breakdown, arc and glow. The breakdown is characterized by a sudden increase of current between electrodes to O(100 to 1000A) and voltage difference smaller than 100 V that takes place in the order of nanoseconds [77]. This generates a plasma with a high degree of ionization. The pressure between the electrodes increases to several hundred bars and the temperature increases to 60000 K [77]. Because of its short duration, there are almost no energy losses. In addition to that, radiation losses at breakdown are very small because radiation is trapped inside the plasma channel [78]. The growth of the kernel generated from the breakdown phase is mainly governed by the shockwave, with negligible contribution of chemistry [62], as indicated in Fig.   2-1.
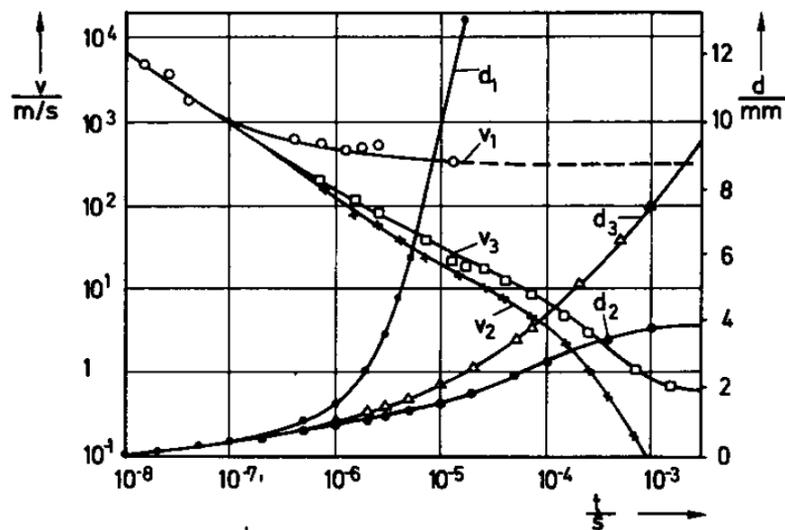
Figure 2-1: Diameters (d) and expansion velocities (v) of the kernel in an ignition experiment from [78] consisting of an automotive pin-pin igniter showing that the kernel expansion is governed by the movement of the shock for t<0.5 μs. The indices indicate: 1: shock in air at 1 bar; 2: plasma in air at 1 bar; 3: electrical and chemical plasma respectively in a stoichiometric CH_4-air mixture at 1 bar

An increase in breakdown energy does not change temperature of the initial kernel,

but the size of region where energy is deposited [72, 77]. After the breakdown, a jet of hot gases at high velocity is ejected from the electrode space, which creates a low-pressure region. This leads to an inflow of cold gases to the place occupied by the plasma channel which induces mixing [124]. Meanwhile, the jet of hot gases takes a toroidal shape.

After breakdown, the arc phase ensues, which is characterized by currents in excess of 100 mA with the upper limit set only by the external electrical impedances [77]. The burning voltage is very low ($\simeq 50$ V at 1 bar in air and 1-mm gap). The stationary values of the center temperature is 5000 K from experiments in [73, 109, 136, 137], and vary only slightly with the arc current [77]. Appreciable radiation losses occur because of longer time for emission and no radiation trapping. As in the breakdown phase, increased energy affects arc size [72] and not much the temperature [77]. Large eddies may change the plasma location. During this time the first chemical reactions take place at the boundary of the plasma kernel.

The third and final phase, the glow, is characterized by current below 0.1A. The steady-state values for the kernel temperature is 3000 K [77].

Theoretical models for the spark process can be found in [114] and numerical simulations in [61, 93, 124, 129, 130]. An example of a reduced order to describe this phase can be found in [85]. According to [43], the duration of the spark effect on the ensuing flame is between 0.4 and 1.1 ms.

2.2   Kernel Formation

The process of kernel formation in sprays is the following: First, individual droplets ignite, then their flames merge to form a "distorted and highly-curved flame sheet" [96] as shown in Fig. 2-2, which is a DNS study of a homogeneously distributed monodisperse spray in air with a detailed n-heptane chemical scheme. The wrinkling
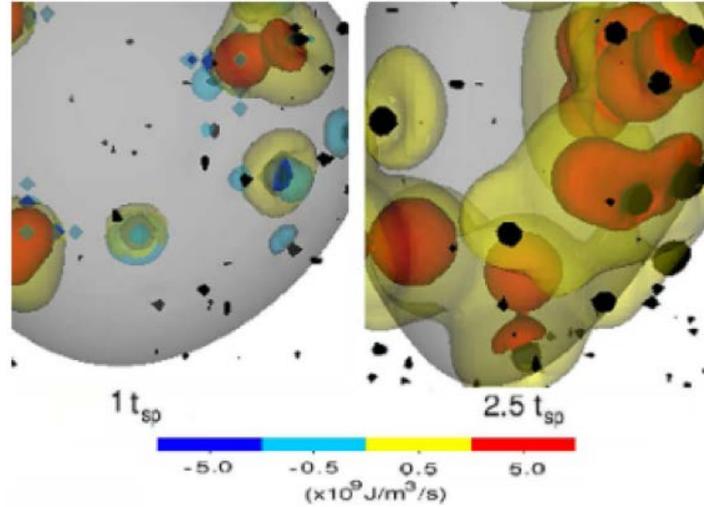
Figure 2-2: Isosurface of heat release (colors) and isosurface of T=1400K (in grey) of a DNS of a monodisperse spray of droplets in homogeneous isotropic turbulence. Left images shows the formation of flame around droplets. Right image shows its merging in a wrinkled flame [96]

comes from large variations of mixture fraction in the inter-droplet space [82]. In this phase, the chemical heat release must overcome the rate of heat losses to the surroundings for the kernel to survive. Small kernels cannot survive the heat loss rate and are generally quenched. During the early instants of the kernel growth, the flow is laminar because of the small size of the kernel and the increase of viscosity with temperature [46].

The success in this phase is usually studied by the concept of minimum ignition energy (MIE) which is the value of energy that allows for 50% of probability of successful ignition [13]. The stochastic character of ignition originates from turbulence inducing mixture fraction fluctuations [22], and velocity fluctuations at the spark location [10]. MIE depends on several factors [36]:

- Igniter parameters: The electrode geometry and the temporal power supply distribution control the spatial distribution and intensity of the deposited energy.

- Gas-phase parameters: The mean and fluctuating flows have a direct impact

through mixing while local conditions may favor or disadvantage chemical activity. This effect is illustrated in Fig. 2-3.

- Liquid-fuel parameters: Volatility and spray characteristics such as droplet density and size distribution are of primary importance for the vapor distribution.

MIE can be defined as [13]:

$$MIE = C_{p,A}\rho_A \Delta T_{st} \frac{\pi}{6} d_q^3 \tag{2.1}$$

where $C_{p,A}$ is the specific heat at constant pressure of the air mixture, ρ_A its density, ΔT_{st} is the temperature difference to reach the stoichiometric flame temperature and d_q is the quenching distance. Ballal and Lefevbre [14] performed measurements of quenching distance for different pressure, velocity, turbulence intensity, turbulence scale and equivalence ratio in gaseous mixtures and found the following dependencies for different turbulence levels:

$$d_q = \frac{\frac{10k}{c_p\rho}}{S_L - 0.16u'} \quad for \quad u' \leq 2S_L \tag{2.2}$$

$$d_q = \frac{\frac{10k}{c_p\rho}}{S_T - 0.63u'} \quad for \quad u' > 2S_L \tag{2.3}$$

where λ, ρ, c_p being respectively the heat conductivity, density and specific heat at constant pressure of the air mixture and S_L, S_T are respectively the laminar and turbulent flame speeds. A rise in the mean flow velocity increases heat losses and consequently increase the value of MIE.

Ballal and Lefevbre [17] investigated the influence of the liquid phase on the MIE for several SMD (Sauter Mean Diameter). The presence of the liquid phase generally increases the MIE with respect to gaseous fuels due to the necessity to evaporate droplets [14, 15, 16, 17, 70]. Lefevbre [70] describes the dependency of quenching dis-
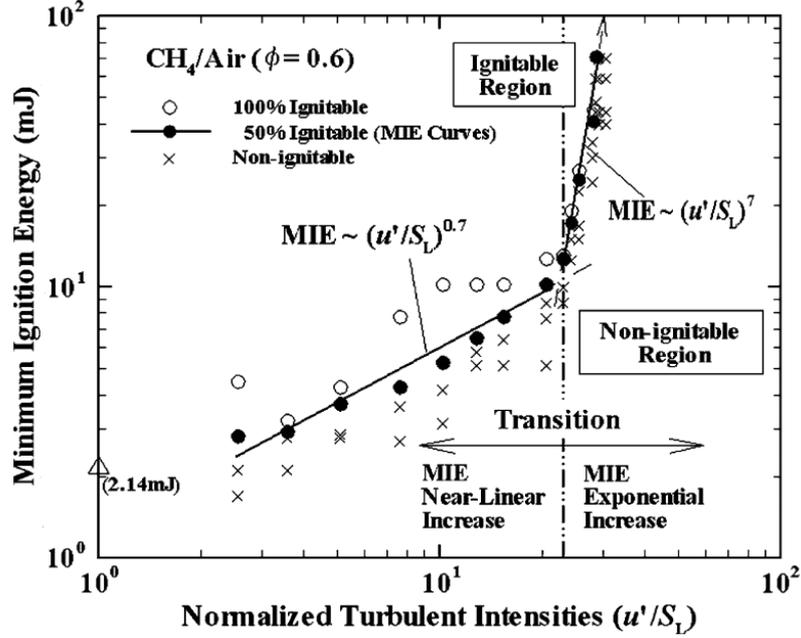
Figure 2-3: MIE of a uniform methane-air mixture in isotropic turbulence for different turbulent levels showing a change of behavior at $\frac{u'}{S_L} \approx 20$ [55]

tance in presence of a polydisperse spray and considering finite-rate chemistry as:

$$d_q = \left[\frac{\rho_F D_{32}^2}{\rho_A \phi \ln(1 + B_M)} + \left(\frac{10\alpha}{S_L} \right)^2 \right]^{0.5} \qquad (2.4)$$

where ρ_F is the fuel density, D_{32} is the Sauter mean diameter, ρ_A the air density, B_M is the mass transfer number at the steady-conditions during evaporation ($B_M = (Y_s - Y_\infty)/(1 - Y_s)$ with Y_s the mass fraction of fuel at the droplet surface) and α is the thermal diffusivity of the gaseous mixture.

The dependency of MIE on pressure varies between $MIE \propto p^{-0.5}$ when evaporation is the sole limiting factor and $MIE \propto p^{-2}$ when chemical effects control ignition [70]. A comparison with experimental results is presented in Fig. 2-4 and 2-5.

On the other hand, it has been shown both analytically [6] and experimentally [41,126] that the MIE in a spray can have a minimum for droplets with an intermediate

46
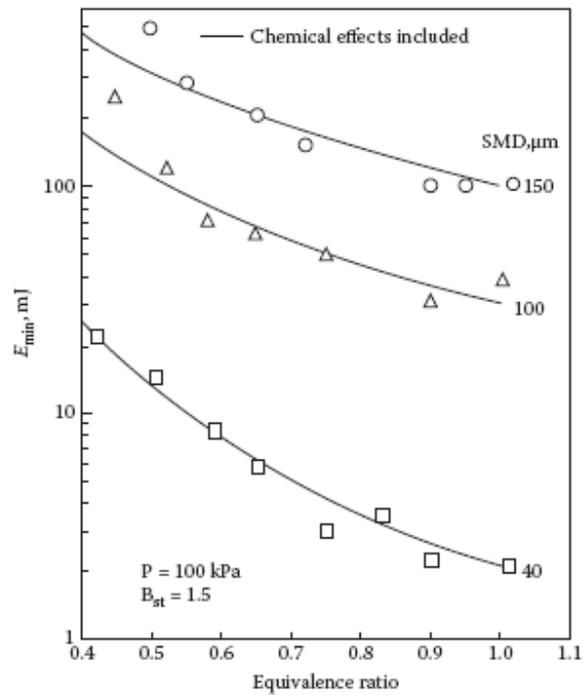
Figure 2-4: MIE for heavy fuel at quiescent conditions showing fair agreement for experiments and the analytical formula in Eqs. 2.1 and 2.4 [17]
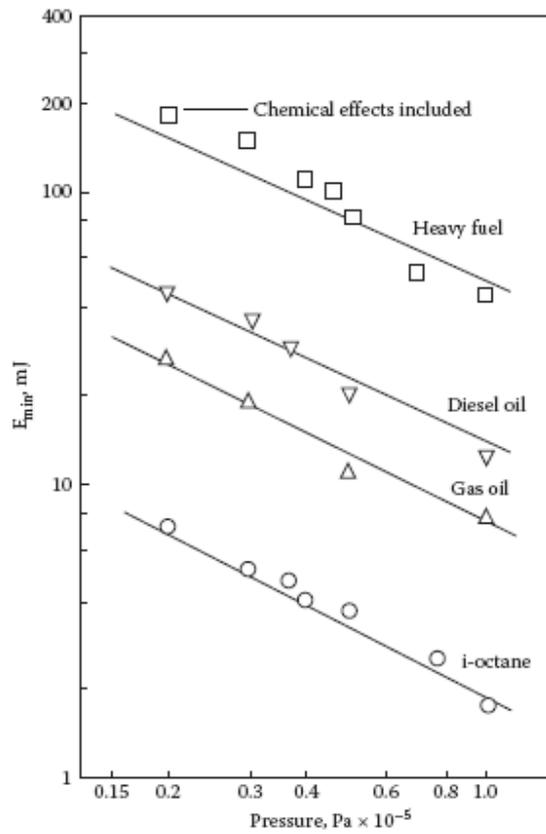
Figure 2-5: MIE dependence with pressure for mean flow velocity=15 m/s, ϕ=0.65, SMD=60μm showing fair agreement for experiments and the analytical formula in Eqs. 2.1 and 2.4 [17]

size. This is explained by the fact that intermediate size droplets can maximize the region under stoichiometric conditions, which enhance reactivity. For this same reason, the flame speeds in two-phase flames can be higher than the case where the fuel had been completely vaporized [54, 88, 89, 106].

Higher volatility lowers MIE, and a small percentage of volatile fuel blended with a less volatile component can significantly enhance the spray ignition properties [69].

Several researchers [41, 52] found a minimum for MIE at equivalence ratio ranging between 1 and 2. Both the optimum equivalence ratio and the optimum diameter vary according to fuel volatility, for a more volatile fuel it leads to a decreasing value of diameter [5]. For each equivalence ratio, there is an optimum diameter and vice versa. The optimum droplet diameter decreases as the oxygen mass fraction is increased.

Turbulence affects spray ignition in a similar way to gaseous fuels [82]. The increase in turbulence intensity for a particular length scale leads to higher heat losses from the kernel to the surroundings [138]. The effect of turbulence on the kernel structure depends on the relative size of the eddies to the kernel [3], which may be evaluated with the ratios u'/S_L and L/d_k where u' is the velocity fluctuation, S_L the laminar flame speed, L a turbulent scale and d_k is the kernel size. If kernel is small compared to the turbulent scales, it is convected by eddies. If they are of similar size, the kernel is broken up. In this regime, vortices enter the preheat layer of the flame [46]. Finally, if the kernel is much larger than the turbulent scales, the kernel surface is wrinkled. These effects are summarized in Fig. 2-6.

The overall growth rate of the kernel during the laminar phase strongly depends on the Lewis number of the fuel: for $Le_F < 1$ (e.g. hydrogen-rich flames), the stretch increases the flame consumption rate. The opposite happens for $Le_F > 1$ (e.g. propane) [46]. Therefore the Lewis number plays a role in the growth of the kernel during the first instants.

The probability for the kernel to grow (P_{ker}) is usually, but not directly, correlated
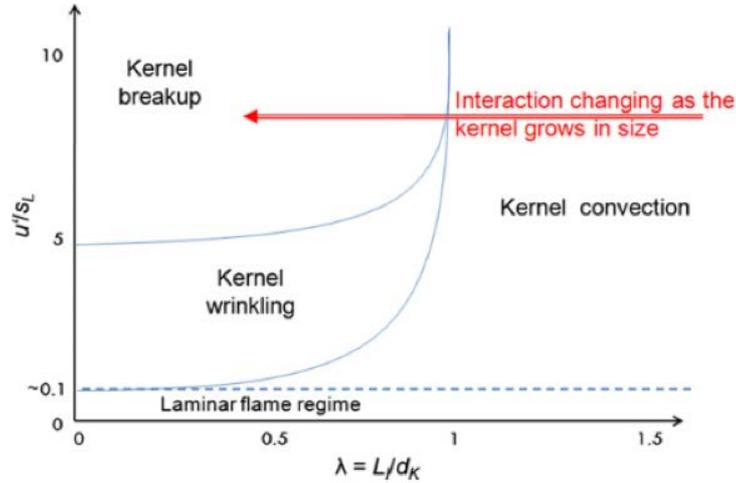
Figure 2-6: Turbulence regime map [3]

to the probability of finding a flammable mixture mixture at the spark position (F). In particular, P_{ker} can be smaller than F because intense strain or scalar gradients quench the kernel [82]. On the contrary, P_{ker} can be bigger than F if enough heat from the spark is diffused into a flammable region, as observed in [9, 11].

2.3   Flame Growing beyond the Integral Length Scale

After the kernel has grown to the size of the integral length scale, its evolution will depend on the conditions encountered during the flame propagation [29, 116]. Depending on the homogeneity of the mixture, two different flame growth modes are found. If there are large mixture fraction fluctuations, the flame develops in an edge flame mode [82]. In this regime, flame speed is small and lower than the unstretched laimnar flame speed $S_{0,L}$. Turbulence levels decrease flame speed in this regime. Furthermore, this flame, expanding spherically, can be quenched by stretch. Figure 2-7 shows an edge flame.
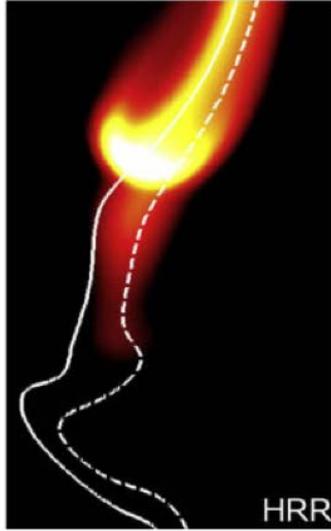
Figure 2-7: Edge flame [59]

On the other hand, if the kernel develops through regions of homogeneous mixture fraction, the flame evolves as a premixed or stratified flame. The propagation speed of these flames is higher and increase with higher turbulence intensity. Several types of the previously described flames (edge, stratified and premixed) can co-exist in this phase [82]. For rich mixtures, the flame speed can be large due to the presence of stoichiometric conditions in the inter-droplet region. Also, for rich sprays the droplets can reach a hot zone with low O_2 concentration, which causes pyrolysis, which creates hydrogen and acetylene which in turn increase the flame speed [82].

Success in this phase does not only depend on the value of the mixture fraction at the spark location but also on the conditions encountered during the flame growth [30, 116]. For that purpose, some authors use the Karlovitz number to determine success of this stage [38] despite not being the only decisive parameter [82]. Failure in this phase is related to the second mode or "long" failure mode discussed in [82] which consists in an ignition sequence in which a flame kernel is formed but it fails to result in a self-sustaining flame due to excessive heat losses or aerodynamic quenching (reduced flame residence time) or fuel starvation.
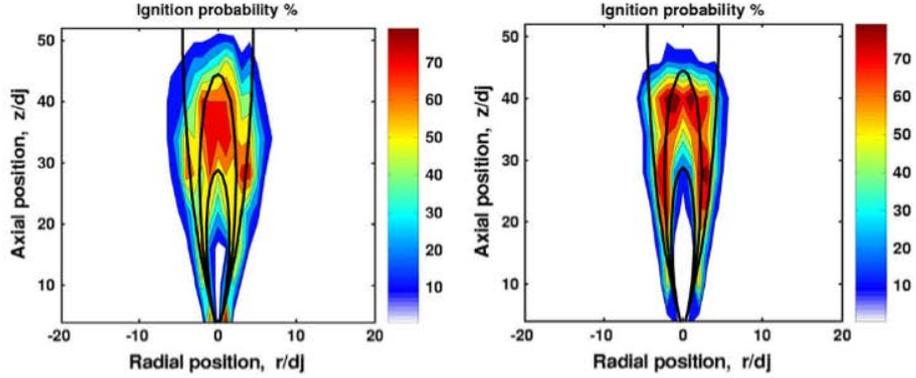
Figure 2-8: Ignition probability map with contours of flammability limits, the black line indicates unity equivalence ratio, showing correspondence of high success rate with stoichiometric conditions [10]

Experiments [10, 113, 116] have shown correspondence between higher success rate in this phase when sparking in regions where equivalence ratio is close to 1, flow velocity favorable for upstream flame propagation, and the turbulence level and fuel mass ratio giving high initial kernel survival rates. An example of this is shown in Fig. 2-8.

In the case of liquid fuels, different modes of flame propagation can be found depending on the group combustion number (a measure of the number and relative size of droplets and the spray size) and the equivalence ratio. The group combustion number G has several definitions depending on the author. A comprehensive set of definitions can be found in [12] and [98]. In the study [43], the definition in Eq. 2.5 is used. Three flame propagation modes are distinguished in the study by [43], which consists of an ignition study of aviation-fuels by a laser device: gaseous-like propagation, droplet propagation and inter-droplet propagation. The conditions for each propagation mode is shown in Fig. 2-9 and are described in detail in the following paragraphs.

$$G = 3(1 + 0.276 Re_d^{0.5} Sc^{1/3}) Le N^{2/3} \frac{d}{l_d} \qquad (2.5)$$

where Re_d is the droplet Reynolds number, and Sc and Le are the Schmidt number and the Lewis number of the fuel vapour- air mixture respectively. The parameter d is the Sauter mean diameter (SMD), N the number of droplets in the cloud and l_d the mean droplet spacing.
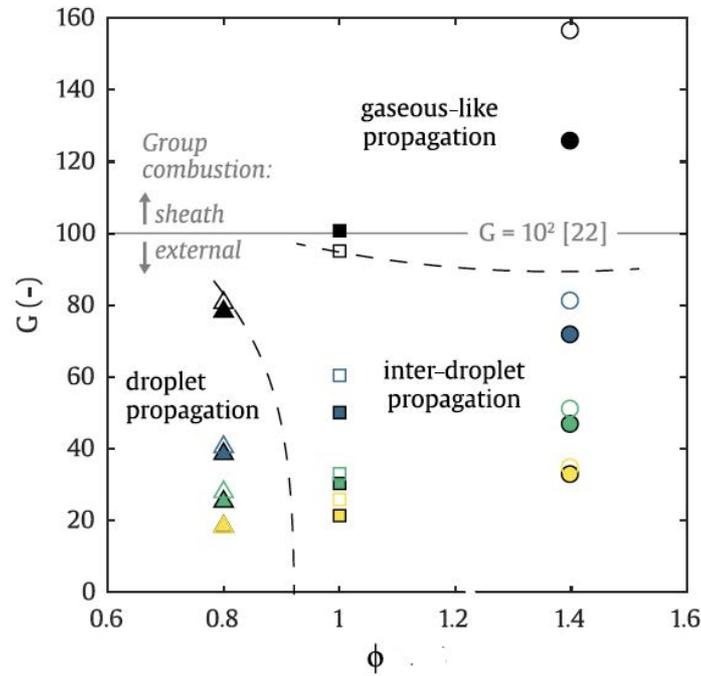
Figure 2-9: Different ignition modes depending on the group combustion number (G) and equivalence ratio for two different fuels (Jet A, hollow points) and a renewable fuel (ATJ-8, filled points) [43]. Black, blue, green and yellow colors correspond to a SMD of 15, 20, 27, 33 μm

First, the droplet-propagation mode consists of concentrated reactions around large droplets or groups of droplets immediately next to the spark. The space between droplets features a very lean mixture. Local diffusion flames appear surrounding droplets [96]. The flame front propagates towards the fresh mixture due to the burning droplets. This regime is characterized by low heat release levels and successful flame propagation is conditional on the proximity of groups of droplets to the front which can be ignited. Figure 2-10 shows OH* and OH*/Fuel images for this regime.
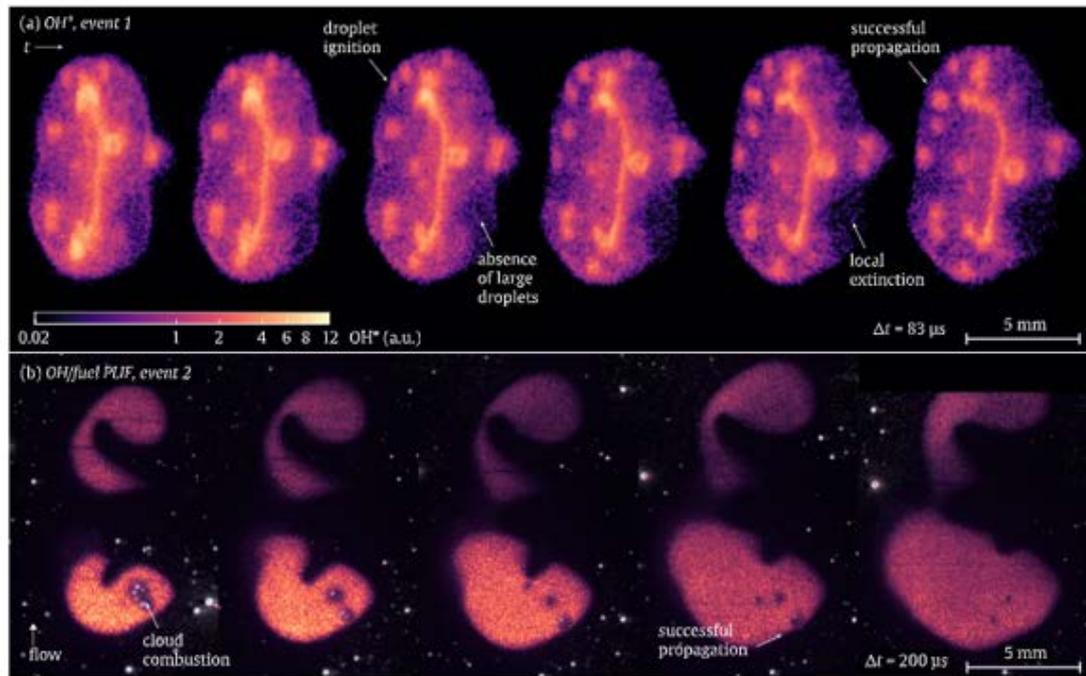
Figure 2-10: (a) OH* and (b) OH/fuel PLIF images indicating heat release zones and physical effects for the droplet propagation regime [43]

The other two modes (interdroplet propagation and gaseous-like propagation mode) have higher heat release rates and are less dependent on the fuel mixture fraction near the initial kernel. The inter-droplet propagation regime consists of a field of droplets surrounded by a more homogeneous fuel gas fraction, with the equivalence ratio near the droplets richer than the total equivalence ratio. In this regime, large droplets can pass through the flame, and evaporate shortly after generating curvature in the flame as shown in Fig. 2-11.

Lastly, in the gaseous-like propagation, there is a fully gaseous preheat layer where combustion occurs. Figure 2-12 and 2-13 shows OH* and OH*/Fuel images for the inter-droplet and gaseous-like regimes.

DNS of sprays [95,138] and stratified gaseous mixtures [29], indicate that mixture non-uniformities create regions near stoichiometry which may produce high reaction
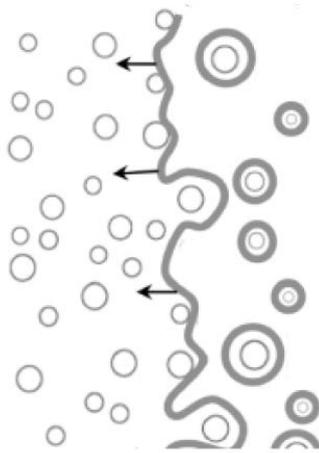
Figure 2-11: Flame curvature induced by droplets evaporating in the flame region
[98]
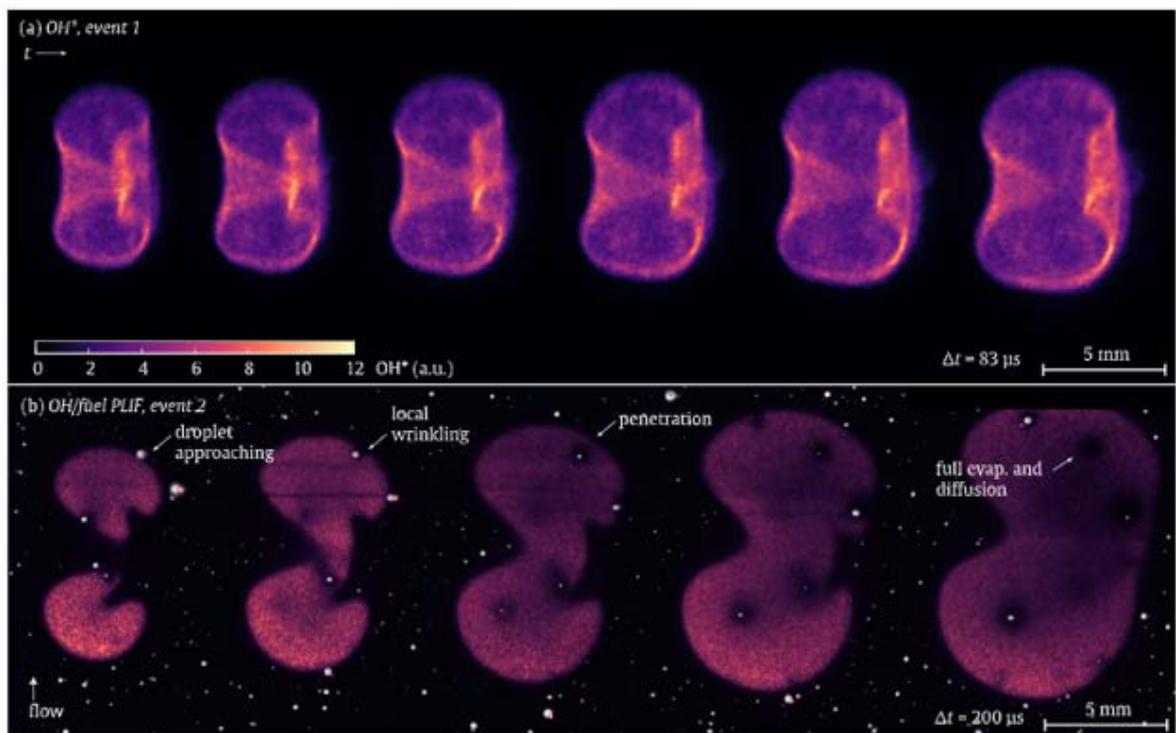
Figure 2-12: (a) OH* and (b) OH/fuel PLIF images indicating heat release zones and
physical effects for the inter-droplet propagation regime [43]
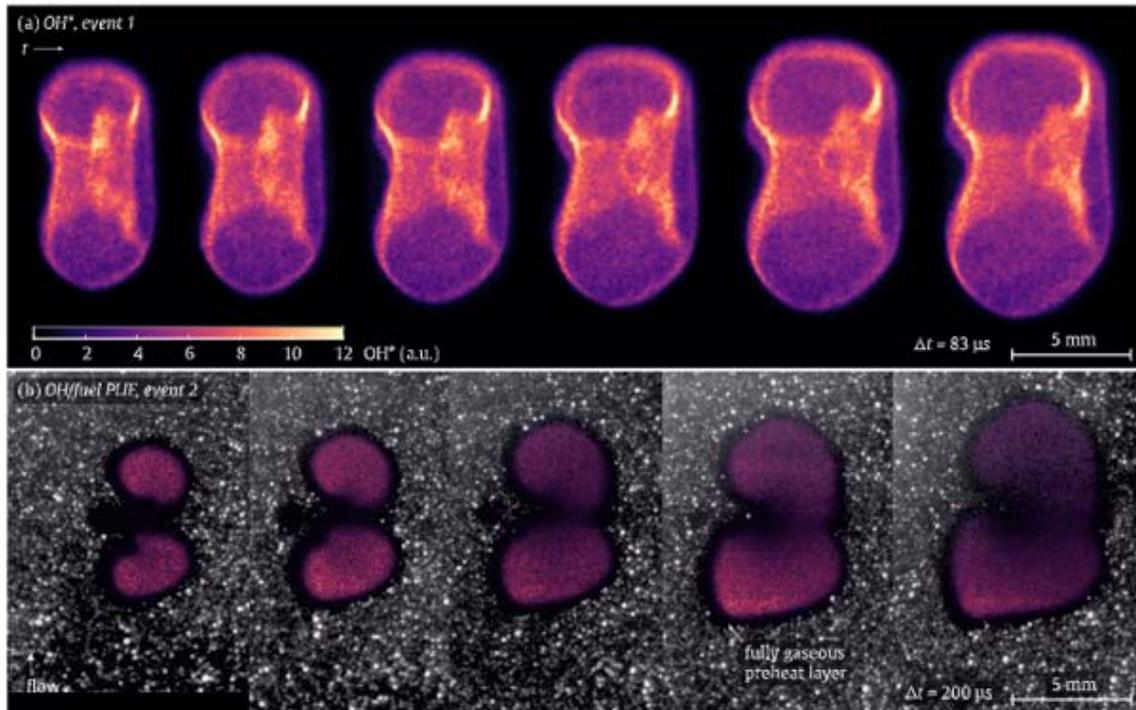
Figure 2-13: (a) OH* and (b) OH/fuel PLIF images indicating heat release zones and physical effects for the inter-droplet propagation regime for the gas-like propagation regime [43]

zones and lead to an enhanced overall ignition of the flame.

For lean conditions, increasing SMD leads to higher flame velocity, although the flame velocity remains low (close to 0.1 m/s). For rich mixtures, increasing SMD reduces flame velocity. In addition to that, for rich mixtures, increasing the turbulence up to $u'/s_L = 2$ has been found to increase the flame speed [42].

2.4 Burner Ignition

Success in this phase consists in the flame reaching a stable position. Experiments [9,71,79] show that the flame must be trapped by the recirculation zone, have enough time to grow, and also be able to ignite the region near the anchoring point.

Failure in this phase can occur in different modes [9, 71, 79]:

1. "Extinction" failure mode in which the ignition kernel moves upstream to the central recirculation zone and it is quenched while being transported. It is related to the kernel experiencing heat losses to the fluid for a long time while it travels from the igniter to the flame anchoring position.

2. "Downstream movement" in which the kernel moves downstream where little fuel exists.

3. "Breakup" failure mode in which the ignition kernel breaks up and the individual pieces do not have enough energy to establish a stable flame. It takes more time than the "extinction" and "downstream" failure modes, possibly due to multiple breakups.

The probability of success in this phase was studied in [9] in a bluff-body burner when changing air, fuel (methane) and swirl velocities, and this is shown in Fig. 2-14. All cases showed highest probability of ignition when sparking near the bluff body edges. The case without swirl ($\phi = 0.55$) indicated that the regions which had the highest probability for ignition were close to the regions at stoichiometric conditions. While increasing fuel and swirl did not produce qualitative changes in the probability map, increasing air resulted in an increase of probability in the entire span immediately downstream the bluff body. The high strain rate cases had a smaller burner ignition probability, and ignition was not possible when the strain rate was about 90% of the extinction strain rate of the stable flame, which is in agreement with [116]. Finally, the case with swirl (60° vane angle, $\phi = 0.55$) showed an overlap of ignition probability regions with high flammability factor regions (flammability factor defined as the probability of having an equivalence ratio inside the flammable limits).

The work in [79] studied the influence on ignition of a single spark versus intermit-
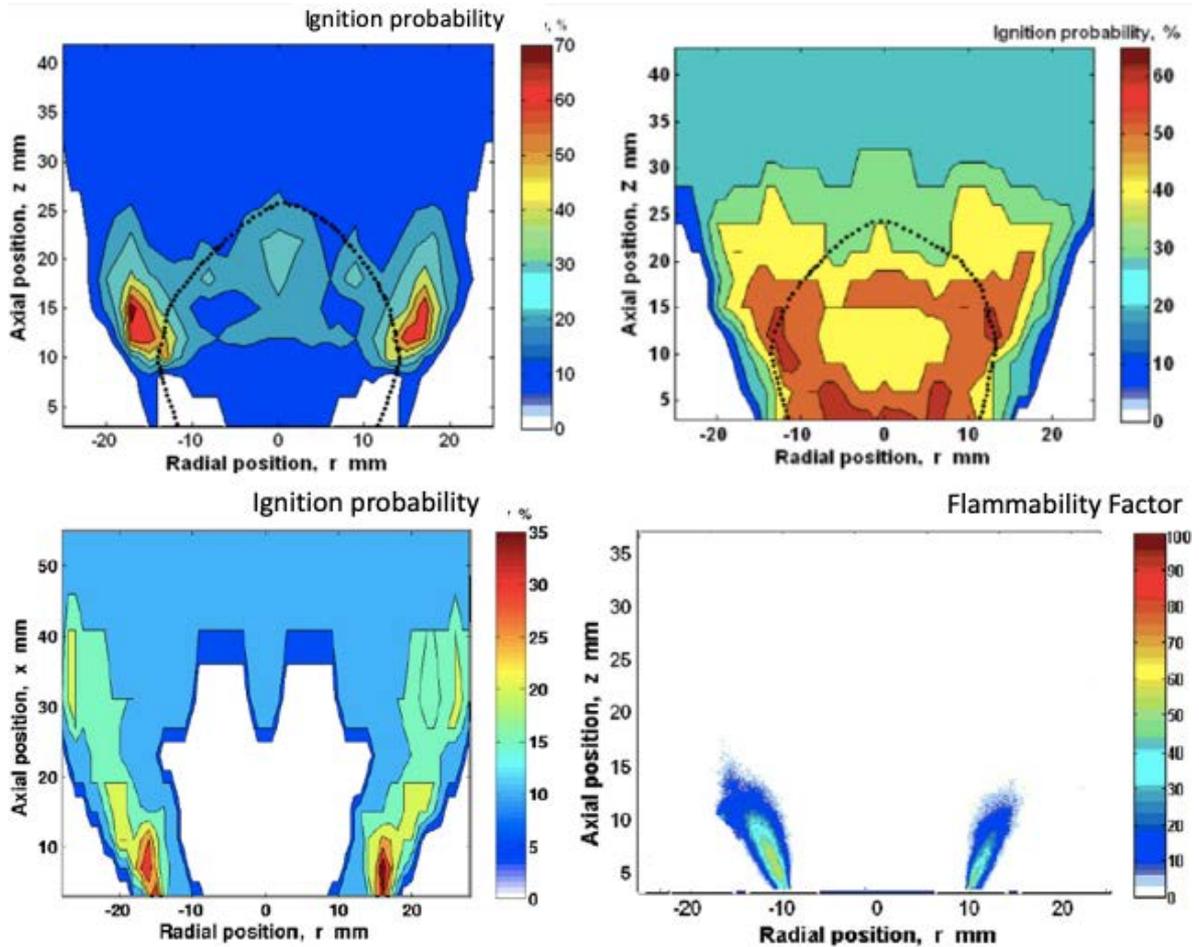
Figure 2-14: Burner ignition map. Top left: base case (no swirl, $\phi = 0.55$, $U_{fuel} = 5$ m/s ,$U_{air} = 10$ m/s) showing the highest ignitability regions close to the ξ_{stoch} contour indicated by the black dotted line. Top right: Increased air velocity case (no swirl, $\phi = 0.55$, $U_{fuel} = 7.5$ m/s, $U_{air} = 15$ m/s) showing an increase of burner ignition probability in the entire span immediately downstream the bluff body. Bottom: base case with a 60° vane swirl showing correspondence between ignition probability (left) and flammability (right) [9]

tent sparking applied to a spray of n-heptane. The results were different for the two cases. For the single spark, the most successful conditions occurred when the spark is located inside the spray, in a region with velocity towards the bluff body, small SMD, and equivalence ratio within the flammability limits. In this case, successful ignition was related to flamelets propagating back towards the spray injector. On the other

58

hand, the case of multiple sparks reached 100% probability when sparking at an axial distance which coincides with the maximum width of the recirculation zone, including regions where the single spark could not ignite. In both the single and multiple spark settings, the successful cases were those in which the kernel could move towards the bluff body without being quenched. None of the sequences tested ignited the burner when sparking at a distance of two burner diameters downstream the bluff body. A sketch of the regions with highest probability is shown in Fig. 2-15.
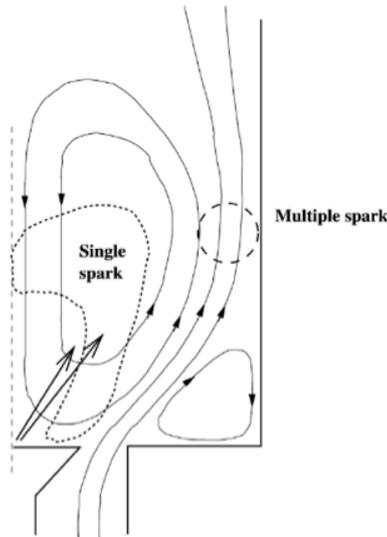
Figure 2-15: Sketch showing the regions with highest probability of ignition for the single and the multiple spark case for an experiment featuring a spray of n-heptane [79]

The combination of (fuel-air ratio) FAR and combustor liner velocity create a limit of ignitability as shown in Fig. 2-16. This relationship can be equivalently expressed in terms of FAR and pressure loss across the combustor. According to [86], the reduction in ignitability for a low pressure drop across the combustor is explained by low air velocity leading to a less homogeneous mixture of fuel and air and an atomization consisting of larger droplets which take longer to evaporate.
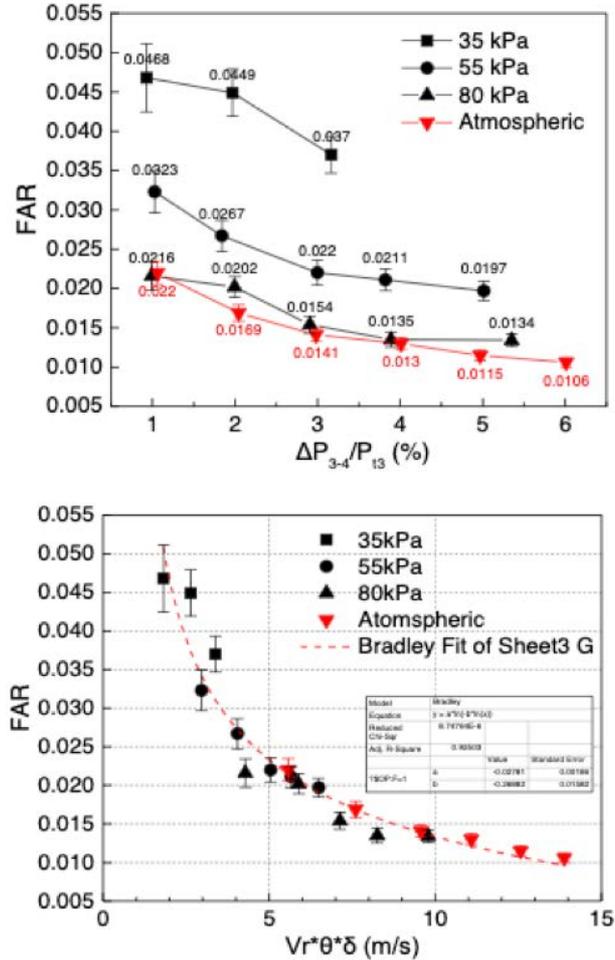
Figure 2-16: Burner ignition boundary line indicated by minimum fuel-air ratio (region above line permits burner ignition) depending on pressure loss across combustor ΔP and lining velocity v_r at different operating pressure. The bottom figure uses the non-dimensional temperature $\theta = T/(288\ K)$ and pressure $\delta = p/(1\ bar)$ [86]

2.5 Inter-Burner Propagation

The final phase consists in the flame propagation between injectors until all injectors hold stable flames. The ratio of inter-swirler space to swirler diameter affects the speed and flame propagation mode. Computations using methane as fuel [18] found that low spacing in a linear array of swirlers (KIAI experiment at Coria) promoted a rapid suction of hot gases by the neighbors leading to a spanwise flame propagation

mode. On the other hand, for high inter-injector spacing, a different flame propagation was found in which hot gases travelled downstream a significant amount before being able to ignite neighboring burners. This mode was named "arc mode". These two modes are shown in Fig. 2-17. The propagation speed for the spanwise mode was double of the arc mode. Computations for the same experiment but using liquid fuel (n-heptane) [36] retrieved the same two inter-burner propagation modes. The thesis in [36] underlined that the spanwise mode is controlled by burnt gas expansion, which leads to short ignition times and low variability. On the other hand, the "arc" mode is controlled by local flame-turbulence interaction and mixing properties along the flame propagation path, which leads to longer ignition and more variability. Experimentally, these modes were found in [80].

Figure 2-17: Above: spanwise mode of propagation for low inter-burner space. Below "arc" mode for high inter-burner space [18]

In both computational studies [18, 36], ignition was simulated using the energy deposition model developed in [65]. While [18] made calculations using a two step chemistry, calculations in [36] were done with ARC chemistry.

Lancien [68] performed a computational study of the light round in the MICCA

spray experiment and it is shown in Fig. 2-18. This setup emulates a helicopter combustor. This study used an Eulerian treatment for the liquid phase, a 2-step chemical scheme developed in [98,125] and the thickened flame model [35]. The same setup was calculated in [36] using an Euler-Lagrange treatment. The results in [68] showed that the volumetric expansion of the burning gases accelerates the flame displacement in the following way: the burnt gases tend to expand, which generates an azimuthal flow in the burnt and fresh gases, which accelerate flame velocity, which creates more burnt gases and the loop is closed. Thus, azimuthal velocity is increased, and a constant value is attained when the flame starts to propagate in two fronts in opposite directions. This effect, named as "thrust effect" by [68], had been already mentioned in the seminal calculation by [23] and its effects can be observed in regions several sectors ahead of the flame.
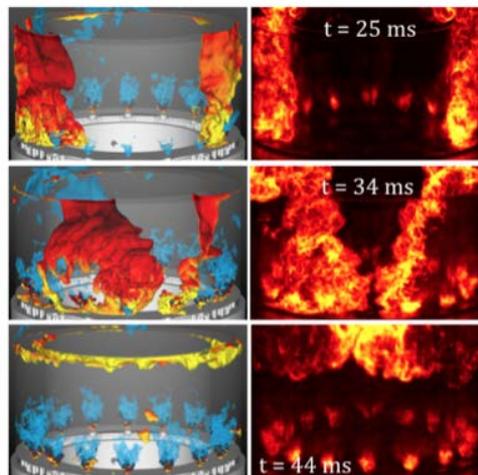
Figure 2-18: Ignition sequence in MICCA experiment, (left) LES calculations, (right) experiments [68]

The "thrust effect" also affected the sprays, with droplets pushed towards the flame [36,68]. Consequently, the flame burns at an overall richer condition than the one provided by injection as seen in Fig. 2-19.

Heat losses can have an important effect on the development of this phase. Lancien
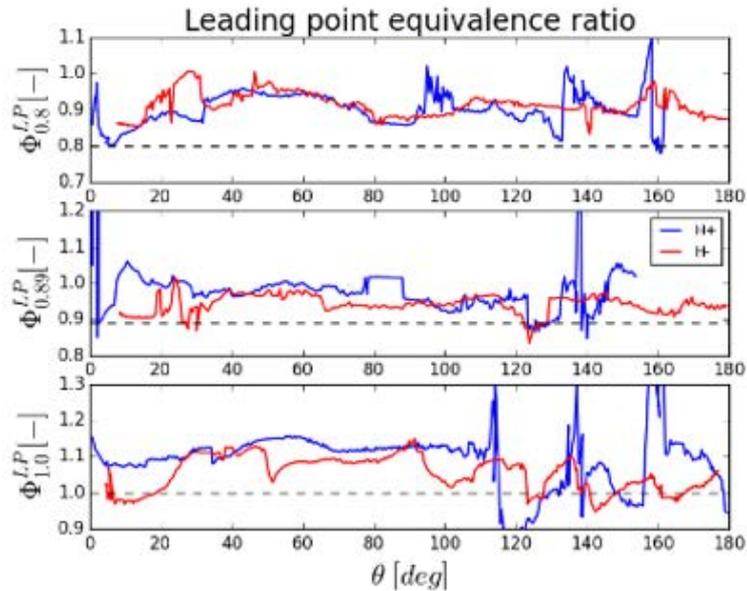
Figure 2-19: Equivalence ratio at the leading point along the azimuth of the rig during ignition (MICCA experiment) showing richer conditions than the ones at the injection point marked by black discontinuous line [68]. H+ indicates the flame branch travelling in clockwise direction and H- the one travelling anticlockwise.

[68] exposed that light-around time for the case for walls at steady temperature is 50% less than that of the case where the walls are at ambient temperature. This same reduction coincides with the amount of heat losses transferred through the walls for the case where walls were at ambient temperature as shown in Fig. 2-20. In addition to that, the study in [68] indicates a 2% difference in the light around time when radiative effects were considered.

The simulations performed in [68] show an agreement within 7% with experiments for the case of pre-heated walls and equivalence ratio less than one. Differences are of the order of 25% for stoichiometric conditions and the case with walls at ambient temperature. One of the possible explanations for the discrepancies in the case at stoichiometric conditions is the inaccuracies of the combustion model employed in this case, where there is the highest equivalence ratio inhomogeneity and overall rich
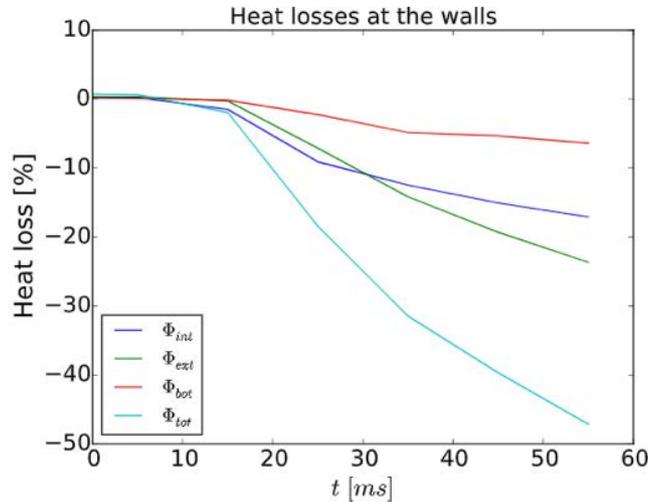
Figure 2-20: Heat flux evolution vs time. Blue is the heat transferred across the inner radius wall, green: outer radius wall, red: chamber bottom, cyan is the total heat transferred [68]

conditions (bottom image of Fig. 2-19). The differences found for the cold wall case were attributed to inaccuracies of the wall model employed. Figure 2-21 shows a comparison of experimental and computation results.

Both Euler-Euler [68] and Euler-Lagrange formulation studies [36] show differences smaller than 5% in the flame propagation during the phase of flame propagating in fronts.

Collin [36] underlined the difference in equivalence ratio homogeneity seen by the fronts propagating in opposite directions. The front propagating in the opposite direction to the swirler motion (H-) sees a more homogeneous flow. This is explained by the fact that the H- branch faces pushing in the favorable velocity direction when propagating in the inner radius, and propagates along the bottom of the chamber, at a more homogeneous condition. On the other hand, the opposite branch H+, also initially propagating along the inner radius, experiments opposite pushing by the swirler-induced flow, and propagates at a higher axial location, which is less heterogeneous during the light-around process. This is shown in Fig. 2-22. A top
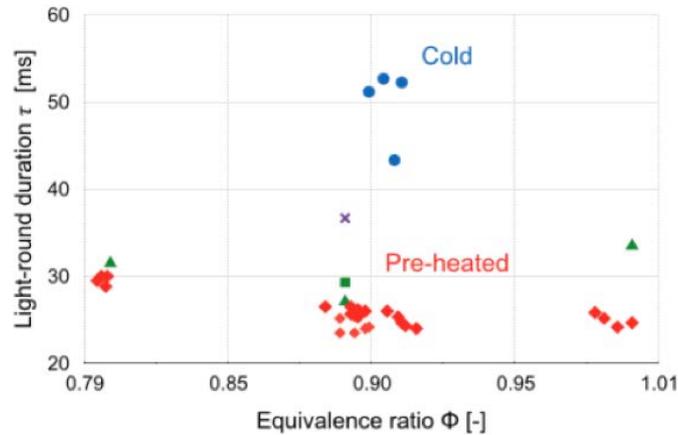
Figure 2-21: Comparison of CFD results to experiments for light around duration in the MICCA experiment. Red diamods are experimental results for the case where walls are preheated, green triangles are CFD results for the same conditions, blue circles are experimental results for the case where walls are at ambient temperature, the purple cross indicates CFD result for that condition.

view of the leading point evolution is shown in Fig. 2-23.

Boileau [23] described the ignition sequence in an helicopter combustor using an Eulerian treatment and liquid fuel (JP10). In this case, the author claimed that chemistry did not have a direct impact on trans-injector flame propagation speed since equivalence ratio fluctuations were found not to be generally related to trans-injector flame propagation speed fluctuations. This claim is restricted to cases where the spray is fully vaporized and there is a homogeneous field in equivalence ratio. The vortex field was not symmetric with respect to the igniter axis as shown in Fig. 2-24 and, in this case, vortex aerodynamics were responsible for the variations in trans-injector flame propagation speed. These variations also generated flame front curvature changes: wrinkled when approaching the injector location, blunter at the injector location.

In this case, three types of ignition times variations were observed:

1. An sector-to-sector variation depending on the axial position of the leading
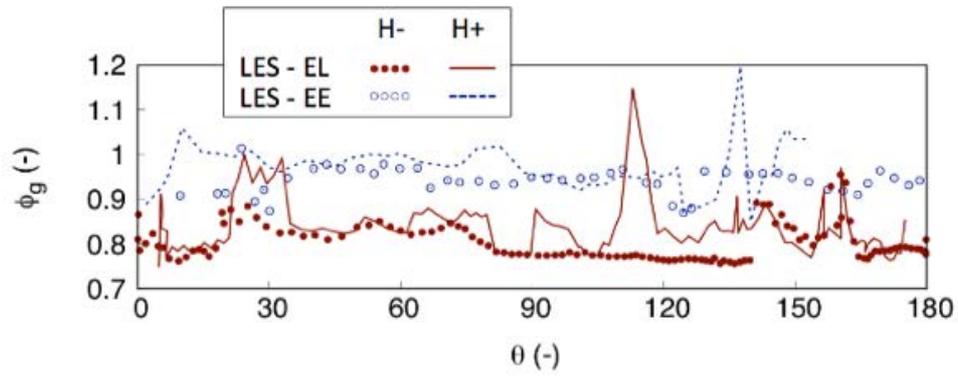
Figure 2-22: Equivalence ratio variation encountered by the leading point showing higher inhomogeneity for the H+ branch (clockwise direction). MICCA spray experiment LES simulations [36]
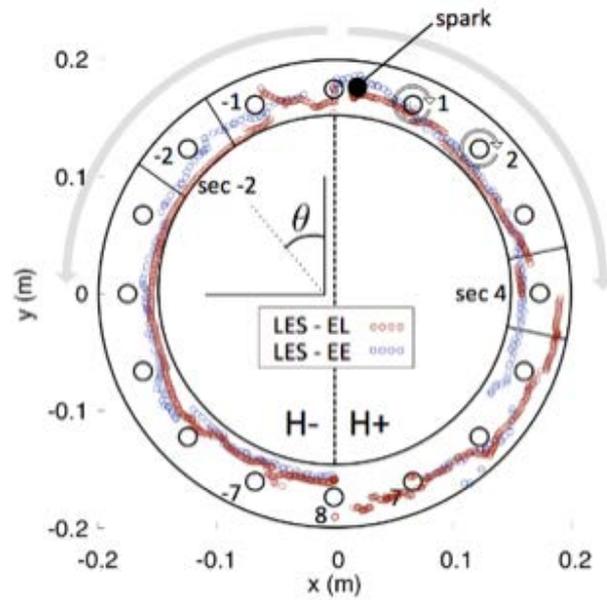
Figure 2-23: Top view of the leading point evolution in the MICCA spray experiment LES simulations [36]
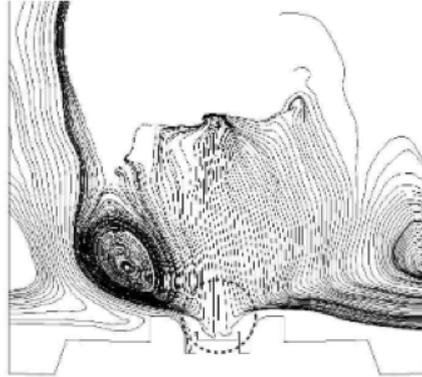
Figure 2-24: Vortex aerodynamics asymmetry with respect to the axis for the setup in [23]

point.

2. A quadrant-to-quadrant variation according to the azimuthal direction of the flame progress. This variation was also due to the asymmetric vortex field, which favors propagation in either clockwise or anticlockwise direction. Figure 2-25 shows the flame propagation.

3. Both quadrants and sectors variations due to randomness of the turbulent resolved structures.

The spinning combustion technology shares most of the above-cited inter-burner propagation characteristics. However it also introduces specific challenges due to the particular arrangement of the injectors, enhancing flame kernel convection in the azimuthal flow. It is therefore possible that the stability of combustion at one injector depends on the conditions on the injectors upstream. Finally, SCT is a relatively modern technology and, consequently, there is no established model to study ignition and the available literature is less wide than for conventional engine designs.
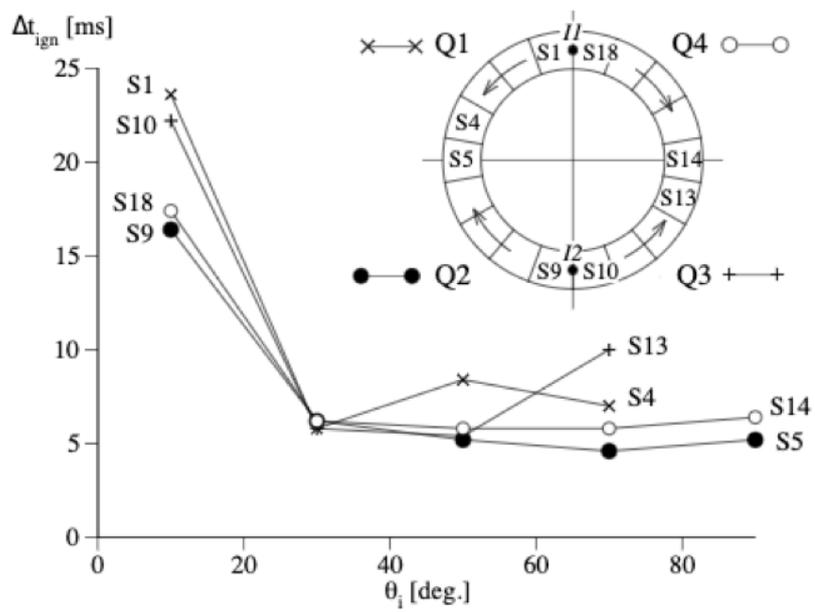
Figure 2-25: Ignition time variation showing that anticlockwise sectors (e.g. 1-4) have higher delays with respect to clockwise (e.g 18-14) [23]

Chapter 3

Theoretical and Numerical Concepts of Combustion

Contents

This chapter covers some of the theoretical basis of laminar and turbulent combustion and its implementation in numerical modelling. Firstly, premixed and diffusion flames are discussed. Some definitions and results are highlighted for both laminar and turbulent regimes. Finally, two-phase flames are covered.

Flame behavior is different depending on the level of mixing between the fuel and air before combustion. If fuel and air are homogeneously mixed, the result will be a premixed flame. Otherwise, the result is a diffusion flame. In addition to that, depending on the turbulence regime, two different flame structures are found.

3.1   Premixed combustion

Laminar Flames
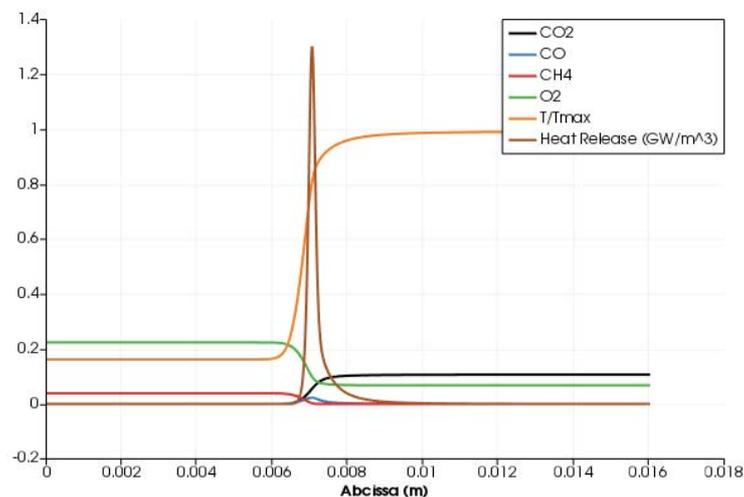
Figure 3-1: Example of a 1D premixed flame. It shows the mass species fractions, temperature and heat release variation across the flame.

Figure 3-1 shows the typical structure of a laminar premixed flame. It can be divided into three regions:

- The pre-heat zone composed of fresh gases which are heated by thermal diffusion.

- The reaction zone where the temperature is high enough for the chemical reactions to proceed. In this zone, a high number of intermediate species can coexist (e.g. CH_2) even for the simplest fuels.

- The post-flame zone where chemical equilibrium has been attained and it is characterized by the predominance of final combustion products (H_2O, CO_2, CO). Some slow reactions can still occur, for example those corresponding to NO_x formation.

A useful and widely used parameter to describe the flame structure is the progress variable, c. It can be defined based on temperature as in Eq. 3.1 or the mixture composition (Eq. 3.2) where T_f and T_b correspond to the fresh gas and burnt gas temperature respectively and Y_c is any composition index which varies between 0 (when combustion has not started) and Y_c^{eq} (when equilibrium has been reached). A usual definition is $Y_c = Y_{CO_2} + Y_{CO} + Y_{H_2O}$ [56]. The advantages of using the progress variable is the ability to directly compare flames with different flame thicknesses, and the computation of the normal direction of the flame towards the fresh gases as the normalized gradient of the progress variable.

$$c = \frac{T - T_f}{T_b - T_f} \tag{3.1}$$

$$c = \frac{Y_c}{Y_c^{eq}} \tag{3.2}$$

If we assume steady conditions, a 1-step irreversible reaction for chemistry and equal molecular weight, heat capacity C_p and mass diffusion coefficient (D), the equations for a 1D premixed flame take the following form:

$$\rho u = cst = \rho_f S_L \tag{3.3}$$

$$\rho_f S_L \frac{dY_F}{dx} = \frac{d}{dx}\left(\rho D \frac{dY_F}{dx}\right) + \dot{\omega}_F \tag{3.4}$$

$$\rho_f C_p S_L \frac{dT}{dx} = \frac{d}{dx}\left(\lambda \frac{dT}{dx}\right) - Q\dot{\omega}_F \tag{3.5}$$

Premixed flames have an intrinsic characteristic speed, the laminar flame speed s_L. It depends on gases composition, and the pressure and temperature in the fresh gases. From [141], it can be shown that, for one-step chemistry, the laminar flame speed is proportional to the square root of the thermal diffusivity and the Arrhenius pre-exponential constant A.

$$S_l \propto \sqrt{D_{th}A} \tag{3.6}$$

The laminar flame speed typically decreases with increasing pressure [105]. However, the reaction rate increases with pressure because the density increases faster than the reduction in flame speed. On the other hand, the temperature of the inlet gases also affects the flame speed, increasing with higher inlet temperatures since the chemical reactions can occur faster. In addition to that, a characteristic thickness can be defined as in Eq. 3.7, and it is inversely proportional to the laminar burning velocity.

$$\delta = \frac{\lambda_f}{\rho C_p S_l} = \frac{D_{th,f}}{S_l} \tag{3.7}$$

In practice, another definition for flame thickness is usually employed (Eq. 3.8):

$$\delta_l = \frac{T_b - T_f}{\max(\|\frac{dT}{dx}\|)} \tag{3.8}$$

Flame Front Speed Definitions

72

The speed of the flame front can be defined in different reference ways depending on the reference frame [105]:

- Absolute speed: It is the flame front speed in the absolute reference frame. Its value depends on the temperature isoline adopted as the flame front position.

$$S_a = \vec{w} \cdot \vec{n} = \frac{1}{|\nabla\theta|} \frac{\partial\theta}{\partial t} \tag{3.9}$$

  where $\vec{w}$ is the flame speed in the absolute frame, $\vec{n}$ is the normal vector to the flame surface pointing towards the fresh gases and $\theta = (T - T_{fresh})/(T_{burnt} - T_{fresh})$

- Displacement speed: It is the flame front speed in a reference frame that moves with the local flow velocity ($\vec{u}$). In addition to depending on the temperature isoline, it is difficult to measure across the flame since the flow accelerates in this region.

$$S_d = (\vec{w} - \vec{u}) \cdot \vec{n} = S_a - \vec{u} \cdot \vec{n} = \frac{1}{|\nabla\theta|} \frac{D\theta}{Dt} \tag{3.10}$$

- Consumption speed which is only based on reaction rates and does not depend on the spatial position or a temperature isoline:

$$S_c = -\frac{1}{\rho_u Y_u^F A} \int_{-\infty}^{+\infty} \dot{\omega}_F dV \tag{3.11}$$

  where A is the flame surface area and the subscript "u" refers to the fresh or unburnt gases.

These concepts are shown in Fig. 3-2

73
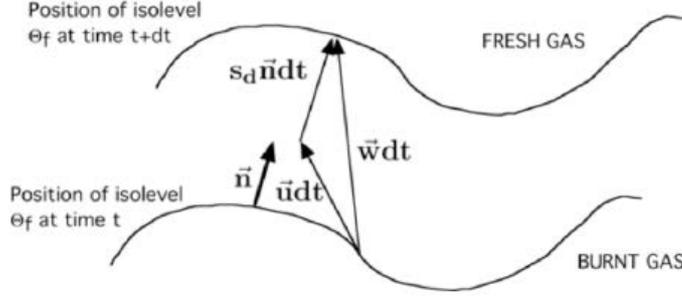
Figure 3-2: Flame speed definitions from [105]

Flame Stretch

A flame changes area due to strain and curvature effects [141]. This change of area (A) is defined as the flame stretch and can be written as:

$$\kappa = \frac{1}{A}\frac{dA}{dt} \qquad (3.12)$$

From kinematic considerations, it can be written as [27]:

$$\kappa = -\vec{n}\vec{n} : \nabla\vec{u} + \nabla \cdot \vec{u} + s_d(\nabla \cdot \vec{n}) = (\vec{m}\vec{m} + \vec{p}\vec{p}) : \nabla\vec{u} + s_d(\nabla \cdot \vec{n}) \qquad (3.13)$$

The first term in the last form of Eq. 3.13 accounts for the deformation along a plane tangent to the flame at the specified point (i.e. the strain), while the second accounts for the deformation along the normal direction to the flame (i.e. the curvature). Flames can experiment different stretch modes as shown in Fig. 3-3.

From asymptotic theories [25, 26, 34, 99], in the limit of small strain and curvature terms, the flame structure and velocities depend only on stretch through a linear relationship as indicated in Eqs. 3.14.
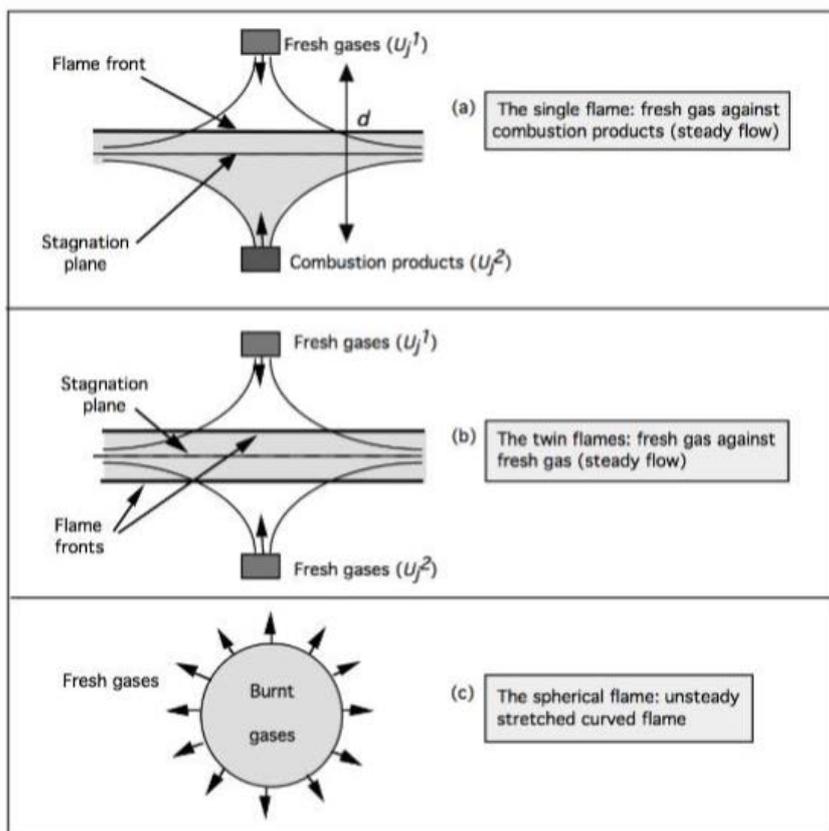
Figure 3-3: Examples of stretched flames [105]. The first two are purely strained flames, while the bottom one experiments only curvature

$$\frac{S_d}{S_l} = 1 - Ma_d \frac{\delta_{th}}{S_l} \kappa \tag{3.14}$$

$$\frac{S_c}{S_l} = 1 - Ma_c \frac{\delta_{th}}{S_l} \kappa \tag{3.15}$$

Ma_c and Ma_d are the Markstein number for the displacement and consumption speeds, and are proportional to $(Le_{fuel} - 1)$. When $Le_{fuel} > 1$, the Markstein numbers are positive and the consumption speed decreases when stretch increases. On the other hand, if $Le_{fuel} < 1$ the Markstein numbers are negative and consumption speed increases with stretch.

3.1.1 Flame-turbulence interaction for premixed flames

The flame may be affected by all the turbulent scales. In order to study the flame and turbulence interaction, two non-dimensional numbers are widely used:

1. Damköhler number, defined as the ratio between the time scale associated to the turbulent integral length scale with respect to the chemical characteristic time.

$$Da = \frac{\tau_t}{\tau_c} \tag{3.16}$$

2. Karlovitz number, defined as the ratio between the chemical characteristic time and the time scale associated to the Kolmogorov length.

$$Ka = \frac{\tau_c}{\tau_k} \tag{3.17}$$

For premixed flames, these numbers can be expressed in the following way [105]:

$$Da = \frac{l_t / u'(l_t)}{\delta_L^0 / s_L^0} \tag{3.18}$$

76

$$Ka = \left(\frac{\delta_L^0}{\eta_k}\right)^2 \tag{3.19}$$

Both numbers are related $Re_t = (Da \cdot Ka)^2$. Using these two dimensional numbers, different combustion regimes exist:

1. Ka<1 (and Da>1), the flamelet regime. The chemical time is smaller than any other characteristic time. In this situation, the flame front is thin, has an inner structure resembling a laminar flame but, along the flame front length the flame is still wrinkled by turbulence.

   If $u' < s_L^0$, the turbulent fluctuations are not able to create flame front interactions and the flame front is only wrinkled. This regime is called the "wrinkled flamelet regime".

   If $u' > s_L^0$, the turbulent fluctuations are able to create isolated pockets of fresh and burnt gases. This regime is called "thin flame regime with pockets" or "corrugated flamelet regime".

2. Ka>1 and Da>1, the thickened flame regime or "distributed reaction zones". In this regime, the integral time scale is larger than the chemical time, and the Kolmogorov structures are smaller than the flame thickness and are able to enter and affect the inner flame structure.

3. Da<1, chemistry characteristic time is larger than the integral time scale. In this regime, combustion takes place under well-mixed conditions and the reaction rate is controlled by chemistry. The limit $Da << 1$ is called the "well-stirred reactor limit". In this case, the flame has no distinct laminar structure [56].

The "flamelet" regime and the "distributed reaction" or "thickened flame" regime are separated by the line Ka=1 which is called Klimov-Williams criterion.

Premixed-flames may experiment quenching at specific turbulent conditions if Lewis number is greater than unity and/or enclosed in a non-adiabatic environment.
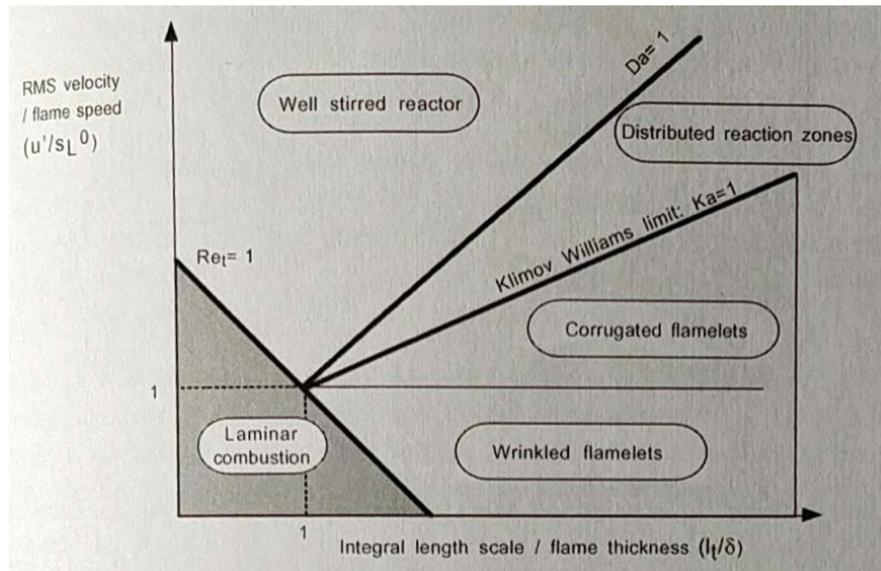
Figure 3-4: Combustion diagram for premixed turbulent combustion from [105]

The combustion diagram in Fig. 3-4 has some limitations. For example [105]:

1. The diagram assumes homogeneous isotropic turbulence not affected by heat release.

2. Boundaries are only to be understood as an order of magnitude value, not as a precise condition.

3. The Kolmogorov scale may be too small or have too small velocity fluctuations to affect the flame. In addition to that, its short life time will also restrict the effect on the flame.

4. Thermo-diffusive effects arising from high local curvature induced by small turbulent scales may not be well represented.

5. The diagram does not take into account that flame turbulence interaction is an unsteady process and that time duration plays a role.

78

3.2 Non-premixed combustion

A diffusion flame, with different properties to the premixed flame, appears when fuel and oxidizer are not mixed before combustion occurs. In this case, combustion occurs around a location where the local equivalence ratio is unity. The reaction zone does not move appreciably with respect to the mean flow, since the flame cannot propagate towards the fuel side due to the absence of oxidizer and vice versa. For this reason, diffusion flames do not have a characteristic speed. Since diffusion flames do not propagate towards the fresh gases unlike the premixed flames, they are more sensitive to the velocity perturbations and turbulence. In addition to that, diffusion flames do not have a characteristic thickness, unstretched flames can grow indefinitely and the typical thickness of stretched flames varies more strongly than premixed flames depending on stretch [105]. Figure 3-5 shows the structure of a 1D diffusion flame.
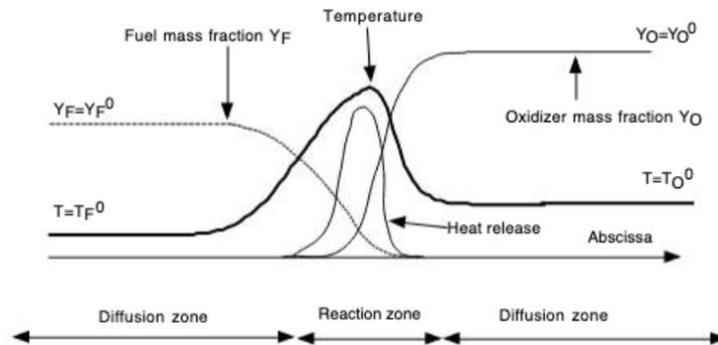
Figure 3-5: Structure of a 1D diffusion flame from [105]

Most theories of laminar diffusion flames make use of the mixture fraction Z, which is a measure of the local fuel/oxidizer ratio. According to [21], Z can be defined as:

$$Z = \frac{\beta - \beta_0}{\beta_f - \beta_0} \tag{3.20}$$

79

and β (subscript f indicates fuel side, subscript o the oxidizer side) [21]:

$$\beta = \sum_{i=1}^{N_a} \gamma_i Z_i = \sum_{i=1}^{n_{spec}} \gamma_i \sum_{j=1}^{N_a} n_{ij} \frac{W_i Y_j}{W_j} \tag{3.21}$$

where N_a is the total number of atoms and n_{ij} is the number of atoms of the ith element in the jth specie. γ_i for C, H and O are $\gamma_C = 2/W_C$, $\gamma_H = 1/(2W_H)$, $\gamma_O = -1/(W_O)$.

The mixture fraction allows decoupling the diffusion flame calculations into two problems:

- A mixing problem, i.e. finding Z as function of spatial coordinates and time.

- A flame structure problem, i.e. finding T and Y_k as a function of the mixture fraction and time.

Thus, the mixture fraction describes the mixing state in the flame and it is not modified by chemical reactions. If we assume all species have the same Schmidt number, the mixture fraction is a passive scalar whose evolution is described by Eq. 3.22.

$$\frac{\partial \rho Z}{\partial t} + \frac{\partial(\rho Z u_j)}{\partial x_j} = \frac{\partial}{\partial x_l}\left[\rho D \frac{\partial Z}{\partial x_l}\right] \tag{3.22}$$

Under the flamelet assumption, the remaining variables (the species mass fractions and temperature) may be assumed to be locally one-dimensional, and only to depend on Z and t. If we assume unity Lewis number, the "flamelet" equations for temperature and mass fractions can be written as [101]:

$$\rho \frac{\partial Y_k}{\partial t} = \frac{1}{2}\rho\chi \frac{\partial^2 Y_k}{\partial Z^2} + \dot{w}_k \tag{3.23}$$

$$\rho \frac{\partial T}{\partial t} = \frac{1}{2}\rho\chi \frac{\partial^2 T}{\partial Z^2} + \dot{w}_T \tag{3.24}$$

where χ is the scalar dissipation rate, and is:

$$\chi = 2D|\nabla Z|^2 \tag{3.25}$$

In Eqs. 3.23 the scalar dissipation rate χ, which controls the mixing, is the only parameter which may be a function of space and time. Therefore, if we know how χ varies in space, T and Y_k in Eqs. 3.23 can be solved as a function only of the mixture fraction Z and the time.

The mixing layer thickness can be defined as:

$$l_Z = \frac{1}{|\nabla Z|} = \sqrt{2D/\chi} \tag{3.26}$$

An important case for laminar diffusion combustion is the steady strained one-dimensional diffusion flame which serves as the basis for tabulated models. An sketch of a steady strained one-dimensional diffusion flame is shown in Fig. 3-6.
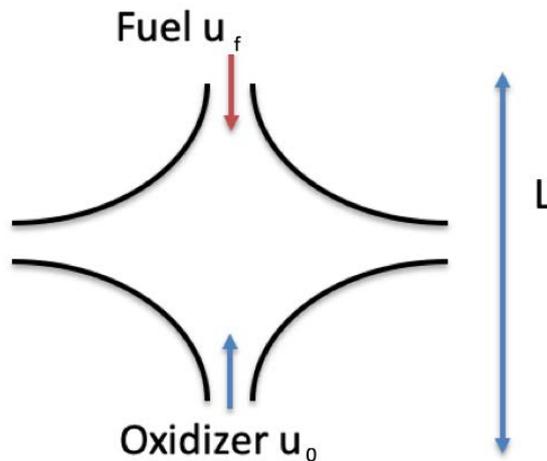
Figure 3-6: Example of a 1D steady diffusion flame

In this type of flames, strain is a function of space, but a global strain can be

defined as:

$$a = \frac{u_f + u_0}{L} \qquad (3.27)$$

If we assume infinitely fast chemistry, it can be derived that [105]:

$$\dot{\Omega}_{fuel} = \int \dot{\omega}_{fuel} dV \propto \sqrt{aD} \qquad (3.28)$$

and that χ is directly proportional to the strain rate. Eq. 3.28 underlines the fact that, in diffusion flames, the stretch controls consumption speed while, in premixed flames, stretch generally acts as a small linear correction (see Eq. 3.13).

When finite chemistry is considered, Eq. 3.28 is a good approximation for low strain values (high Damköhler number), while for high strain values, there is a level of strain in which consumption speed ceases to increase and quenching occurs. This is shown graphically in Fig. 3-7.
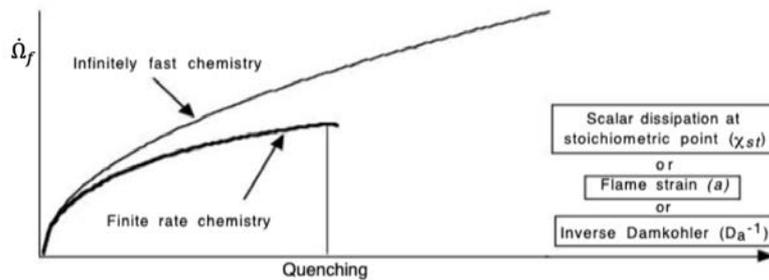
Figure 3-7: Integrated reaction rate as a function of strain in diffusion flames. From [105].

3.2.1 Flame-turbulence interaction for diffusion flames

For diffusion flames, the same non-dimensional numbers (Da, Ka) as introduced in Section 3.1.1 are used to describe the flame turbulence-interaction. On the other

hand, for non-premixed combustion, a different combustion diagram may be envisaged. However, as diffusion flames do not feature neither a characteristic thickness nor a characteristic speed, the derivations in Eqs. 3.18 and 3.19 do not apply to diffusion flames.
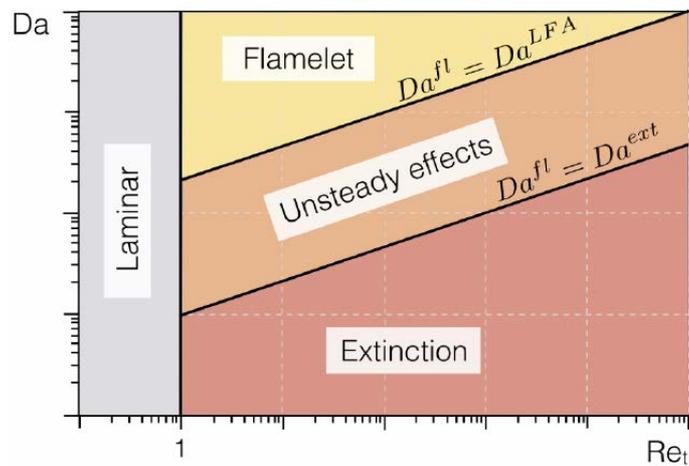
Figure 3-8: Combustion diagram for diffusion turbulent combustion [40]

A simplified diagram can be drawn as shown in Fig. 3-8 based on the Damköhler number. For a sufficiently high turbulent Reynolds number Re_t, three regimes are found. For high Da, the flame has a structure similar to its laminar structure. On the contrary, for low Damköhler number, quenching may happen since the chemical time scale is too high compared to the turbulent time scale. There is an intermediate region in which the relative ratio of the chemical scale to turbulence allows for the presence of unsteady effects.

3.3 Two-phase Combustion

3.3.1 Laminar regime

Spray flames adopt different structures depending on the ratio between evaporation time (τ_e) and residence time from the injector to the flame (τ_r) and the combustion group number G.

According to the ratio of timescales:

1. If $\tau_e < \tau_r$ the fuel will have changed to gaseous phase before combustion occurs. Combustion occurs in the same way as previously described in gaseous flames depending on the relative mixing of fuel and air.

2. If $\tau_e \sim \tau_r$ part of the fuel is evaporated before the flame, and the rest of the fuel is vaporized when the droplets enter the flame. The fact that the droplets enter the flame alters the flame structure.

3. If $\tau_e > \tau_r$ fuel droplets enter the flame, and some still survive in the burnt gas region. In this case, the flames are usually thicker.

The group number G can be defined as a ratio between the droplet evaporation time and the time for the hot gases to diffuse within the droplet cloud [115]. For the case in which convection is more important than diffusion, the group number can be written as:

$$G \approx 5 \frac{N_p^{2/3} \delta_{diff,f}}{\delta_{inter,drop}} \tag{3.29}$$

Where N_p is the number of droplets, $\delta_{diff,f}$ is a characteristic diffusion flame radius and $\delta_{inter,drop}$ is the characteristic space between droplets. When $G >> 1$, the spray is dense and thus the interior volume in the spray is supersaturated, and only the droplets located in the external surface of the spray can evaporate. Consequently,

the flame takes the shape of an external sheath around the spray ("external sheath combustion"). For $G << 1$, the spray is diluted and flames are formed around each individual droplet. For $G > 1$, but not large, some evaporation can occur inside the spray, but the flame is still established as an external sheath. For $G < 1$, but not small, the droplets located in the outer surface of the spray may burn individually while those at the interior are enough closely packed so as to support an external flame. These regimes are shown in Fig. 3-9.
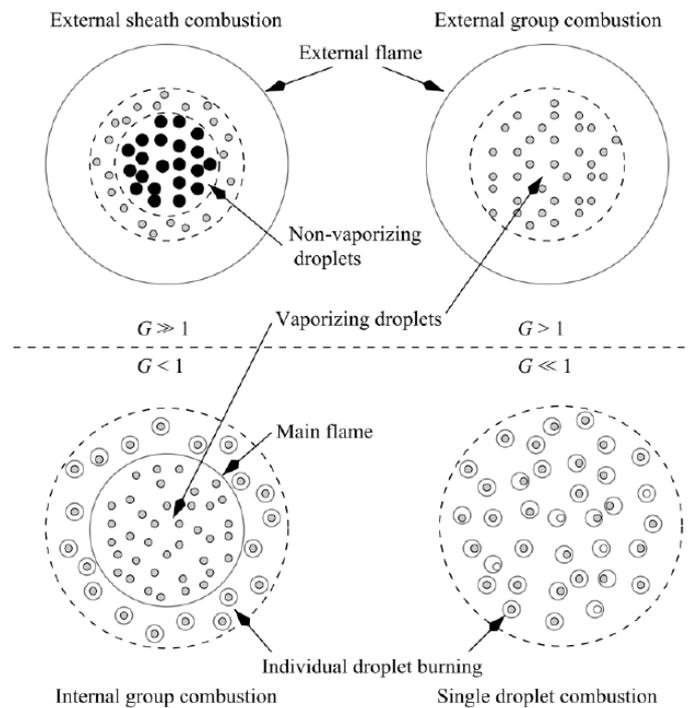
Figure 3-9: Combustion regimes of a droplet cloud for different group number [33,63, 115]

Phenomenological description of two-phase propagation

Depending on the relative droplet spacing and the dimensionless gas temperature, flames with two-phase fuels propagate in different modes. By using an experiment consisting on a linear array of droplets in microgravity, researchers in [132] derived

a diagram summarizing the different modes of flame propagation which is shown in Fig. 3-10.
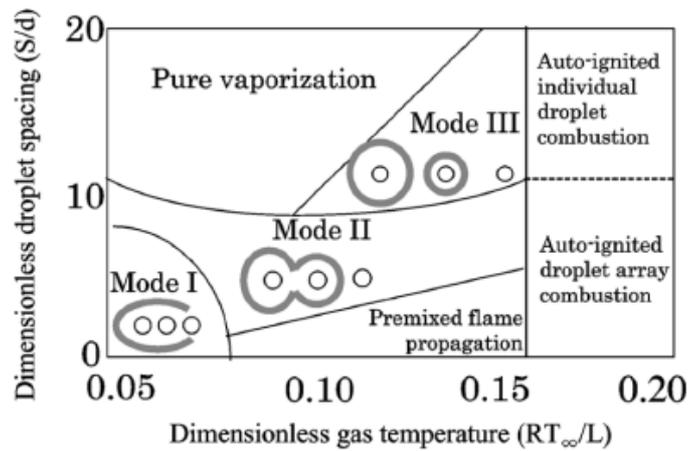
Figure 3-10: Different modes of inter-droplet flame propagation [132]

1. Premixed flame propagation (S/d < 3 and $0.07 < RT_\infty/L_v < 0.15$) where S is the droplet spacing, d droplet diameter, T_∞ the temperature far from the droplet and L_v the heating value to vaporize the droplets: The droplets are volatile enough to produce a substantial amount of fuel in gaseous phase. The droplets are closely packed, so a continuous and approximately premixed flame propagates across the droplets. Conceptually it is similar to the flame propagation if the fuel were all gaseous. However, the flame is usually thicker and its propagation velocity can be both smaller or higher than the equivalent flame under gaseous conditions.

2. Mode I. The droplets are closely packed, but contrary to the previous case, they lack sufficient volatility to create substantial fuel in gaseous phase. As a result of this, a diffusion-like flame appears which grows to surround a group composed of a high number of droplets.

3. Mode II: The inter-droplet spacing increases with respect to mode I and, as a

86

result, there is a diffusion flame which surrounds a group composed of a lower number of droplets.

4. Mode III: If the inter-droplet spacing is very high, but the droplets are volatile enough, the flame can propagate from individual droplets to neighbours by heat transfer. This process heats the neighbouring droplet until it reaches its self-ignition temperature.

5. Limit of high volatility. If $RT_\infty/L_v > 0.15$, then the droplets can reach self-ignition.

6. Limit of high inter-droplet spacing. The flame cannot propagate between droplets and the existing flame only serves to vaporize a fraction of the droplets before quenching. It corresponds to the "Pure vaporization" region in Fig. 3-10.

Two-phase flame properties

The authors in [16] obtained a correlation for estimating the laminar flame speed for two-phase flames. According to this formulation, whose accuracy is restricted to overall lean mixtures and certain range of droplet diameters [94], the flame speed under these conditions can be calculated with the gaseous flame speed plus a correction accounting for the evaporation time.

$$s_L^{tp} = \left(\frac{\tau_{evap}}{D_{th}} + \frac{1}{S_L^{0\,2}} \right)^{-1/2} \tag{3.30}$$

with s_L the flame speed of the equivalent fully vaporized mixture.

On the other hand, a recent investigation [119] has derived analytical formulae based on relating the two-phase laminar flow velocity to the velocity of a equivalent gaseous flame at an effective equivalence ratio. These relationships take into account the effects of relative velocity between liquid and gas phase.

For weakly controlled evaporation flames (those whose pre-vaporized fuel content allows for combustion or those whose evaporation is fast enough to reach a flammable mixture before the flame) Eq. 3.31 holds.

$$\phi_{eff} = \left(\frac{\delta_L^0}{\max(\delta_L^0, \delta_{evap})}\right)^{2/3} \phi_l + \phi_g \tag{3.31}$$

where δ_{evap} is the distance travelled by the droplet while it evaporates ($\delta_{evap} = u_l \cdot \tau_{evap}$) and δ_L^0 is the flame thickness considering pure gaseous fuel. Eq. 3.31 indicates that a weakly controlled evaporation flame can propagate faster than the equivalent flame with fully evaporated fuel if $\phi_{total} = \phi_l + \phi_g > 1$ but $\phi_{eff} \approx 1$ (close to stoichiometric conditions). All in all, this suggests there is an optimum droplet diameter to obtain a maximum of flame speed under those conditions.

For evaporation controlled flames (those who reach the flame region with a fuel content below the flammability limit), combustion is very different to the case of vaporized fuel. The flame laminar speed cannot be expressed as a function of the equivalent gaseous flame properties, and can only be estimated by comparing the flame thickness and the evaporation time according to Eq. 3.32.

$$S_L^{tp} = \frac{\delta_{L,\phi_g=min(\phi_{tot},1)}^0}{\tau_{evap}} \tag{3.32}$$

where $\delta_{L,\phi_g=min(\phi_{tot},1)}^0$ is the unstretched laminar premixed flame thickness at a equivalent ratio equal to the total equivalence ratio, which cannot surpass one.

3.3.2 Turbulent regime

The interaction between turbulence, spray and combustion is a currently highly-active research field [36, 117] and all the effects are not fully understood. The first difficulty arises from the interaction of the reacting spray with turbulence. Turbulence enhances mixing and relative velocity between liquid and gas phases, which

leads to higher rates of evaporation. If turbulence is strong, it may distort the droplet surface and even break up the fuel droplets into smaller sizes generating a polydisperse size droplet field. On the other hand, if the Stokes number of droplets ($St = \tau_{drop-inertia}/\tau_{fluid}$) is small, droplets will respond quickly to fluid motion and may be trapped by large turbulent structures and accumulate in zones of lower vorticity. Consequently, turbulence will also generate fuel mixture inhomogeneity. This effect is shown in Fig. 3-11
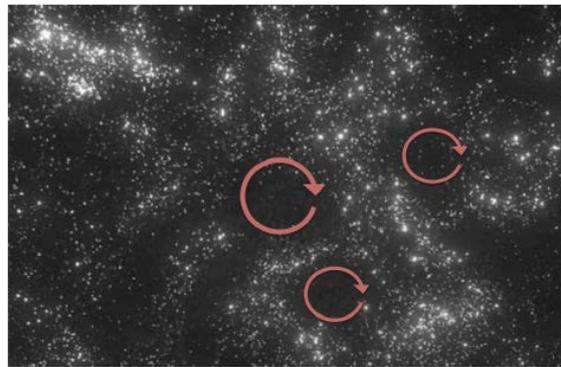
Figure 3-11: Preferential segregation caused by homogeneous isotropic turbulence. Large turbulent structures are marked with an arrow [142]

A more systematic study can be found in [44] and identifies four non-dimensional numbers to characterize turbulent liquid-gas phase combustion:

1. L_{spray}/L_{ent} which compares the length of the dense core of the spray to an equivalent length containing enough oxidizer to successfully burn the mixture and indicates whether the spray will have enough space to mix with the oxidizer (in this case the ratio will have a high value, i.e. it requires a small oxidyzer length).

2. τ_{mix}/τ_c compares the turbulent mixing time to the chemistry characteristic time.

3. τ_{evap}/τ_c compares the evaporation time to the chemistry characteristic time.

4. d_{SMD}/d_{inj} compares the SMD with the injector diameter. A low value indicates finer atomization.

In a more general sense, two distinct regimes can be observed depending on whether the spray becomes a homogeneous flammable mixture before the flame or not. In the first case, the combustion effects will be closer to premixed combustion and this regime has been called as "homogeneous combustion" [98]. In the latter case, a heterogeneous mixture will enter the flame, and diffusion-like flames will occur. This regime has been called "heterogeneous combustion" in [98]. Both regimes are shown in Fig 3-12.
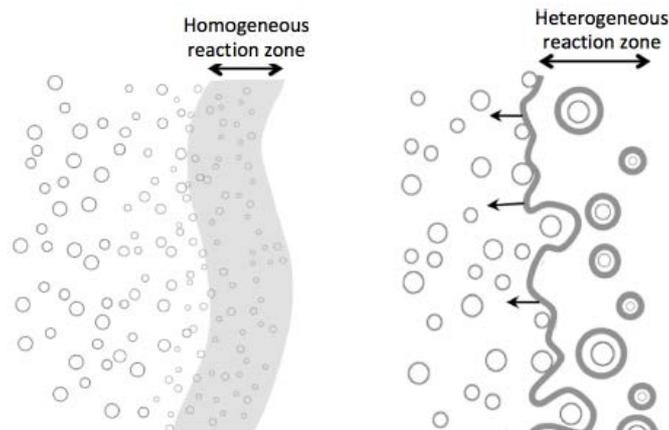
Figure 3-12: "Homogeneous" (Left) and "heterogeneous" combustion modes [98]

All in all, the presence of liquid phase involves additional complexity. Two-phase flames remain currently an active research field as shown by the recent theses of [28] and [117].

In summary, this work involves a fluid dynamics study in which the three main factors are: turbulence, combustion and the presence of a disperse phase. These factors mutually-influence each other (e.g. combustion affects turbulence and vice versa). This results in a multi-scale problem (both in space and time) whose solution

can only be generally obtained by employing numerical methods as those which will be described in Chapter 4 and 5.

3.4 Chemical Description in Numerical Models

A detailed chemical description is necessary to predict all the flame properties and characteristics (e.g. thickness, flame speed, autoignition time, response to strain, production of pollutants...)

However, a chemical mechanism including all species and reactions is not realizable in current computations due to the need for small time steps ($10^{-9}s$), small grid scale, and high number of reactions. For that reason, several alternative methods have been developed.

A detailed description of chemistry has to take into account several factors: complex flow/flame interactions, the range of operating conditions, the multiple chemical time scales and the numerical cost [56]. There are several methods, among which the tabulated chemistry, globally reduced chemistry, the skeletal mechanisms and the analytically-reduced chemistry are discussed.

3.4.1 Tabulated Chemistry Method

The first method discussed is the tabulated chemistry method, in which chemical reaction rates are parameterized using a reduced set of variables. In order to build the parameterization, a reference problem has to be chosen beforehand. For the case of premixed or partially-premixed (or stratified) applications, laminar premixed flames are generally chosen as the reference problem. In this case, the parameters usually employed are the mixture fraction Z and a progress state variable. On the other hand, for the case of non-premixed conditions, the reference problem are usually counterflow diffusion flames. In this case, the parameters usually employed are the

mixture fraction Z and the scalar dissipation rate χ.

The main advantage of this approach is its simplicity and reduced computational cost. On the other hand, some disadvantages of this approach are that they usually cannot correctly represent the chemical changes due to strain, curvature and dilution. In addition to that, practical combustors display a wide range of combustion regimes, thus establishing the reference flame is difficult. Finally, including the effect of heat losses and slow chemical processes such as NO_X production requires additional assumptions or increasing the tables [56].

3.4.2 Globally Reduced Chemistry

These methods consider a reduced number of species and adjust the chemical reactions so as to reproduce properties of the flame such as the laminar flame speed or the flame temperature over a particular range of operating conditions. An example of these methods are the family of two-step mechanisms derived in [49], which assumes two reactions:

$$C_nH_m + \left(\frac{n}{2} + \frac{m}{4}\right) * O_2 \rightarrow n * CO + \frac{m}{2} * H_2O \tag{3.33}$$

$$CO + \frac{1}{2}O_2 \rightarrow CO_2 \tag{3.34}$$

The reaction rates have a generalized Arrhenius form:

$$\dot{\omega} = f(\phi)k[Fuel]^{n_1}[Oxidizer]^{n_2}T^{\beta}\exp\left(\frac{-E_a}{RT}\right) \tag{3.35}$$

The function f(ϕ) is used to recover the flame speed for rich mixtures, k and E_a are adjusted to match laminar flame speeds, and the concentration exponents n_1 and n_2 are adjusted to retrieve the correct dependency of the laminar flame speed with

pressure [50].

The disadvantages of this approach is the restriction of validity of mechanism for the operating conditions for which it was derived, and the impossibility to predict pollutant emission due to the elimination of intermediate species.

3.4.3   Skeletal Mechanisms

Skeletal reduction methods consists in eliminating species and reactions that have a small impact on a specified set of targets. An example of these methods is the Directed Relation Graph method with Error Propagation (DRGEP) presented in [100].

The Directed Relation Graph method with Error Propagation (DRGEP) is based on evaluating the importance of the interaction between species by using a relation graph method such as the one depicted in Fig. 3-13.
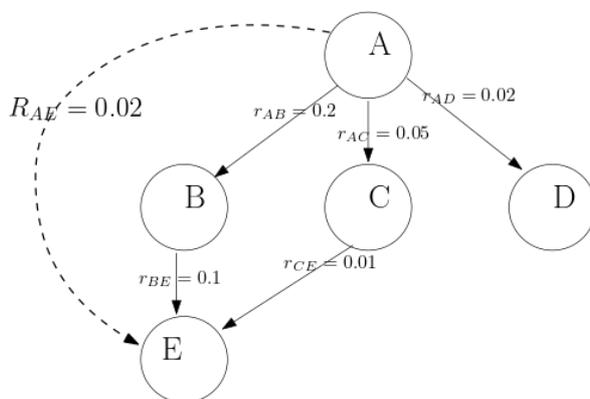
Figure 3-13: Graphical example of a part of a directed relation graph

Species interact when they both appear in the same chemical reaction. The importance of species B for the correct prediction of species A is denoted by the interaction coefficient r_{AB} which is defined as:

$$r_{AB} = \frac{|\sum_{i=1,n_{reac}} \nu_{i,A} \omega_i \delta_B^i|}{\max(P_A, C_A)} \tag{3.36}$$

93

where $\nu_{i,A}$ are the stoichiometric coefficient of species A in the ith reaction, and ω_i is the rate of reaction i^{th}, and δ_B^i is Dirac's delta equal to 1 only when species B appears in reaction i^{th}. P_A and C_A are normalization coefficients that ensure that the interaction coefficient r_{AB} is bounded between 0 and 1.

$$P_A = \sum_{i=1}^{n_{reac}} \max(0, \nu_{i,A}\omega_i) \tag{3.37}$$

$$C_A = \sum_{i=1}^{n_{reac}} \max(0, -\nu_{i,A}\omega_i) \tag{3.38}$$

Species A and B can be connected through different paths of intermediate species (for example see A and E in Fig. 3-13, which are connected through C or though D). For a path p involving species $\{A, S_2, S_3, ..., S_{n-1}, B\}$ we can obtain a interaction coefficient between A and B following path p (denoted as $r_{AB,p}$) as:

$$r_{AB,p} = \prod_{i=1}^{n-1} r_{S_i S_{i+1}} \tag{3.39}$$

Eq. 3.39 implies that the interaction coefficient between A and B following path p will be smaller the larger number of intermediate species are in path p (i.e. the longer the path is). Finally, the global interaction coefficient between A and B R_{AB} is the maximum of all $r_{AB,p}$:

$$R_{AB} = \max_{for\ all\ paths\ p} r_{AB,p} \tag{3.40}$$

In the example of Fig. 3-13, considering the relationship between species A and species E, species D does not have any influence. Furthermore, the path p which contains A, B, E has an interaction coefficient $r_{AB,p}$ equal to 0.02. On the other hand, the path q which contains A, C, E has an interaction coefficient $r_{AB,q}$ equal to 0.005. Therefore, the global interaction coefficient between A and E is $R_{AE} = 0.02$.

Skeletal mechanisms are not generally used in LES computations due to its computational cost. Firstly, even though the number of species to be transported has been

reduced, it remains generally computationally unaffordable without further species reduction. Secondly, skeletal mechanism still contain highly reacting intermediate species which require costly spatial and temporal discretization.

3.4.4 Analytically Reduced Chemistry

Some authors have developed certain techniques to further reduce the number of species transported and remove the need for short time-steps. One example of this is using analytically reduced chemistry (ARC). This technique is usually based on two approximations: the partial equilibrium assumption (PEA) and the quasi-steady state approximation (QSSA).

Partial Equilibrium Assumption (PEA)

PEA aims to circumvent the numerical resolution problems occurring in fast reversible reactions. In these reactions, equilibrium is rapidly reached. However, there can be problems in the numerical implementation due to the subtraction of two stiff terms. In order to avoid this problem, the PEA equates the net reaction rate of these reactions identically to 0. This assumption imposes the following constraint in the species concentration:

$$\prod_{k=1}^{n_{spec}} c_k^{\nu_{ik}} = K_i^{eq} \tag{3.41}$$

where c_k is the kth species concentration, ν_{ik} the stoichiometric coefficient of species k^{th} for reaction i^{th}, and K_i^{eq} is the chemical equilibrium constant of reaction i^{th}. In order to ensure this constraint is satisfied at the end of each time step, a correction term is introduced in the reaction rates of these equations.

Quasi Steady State Approximation (QSSA)

The authors in [75] defined a QSS species as: "A QSS species typically features a fast destruction time scale, such that its small or moderate creation rate is quickly balanced by the self-depleting destruction rate, causing it to remain in low concentration after a transient period. The net production rate of the QSS species is therefore negligible compared with both the creation and the destruction rates, resulting in an algebraic equation for its concentration". Thus, the objective of the QSSA is to identify species which can be catalogued as QSS. Once a species is catalogued as QSS, its production rate is set to 0 and its concentration is calculated through algebraic equations. In this manner, the restriction of these species on the time-step is eliminated. There exists several methods to select QSS candidates [74, 76, 131].

In conclusion, analytically reduced chemistry (ARC) is an approach that permits a semi-detailed description of chemistry at a reduced cost. ARC is especially useful for studies such as ignition [36, 47], prediction of pollutants [56] or the response of the flame to strain where more simplified approaches (e.g. globally reduced chemistry) are unable to provide accurate results.

Chapter 4

Governing Equations for the Gaseous Phase

Contents

In this chapter the physical modelling and numerical implementation of the conservation equations for the gas phase are presented. In addition to that, the fundamental concepts of LES are briefly covered.

4.1 Governing Equations for the Gaseous Phase

Note: Einstein's rule of index summation is used throughout unless explicitly stated otherwise.

4.1.1 Navier-Stokes Equations

The equations solved for the gaseous phase are as follows:

- Mass conservation

$$\frac{\partial \rho}{\partial t} + \frac{\partial(\rho u_i)}{\partial x_i} = 0 \tag{4.1}$$

- Momentum conservation

$$\frac{\partial \rho u_i}{\partial t} + \frac{\partial(\rho u_i u_j)}{\partial x_j} = -\frac{\partial(P\delta_{ij} - \tau_{ij})}{\partial x_j} + \rho \sum_{k=1}^{N} Y_k f_{k,i} \tag{4.2}$$

where $f_{k,i}$ is any "body"-force (e.g. gravity) in direction "i" on species k.

- Energy conservation

$$\frac{\partial \rho E}{\partial t} + \frac{\partial(\rho E u_j)}{\partial x_j} = -\frac{\partial[u_i(P\delta_{ij} - \tau_{ij}) + q_j]}{\partial x_j} + \dot{\omega}_T + \dot{Q} + \rho \sum_{k=1}^{N} Y_k f_{k,i}(u_i + v_{k,i}) \tag{4.3}$$

where E is the total non-chemical energy, i.e. $E = \int_{T_0}^{T} C_v dT - RT_0/W + 1/2 u_i u_i$ and $\dot{Q}$ is a heat volumetric term (e.g. energy deposition due to electric spark, or radiation)

- Species conservation

$$\frac{\partial \rho Y_k}{\partial t} + \frac{\partial(\rho Y_k u_j)}{\partial x_j} = -\frac{\partial J_{j,k}}{\partial x_j} + \dot{\omega}_k \tag{4.4}$$

Throughout this work, the ideal gas assumption is adopted:

$$R = R_{univ,gas}/W \tag{4.5}$$

where $R_{univ,gas} = 8.3145$ J/(mol K)

$$p = \rho R T \tag{4.6}$$

The mean molecular weight W is defined as:

$$\frac{1}{W} = \sum_{k=1}^{n_{spec}} \frac{Y_k}{W_k} \tag{4.7}$$

4.1.2 Viscous Stress Tensor

The Stokes assumption gives the viscous stress tensor τ_{ij} as:

$$\tau_{ij} = 2\mu \left(S_{ij} - \frac{1}{3}\delta_{ij} S_{ll} \right) \tag{4.8}$$

where S_{ij} is the strain tensor:

$$S_{ij} = \frac{1}{2} \left(\frac{\partial u_i}{\partial x_j} + \frac{\partial u_j}{\partial x_i} \right) \tag{4.9}$$

4.1.3 Species Diffusion Flux

According to the Hirschfelder-Curtis approximation with a correction term to ensure mass conservation, the diffusion velocity of species can be written as:

$$v_{kj} = -\frac{D_k}{X_k} \frac{\partial X_k}{\partial x_j} + V_j^c \tag{4.10}$$

where

$$V_j^c = \frac{1}{W} \sum_{i=1}^{n_s pec} D_i W_i \frac{\partial X_i}{\partial x_j} \tag{4.11}$$

Therefore, the species diffusion flux J_{ik} can be expressed as:

$$J_{jk} = -\rho \left(\frac{D_k}{X_k} \frac{\partial X_k}{\partial x_j} - \frac{1}{W} \sum_{i=1}^{N} D_i W_i \frac{\partial X_i}{\partial x_j} \right) = \rho v_{kj} \tag{4.12}$$

4.1.4 Energy Flux

The energy flux is composed of two terms. The former accounts for heat conduction and is modelled with the Fourier approximation. The latter accounts for the transport of energy due to the species diffusion.

$$q_i = -\lambda \frac{\partial T}{\partial x_i} - \rho \left(\frac{D_k}{X_k} \frac{\partial X_k}{\partial x_i} + \frac{1}{W} \sum_{j=1}^{N} D_j W_j \frac{\partial X_k}{\partial x_i} \right) h_{s,k} \tag{4.13}$$

where $h_{s,k}$ is the k-th species sensible enthalpy.

4.1.5 Modelling Transport Coefficients

The fact that thermodynamic variables such as molecular viscosity vary with temperature are accounted through the use of models such as the Sutherland law.

$$\mu = c_1 \left(\frac{T}{T_{ref}} \right)^{\frac{3}{2}} \frac{T_{ref} + c_2}{T + c_2} \tag{4.14}$$

Alternatively, the "power law" model can be used

$$\mu = c_1 \left(\frac{T}{T_{ref}} \right)^b \tag{4.15}$$

with b typically varying between 0.5 and 1. In CERFACS code AVBP V7, a single Prandtl number are considered for the gas mixtures. On the other hand, each species has a different but constant Schmidt number.

4.1.6 Numerical Methods to Simulate Turbulent Flows

Eqs. 4.1 to 4.3 are able to describe the majority of fluid motions, both laminar and turbulent. The size of the fluid scales will determine the number of points needed to discretize our numerical domain. In homogeneous isotropic turbulence, it has been experimentally demonstrated [108] that the energy (E) and the scale of turbulent structures are characterized by the ordering shown in Fig. 4-1. The length scales are characterized using the wave number k ($k = 2\pi/\lambda$ where λ is the length scale). The energy content increases up to a size called the "integral length scale". If we decrease in size, we approach the "inertial range" in which $E \propto k^{-\frac{5}{3}}$. If we further decrease in size, we approach the Kolmogorov scales. The scaling in the inertial range is no longer valid and a rapid decrease of energy with decreasing size occurs.

In order to represent the effect of these scales, one approach is to explicitly represent all turbulent structures, which is also known as performing a Direct Numerical Simulation (DNS). This approach requires a mesh size of the order of the smallest turbulent scale, the Kolmogorov scale. From homogeneous isotropic turbulence theory, it can be demonstrated that the relationship in Eq. 4.16 holds, relating the necessary number of grid points to the turbulent Re number ($Re_t = \frac{u'L}{\nu}$) rendering DNS unaffordable for the calculations of high Reynolds number flows.

$$N_{points} \propto \left(\frac{l_t}{\eta}\right)^3 = Re_t^{\frac{9}{4}} \qquad (4.16)$$

Another technique is to build a physical model for the effect of all turbulent structures. One such approach is referred to as Reynolds-Averaged Navier Stokes (RANS).
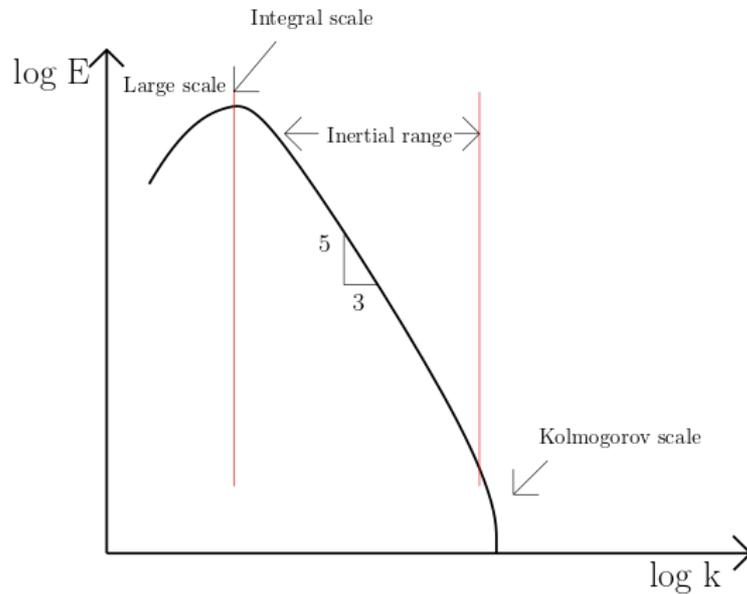
Figure 4-1: Logarithm of the energy vs logarithm of the wave number ($k = 2\pi/l$) showing low wave number structures (big scales) having the highest energy. After the integral scale is attained, the logarithm of energy decays at a constant rate until the dissipation scales where energy rapidly decays

In this approach, each variable is decomposed into an ensemble-averaged value and a fluctuating quantity, whose ensemble-average is 0, as can be seen in Eq. 4.17 and Eq. 4.18. Thus, conservation equations can be written for the ensemble-averaged quantities. On the other hand, the ensemble-average of the product of two fluctuating quantities is undetermined and requires the adoption of a form of modelling. This approach has the advantage of being the least computationally expensive, but requires some a priori knowledge of the turbulent field for the modelling to be accurate and its validity cannot generally be assured.

$$Q = <Q> + Q' \tag{4.17}$$

$$<Q'> = 0 \tag{4.18}$$

Lastly, there is an approach that combines some of the concepts of DNS and RANS techniques, the Large Eddy Simulation or LES. It consists in explicitly calculating the large turbulent scales of the flow, which tend to have the greatest energy content, while mathematically modelling the contribution of the smaller turbulent scales. In this method, the distinction between large and small turbulent scales is made using a filter scale Δ. Therefore, in LES, a filtering operator is applied to the governing equations.

Governing Equations for Large Eddy Simulation

The filtering operator in LES will be marked by the overbar symbol. When applied to a generic variable, it reads (where F_Δ is the filtering function and in this work is a Gaussian filter as indicated in Eq. 4.20):

$$\bar{Q}(x) = \int Q(y) F_\Delta(x - y) dy \tag{4.19}$$

$$F_\Delta(x_1, x_2, x_3) = \left(\frac{6}{\pi \Delta^2}\right)^{3/2} \exp\left[-\frac{6}{\Delta^2}(x_1^2 + x_2^2 + x_3^2)\right] \tag{4.20}$$

In order to derive the governing equations, Favre-filtering is introduced, which is marked by a tilde:

$$\bar{\rho}\tilde{Q}(x) = \int \rho Q(y) F_\Delta(x - y) dy = \overline{\rho Q} \tag{4.21}$$

On the condition that the filter and the derivative operators are commnutative, the conservation equations for LES can be written as (the subgrid terms are marked by upperscript "t"):

$$\frac{\partial \bar{\rho}}{\partial t} + \frac{\partial(\bar{\rho}\tilde{u}_i)}{\partial x_i} = 0 \tag{4.22}$$

103

$$\frac{\partial \bar{\rho} \tilde{u}_i}{\partial t} + \frac{\partial (\bar{\rho} \tilde{u}_i \tilde{u}_j)}{\partial x_j} = -\frac{\partial (\bar{P} \delta_{ij} - \bar{\tau}_{ij} - \bar{\tau}_{ij}{}^t)}{\partial x_j} \tag{4.23}$$

$$\frac{\partial \bar{\rho} \tilde{E}}{\partial t} + \frac{\partial (\bar{\rho} \tilde{E} \tilde{u}_j)}{\partial x_j} = -\frac{\partial [\overline{u_i(P \delta_{ij} - \tau_{ij})} + \bar{q}_j + \bar{q}_j{}^t]}{\partial x_j} + \bar{\dot{\omega}}_T + \bar{Q} \tag{4.24}$$

$$\frac{\partial \bar{\rho} \tilde{Y}_k}{\partial t} + \frac{\partial (\bar{\rho} \tilde{Y}_k \tilde{u}_j)}{\partial x_j} = -\frac{\partial [\overline{J_{j,k}} + \overline{J_{j,k}^t}]}{\partial x_j} + \bar{\dot{\omega}}_k \tag{4.25}$$

In this work, the filtered viscous flux, heat flux and species diffusion terms are modelled as:

$$\bar{\tau}_{ij} \approx \bar{\mu}\left(\frac{\partial \tilde{u}_j}{\partial x_i} + \frac{\partial \tilde{u}_i}{\partial x_j} - \frac{2}{3}\delta_{ij}\frac{\partial \tilde{u}_k}{\partial x_k}\right) \tag{4.26}$$

$$\bar{q}_i \approx \bar{\lambda}\left(\frac{\partial \bar{T}}{\partial x_i} + \sum_{k=1}^{N} \overline{J_{i,k}\widetilde{h_{s,k}}}\right) \tag{4.27}$$

$$\overline{J_{i,k}} \approx -\bar{\rho}\left(\bar{D}_k \frac{W_k}{W}\frac{\partial \tilde{X}_k}{\partial x_i} - \tilde{Y}_k \tilde{V}_i^c\right) \tag{4.28}$$

And the filtered coefficients are approximated as:

$$\bar{\mu} \approx \mu(\tilde{T}) \tag{4.29}$$

$$\bar{\lambda} \approx \frac{\bar{\mu}\overline{C_p}(\tilde{T})}{Pr} \tag{4.30}$$

$$\overline{D_k} \approx \frac{\bar{\mu}}{\bar{\rho}Sc_k} \tag{4.31}$$

Subgrid Scale Term Closures

The subgrid scale Reynolds stress tensor $\bar{\tau}^t = -\bar{\rho}(\widetilde{u_i u_j} - \tilde{u}_i \tilde{u}_j)$ is usually modelled by an eddy-viscosity approximation in the following form:

$$\bar{\tau}^t = 2\mu_t \left(\tilde{S}_{ij} - \frac{1}{3}\delta_{ij}\tilde{S}_{ll} \right) \tag{4.32}$$

The turbulent viscosity μ_t requires additional modelling and several turbulence subgrid models are available.

The subgrid scale species and enthalpy fluxes are usually modelled considering a turbulent mass diffusivity:

$$\overline{J_{i,k}}^t = \bar{\rho}\left(\widetilde{u_i Y_K} - \tilde{u}_i \tilde{Y}_k \right) \approx -\bar{\rho}(D_k^t \frac{W_k}{W}\frac{\partial \tilde{X}_k}{\partial x_i} - \tilde{Y}_k \tilde{V}_i^c) \tag{4.33}$$

Likewise, the turbulent mass diffusivity is defined as:

$$D_k^t = \frac{\mu_t}{\bar{\rho}Sc_k^t} \tag{4.34}$$

In this work it will be modelled assuming a constant Sc_k^t equal to 0.6.

The turbulent correction velocity used to ensure mass conservation in the sum of the species equations is written as:

$$\tilde{V}_i^c = \sum_{k=1}^{n_{spec}} D_k^t \frac{W_k}{W}\frac{\partial \tilde{X}_k}{\partial x_i} \tag{4.35}$$

The subgrid heat flux $\overline{q_i}^t = \bar{\rho}(\widetilde{u_i E} - \tilde{u}_i \tilde{E})$ is usually modelled considering a turbulent heat diffusivity

$$\lambda_t = \frac{\mu_t \overline{C_p}}{Pr^t} \tag{4.36}$$

In this work it will be modelled assuming a constant Pr^t equal to 0.6.

$$\bar{q}_i \approx \lambda_t(\frac{\partial \bar{T}}{\partial x_i} + \sum_{k=1}^{N} \overline{J_{i,k}}\widetilde{h_{s,k}}) \tag{4.37}$$

Finally, the filtered chemical source terms $\bar{\dot{\omega}}_k$ and $\bar{\dot{\omega}}_T$ require additional modelling, which will be discussed in a later section.

Turbulent viscosity models

In this section, all the available models in AVBP V7 are presented. All of them are based on the eddy-viscosity concept. This concept implicitly assumes that energy is only transferred from filtered scales to the subgrid turbulent scale (Therefore, these models will lose accuracy in the special cases in which the subgrid turbulent scales provide energy to the filtered scales through the "backscatter" mechanism [108]).

The Smagorinsky model assumes the following form for the turbulent viscosity:

$$\nu_t = (C_s\Delta)^2(2\overline{S_{ij}S_{ij}})^{1/2} \tag{4.38}$$

The constant C_S has a typical value of 0.17. This model is able to predict the correct turbulent decay for homogeneous isotropic turbulence. However, it predicts a non-zero value of turbulent viscosity in pure shear conditions and it is regarded as too dissipative near the walls. This model can be extended by having a spatially and temporally varying C_s whose value is obtained using a test-filter scale and the Germano identity [51], leading to the so-called Smagorinsky Dynamic Model.

The WALE (Wall Adapting Local Eddy viscosity) model [45] was developed to have the right scaling laws near wall regions in wall-bounded flows:

$$\nu_t = (C_w\Delta)^2 \frac{(S_{ij}^d S_{ij}^d)^{3/2}}{(S_{ij}S_{ij})^{5/2} + (S_{ij}^d S_{ij}^d)^{5/4}} \tag{4.39}$$

where S_{ij}^d is the traceless symmetric part of the velocity gradient tensor. This model has the correct behavior near walls, but it incorrectly predicts a non-zero turbulent viscosity in solid rotation and axisymmetric expansion conditions.

The SIGMA model [97] is a further improvement over the WALE model especially targeted at swirling flows. It will be employed in the simulations of chapter 6 and 8. It correctly predicts zero turbulent viscosity at solid rotation and axisymmetric conditions. The singular values (σ_i) of the velocity gradient tensor are used to construct the turbulent viscosity.

$$\nu_t = (C_\sigma \Delta)^2 \frac{\sigma_3(\sigma_1 - \sigma_2)(\sigma_2 - \sigma_3)}{\sigma_1^2} \tag{4.40}$$

A summary of the properties of these models is written in Table 4.1

Table 4.1: Summary of the properties of the turbulent viscous diffusivity models (Adapted from [97])

Model	Smagorinsky	WALE	SIGMA
Correct behavior near walls	NO	YES	YES
Correct value at solid rotation	NO	NO	YES
Correct value at axisymmetric and isotropic expansion	NO	NO	YES

Modelling of Filtered Chemistry Source Terms

The typical mesh size in LES is larger than the typical flame thickness, therefore the flame structure cannot be accurately calculated. In addition to that, chemistry is supposed to be affected by all the turbulent scales, some of which are not explicitly represented in LES, requiring additional modelling. A complete review of modelling of the filtered chemistry source terms can be found in [105]. The use of detailed chemical schemes restricts the choice of models because accounting for a large number of species represents an additional complexity in these models. A general overview of modelling techniques is as follows:

- For premixed combustion, there are models like the Bray-Moss-Libby model [24] or the G-equation model [60] which assume an infinitely thin flame. On the other hand, if we assume a non-negligible reaction thickness, there is the F-TACLES model [48] which is based on relating the reaction rate to a-priori made 1D laminar flame calculations. In addition to this, there is the artificially thickened flame model [35] in which the flame thickness is artificially increased numerically while other parameters are modified to recover the correct effect of turbulence on the flame.

- For non-premixed combustion, there also exists several methods among which we can find the probability density function (PDF) or conditional moment closure (CMC) which will be detailed later.

The basis of the artificially thickened flame is to produce an artificial increase of the flame thickness so that its structure can be correctly represented in the LES mesh. However, in order to conserve the same laminar flame velocity, a correction term must be introduced in the flame diffusivity. Since the laminar flame speed scales as $S_L \propto \frac{D_{th}}{\delta}$ an increase in flame thickness by a factor F must be accompanied by an increase in mass diffusivity by the same factor F. Additionally, it can be shown [141] that the laminar flame speed scales as $S_L \propto \sqrt{D_{th}\bar{\omega}}$. Therefore, to conserve the laminar flame speed, the production term must be reduced by a factor F.

Despite conserving the laminar flame speed, thickening the flame alters how the turbulent scales affect the flame as shown in Fig. 4-2 , and modifies the ratio of turbulent to chemical time-scales, thus altering the effective turbulent flame speed. In order to recover the correct turbulent flame speed, another factor, the wrinkling factor (Ξ_Δ) needs to be introduced. It is defined as:

$$\Xi_\Delta = \frac{S_{T\Delta}}{S_l^0} = \frac{A_{sgs}}{\Delta^2} \tag{4.41}$$

108
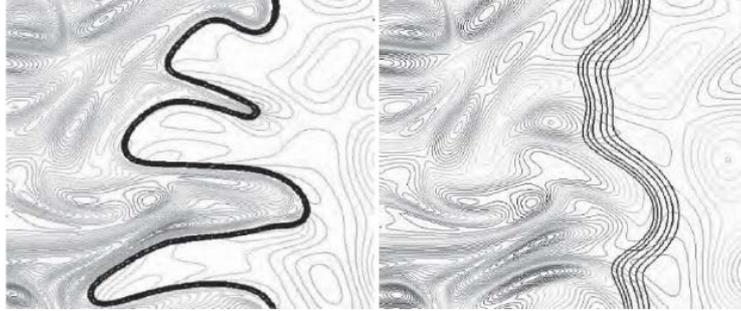
Figure 4-2: Comparison of a fully resolved flame with a flame computed using the thickened flame model showing the model reduces the flame wrinkling due to turbulence in the thickened flame [105]

where Δ is the length scale associated to the LES filtering, $S_{T\Delta}$ is the turbulent flame speed at the subgrid scale level, S_L^0 is the laminar unstretched flame speed and A_{sgs} the subgrid scale flame surface. It is a parameter of critical importance since it contains the information of how turbulence affects chemistry.

Examples of efficiency models are the Charlette static and dynamic efficiency formulations [31, 32]. In both formulations , the wrinkling factor of a flame is written as:

$$\Xi_\Delta = \left(1 + \min\left[\frac{\Delta}{\delta_L^0}, \Gamma\left(\frac{\Delta}{\delta_L^0}, \frac{u'_\Delta}{s_L^0}, Re_\Delta\right)\frac{u'_\Delta}{s_L^0}\right]\right)^\beta \qquad (4.42)$$

where Re_Δ and u'_Δ are the Reynolds number at subgrid-scale and the corresponding velocity fluctuation, δ_l^0 is the laminar unstretched flame thickness and Γ_Δ is a function that accounts for the straining effects of the vortices smaller than Δ on the flame, obtained in [32] from DNS calculations and whose values for different Δ/δ_L^0 are shown in Fig. 4-3.

In this study, following the formulation introduced in [35], the velocity fluctuation is calculated from the rotational part of the resolved velocity field as indicated in Eq. 4.43 where c_2 is a model constant, obtained from isotropic homogeneous turbulence

109
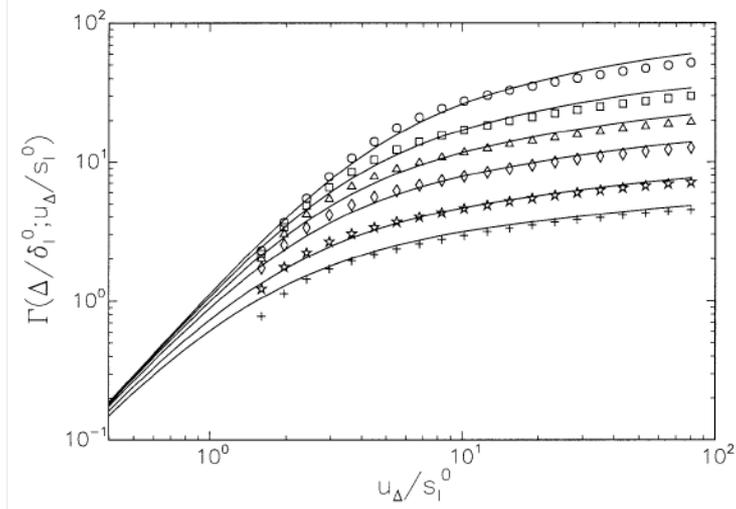
Figure 4-3: Γ function values (points) and fits (lines) from [32]

test cases, and equal to 2.

$$u'_{\Delta} = c_2 \Delta^3 |\nabla \times (\nabla^2(\tilde{u}))| \qquad (4.43)$$

In the static formulation, a constant value of $\beta = 0.5$ is usually used as suggested in [32]. The dynamic formulation introduces a non-constant β coefficient, which is dynamically computed. The static formulation assumes an equilibrium between the turbulent motion and the flame wrinkling. This assumption is valid as long as the time scales associated to subgrid-scale flame dynamics are much smaller than the other time scales of the flow field [32]. On the other hand, the dynamic formulation is able to handle situations where there is no equilibrium between turbulence and flame wrinkling [134]. The dynamic computation is performed with a double filtering operation, equating the flame surfaces calculated at a filtered and test-filtered scales and employing a "Germano-like" equation (Eq. 4.44). Applying the saturated value of the wrinkling factor in Eq. 4.42 to Eq. 4.44 gives an equation for β, and its formula is indicated in Eq. 4.45. The notation of the different filter widths are

110

explained in Table 4.2.

$$\left\langle \widehat{\Xi_\Delta |\nabla \bar{c}|} \right\rangle = \left\langle \Xi_{\gamma\Delta} |\nabla \hat{\bar{c}}| \right\rangle \tag{4.44}$$

$$\beta = \frac{\log \left(\left\langle |\widehat{\nabla \tilde{c}}| \right\rangle / \left\langle |\nabla \hat{\tilde{c}}| \right\rangle \right)}{\log \gamma} \tag{4.45}$$

Table 4.2: Explanation of the different filter width for the dynamic formulation of wrinkling factor in [31], as indicated in [135]

Symbol	Meaning	Expression
Δ	Combustion filter size	$\alpha F \delta_l^0$
$\hat{\Delta}$	Test filter size	$c_1 \Delta$
$\check{\Delta}$	Effective test filter size	$\gamma \Delta$
Δ_{avg}	Average filter size	$c_2 \Delta$

The combustion test filter Δ is different from the LES filter size because thickening a flame in the TFLES approach is not exactly equivalent to filtering a flame front following the standard LES definition [139]. The "hat" indicates test-filtering. The combination of two Gaussian filters of width Δ and $\hat{\Delta}$ results in a filter whose effective width is $\check{\Delta} = \gamma\Delta$ with $\gamma = \sqrt{1 + \left(\frac{\hat{\Delta}}{\Delta}\right)^2}$ (Therefore, parameters γ and c_1 are related). The "bar" indicates Gaussian filtering at width Δ. The equality in Eq. 4.44 is enforced over a control volume denoted by $\langle \cdot \rangle$. In order to save computational time, especially in unstructured meshes, this is performed by a Gaussian filter of width Δ_{avg} [90]. In this work, the progress variable c is based on temperature $c = (T - T_u)/(T_b - T_u)$ where T_u and T_b are the fresh and burnt gas temperature.

The dynamic formulation produces accurate results over a wide range of turbulent conditions, but requires additional filtering operations, increasing the computational cost. However, several researchers [135], [139], [111] argue that the time step usually employed in LES is much smaller than the characteristic time for a change in β and have carried out simulations performed by calculating β at fixed temporal intervals,

with an overhead of 20% due to the use of the dynamic model.

In summary, the final form the species "k" equation with the artificial thickened flame model is:

$$\frac{\partial \rho Y_k}{\partial t} + \frac{\partial (\rho u_i Y_k)}{\partial x_i} = \frac{\partial}{\partial x_i}\left[\frac{FD_k \Xi_\Delta}{X_k}\frac{\partial X_k}{\partial x_i}\right] + \frac{\Xi_\Delta}{F}\dot{\omega}_k \qquad (4.46)$$

In order that the modified mass diffusivity effects are restricted to the reaction regions, several sensors that control the activation of the thickened flame model have been developed.

The first example of sensor formulation, the dynamic sensor, is based on detecting the activation zones by comparing the actual reaction rate to a predefined reaction rate at the same fluid conditions (e.g. equivalence ratio, temperature, pressure), usually obtained through previously made 1D premixed calculations.

This sensor formulation S is:

$$S = \tanh(\beta'\frac{\Omega}{\Omega_0}) \qquad (4.47)$$

where Ω is the LES Arrhenius chemical term:

$$\Omega = \tilde{Y}_F^{n_F}\tilde{Y}_O^{n_O}\exp\left(-\Gamma\frac{E_a}{R\tilde{T}}\right) \qquad (4.48)$$

where Y_F and Y_0 are the mass fractions for the fuel and oxidizer respectively, n_f and n_0 are the respective forward Arrhenius coefficients, E_a is the activation energy and Ω_0 is the maximum reaction rate obtained from 1D premixed simulations. Γ is a parameter that regulates at which level the sensor is activated and is used to ensure thickening is applied to regions where reactions are starting to occur. β' is a smoothing parameter usually set to 50.

112

Finally, the thickening F is applied as:

$$F = 1 + (S - 1)F_{max} \qquad (4.49)$$

where:

$$F_{max} = \frac{N_c \Delta x}{\delta_l} \qquad (4.50)$$

with δ_l^0 (the unstretched laminar flame thickness) obtained from the 1D premixed calculations, Δx is the cell size and N_c is the number of cells on which the flame is discretized.

Despite being accurate at many operating conditions, this sensor may be inaccurate when the flame conditions depart from 1D premixed flame characteristics (e.g. diffusion flames, strained and stretched flames, two-phase conditions...)

Another sensor formulation has been developed recently in [117], the generic sensor, which does not depend on the relative behavior of the flow with a predefined flame. In this sensor formulation, the flame front is detected by looking at the Hessian matrix of the heat release rate surface or any equivalent surrogate. By looking at the sign of the eigenvalues of the Hessian matrix, it is possible to detect whether the heat release rate has attained a maximum (both eigenvalues negative), minimum (both positive) or a saddle point (negative and positive signs). This method identifies the flame presence in the regions where the largest absolute value of an eigenvalue of the Hessian matrix corresponds to an eigenvalue which is negative.

Once this region has been detected, the so-called "ridge-line" is available and thickening needs to be applied in a direction perpendicular to this line. It is necessary to determine the distance to the ridge where thickening will be applied. Since in an unstructured mesh the cell centers may be at an arbitrary distance of the ridge and/or belong to the partition of a different processor, a Lagrangian algorithm originally

developed for particle-localization [53] is used. This is shown in Fig. 4-4.
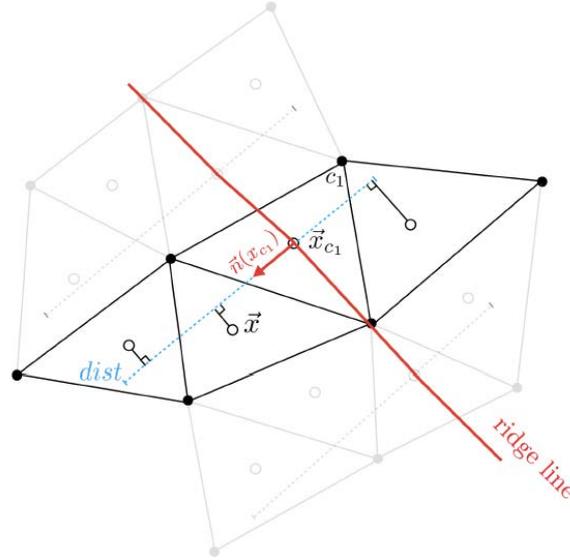
Figure 4-4: Illustration of the application of thickening in a direction normal to the ridge line. The process is the following: The point C1 is detected to be in the flame region. Then, its perpendicular direction and distance to the ridge line is computed. Finally, thickening is applied to the cells whose center are closer than a certain distance "dist". The "dist" parameter is user-defined. From [117]

Finally, in order to determine the value of F for the generic sensor approach, the flame thickness needs to be estimated. The flame is approximated as a parabola around the maximum point as:

$$f(\vec{x}) = f(\vec{x}_{C1}) + J \cdot \vec{n} \cdot (\vec{x} - \vec{x}_{C1}) + \vec{n}^T \cdot H \cdot \vec{n}||\vec{x} - \vec{x}_{C1}|| \qquad (4.51)$$

where $\vec{n}$, J and H are respectively the normal vector, the Jacobian and the Hessian evaluated at the position $\vec{x}_{C1}$. Then, this modified-flame thickness δ can be obtained by measuring the distance between the roots of this function. Once the resolved-flame thickness has been calculated, the actual flame thickness δ_L can be calculated as δ/F.

The determination of F is based on an iterative procedure and can be expressed in the following manner where F^n is the value of thickness at iteration "n" and δ_L^{n-1}

the actual flame thickness estimated at iteration "n-1":

$$F^n = \frac{N_c \Delta x}{\delta_L^{n-1}} = \frac{N_c \Delta x}{\frac{\delta^{n-1}}{F^{n-1}}} \qquad (4.52)$$

It is to be noted that despite the flame thickness derived from Eq. 4.51 is generally not equal to physical thickness definitions such as the Blint thickness, its value only enters in the ratio with respect to the previous thickness. Therefore, its absolute value is not critical, and the only user-defined parameter is N_c, which is related to the "dist" parameter in Fig. 4-4. Several validation tests can be found in chapter 6 in [117].

Probability Density Function Methods

An alternative model for the filtered chemistry source term is PDF-based methods. They are based on the concept that $\bar{\dot{\omega}}_k$ can be computed using a probability density function $P(\Psi)$ where Ψ depends on the chemical state of the system $\Psi = (Y_1, Y_2, ..., Y_{nspec}, T)$. Finally the filtered source term is computed as:

$$\bar{\dot{\omega}}_k = \int \dot{\omega}(\Psi) P(\Psi) d\Psi \qquad (4.53)$$

There are several methods for obtaining a probability density function. A first approach is to assume a shape function such as β-pdf, parametrized with quantities which must be determined.

Another approach is not to assume a predefined PDF, but calculate its evolution through an equation, notably a Boltzmann transport equation. The solution to this equation is approached by using either Eulerian stochastic fields or a Lagrangian Monte Carlo method. In the Eulerian method [57,58,133], stochastic fields are transported. In the Lagrangian Monte Carlo method [107], the phase space is represented

by fluid particles at a particular chemical state Ψ and their evolution is calculated following a Lagrangian formulation.

Finally, another formulation is the Conditional Momentum Closure (CMC). The underlying concept is to solve balance equations for conditional species mass fraction $\overline{\rho Y_k | z^*}$ which represents the mean value of mass fraction Y_k at a given value of mixture fraction $z = z^*$ [105]. The mean species mass fractions are recovered as:

$$\bar{\rho}\tilde{Y}_k = \int_0^1 \overline{\rho Y_k | z^*} p(z^*) dz^* \tag{4.54}$$

This approach consists in solving $\overline{\rho Y_k | z^*}$ at several values of z^*. Finally, this model requires the probability density function $p(z^*)$, which is usually presumed from $\tilde{z}$ and $\widetilde{z''^2}$. This approach needs to solve $N_{spec} * N_z$ additional equations where N_z is the number of levels of z^* at which $\overline{\rho Y_k | z^*}$ is solved and N_{spec} is the number of species.

Numerical Aspects of AVBP V7 solver

The AVBP solver is a code for the simulation of compressible reacting flows [120], able to scale efficiently over a large number of processors. It was developed by CER-FACS and IFPEN. It solves the Navier-Stokes in unstructured and hybrid grids. It relies on the cell-vertex discretisation in which the conservation relations are applied to the grid cells, while solution is stored at the grid nodes. It contains a Navier Stokes Characteristic Boundary Conditions (NSCBCs) treatment for the boundaries conditions [104]. The code can handle multi-component reacting flows [91].

Several numerical schemes for the convective terms are available and a complete review is found in [67]. The two schemes used in this work are:

- Lax-Wendroff scheme (LW). It is based on the finite volume formulation. It is second order accurate in space and time. Its computational cost is low and it is widely used. However, strong gradients in the solution can lead to oscillatory

behavior.

- Two-step Taylor Galerkin Scheme (TTGC). It is based on the finite element formulation. It is third-order accurate in space and time. It is used for "fine" LES calculations. Despite its advantages, it is more than twice as expensive as the LW scheme.

Chapter 5

Equations and Models for the Liquid Phase

Contents

This chapter covers the modelling, equations, and numerical description of the liquid phase.

5.1 Modelling

The equations for the liquid phase can be written according to two frameworks:

1. The Eulerian-Eulerian framework (EE) in which the liquid phase is considered a continuous phase and is calculated using continuum equations in the same grid as the gaseous phase.

2. The Eulerian-Lagrangian (EL) framework in which each individual droplet is

tracked individually and whose evolution is calculated using Newtonian equations of motion.

The EE treatment has the advantage of better scalability for parallel computing because the liquid and gaseous phase are solved in the same mesh. However, it requires modelling assumptions to describe how the particles and fluid interact. Furthermore, in case of polydispersity, the computational cost increases as each family of droplets requires their set of continuum equations. In addition to that, the interaction between droplet families has to be modelled. Finally the EE framework needs further modelling for situations which challenge the continuous assumption for the liquid phase such as droplets colliding with one another and modifying its trajectories as a result [128]. On the other hand, the EL framework can account for most of the liquid-gas interaction effects but at an increased computational cost since, in principle, it needs to track the evolution of every droplet.

Depending on the liquid phase density $\alpha_l = V_{liq}/V_{tot}$, three different regimes of liquid-gas interaction can be determined:

1. If the spray is very dilute ($\alpha_l < 10^{-6}$), then the liquid phase has a very small impact on the gas phase. Therefore, effects of the liquid on the gas may be neglected. This approach is called one-way coupling as only the effect of the gas phase on the liquid is retained.

2. If the spray is moderately dense ($10^{-6} < \alpha_l < 10^{-3}$), then the two-way interaction between the liquid phase and gas phase needs to be captured.

3. If the spray is very dense ($\alpha_l > 10^{-3}$), then the liquid droplets may interact with each other via collision or coalescence. In this case, droplet-droplet interaction is an additional effect to account for and this approach is called four-way coupling.

In AVBP V7, the current modelling assumes a two-way coupling. In particular, drag, evaporation and breakup mechanisms are accounted for. In addition to that,

advanced treatments of liquid-solid boundaries are available such as the formation of films, inelastic rebounds and splashing against the wall with the creation of new droplets. Droplets are considered spherical, which is a valid assumption as long as Weber number (the ratio between the drag force and the cohesive surface tension effect) is not high. In this work, the Euler-Lagrange formulation has been followed.

5.2 Equations

Taking into account the assumptions described above, the equations for each droplet of the disperse phase are:

$$\frac{d\vec{x}_p}{dt} = \vec{u}_p \tag{5.1}$$

$$\frac{d(m_p\vec{u}_p)}{dt} = \vec{F}_{drag} + \vec{F}_{grav+buoyancy} \tag{5.2}$$

$$\frac{dm_p}{dt} = \dot{m}_{evap} \tag{5.3}$$

$$\frac{dm_p h_{s,p}}{dt} = \dot{\Phi}_p \tag{5.4}$$

$$\tag{5.5}$$

where $\vec{x}_p, \vec{u}_p, m_p$ are the particule position, velocity and mass respectively. F_{drag} is the drag force, $F_{grav+buoyancy}$ are the gravity and buoyancy forces, $\dot{m}_{evap}$ is the evaporation rate and $\dot{\Phi}_p$ the rate of change in time of the particule's sensible enthalpy.

Exchange terms

The buoyancy and gravity term can be written as:

$$\vec{F}_{grav+buoyancy} = \rho_l V_p \vec{g} \left(1 - \frac{\rho_g}{\rho_l} \right) \tag{5.6}$$

where V_p is the volume of the particule.

The drag force is expressed as:

$$\vec{F_D} = \frac{1}{2}\rho_g C_D A ||\vec{u}_g - \vec{u}_p||(\vec{u}_g - \vec{u}_p) \tag{5.7}$$

where A is the transverse area of the spherical particle.

The drag coefficient C_D is a function of Reynolds number. In this work, the Schiller & Naumann [122] drag coefficient empirical correlation is used, which has been seen to be accurate up to Re=800 which and it is written in Eq. 5.8 and shown in Fig. 5-1.

$$C_D = \frac{24}{Re_p}(1 + 0.15Re_p^{0.687}) \tag{5.8}$$
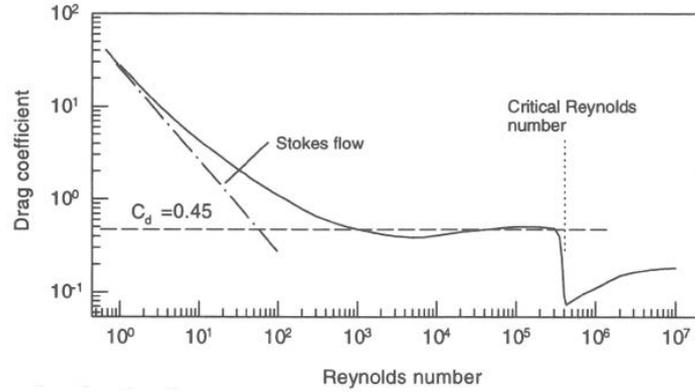
Figure 5-1: Variation of drag coefficient of a sphere with Reynolds number [39]

Usually drag and gravity forces are combined, and buoyancy neglected since $\rho_g/\rho_l \approx 10^{-3}$. In this way, the momentum equation for the particles is:

$$\frac{d\vec{u}_p}{dt} = \frac{1}{\tau_p}(\vec{u}_g - \vec{u}_p) + \vec{g} \tag{5.9}$$

where τ_p can be understood as a relaxation time for the particle to alter its inertial

122

motion.

$$\tau_p = \frac{\rho_l d_p^2}{18\mu_g(1 + 0.15Re_p^{0.687})} \tag{5.10}$$

The evaporation term requires additional explanations detailed in next section.

Evaporation

In this section, the classical development of Spalding [127] and the posterior remarks by Abramzon and Sirignano [4] are explained.

Spalding developed a model to describe droplet evaporation making the following assumptions:

- Droplets remain spherical and are not affected by neighbouring droplets. This implicitly assumes that droplets do not interact and restrict its accuracy up to moderately dense sprays.

- The temperature of the droplet is uniform in all its volume. This is justified by the fact that the thermal conductivity of liquids is one order of magnitude higher than that of the gases.

- The gas conditions are quasi-stationary and the position of the liquid-gas interface remains fixed. The latter assumption relies on the fact that the velocity of regression of the droplet interface is much smaller than that of the gas emitted from the interface.

Using these assumptions, the conservation equations for the gas phase become:

$$\rho_g u r^2 = constant = \frac{\dot{m}_F}{4\pi} \tag{5.11}$$

$$\rho_g u r^2 \frac{dY_F}{dr} = \frac{d}{dr}\left(\rho_g D_F r^2 \frac{dY_F}{dr}\right) \tag{5.12}$$

$$\rho_g u r^2 \frac{dC_p T}{dr} = \frac{d}{dr}\left(\frac{\lambda}{C_p} r^2 \frac{dC_p T}{dr}\right) \tag{5.13}$$

where r is the radial coordinate with origin at the droplet center.

Integrating twice the species equation, it is possible to obtain that the gas evaporated from the droplet is:

$$\dot{m}_p = -\dot{m}_F = -\pi d_p Sh \rho_g D_F \ln(1 + B_M) \tag{5.14}$$

where Sh is the Sherwood number which represents the ratio between the convective and diffusive mass transport and it is equal to 2 under quiescent conditions. B_M is the Spalding mass number defined as:

$$B_M = \frac{Y_{F,S} - Y_{F,\infty}}{1 - Y_{F,\infty}} \tag{5.15}$$

where the subscript "S" indicates the position at the droplet surface and its fuel fraction can be obtained from the partial pressure of the fuel obtained with the Clausius-Clapeyron equation.

$$X_{F,S} = \frac{p_{F,S}}{p} \tag{5.16}$$

$$p_{F,S} = p_{ref} \exp\left(\frac{W_F L_v(T_{ref})}{R}\left(\frac{1}{T_{ref}} - \frac{1}{T_{F,S}}\right)\right) \tag{5.17}$$

Eq. 5.14 determines a linear decay between the square of the droplet diameter with time. A characteristic evaporation time can be obtained:

$$\tau_{ev} = \frac{\rho_l d_{p,0}^2}{8\rho_g D_F \ln(B_M + 1)} \tag{5.18}$$

Droplet's Temperature

124

In order to calculate the droplet's temperature, we can first perform an energy balance across the droplet interface, which does not store energy, and it is shown in Fig. 5-2:

$$-\Phi_{l \to g} - \dot{m}_F h_{s,F} + \dot{m}_p h_{s,p} + \Phi_{g \to l} = 0 \tag{5.19}$$

where $\Phi_{l \to g}$ is the heat transfer from the droplet to the surrounding gas.
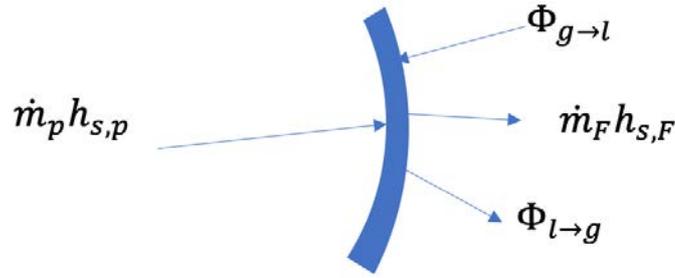
Figure 5-2: Energy balance across the droplet surface

Therefore, we can determine that:

$$\Phi_{l \to g} = \Phi_{g \to l} - \dot{m}_p L_v(T_p) \tag{5.20}$$

where L_v is the latent heat of evaporation.

On the other hand, by a control volume analysis of the droplet energy we can determine:

$$\int_V \frac{\partial m_p h_{s,p}}{\partial t} dV + \int_S \rho h_{s,p} \vec{v} \cdot \vec{n} dS = -\Phi_{l \to g} \tag{5.21}$$

125

consequently:

$$m_p \dot{h}_{s,p} = -\Phi_{l \to g} \tag{5.22}$$

which using Eq. 5.19 gives:

$$m_p C_p \frac{dT_p}{dr} = \dot{m}_p L_v(T_p) - \Phi_{g \to l} \tag{5.23}$$

Equation 5.23 determines the temporal evolution of the droplet if we determine a model for the heat transferred from the liquid to the gas, which is modelled as:

$$\Phi_{g \to l} = \pi d_p \lambda_g Nu(T_p - T_\infty) \frac{\ln(B_T + 1)}{B_T} \tag{5.24}$$

where B_T is the Spalding thermal number that is a function of the Spalding mass number:

$$B_T = (1 + B_M)^\beta - 1 \tag{5.25}$$

and:

$$\beta = \frac{ShPr}{NuSc_F} \tag{5.26}$$

where Nu is the Nusselt number and is equal to two for a sphere in a quiescent atmosphere.

It is important to notice that the temperature of the droplet is controlled by the heat from droplet to gas ($\Phi_{l \to g}$). This term tends to zero as the evaporation proceeds since $\Phi_{g \to l}$ and L_v reach an equilibrium. Thus, the droplet temperature tends to an equilibrium called "wet-bulb temperature". This assumption is implicitly made in the law that indicates the quadratic decay of the diameter with time.

More refined models take into account the effect of the relative flow on the droplet

126

evaporation:

- A boundary layer is generated around the droplet which may enhance mass and heat transfer rates.

- The relative flow induces a shear stress at the surface of the droplet which results in internal liquid motion inside the droplet which homogenize the droplet temperature.

Abramzon and Sirignano [4] proposed to account for the effect of the boundary layer by modifying the Sherwood and the Nusselt numbers according to:

$$Sh^* = 2 + \frac{Sh - 2}{F_M} \tag{5.27}$$

$$Nu^* = 2 + \frac{Nu - 2}{F_T} \tag{5.28}$$

where F_T and F_M are calculated using Eq. 5.29 employing B_T or B_M respectively.

$$F_x = (1 + B_x)^{0.7} \frac{\ln(1 + B_x)}{B_x} \tag{5.29}$$

Effect on the Continuous Phase Equations

The effect of the droplets on the continuous phase equations are introduced as sources on the right hand side of the gas phase equations.

In the mass equation:

$$S_m^{l \to g} = \frac{1}{\Delta V} \sum_{n=1}^{N_p} \Psi_n(x_{p,n}) \dot{m}_{p,n} \tag{5.30}$$

127

In the momentum equations:

$$S_{mom}^{l \to g} = \frac{1}{\Delta V} \sum_{n=1}^{N_p} \Psi_n(x_{p,n}))(-m_{p,n}\vec{F}_{p,n}^{ext} + \dot{m}_{p,n}\vec{u}_{p,n}) \tag{5.31}$$

In the energy equations:

$$S_E^{l \to g} = \frac{1}{\Delta V} \sum_{n=1}^{N_p} \Psi_n(x_{p,n}))(-m_{p,n}\vec{F}_{p,n}^{ext} \cdot \vec{u}_{p,n} + \frac{1}{2}\dot{m}||\vec{u}_{p,n}||^2 - \dot{\Phi}_{p,n}) \tag{5.32}$$

where ΔV is the control volume, N_p the number of droplets inside this volume and $\Psi_n(x_{p,n})$ is the interpolation function. The interpolation is done between the droplet location and the nodes of the cell containing the droplet. The interpolation function is inversely proportional to the distance of the droplet to the node.

Chapter 6

Radius Chamber

Contents

In the first part, this chapter explains the characterization process of the igniter employed in this study. In particular, the two approaches to numerically model the effect of the igniter on the flow during the ignition process are explained. The novelty of this work is the application of the energy deposition model to an actual aeronautical igniter in which the experimental temporal evolution of energy is available and diagnostics are available for $20 < t < 150 \ \mu s$ after the spark. In the second part, the ignition model is applied to the Radius Chamber setup (PPRIME Institute). This experimental setup emulates the flow conditions occurring in spinning combustion technology chambers at ignition and first instants of flame development. The temporal pressure measurements as well as Schlieren images will be used to evaluate the capability of large-eddy simulations to replicate ignition. In particular, two approaches are tested: a static and a dynamic formulation for the subgrid turbulence-chemistry interaction.

6.1 Characterization of the Ardiden Igniter

The igniter under study, which is employed in Safran Helicopter's Ariden 3 engine, is shown in Fig. 6-1.

The measurement of current and voltage characteristics consumed by an igniter is usually impeded by the coaxial cable which connects directly the igniter to its electric controller. In this study, to circumvent this problem, an adaptive part was placed between the igniter and the coaxial cable to measure the current and voltage temporal evolutions: the current probe (Pearson probe model 101) is placed around a copper rod, isolated by a POM-C case. This rod connects the high voltage electrode to its coaxial cable. A mass cable connects the mass electrode to the coaxial cable corresponding part. The voltage signal applied to the Ardiden 3 igniter is measured
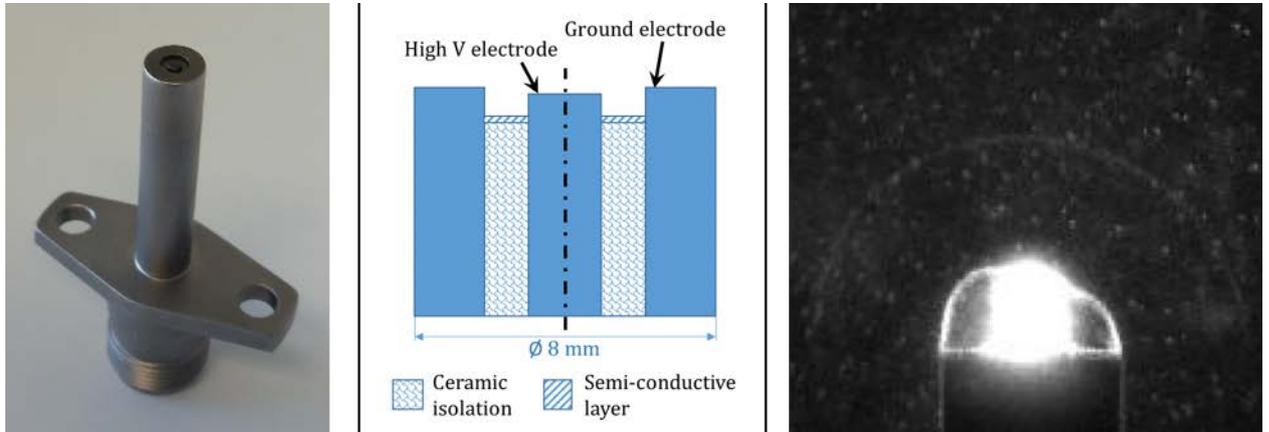
Figure 6-1: (Left) View of the aeronautical igniter used in this study, (Center) dimensions and characteristics, (Right) direct visualization of the igniter in the early instants of energy deposition (Courtesy of Institut Pprime Poitiers)

with a Tektronix P6015A probe. Figure 6-2 shows graphically this arrangement.

During electrical discharges, voltage and current variations occur in the order of tens of ns (in particular, hot plasma discharge breakdown voltage drops in tens of nanoseconds), so wideband electrical probes are required. The Tektronix P6015A probe was chosen to measure voltage as it features a 75 MHz bandwidth and a maximum limit of 40 kV. Concerning the current, the Pearson current monitor model 101 was used as high currents were expected with such igniter system, and it measures up to 50 kA with a 4 MHz bandwidth. Uncertainty for voltage and current are estimated to 3% and 1% respectively.

Finally, the temporal evolution of current and voltage (cf. a typical signal in Fig. 6-3) allows the determination of the electrical power and the total electrical energy (see Fig. 6-4) delivered to the electrodes of the Ardiden 3 igniter. For this igniter, the overall electrical energy is approximately 625 mJ per discharge, with a maximum power peak of 13.5 kW. By looking at the images Fig. 6-3 and Fig. 6-4, it is possible to detect the sudden peak at t=0 corresponding to the breakdown phase. For the rest of the deposition time, this igniter seems to work in an "arc-like" fashion due to its relatively high current and low voltage.

131

Figure 6-2: Adaptation to measure temporal current and voltage evolution
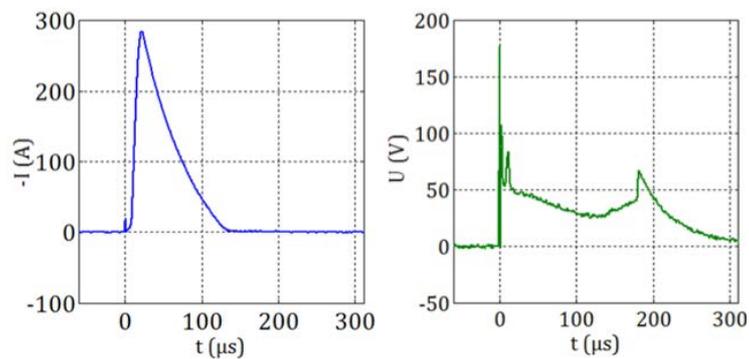
Figure 6-3: Typical electrical signals: Current (inversed, left) and Voltage (right).

6.1.1 Thermal Energy Released by the Ardiden 3 Igniter

The electrical energy determined by the current-voltage time evolution does not correspond to the thermal energy deposited into the fluid, which originates ignition. There is a transmission efficiency between the energy consumed at the igniter and that transmitted to the flame kernel. For that reason, a calorimetry methodology is followed to measure the energy absorbed by the flame kernel.

The chosen calorimetry methodology consisted in measuring the pressure increase induced by an electrical discharge in a closed vessel filled by inert gas at a given
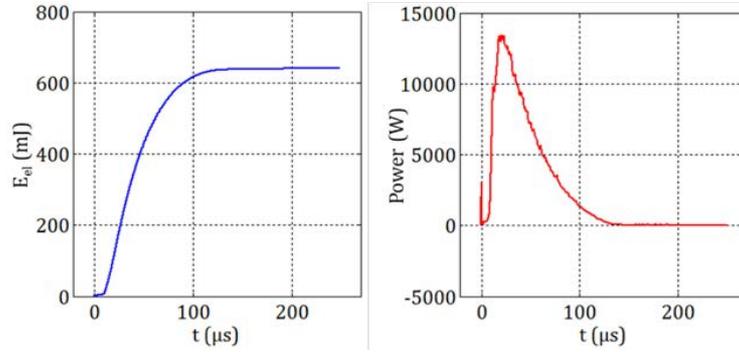
Figure 6-4: Typical electrical energy E_{el} (left) and electrical power (right).

pressure. Considering the small volume of hot kernel compared to the chamber size, a single zone model could be used. As the pressure increase was small, a constant gas density was assumed, as well as an ideal gas behaviour. The thermal energy remaining into the gas after the discharge (E_{th}) was obtained from the pressure increase in the given chamber volume as:

$$E_{th} = \int_V \rho C_V \Delta T dV = \frac{1}{\gamma - 1} \Delta PV \qquad (6.1)$$

where ΔT and ΔP are the temperature and pressure increase in the test volume. Heating capacities C_V, heat capacity ratio γ and the chamber volume V were assumed to be constant.

The closed volume was a cylindrical chamber. It was made of POM-C, to reduce heat losses through the walls, and there were 25 mm diameter silica windows with anti-reflection coated surfaces (W2-PW1-2506M-UV-1064-0) at the cylinder bases. This chamber ensemble is shown in Fig. 6-5. The resulting volume of the chamber was $V = 19.6 \pm 0.2$ ml and it was chosen in order to facilitate the pressure rise measurement. The volume was verified by filling it with water with a volumetric syringe. Because the transient increase pressure produced by an electrical discharge of few hundred mJ is of a few mbar in such a volume, a piezoresistive differential pressure transducer Meggitt 8510B-1 (0-1 psi range) is used. It is connected to a Meggitt DC

133

Amplifier model 136, which also adapted and filtered the pressure signal, with an integrated 10 kHz Butterworth physical filter (cf. red curve in Fig. 6-6). Signals were recorded by a LeCroy waverunner 104Xi high speed sampling oscilloscope. The transducer was located at least 1 cm from the electrodes tips and was protected by a porous metallic disc (around 50% porosity) to reduce the direct impact from the shockwave at breakdown. In this chamber, the maximum uncertainty was estimated at 6% for a value of energy absorbed by the fluid $E_{th} = 100$ mJ. A pressurized system (a parallelepipedal counter pressure chamber) was used for experiments involving different gas pressures. It consisted of an outer metallic chamber which contained the calorimetry chamber test (see Fig. 6-5). The counter pressure chamber was made of stainless steel, measuring 120x76x70 mm^3, with a 0.64 dm^3 inner volume. It served as a reference pressure for the piezo-resistive differential pressure transducer. Such configuration allows keeping a good accuracy on the pressure measurement in the calorimetry chamber test. A gas inlet at the base, closed by a valve, allowed filling and emptying the volume with gas at different pressures. Two opposite sides of the chamber held 125x75 mm² windows for visualization diagnostics.
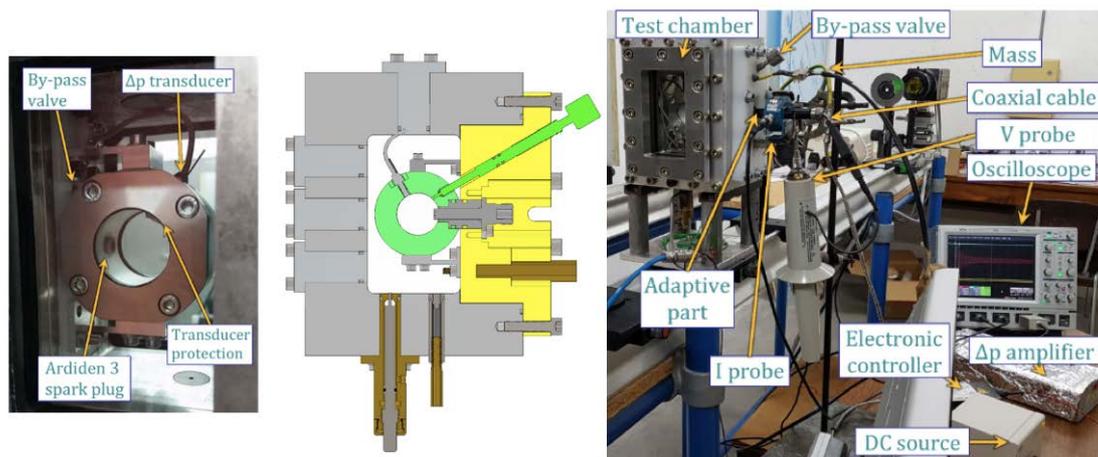
Figure 6-5: Calorimetry setup: detail of the 20 ml cylinder (left) and sketch and overview of the full calorimetry setup with the counter pressure chamber (center and right): 20 ml inner volume chamber (light green), by-pass valve (green), pressure transducer and spark plug (grey) and POM-C wall (yellow).

In order to remove the resonance frequency of the chamber, the recorded pressure signal was pre-processed and frequencies over 4 kHz were suppressed before performing the inverse Fourier transform (blue curve in Fig. 6-6 left). The thermal energy released to the gas was then obtained from the filtered unsteady pressure evolution a few milliseconds after the discharge, averaged over 1 ms (green curve in Fig. 6-6 left). A set of 45 tests, performed at ambient pressure in air, indicated that the electrical to thermal efficiency of this igniter is on average 13.7%, with an average electrical energy used of 625 mJ (see Fig. 6-6 right). The corresponding standard deviations were 49 mJ, 7 mJ and 0.4% for the electrical energy, thermal energy and efficiency respectively. This scattering results from the stochastic nature of the ignition process. Among the different causes, one may evoke microscopic differences in the surface of the electrodes between consecutive discharges and the scattering in the formation process of the plasma channel. Tests performed at different pressures showed a weak influence of gas pressure on the global features of the discharges of this igniter. The efficiency ranged from 12 to 14% when increasing gas pressure from 0.25 to 2 bar (in particular: 12.5% for 0.5 bar and 13.7% for 1 bar).
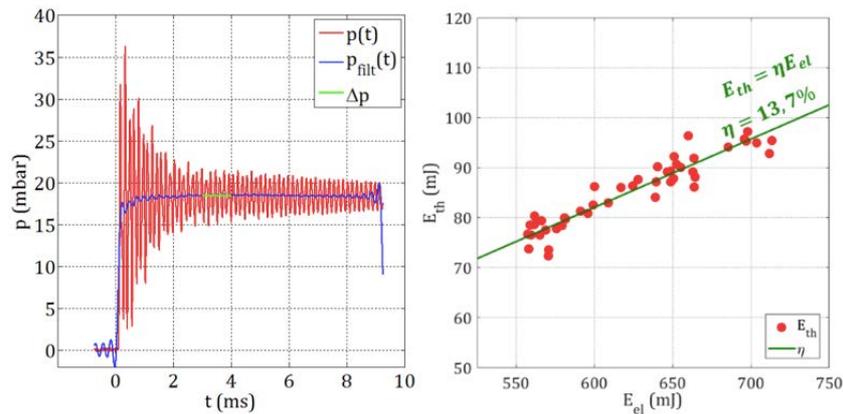
Figure 6-6: Typical time-pressure evolution measured and filtered in the microcalometric chamber (left). Thermal-electrical energy correlation for the Ardiden 3 igniter at ambient pressure (right).

6.1.2 Ignition Kernel Spatial Characteristics

To determine the kernel size evolution and its projection distance from the igniter, high magnification Speckle Background Oriented Schlieren (SBOS) visualization developed in a previous study [87] was used. Such technique highlights the density gradient, which is related to the refraction index gradient through the Gladstone-Dale relation.

The light source was a diode-pumped continuous solid-state laser (MxL-F, $\lambda = 532$ nm, 3 W). The emission power was stabilized for steady conditions at 1%. The beam was expanded to a 45 mm diameter parallel beam by a collimator impacting a 1 mm wide ground glass that produced the speckle by scattering effects. In order to record sufficiently sharp images of the kernel and of the generated shock wave, the exposure time was reduced down to 1 μs using a Princeton CCD intensified camera (PiMax 1k GenII RB-SG). A 532 nm interferometric filter was used to reduce the light emission from the hot kernel. The deviations of light rays due to refractive index variations induced displacements of the speckle patterns that were analyzed using PIV-like multipass cross correlation processing [87]. Time evolution of the kernel was then reconstructed by test repetition, shifting the delay between the spark trigger and the image timing. The resulting displacement fields are reported in Fig. 6-7 for ambient pressure showing the expansion of the kernel with time as well as the shock wave propagation.

The kernel penetrations, defined as the distance between igniter surface and the tip of the kernel and the kernel volume obtained from a cylindrical symmetry assumption, were determined from these visualizations for two pressure values, as reported in Table 6.1 at a given delay after the spark.
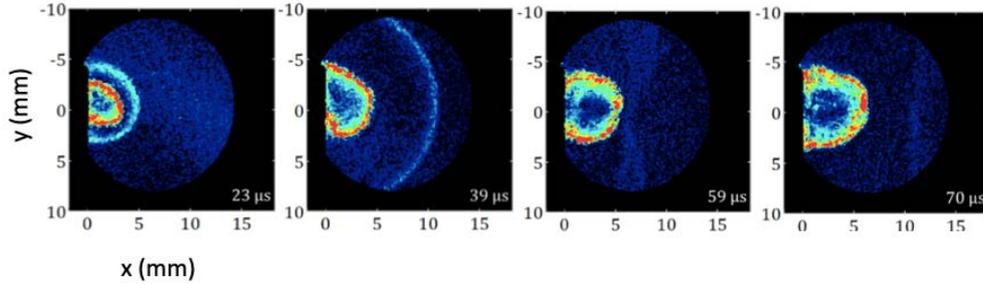
Figure 6-7: Ardiden 3 igniter discharge kernel evolution for P=1 bar and T=293 K. Visualisation from 23 μs to 70 μs. Positions are reported in mm from the igniter surface, along the symmetry axis.

Table 6.1: Geometrical characteristics of the hot kernel obtained from Schlieren images

Pressure (bar)	Kernel thermal Energy (mJ)	Penetration (mm)	Kernel Vol. (mm^3)	Delay (μs)
0.5	72	6.2	≈ 330	57
1	85	5.3	≈ 280	48

6.1.3   Ignition Modelling

In order to model ignition in the AVBP code, two approaches were evaluated. Both are based on the energy-deposition method developed in [65], which consists in adding a source of energy at the nodes located in a user-defined ignition region. It differs from other approaches available, such as imposing a volume of hot gases, by not altering the values of the species and replicating the overpressure created by the sudden energy deposition. This model has been successfully applied to different configurations in [19] and [46]. In addition to that, [36] included a refined study to accurately simulate the ignition process in a pin-pin electrode configuration considering also excited species such as N^+. It has to be noted that, for this study and contratry to the pin-pin study in [46], no data visualization was available in the deposition zone, and the images of the kernel are available for $t > 20$ μs. Recent work has been addressed to obtain data visualization during the early instants [83].

Table 6.2 contains a comparison of the main features of the igniter in this study and that of [37] .

Table 6.2: Characteristics of igniter under study (Ardiden 3) and, to underline the difference in magnitude, the characteristics of a typical pin-pin electrode configuration taken from [37]

Igniter	$E_{electrical}$ (mJ)	$t_{discharge}$ (ms)	Average Power (W)
Ardiden 3	624	0.15	4160
Pin-pin	90	2.6	34

6.1.4 Sparking Phase First Approach: Deposition in a Cylindrical Region

In a first attempt, the igniter effect on the fluid was modelled as an energy deposition in a cylindrical region in the electrode region following the detailed study in [37] and coherently with experimental observations conducted at the PPRIME laboratory [20]. Two distinct phases of sparking were considered: the breakdown phase ($0 < t < 20$ ns, with a electrical to kernel thermal energy transmission efficiency $\eta_{elect-thermal}$=95%) and the arc phase ($20ns < t < 150\mu s$ with a $\eta_{elect-thermal}$=13.7%). The electric power profile in Fig. 6-4 was used and multiplied by the corresponding efficiency of each phase. Fig. 6-8 shows a sketch of the location and dimensions of the energy deposition zone. The cylinder is located at the edge of the electrode gap. For the breakdown phase, a cylinder diameter of 0.15 mm was considered (as in the pin-pin study in [37]), while for the arc phase, a parametric study with cylinder radius ranging from 0.75 to 1.5 mm was performed to model the (greater) energy deposited during the arc phase in the case of the aeronautical igniter.

A hyperbolic tangent profile was used to apply the energy both in the axial and radial directions to avoid numerical oscillations. All thermodynamic properties were obtained from the reference NASA database [84]. Properties of several species are generally available up to 20000 K. The properties at temperatures higher than 20000
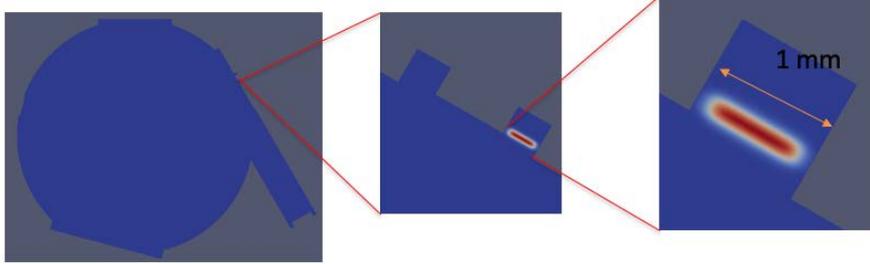
Figure 6-8: Image of the first ignition approach indicating energy deposition in a cylinder of length the distance between electrodes (1 mm)

K were extrapolated considering Cp and γ constant equal to that at T=20000 K due to the absence of experimental data in that temperature range. However, this range of temperatures ($T > 20000$ K) is only attained during a time of the order of $100\mu s$ after the start of the discharge. The calculations were made with air as in the experiments.

AVBP V7 was used, with the Lax-Wendroff convection scheme. While the TTGC scheme has superior dispersion and diffusion characteristics, the fact that the mesh had to be refined to 10 μm around the energy deposition justified the use of a lower-order spatial discretization due to its lower computational cost. The boundaries were set to isothermal no-slip walls because the short energy deposition time ($t \approx 0.1$ ms) and the large volume of the chamber causes the walls to remain near ambient temperature. Figure 6-9 shows the results for pressure, velocity and temperature inmediately after the breakdown phase ($t = 0.86\mu s$). The high velocities and temperatures cause the time step to be controlled by the CFL condition and remain of the order of 0.1ns.

In the above procedure, the radius (R_{arc}) of the cylinder region for energy deposition is unknown and a parametric study is performed to assess the sensitivity to this parameter. Figure 6-10 shows a comparison of results for a radius of 0.75, 1 and 1.5 mm at two instants t=21 and 24 μs. These results indicate a slightly increasing expansion for smaller R_{arc} and similarity with experiments for time t<24 μs for all
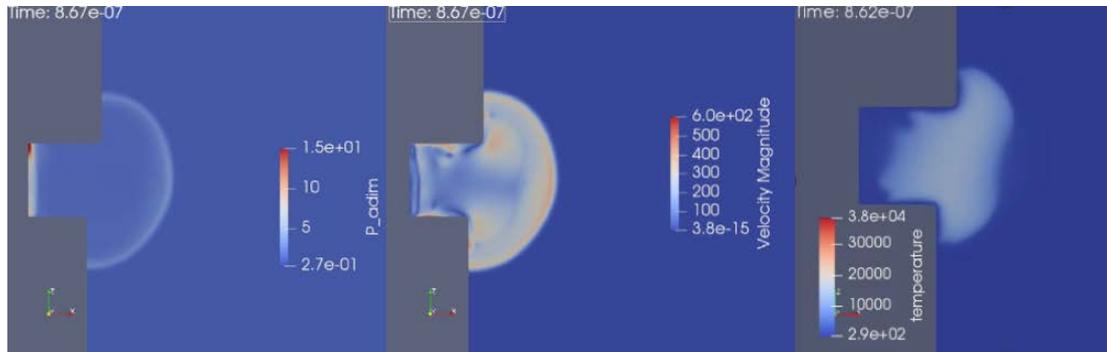
Figure 6-9: Results for $p^* = p/p_{amb}$, velocity (m/s) and temperature (K) for the cylindrical ignition approach at t=0.86 μs after spark (Transition between breakdown and arc phase)

cases.

Figure 6-11 contains a comparison of the LES calculations and the temperature derived from the SBOS images at t=49 μs. At this time, the experiment shows a kernel which has grown symmetrically around the igniter axis, with a temperature varying from 3000 to 3500 K. On the other hand, the LES calculation indicates the same level of penetration into the chamber, but the kernel remains located mainly on the igniter side where energy was deposited (no axisymmetry is observed). Figure 6-12 reveals that there is no flow motion in the transversal direction. On the other hand, the temperature predicted in LES is higher than in the experiment and is characterized by a strong inhomogeneity. The differences between the simulation and experiment are partly attributed to the uncertainty in the substance properties for T>5000 K. In addition to that, it has been hypothesized that the magnetic field generated at the igniter during the spark may have an influence during the early instants of kernel formation. The complexity of adding these effects into AVBP, the attainment of axisymmetry at t=49 μs together with the small time step imposed by the cylindrical approach and the absence of detailed measurements for $t < 20$ μs led to the development of a new approach in which the energy is deposited in a spherical region in the downstream region of the igniter.

140
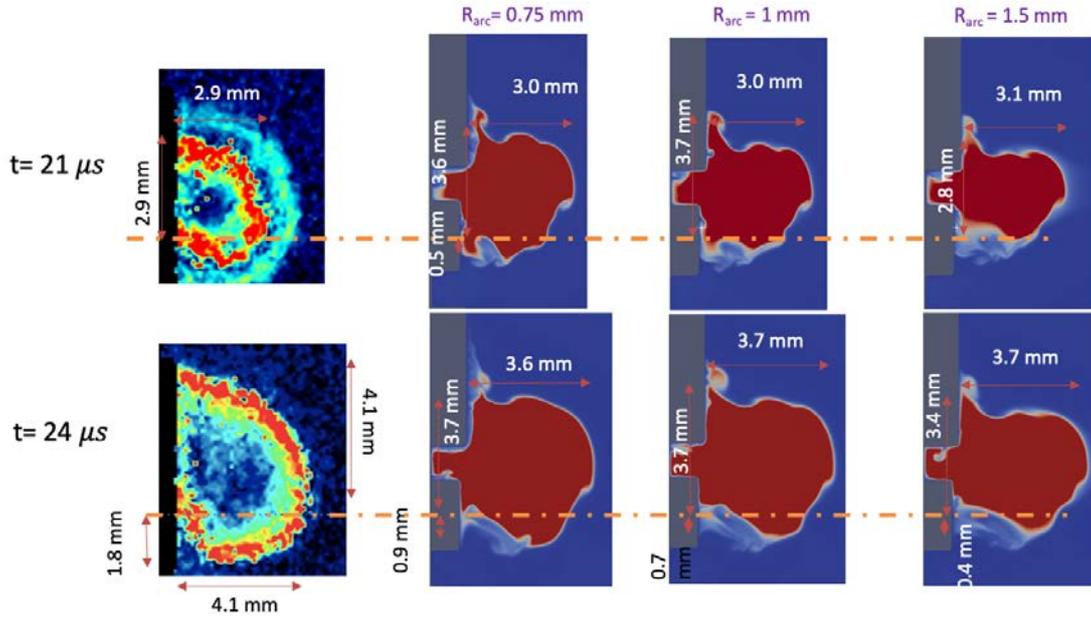
Figure 6-10: (Left) Experimental SBOS images at t=21 μs and 24 μs. (Right) Temperature contours at 620 K for three values of R_{arc}. The dotted line indicates the symmetry axis of the igniter.

All in all, the effect of the cylindrical shape of the deposition zone is the generation of a high overpressure (cf. Fig. 6-9) with a shockwave necessitating additional numerical treatment. In addition to that, the reduced volume and the fact that the deposition zone does not change with time (it remains fixed throughout the whole deposition duration) leads to a high concentration of thermal energy, which constrains the time step to values two or three orders of magnitude lower than usual LES combustion calculations, making this method unaffordable for industrial application.

6.1.5 Sparking Phase Second Approach: Deposition in a Spherical Region

This approach consists in depositing the power profile in Fig. 6-4 in a sphere whose size and position with respect to the electrodes is adjusted to match experimental data. The rationale behind this approach is the kernel attaining axisymmetry

141
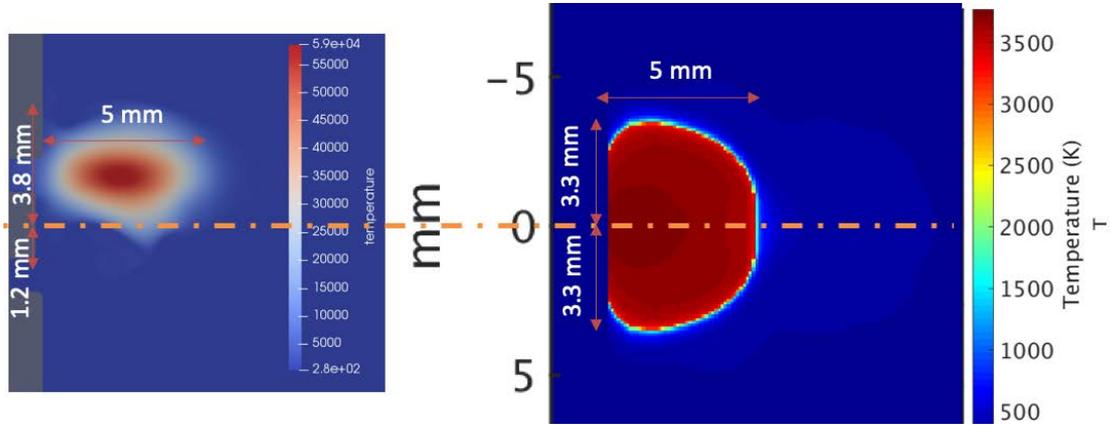
Figure 6-11: (Left) LES and (Right) experimental temperature derived from SBOS at t=49 μs after spark. $R_{arc} = 0.75mm$.

at t=49 μs after spark start. Figure 6-13 displays the definition of these two parameters for this approach: the sphere radius and its distance along the igniter axis. The sensitivity of the kernel penetration to the choice of these parameters is studied later. The numerical settings remained unchanged with respect to the cylindrical deposit approach.

A parametric study was completed varying both "r" and "h" to match the kernel size and penetration seen in the experiments at ambient pressure. The best match was found for an initial kernel radius of 2.3 mm and an initial height over the electrodes equal to 1.9 mm. Figure 6-14 displays a comparison of LES with experiment where the similarity in shape and level of the temperature field values can be observed.

After the kernel size and position was fixed using the experimental values at 1 bar, this method was tested at different initial pressure conditions (0.25<p<2 bar) and the kernel penetration (defined as the isoline of temperature equal to 620 K) was compared to the measurements. Figure 6-15 indicates the kernel penetration when changing the initial pressure conditions. Results indicate that the choice of radius and position of the deposit equal respectively to 2.3 and 1.9 mm above the igniter allows to correctly predict the kernel penetration distance within 0.5 mm margin for

142
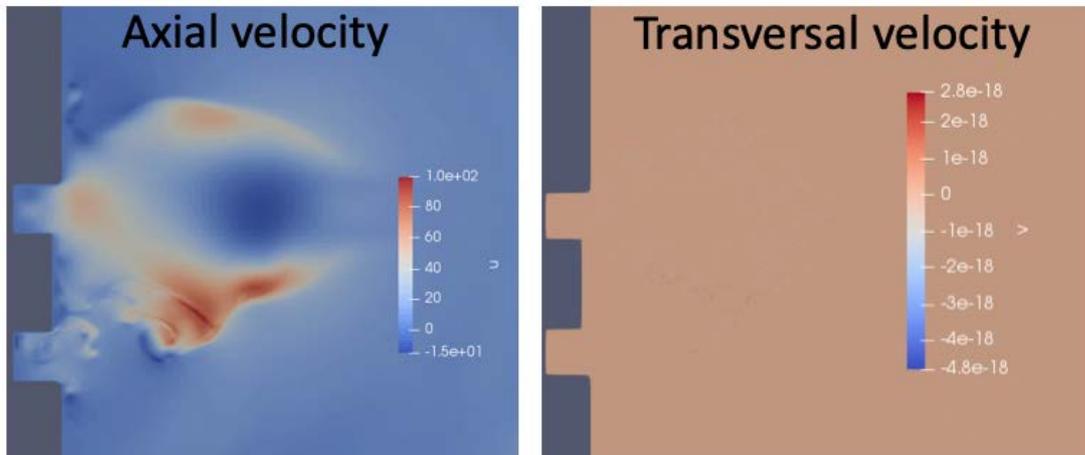
Figure 6-12: Axial and transversal velocity from LES showing the kernel has no transversal movement at t=49 μs after spark. $R_{arc} = 0.75$ mm.

the range of tested initial pressure between 0.25 and 2 bar.

In order to evaluate the sensitivity of this approach to the values of the deposit radius size (r), a study was made with a deposit whose radius was increased by 0.5 mm from the baseline value (i.e. in this case r=2.8 mm), while "h" was kept to the original value. Figure 6-16 shows the comparison between the baseline values (crosses) and the augmented radius results (circles). Results show small differences between the baseline and augmented radius for 0.5<p<2 bar. For the lowest initial pressure (0.25 bar), the augmented radius kernel penetration distance is reduced by an average of 0.7 mm, which is in line with the findings encountered for the cylindrical approach in which smaller deposition sizes led to larger kernel expansions due to higher overpressure and higher diffusion because of higher temperature.

Finally, a corresponding sensitivity study was done varying the height over the igniter (h), while keeping the radius size to its baseline value. Figure 6-17 shows the comparison between the baseline values (crosses) and the augmented height results (circles). For these conditions, the augmented height led to a vertical displacement equal to the increment over the baseline.
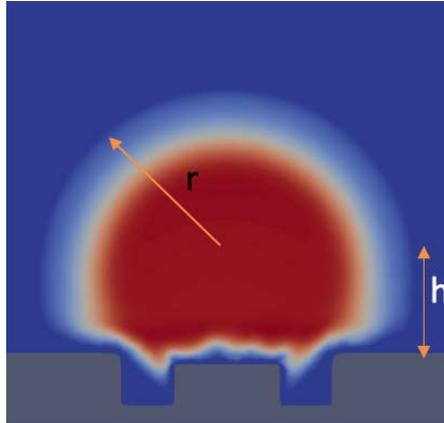
Figure 6-13: Definition of the size (r) and position (h) parameters for the spherical region deposition approach

Conclusion on Igniter Modelling

For the igniter under study, the approach using a cylindrical region in the energy deposition model was not able to accurately represent the physical phenomena for times greater than t>49 μs after sparking. In addition to that, the use of this approach in explicit codes such as AVBP entails a high computational cost due to a small time step imposed by the CFL condition and the mesh size. Finally, the strong temperature gradients for $t < 49 \ \mu s$ require a fine mesh size.

On the other hand, the energy deposition model using a spherical deposition approach, while not being realistic for early instants ($t < 49 \ \mu s$), it is able to represent the physics observed for $t > 49 \ \mu s$ for the Ardiden 3 engine igniter at different initial pressure conditions $0.25 < p < 2$ bar. The change of the radius of the sphere has a low impact on the kernel penetration, while the height of the center of the sphere has a direct linear correspondence with the kernel penetration. Consequently, the energy deposition model using a sphere was retained to model ignition in the radius chamber setup.

As a conclusion, the impact of the shape and size of the energy deposition zone on the ignition success can be described as not-critical for most ignition scenarios.

144
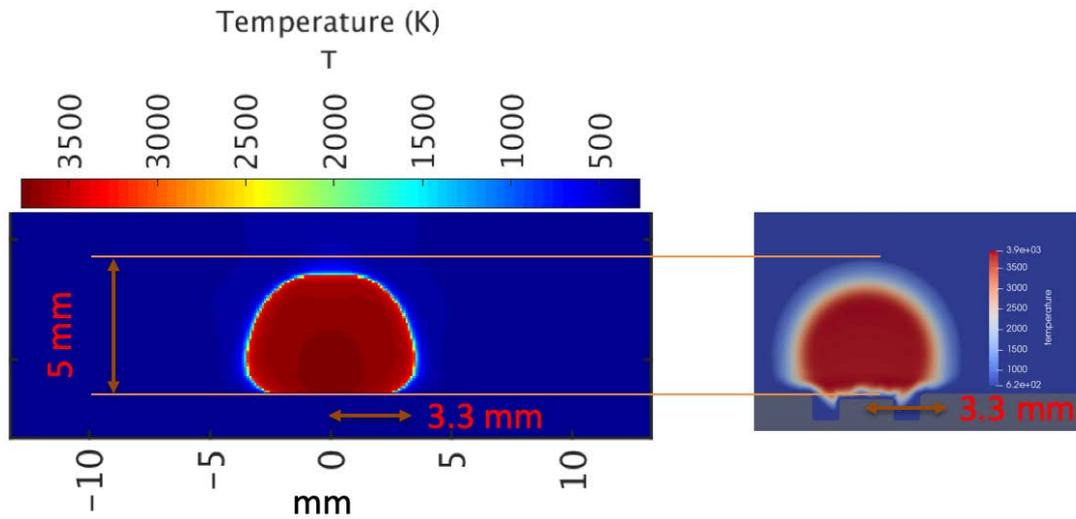
Figure 6-14: Comparison of SBOS (Left) and computations (Right) at t=49 μs after spark start for the spherical deposition approach
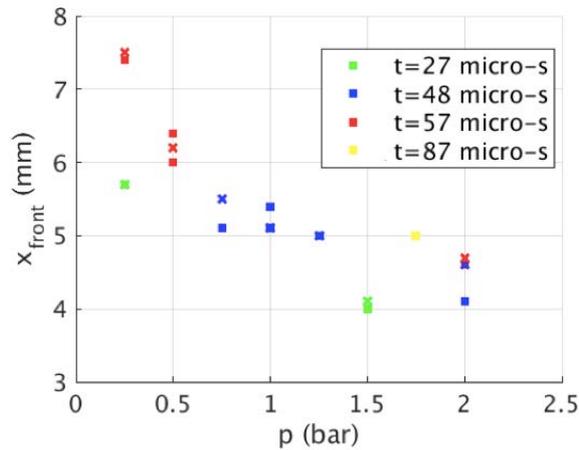
Figure 6-15: Comparison of kernel penetration between experiments (squares) and LES (crosses) for different initial pressure conditions and at different instants after spark

With respect to the shape of the deposition zone, the initial kernel shape is rapidly deformed by eddies, so a detailed initial description is not needed. This is in line with the findings of [124]. On the other hand, the total energy deposited does require an accurate modelling as it directly impacts the success of ignition. Finally, the size of the deposit will only affect the kernel overpressure and maximum temperature (also
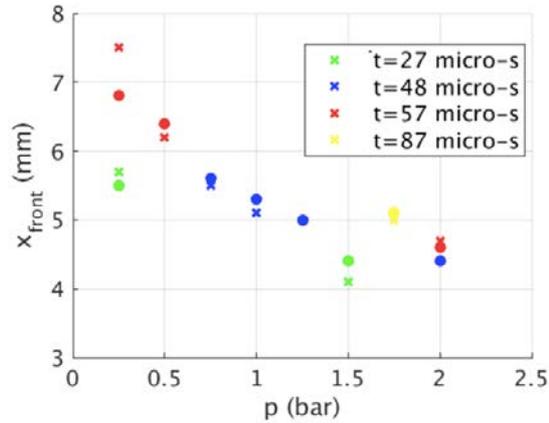
Figure 6-16: Comparison of kernel penetration between the baseline values (r=2.3 mm) (crosses) and a deposit of r=2.8 mm (circles) for different initial pressure conditions and at different instants after spark. Height over igniter is constant equal to the baseline value (h=1.9 mm)
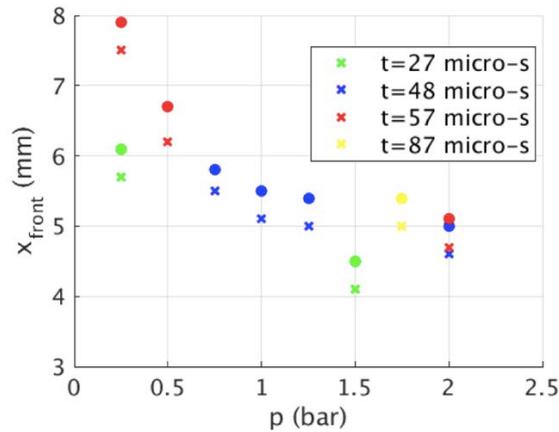
Figure 6-17: Comparison of kernel penetration between the baseline values (h=1.9 mm) (crosses) and an augmented distance over the igniter (h=2.5 mm) (circles) for different initial pressure conditions and at different instants after spark. Radius of the deposit is constant equal to the baseline value (r=2.3 mm)

linked to auto-ignition time). As such, a small kernel will lead to higher overpressures and temperatures (and a shorter auto-ignition time), the contrary happening for a big kernel. Therefore, an initially small kernel will expand more rapidly than a large one through overpressure and faster diffusion, which will tend to decrease the initial difference in size. Consequently, an initial choice of the kernel size between a lower

limit represented by the typical quenching distance for that fuel and conditions and an upper limit of a zone whose temperature allows for an autoignition time smaller than the typical eddy turn-over time leads to a kernel that can replicate a successful ignition.

6.2 The Radius Chamber Experiment

6.2.1 Experimental Setup

The experimental setup was composed of a cylindrical chamber and it was equipped with a dynamic pressure gauge and optical access allowing pressure evolution measurements and high frequency visualization. Initially, the mixture of methane and air was stored at 6 bars in a tank, then it was tangentially injected through a gas injector into the initially empty chamber generating a swirling motion of the flow which simulates the conditions at sparking in helicopter engines featuring the spinning combustion technology. The overall equivalence ratio was constant and set to 0.7. The chamber is initially empty and it was filled by the mixture up to a pressure of 0.5 or 1 bar by varying injection duration. The time delay between the end of injection and the ignition time was varied to obtain different strain rate and turbulence intensity levels. The radius of the chamber is 40 mm and the cylinder height is 35 mm. Figure 6-18 shows a sketch of the experimental setup.

6.2.2 Computational domain

Three different tetrahedral meshes were used during this study. The computational domain includes injector outlet and the chamber. During the filling phase of each case, a coarse 18-million cell mesh was used with a mesh size of 0.2 mm in the injection channel and 0.33 mm for the rest of the chamber. During the ignition phase,
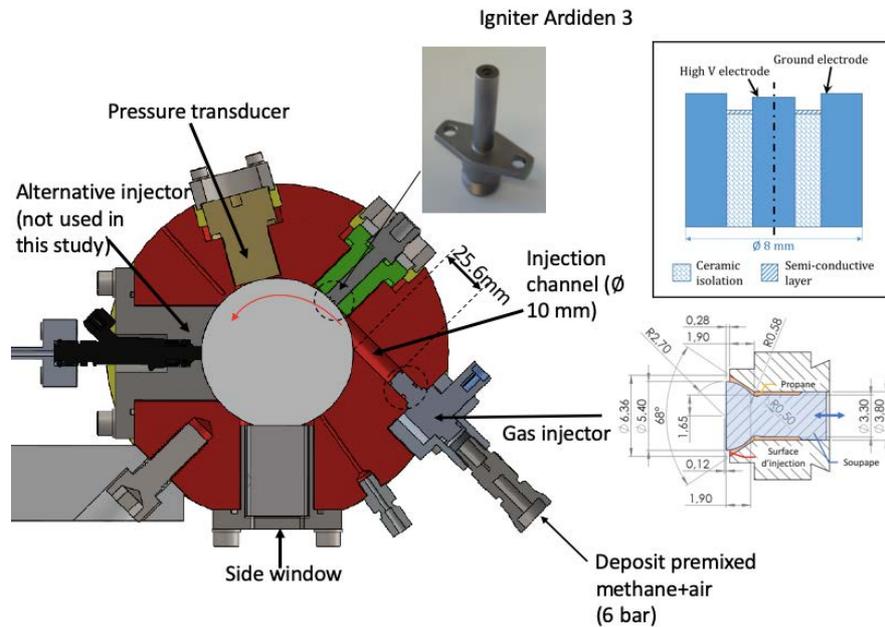
Figure 6-18: Sectional view of the chamber showing injection from the channel on the right, igniter at the top of the cylinder and in anticlockwise order: pressure sensor, liquid injector (not used in this study), window.

this coarse mesh is refined in a spherical region around the igniter of 10 mm of radius with a resolution varying linearly between 75 μm and 0.33 mm at the external radius in order to resolve the strong temperature gradients as shown in Fig. 6-19. Most importantly, this refinement avoids the use of the thickened flame model during the first instants of ignition when the kernel does not have a propagating flame structure [23]. One millisecond after energy deposition finishes it is posited that the flame has a propagating flame structure, which is in accordance with the Schlieren images in the experiment. At this instant, the solution is interpolated into the third and final mesh, which is characterized by a uniform cell size of 0.2 mm everywhere (44 million cells). Note that y^+ remains below 30 in all the wall regions.
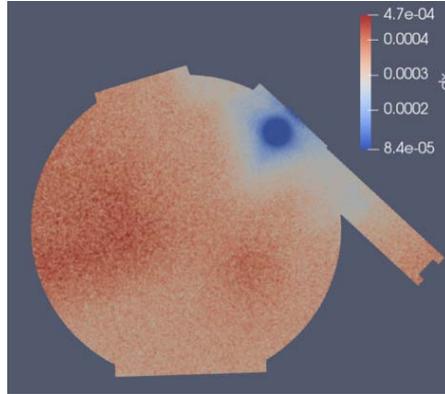
Figure 6-19: Overview of the mesh with mesh sizes in m used during the energy deposition instants showing mesh refinement near the igniter

6.2.3 Initial and Boundary conditions

For the laminar cases, all surfaces were treated as non-adiabatic walls, using heat transfer resistances obtained with the electric analogy and equal to 1.43e-2 m^2K/W for the quartz boundaries (the cylinder faces) and 2.18e-2 m^2K/W for the steel boundaries (rest of boundaries) and assuming the surrounding air at ambient conditions. The laminar cases were initialized with a quiescent premixed mixture of methane and air at the corresponding conditions.

For the turbulent cases, in the experiments, the filling of the chamber starting from vacuum to 1 bar lasts 135 ms (67.5 ms for 0.5 bar). This procedure was reproduced numerically. Due to the pressure ratio between the tank (6 bar) and the chamber ($0 < p < 1$ bar), the injector nozzle is choked throughout the filling process. As a result of that, the massflow entering the chamber is constant and could be calculated from the pressure and temperature at the deposit and the injector nozzle throat area. Furthermore, this information rendered the modelling of the shock unnecessary. Following the measured linear increase in pressure with time during filling, the flow entering the chamber after the injector is at a constant temperature equal to 387 K. Thus, a constant uniform mass flow rate boundary with constant temperature was imposed at the inlet. This approach does not take into account the true shape of the

149

inlet velocity profile, but the lack of measurements at the inlet did not allow to do better. The solid walls are treated with wall-functions. Both pressure and density at the end of injection were verified to be within 1% of the experiment, which gives confidence to the numerical setup during the filling phase. Once the desired pressure is reached, injection stops and the inlet boundary is modelled as a wall.

6.2.4 Chemical scheme

The analytically reduced chemistry for methane/air employed is described in [76] and consists of 19 species and 184 reactions (Lu19). This scheme has been thoroughly validated for auto-ignition (for $1000 < T < 8000$ K), 1D flames, perfectly stirred reactors for $1 < p < 30$ atm and has been recently used in the ignition study in [110]. Within the context of this study, this scheme has been compared to the skeletal mechanism GRI 3.0 and an in-house 22 species methane scheme (S22R195, derived from the detailed scheme from the CRECK group at PoliMi [112]) in a counterflow premixed flame at different operating conditions as detailed in [49]. Results show a maximum difference of 15% in consumption speed and 10% in species profiles for strain levels ranging from 0 to 20000 s^{-1}. A summary of these results for inlet conditions of p=1 bar, 320 K and $\phi = 0.83$ is shown in Fig. 6-20 and Fig. 6-21. These conditions are representative of operating conditions under study. Note that the source term for species H_2O_2 and HO_2 was reformulated in a semi-implicit integration following the methodology described in [56] to avoid numerical oscillations due to stiffness and it is detailed in Eq. 6.2.

$$\dot{\omega} = \frac{\dot{\omega}^+ - \dot{\omega}^- Y}{1 + \dot{\omega}^- \Delta t} \qquad (6.2)$$

where $\dot{\omega}$ is the species source, Y is the species mass fraction and $\dot{\omega}^+$ and $\dot{\omega}^-$ are the creation and destruction rates for the species (both are positive according to the

sign convention in Eq. 6.2)
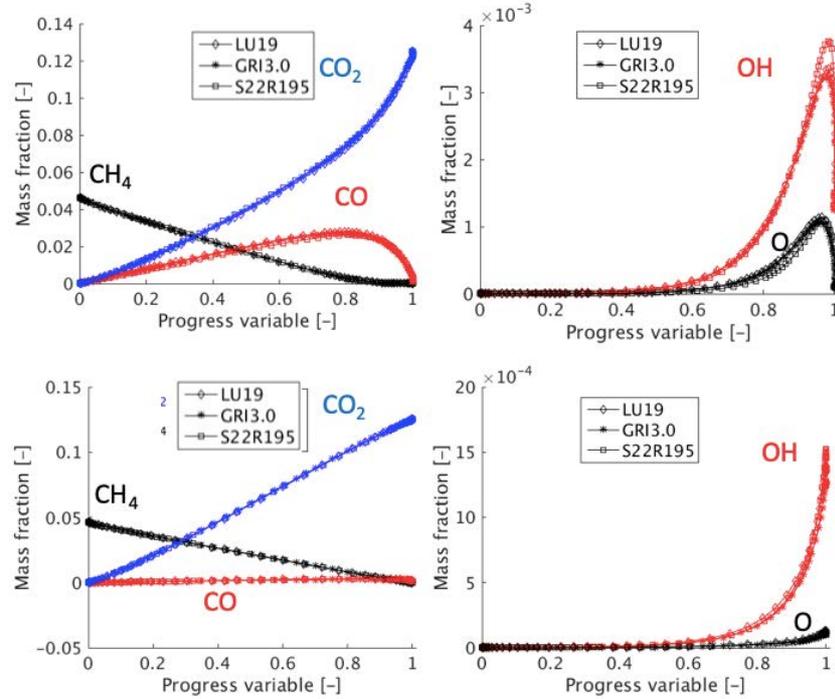
Figure 6-20: Methane-air combustion: comparison of species profiles in a lean pre-mixed flame for inlet conditions of p=1 bar, 320K and $\phi = 0.83$ at strain rate equal to 2000 s^{-1} (top) and 20000 s^{-1} (bottom) or Lu19, GRI3.0 and S22R195. Progress variable based on CH_4.

6.2.5   Numerical Modelling

The interaction of the flame with turbulence is modelled using the thickened flame model. In this study, the flame sensor recently proposed in [118] and detailed in section 4.1.6 is used which automatically identifies the heat release zones and applies thickening according to a single user-specified number of cells within the flame front (in this study 7 cells). This sensor has the advantage of being independent of flow conditions (equivalence ratio, pressure, etc.) and to adapt automatically to the mesh resolution. Since the flame grows in the whole domain and interacts with the chamber walls, there is the need for a high-fidelity description of the turbulence-

151
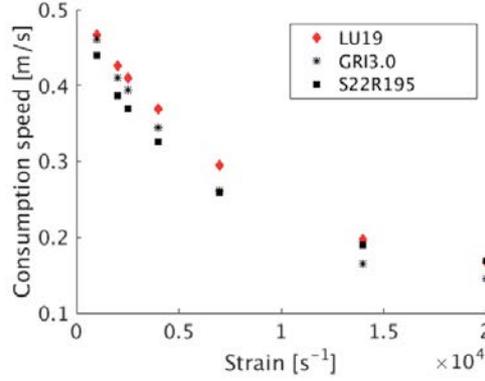
Figure 6-21: Consumption speed versus strain rate for a strained premixed flame at inlet conditions of p=1 bar, 320 K and $\phi = 0.83$ for Lu19, GRI3.0 and S22R195

chemistry interaction in the whole domain. Modelling approaches such as Detached-Eddy Simulation would require additional modelling assumptions, in particular when the flame approaches the walls, so a LES approach was selected. In order to describe the non-resolved flame wrinkling due to subgrid-scale turbulence, the thickened flame model [35] uses the wrinkling factor Ξ_Δ, also known as the efficiency function. In this work, both the static and the dynamic formulations of the efficiency developed in [31] and [32] are tested and compared. The time step was constrained by both the CFL condition and chemical activity and was of order $O(10ns)$. For the closure of the species and energy equation, a constant Schmidt and Prandtl numbers are considered equal to 0.6.

Table 6.3: Choice of filter widths for the dynamic formulation of wrinkling factor

Symbol	Meaning	Expression
Δ	Combustion filter size	$1.4F\delta_l^0$
$\check{\Delta}$	Effective test filter size	1.5Δ
Δ_{avg}	Average filter size	2Δ

Computational Cost

Each calculation with the static version of efficiency necessitated on average 483,000 processor hours to be completed. On the other hand, the use of the dynamic formulation required an average of 1,161,000 processor hours due to the additional filtering operations to calculate the parameter β. However, a recent study [111] has reduced this additional cost to an overload of 15% by introducing a modification in which the additional operations for the dynamic formulation are only performed in the regions of the domain where thickness is greater than one. The study in [111] included a section which verified that the PDF β remained identical to the case where the filtering operations were applied to the whole domain. In addition to that, [111] limited the frequency of calculating β to once every 750 iterations. These modifications could have a similar impact in the radius chamber case, but due to the publication of [111] after the computations were finished, the operations for calculating β in this work are made every iteration in the whole domain.

6.2.6   Results and Discussion

Laminar Case

In order to validate the modelling of the wall heat losses, a laminar case with $p_{ini} = 1bar$, $T_{ini} = 300K$ and $\phi = 0.7$ was performed. Figure 6-22 shows the Schlieren and density gradient images at t=38 ms and Fig. 6-23 shows the temporal evolution of pressure up to 45 ms. The same propagation speed was recovered as in the experiments. This offers evidence that heat losses are well modelled for this configuration.
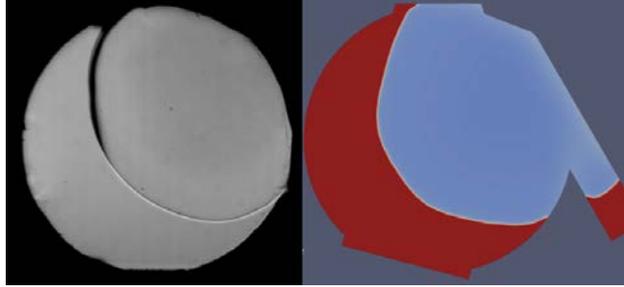
Figure 6-22: Flame visualization at t=38 ms after sparking. Experiment Schlieren (Left). Computation: normalized density field (Right)
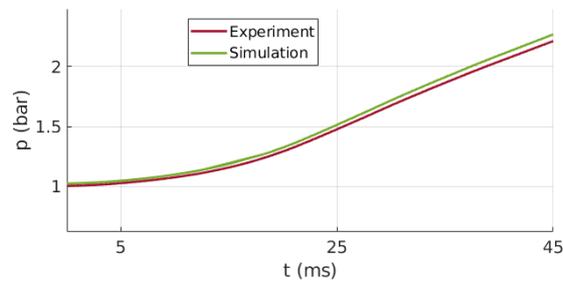
Figure 6-23: Temporal pressure evolution for a case with p_{ini}=1bar, T_{ini}=300 K, ϕ=0.7

Turbulent Cases: Non-Reacting Filling phase

Three operating conditions are discussed in detail and are presented in Table 6.4 and are representative of the operating conditions of an actual Safran SCT engine. All were performed with a $\phi = 0.7$ mixture. Turbulent case A is characterized by injection at 1 bar (lowest injection velocity, note that inlet is a constant mass flow rate boundary, thus velocity diminishes as the density increases as the chamber fills up), and a short delay between end of injection and sparking (5 ms), which results in high turbulence intensity and, therefore, a high Karlovitz number (Ka). Turbulent case B ignition starts 5 ms after the end of injection and it starts at 0.5 bar, thus having a strong inlet velocity and turbulent intensity. However, Ka has changed due to faster diffusion. Finally, turbulent case C also starts at 0.5 bar (higher injection velocity), but its longer delay (30 ms) attenuates the turbulence intensity with respect to cases

A and B. The three cases also feature different strain rate at the igniter location, highest for case B.

Table 6.4: Cases under study. Ignition delay refers to the time between the end of injection and sparking. The turbulence and strain levels are obtained from the tangential velocity at a position 1 mm above the igniter and are averaged values over ± 1ms around the time of sparking

Case name	P at end of injection	Ignition Delay	Strain level at igniter start	Ka	Re
Case A	1 bar	5 ms	3600 s^{-1}	63.2	31200
Case B	0.5 bar	5 ms	5500 s^{-1}	3.4	22200
Case C	0.5 bar	30 ms	3300 s^{-1}	0.6	13900

The turbulent field is well resolved except for small regions where recirculation occurs (injector exit and corners), as can be seen in Fig. 6-24 and Fig. 6-25 showing fields of ν_{turb}/ν_{lam}. Figure 6-26 contains the vorticity fields just instants after the spark, when the kernel has not grown appreciably. Figure 6-27 shows the probability density function (PDF) of tangential and radial velocities around the igniter observed in cases at the sparking instant for cases A, B and C. The wider distributions in A and B (short delays) with respect to C (long delay) give evidence of higher turbulence levels. On the other hand, the mean value of the tangential velocity in B corroborates the higher injection velocity compared to cases A and C.
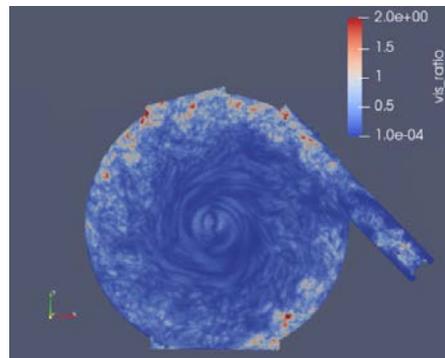
Figure 6-24: Field of ν_{turb}/ν_{lam} after filling up to p=1 bar for case A, before spark
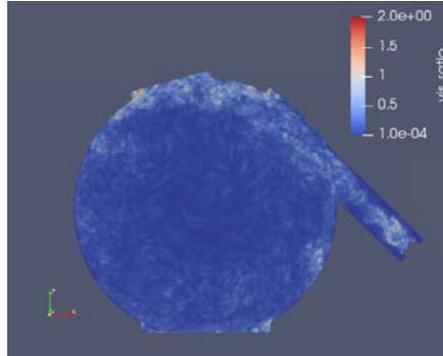
Figure 6-25: Field of ν_{turb}/ν_{lam} after filling up to p=0.5 bar for case B, before spark
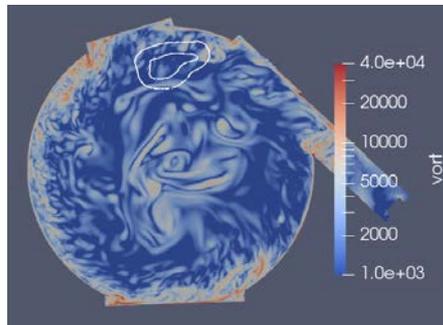
Figure 6-26: Vorticity field (s^{-1}) for case A, two milliseconds after spark. The kernel boundaries are indicated with white contours and has not grown appreciably

Turbulent cases: Reacting Phase using the Static Efficiency Formulation

Figures 6-28, 6-29, 6-30 contain the corresponding images from LES density-gradient line-of-sight integration (LOS). The image series demonstrate an overall good agreement between LES and experiments for all cases in terms of kernel location and size. The differences will be analyzed in detail later in this chapter.

Figure 6-31 shows a comparison of the temporal evolution of pressure between experiments and LES for the three cases. The pressure signals have been postprocessed with a moving average window of period 0.2 ms.

Although the temporal evolution of pressure curves of cases A, B and C are different, they can be decomposed into similar phases, which will be explained. The time for maximum pressure in case A is smaller than cases B and C due to the higher Ka

156
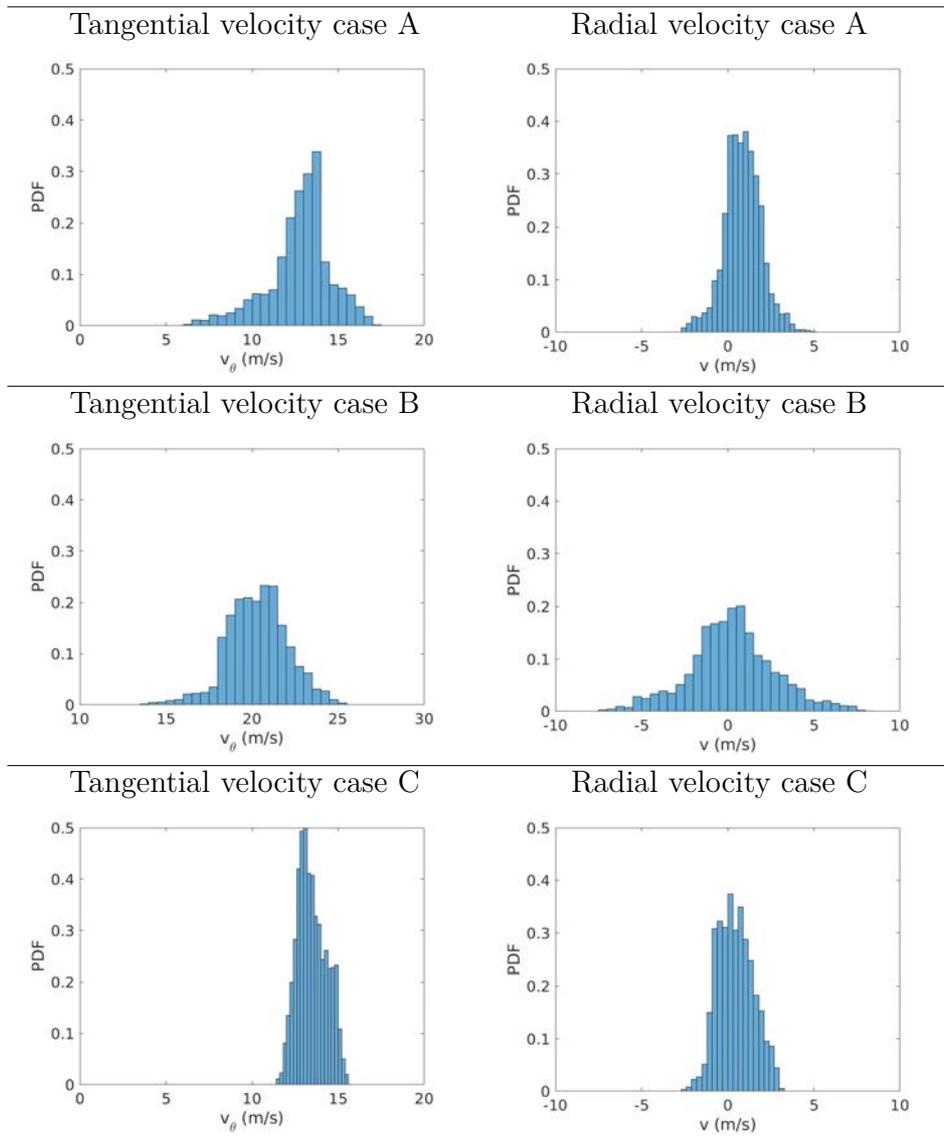
Figure 6-27: Comparison of PDFs of tangential and radial velocities in a sphere of R=3.5cm around the igniter location at the time of spark for the three cases

(more flame surface wrinkling). This is manifested by a higher efficiency value for case A, as it will be shown later in this section.

In case A, both experiment and LES show a small pressure rise during the first 5 ms after spark (phase I), where the flame kernel propagation remains small and is weakly

interacting with turbulence. After the kernel has reached the chamber center at t≈ 5 ms, it starts to expand radially (phase II). This behavior is also shown graphically in the LOS images (cf. Fig. 6-28). LES displays a slightly delayed kernel rotation. This effect may be attributed to the uniform mass flow rate boundary during injection which does not take into account the actual shape of the inlet velocity profile. Around t≈ 10 ms the flame boundary is close to the walls and there is an acceleration of the burning rate (phase III). Complete combustion is reached at t≈ 20 ms.

In case B, identically to case A, both the experiment and LES show a weak pressure rise while the flame kernel is being strained and travels towards the center of the chamber (phase I). It is followed by a radial expansion (phase II), where the flame kernel expands radially at a constant rate. This behavior is well represented in LES. After t≈20 ms, the third phase (phase III) is much more visible. As for case A, in this phase, the consumption speed in LES case B is faster than in experiments. This reaction acceleration when the flame comes closer to the walls is linked to the interaction of the flame with the vorticity generated near the walls.

Case C has an overall similar behavior to cases A and B, but the pressure rise is slower due to the attenuation of turbulence during the delay between end of ignition and sparking. Similarly to case A, the comparison of the Schlieren and LOS images during the first instants ($t < 10$ ms) indicates a slight delay of kernel rotation in computations, which is attributed to the aforementioned uncertainty in the initial inlet velocity profile. The flame anchors at the center of the chamber at t=7 ms in experiments and t=10 ms in the LES and the constant growth phase (phase II) starts. Phase II ends at t≈20 ms, and acceleration occurs then to reach complete combustion at t≈30 ms in the LES. The pressure rises when the flame comes closer to the walls, which results in a narrowing of the delay between LES and the experiment. Similarly to cases A and B, this behavior can also be seen in the LOS images.

Figure 6-32 displays the temporal evolution of the change of pressure with time.

The three distinct phases are clearly visible for case B and C. There is a small pressure rise in phase I, an almost constant value for phase II, and an acceleration for phase III.

Cases B and C, both at an initial pressure of 0.5 bar, permit a direct comparison of the effect of turbulence and strain. In experiments, realizations of case B have a faster pressure rise than case C for $0 < t < 10$ ms after spark. During this time, the kernel growth is mainly governed by the flow straining effects, and the higher strain in case B results in a faster pressure increase. At t=10 ms the pressure curves of B and C intersect and for $t > 10$ ms the pressure growth for both cases are similar, with case C having a slightly faster growth rate. Eventually, case C attains its pressure peak 1 ms before case B. The behavior in the experiments for $t > 10$ ms can be explained by the fact that the pressure rise during this phase is mainly governed by the effect of turbulence. In case B, at t=10 ms, the viscosity has increased due to the earlier growth of the flame kernel during the straining phase. In addition to that, a higher decay rate of turbulence level in case B may rend the turbulence intensity closer to case C for $t \geq 10$ ms. By the combination of these effects, the turbulence levels in B and C may attain similar levels for $t > 10$ ms and, therefore, experience a similar growth rate. The LES calculations replicate the same trend as experiments: during $t < 10$ ms case B rises faster than C, and for $t > 10$ ms the growth rate between B and C is similar. However, LES computations fail to replicate the intersection of pressure curves. The main reason for this is the fact that, for case C, LES predicts that the flame kernel is not wrinkled by turbulence until $t > 10$ ms, while Schlieren images of experiment C indicate a substantial level of wrinkling for $t \geq 7$ ms. For that reason, LES display a delay in pressure rise which originates at $t < 10$ ms which is maintained constant for $10 < t < 20$ ms. For $20 < t < 30$ ms the acceleration in reaction rate predicted by the LES serves to decrease this delay and both LES and experiments attain their peak within 1 ms.

The reason for the delay of LES case C in the effect of turbulence on pressure rise

may be found in the formulation of u'_Δ in [32], which is indicated in Eq. 4.43. This formulation, which has been originally developed in homogeneous isotropic turbulence flows, predicts low values of u'_Δ/S_l near the chamber center in this configuration (which is close to solid rotation conditions) as shown in Fig. 6-33. Consequently, the values of wrinkling factor in case C while the flame surface is located near the center of the chamber ($7 < t < 10$ ms) is low and the pressure rise is slow. The effect of small values of u'_Δ/S_l near the chamber center is not felt as strongly in cases A and B because in these cases the flame grows faster during the phase governed by straining. As a result of that, in cases A and B, the flame surface is located inside the region of high u'_Δ near the wall boundaries by the time the pressure rise becomes governed by turbulence, as shown in Fig. 6-34. The behavior of u'_Δ near the wall boundaries can also be observed in Fig. 6-33 and 6-34.

In summary, the overall agreement is fairly good, and the pressure rise and kernel shape are well modelled with small time differences. In case A, the LES calculation predicts the pressure peak at t=17 ms, 2 ms before the experiment. In case B, the pressure rise during phases I and II follows the experiments. However, the reaction acceleration predicted by the static formulation of the wrinkling factor (phase III) is the origin for the anticipation of the pressure peak instant in LES ($t_{peak} = 21$ ms) with respect to the experiments ($t_{peak} = 28$ ms). Finally, in case C, the time to reach the pressure peak in the calculation is 29 ms, which is 1 ms longer than in the experiment. To better understand the turbulent flame behavior, additional analysis of the LES is now performed.

Figure 6-35 shows the numerical temporal evolution of the resolved surface-to-volume ratio of the flame kernel S/V using an isovolume of progress variable based on temperature at the value $q = 0.65 \pm 0.15$. For all cases, S/V grows with time as the flame becomes more wrinkled due to turbulence. Note that the evolution of S/V shows a linear growth in time that does not replicate the pressure rise acceleration when the flame approaches the walls ($t \approx 10$ ms for cases A and B). The impact of

turbulence on the flame speed is the combination of both the flame wrinkling and the subgrid flame wrinkling. The resolved flame wrinkling can be estimated with S/V: as Fig. 6-35 shows, it does not increase as fast as the pressure does. This leads to the conclusion that the subgrid flame wrinkling has changed.

To further investigate this question, Fig. 6-36 shows the temporal behavior of the volume-average of the efficiency as defined in Eq. 4.41 inside the region $c = 0.65 \pm 0.15$ for the three cases (remember that c is the progress variable based on temperature). Higher efficiency values are accompanied by higher consumption speeds. The evolution of the three cases is very similar to the pressure curves in Fig. 6-31. For $t < 5$ ms (phase I) efficiency decreases and reaches a minimum at the time the flame travels to the center of the chamber. This is due to the fact that the formulation of u'_Δ detailed in Eq. 4.43 predicts low values of the fluctuation of velocity in the center of the chamber as it will be shown later. Efficiency starts to grow again when the flame stabilizes around the center of the chamber (phase II). Finally, there is a noticeable increase of efficiency when the flame comes closer to the walls (phase III) (case A; $t \approx 10$ ms, and case B; $t \approx 20$ ms).

The impact of the walls is confirmed in Fig. 6-37, showing only the regions where wall-originated vorticity interacts with the flame have an efficiency increasing noticeably over 1.

Because the interaction between the turbulence at the walls, and the flame as well as the compression caused by the flame expansion may not be well modelled with the static formulation of efficiency, the dynamic formulation of efficiency is now studied.

Turbulent Cases: using the Dynamic Efficiency Formulation

In the static efficiency formulation, the coefficient β is a constant set to 0.5 based on standard academic turbulent flows. It has been however demonstrated that β may vary significantly in transient cases or complex turbulent flows [140]. As the

discrepancies between LES and experiment are here attributed to the incorrect efficiency function near the walls when β is fixed to 0.5, a more accurate formulation is attempted with the dynamic formulation presented in Section 6.2.5.

Figure 6-38 shows the pressure evolution obtained with both formulations of efficiency. From spark to the middle of the constant radial growth phase (phases I and part of II), both static and dynamic efficiency formulations predict a similar rate of pressure increase because the wrinkling factor is small. The difference becomes visible for phase III, where the dynamic modelling predicts a lower consumption speed, hence slower pressure rise, than the static model for all cases: case A attains its peak at t=19 ms (+2 ms compared to the static efficiency formulation), case B at t=27 ms (+6 ms compared to the static formulation) and C at t=31 ms (+2 ms compared to the static formulation). To be compared to the experimental peaks reached at t=19, 25 and 28 ms respectively. Interestingly in [111], a study of ignition in the MICCA-spray setup, found a 15% to 20% reduction in the consumption speed when employing the dynamic wrinkling factor with respect to the static version. This reduction, which was determined to be linked to a reduction in the subgrid-scale wrinkling, caused a corresponding increase in ignition delay time of the same magnitude as in the present study. It is to be noted that, for case C, both wrinkling factor formulations indicate a delayed initial pressure rise with respect to experiments which has been explained by the low value of u'_Δ/S_L predicted near the chamber center. While this time difference is maintained approximately constant in the dynamic formulation, the overprediction of reaction rate by the static formulation during phase III reduces this time difference, but due to unphysical effects.

The figures in Fig. 6-39 clearly indicate that the lower consumption speed predicted with the dynamic formulation is directly linked to lower values of efficiency at times $t > 7$ ms.

Figure 6-40 displays the temporal evolution of the volume-averaged value of β

162

over the isovolume of $c = 0.65 \pm 0.15$. For all cases, the average β increases from the start to the point of maximum pressure. During the first instants, the kernel develops far from the walls and the effect of turbulence on the kernel is weak. As the kernel expands radially, it interacts with the vorticity generated at the walls and this is translated into higher values of β. The case initially at atmospheric pressure (case A) shows the highest increase, starting at an average value of β equal to 0.2 and increasing to 0.5. For cases B and C, the averaged value of β starts at 0.1 and increases to 0.2 approximately. Results in Fig. 6-40 are consistent with the high Karlovitz number in case A. The average efficiency value being closer to 0.5 is also consistent with the moderate impact of the dynamic efficiency for case A. Finally, the jig-shaw profile of the curve of case A may be due to the fact that the β parameter is updated at every point of the domain at each iteration, while the values in Fig. 6-40 refer to spatial averages realized over instantaneous solution (each taken at a regular period of 1 ms after spark).

Probability density functions of β for cases A, B, C for an isosurface of $c = 0.5$ are shown in the Appendix A. They all show a mostly monomodal distribution with an average of 0.15 (cases B and C) and 0.35 (case A). As a comparison in [111], the ignition of the annular MICCA-spray chamber led to bimodal β distributions, the first peak centered around 0.15 and the second peak at 0.65 (the second peak associated to the flame region near the injectors). In the present configuration, the flame is subjected to comparable levels of wrinkling corresponding to the low values of β. Because there is no flame-anchoring mechanism, no high values of β are found. The PDF of β becomes narrower with time indicating the transition between an isothermal turbulent flow field to a growing hot gas expansion flow. The fact that β in the radius chamber experiment is different and lower than the average value found in [31] can be explained by two factors. First, it has to be noted that β is an increasing function of u'/s_L [31] and cases A, B, C feature $u'/s_L \approx 1$ while cases shown in [31] feature $u'/s_L \geq 10$. In addition to that, the parameter β is case-dependent and the radius

163

chamber turbulent field is different from the decaying isotropic turbulence in [31].

6.3 Conclusions

The energy deposition method using the measured igniter electrical energy, thermal transmission efficiency and a spherical deposition zone allows the reproduction of the first instants of ignition including flame kernel formation and initial propagation with overall good agreement at several conditions relevant to aero-engine operation.

Three different conditions, which are representative of actual engine operating conditions, have been carried out experimentally by varying the initial pressure in the chamber as well as the delay between the end of injection and sparking. The experiment shows that the pressure rise in all cases can be divided into an early phase when the strain effects are dominant, and a later phase when the turbulence governs the pressure rise. In order to perform the LES, a static formulation of the wrinkling factor has been used which, for some cases, indicates a low value of the reaction rate when the flame surface is far from the chamber walls, while it overpredicts the reaction rate when the flame surface is near to the chamber walls. A dynamic formulation of the wrinkling factor has been used which does not present the overprediction of reaction rate near to the walls. The main difference between formulations is the smaller value of wrinkling factor in the dynamic case when the flame interacts with the vorticity generated at the walls. This is due to the fact that the wrinkling factor parameter (β) for this configuration is generally lower than the value proposed in the static formulation (0.5).

| 1 ms | 2 ms | 3 ms | 4 ms | 5 ms |

| 6 ms | 7 ms | 8 ms | 9 ms | 10 ms |

| 11 ms | 12 ms | 13 ms | 14 ms | 15 ms |
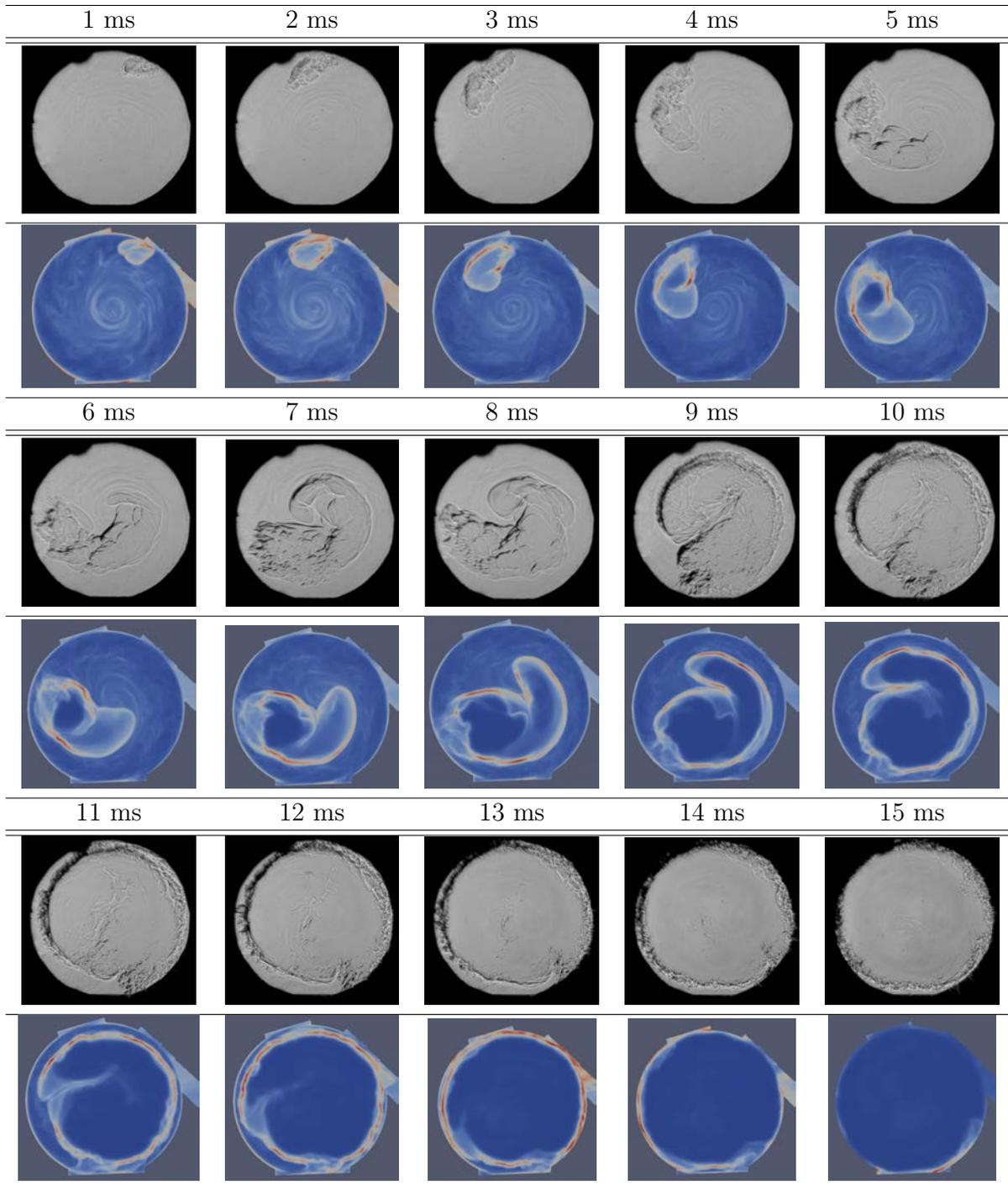
Figure 6-28: Comparison of images with LOS integrated density gradient images from LES for case A ($p_{ini} = 1bar$, $t_{delay} = 5ms$) at various times after spark. Static efficiency formulation

| 1 ms | 2 ms | 3 ms | 4 ms | 5 ms |

| 6 ms | 7 ms | 8 ms | 9 ms | 10 ms |

| 11 ms | 12 ms | 13 ms | 14 ms | 15 ms |
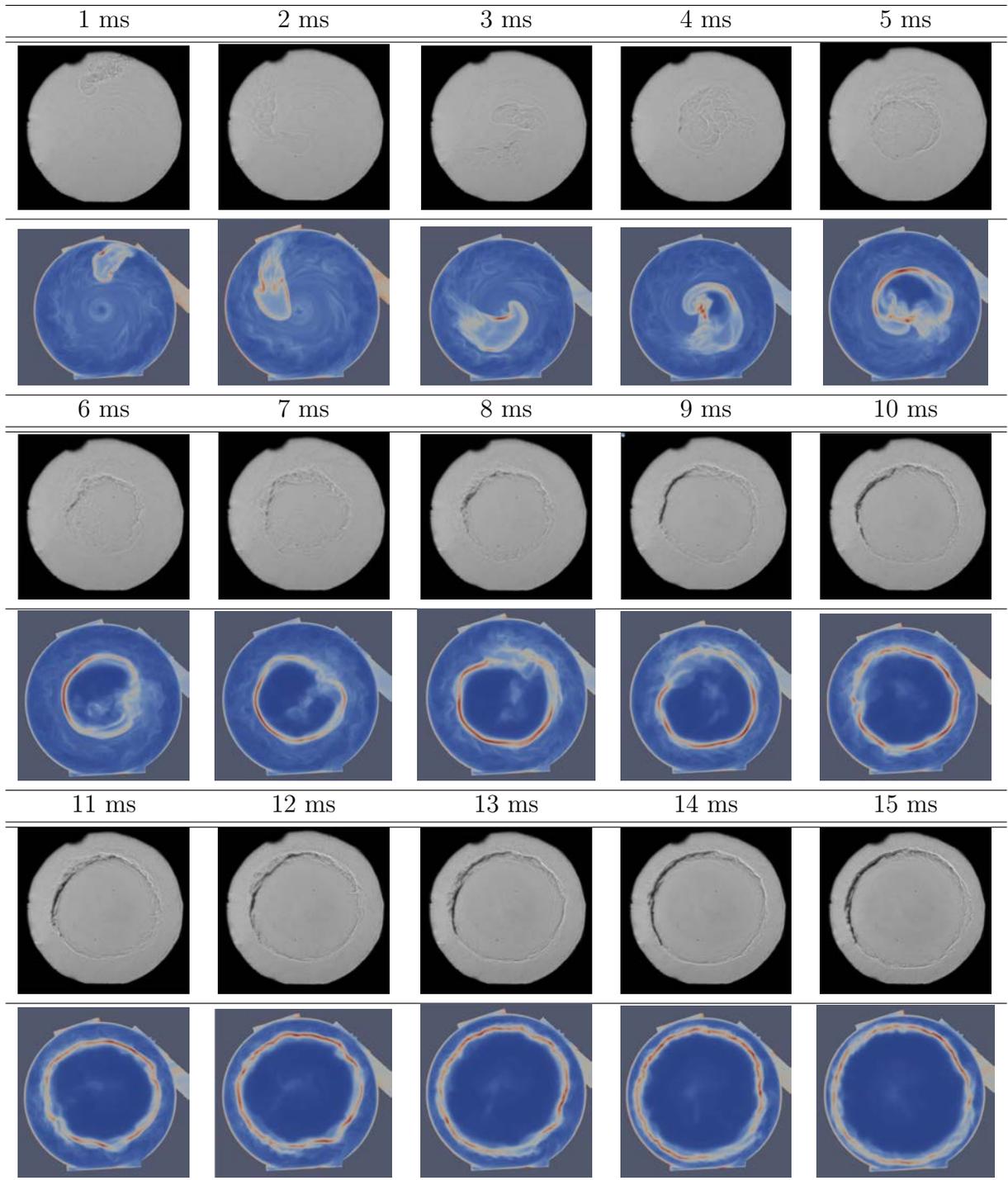
Figure 6-29: Comparison of images with LOS integrated density gradient images from LES for case B ($p_{ini} = 0.5bar$, $t_{delay} = 5ms$) at various times after spark. Static efficiency formulation

1 ms	2 ms	3 ms	4 ms	5 ms

6 ms	7 ms	8 ms	9 ms	10 ms

11 ms	12 ms	13 ms	14 ms	15 ms
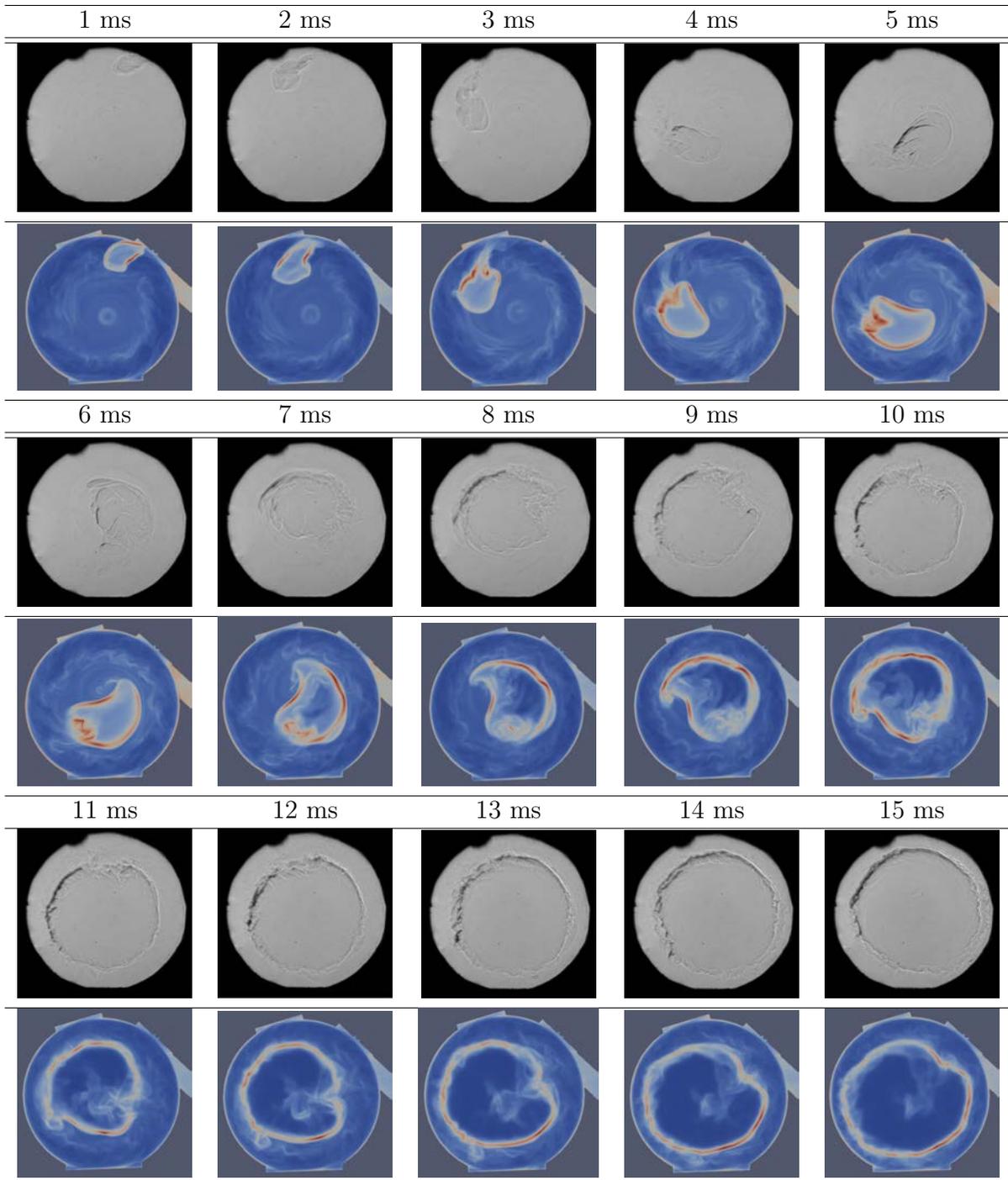
Figure 6-30: Comparison of images with LOS integrated density gradient images from LES for case C ($p_{ini} = 0.5bar$, $t_{delay} = 30ms$) at various times after spark. Static efficiency formulation
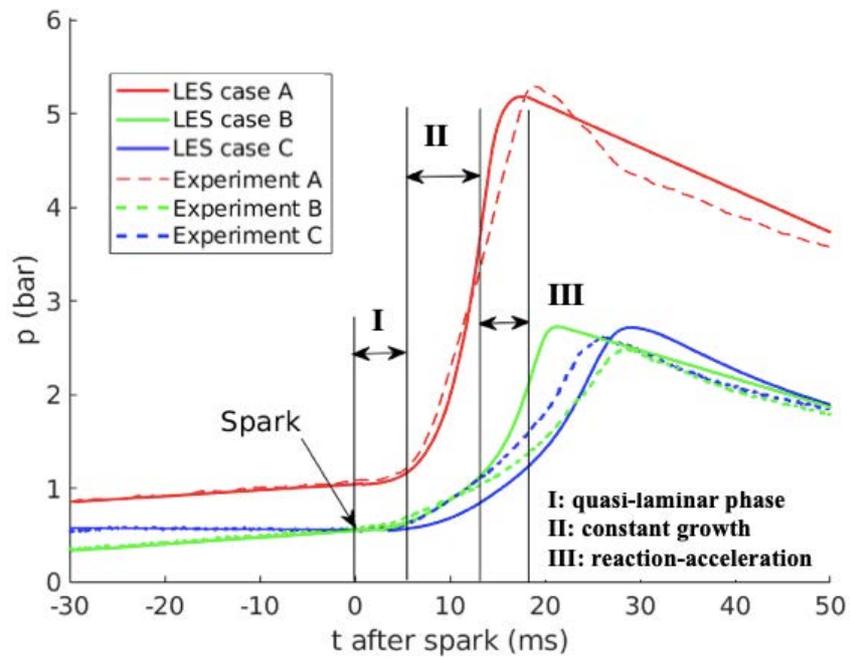
Figure 6-31: Temporal evolution of pressure for cases A ($p_{ini} = 1$ bar, $t_{delay} = 5$ ms), B ($p_{ini} = 0.5$ bar, $t_{delay} = 5$ ms) and C ($p_{ini} = 0.5$ bar, $t_{delay} = 30$ ms). The evolution in all cases can be divided in three phases: a) weak turbulence interaction b) constant flame growth c) burning rate acceleration
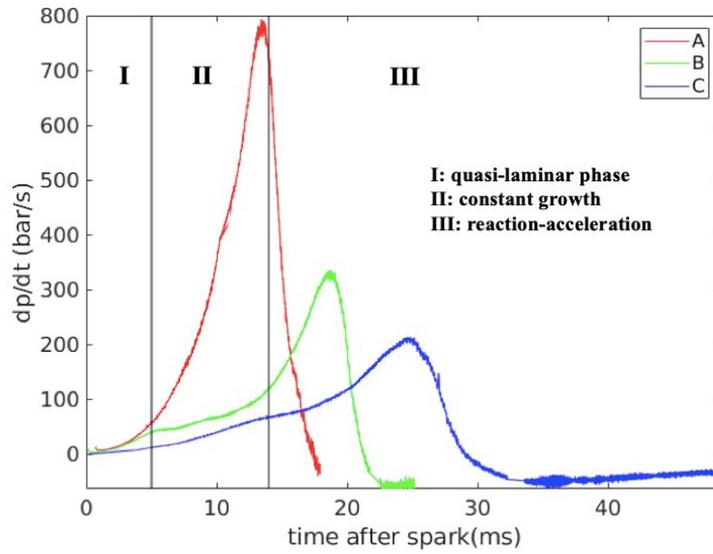
Figure 6-32: Temporal evolution of the change of pressure with time with lines indicating the phase boundaries for cases B and C. For case A, phase II takes place between $5 < t < 10$ ms
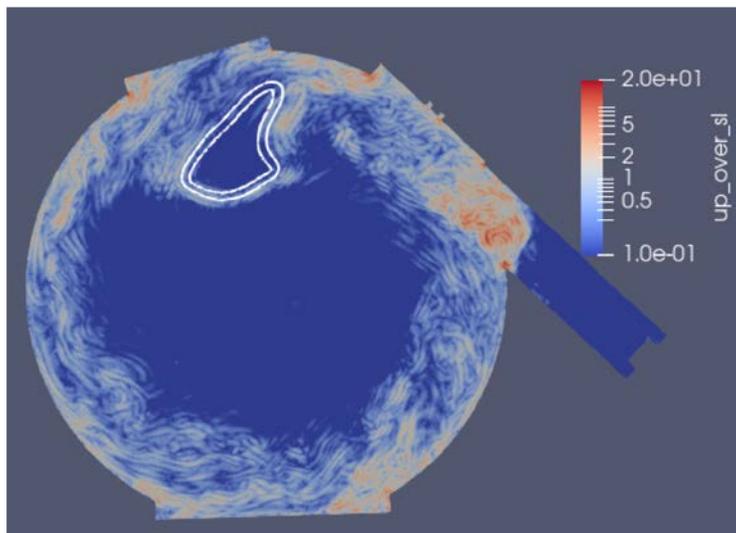
Figure 6-33: Contour fields of u'_Δ/S_l for case C at t=2 ms after spark showing low values near the chamber center with contour showing the flame position

169
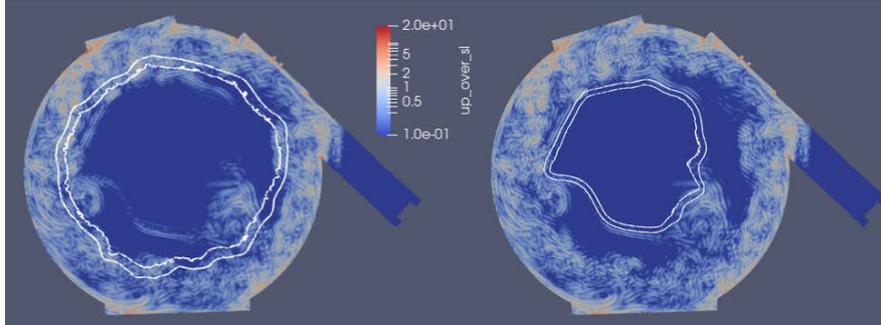
Figure 6-34: Contour fields of u'_Δ / S_l for case C at t=11 ms after spark for case B (left) and case C (right)
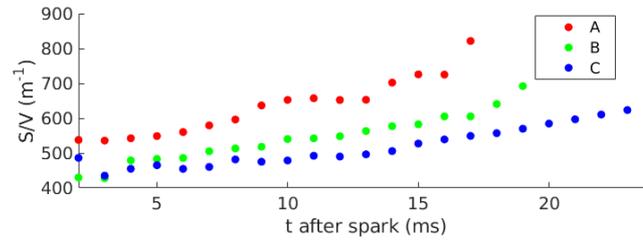
Figure 6-35: Temporal evolution from LES of the surface to volume ratio of the kernel S/V for the three cases. Phases I, II, III indicated for case A as for Fig. 6-31
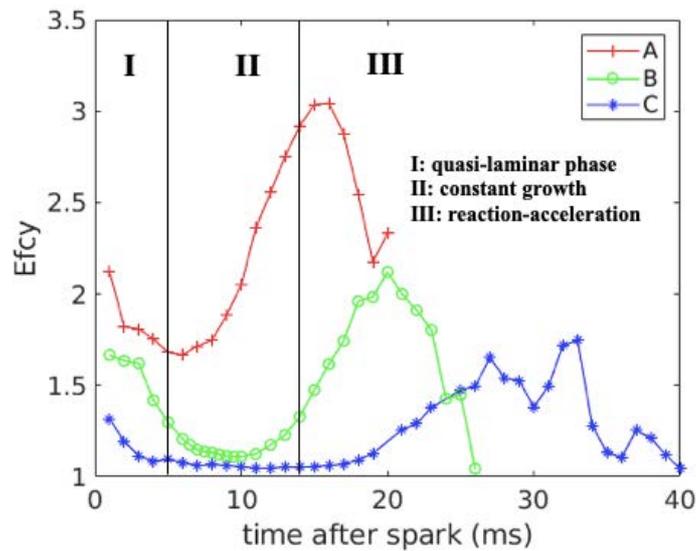
Figure 6-36: Temporal evolution of the average value of efficiency in $c = 0.65 \pm 0.15$ for the three cases
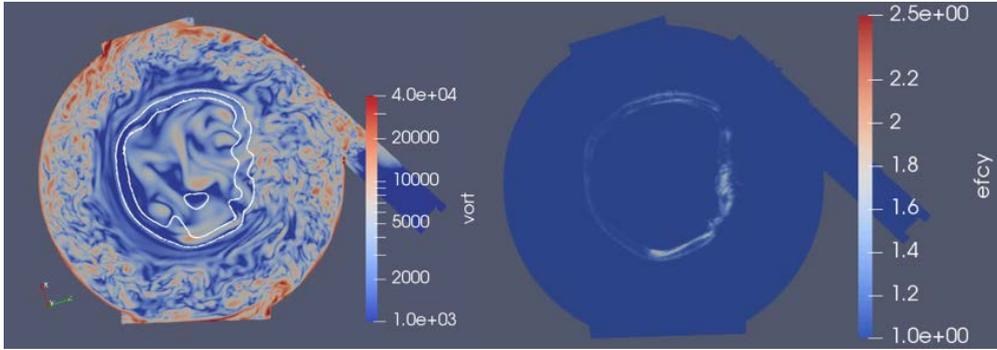
Figure 6-37: Left: Vorticity field with a white contour indicating flame position for case B at t=6ms after spark. Right: Efficiency field showing high values only where wall-originated vorticity is interacting with the flame.
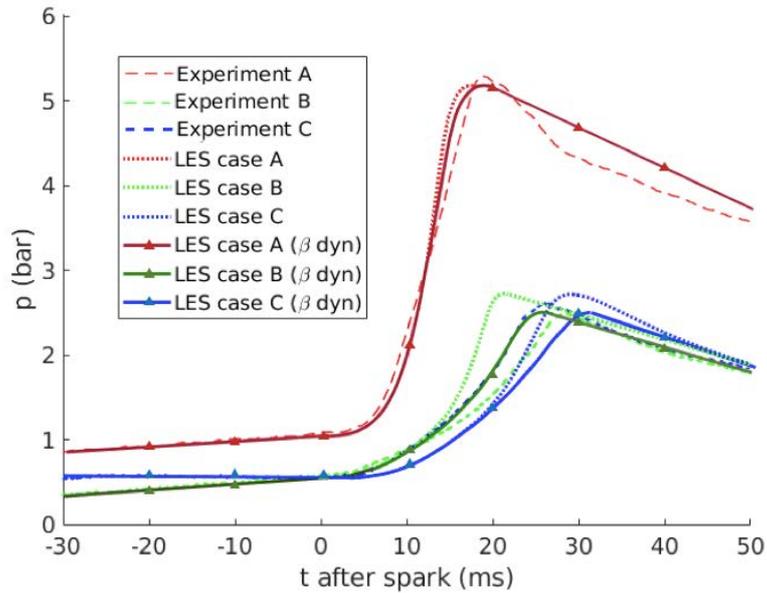
Figure 6-38: Left: Pressure time evolution for the three cases obtained with the staic and the dynamic efficiency formulations and compared to experiments

	Static	Formulation	
1 ms	3 ms	5 ms	7 ms

| 9 ms | 11 ms | 13 ms | 15 ms |

	Dynamic	Formulation	
1 ms	3 ms	5 ms	7 ms

| 9 ms | 11 ms | 13 ms | 15 ms |
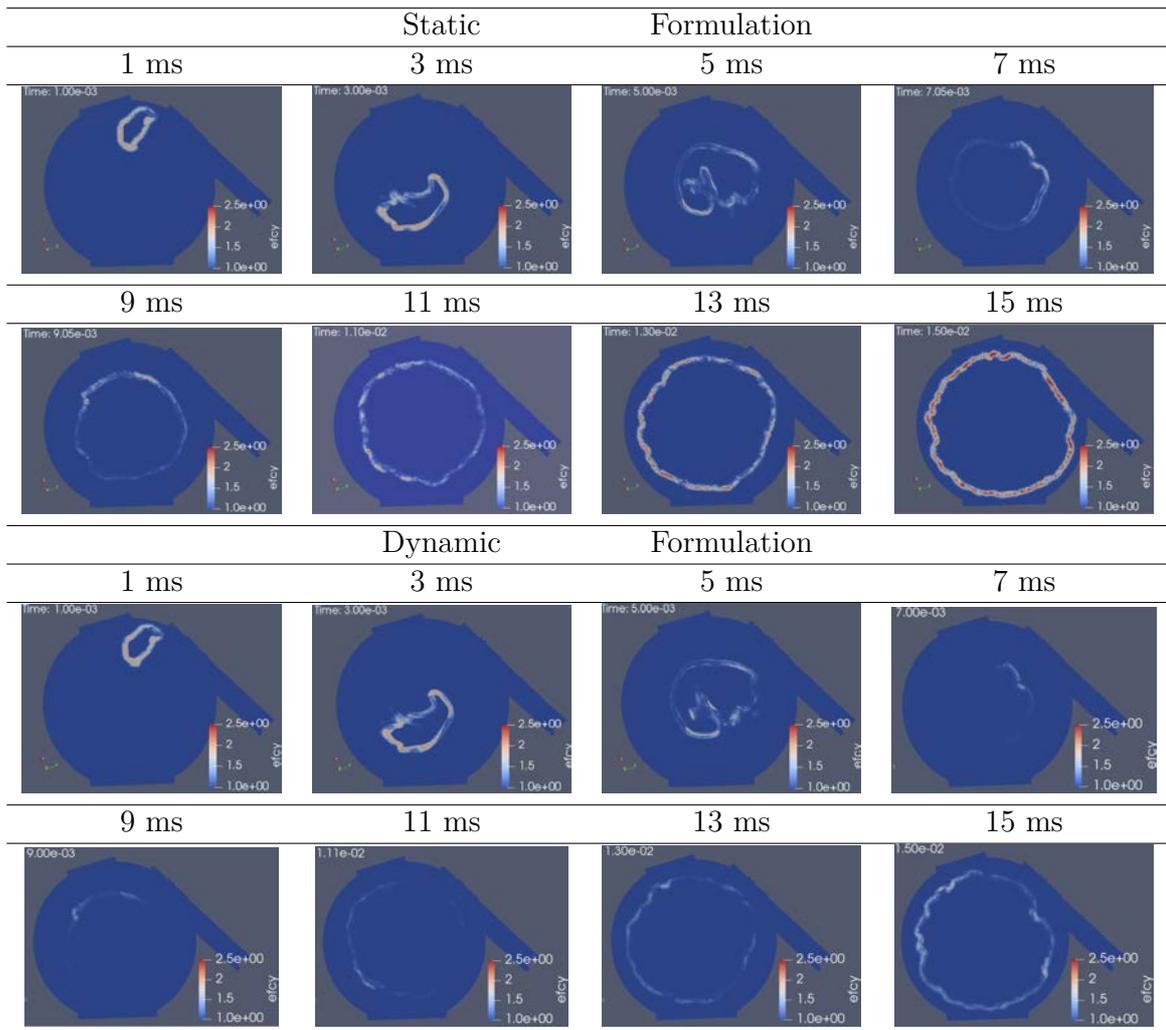
Figure 6-39: Comparison of static and dynamic efficiency values in the middle plane for case B showing lower efficiency values of the dynamic formulation at later instants. Top: static formulation, bottom: dynamic formulation. Time after spark
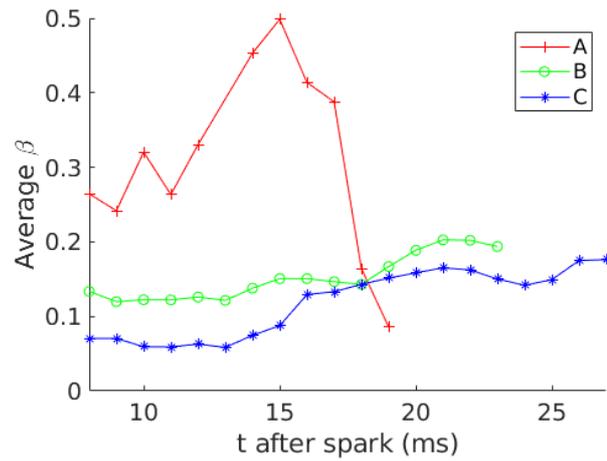
Figure 6-40: Evolution of the volume integral of the wrinkling parameter β over an isovolume of $c = 0.65 \pm 0.15$. Each data point is obtained by a spatial average from a instantaneous solution at a period of 1 ms after spark.

173

Chapter 7

Two-phase flow ignition in CORIA Pin-Pin

Contents

This chapter covers the simulations performed with the CORIA pin-pin configuration with fuel composed of liquid droplets of n-heptane. Its objective is to understand the results of applying the energy deposition model to ignition in a two-phase environment.

7.1 Experimental Setup

The experimental setup consists of a set of pin-pin electrodes at ambient conditions. The electrodes have parabolic shape with an axial length of 2.2 cm and a characteristic tip radius of 150 μm. The gap between electrodes is 3 mm. Figure 7-1 shows an overview of the experimental setup.

Particle Image Velocimetry and Spontaneous Raman Scattering techniques are available, and the amount of energy deposited at the electrodes is analysed by measuring the evolution of voltage and intensity during discharge. Initially, the gas is at rest. A more exhaustive description of the experiment can be found in [66].
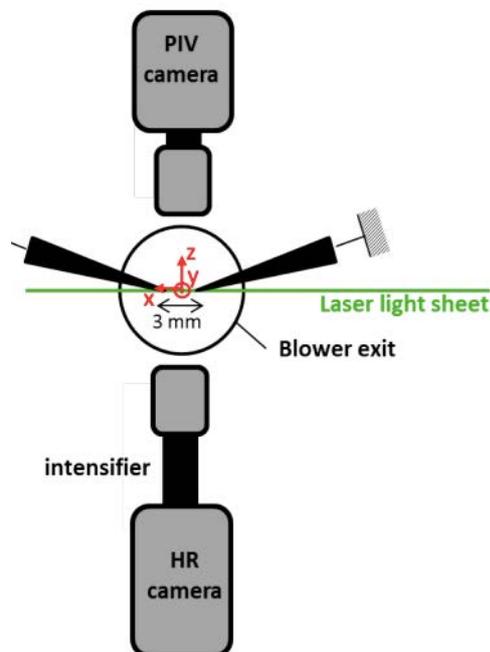
Figure 7-1: CORIA pin-pin experimental setup, adapted from [66]

7.2 Numerical Setup

The experimental setup is assumed to be symmetric with respect to the YZ and XY planes in Fig. 7-1, therefore the numerical domain consists of a one eight of a sphere of radius 100mm. Figure 7-2 shows a sketch of the numerical domain and indicates the boundaries: front (boundary number 1), bottom (2), and left side (3) are symmetry conditions. The pin-walls indicated in black in the figure are adiabatic non-slip walls. The external boundary (number 4) is a pressure outlet at atmospheric conditions with the formalism for characteristics from [103].
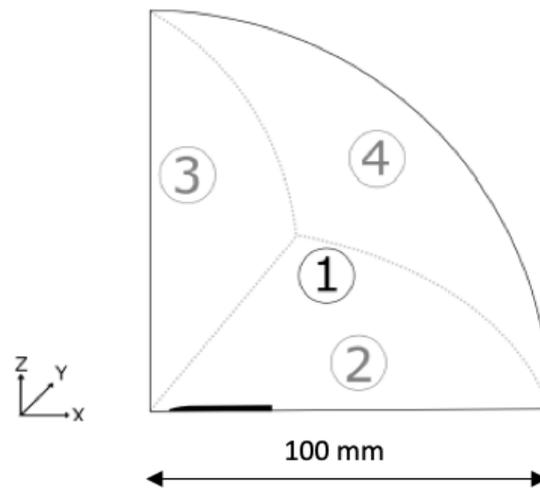
Figure 7-2: Overview of the computational domain for the CORIA pin-pin experiment with boundary names [36]

Simulations were carried out in AVBP with the Eulerian-Lagrangian framework. The Lax-Wendroff second order accurate scheme was used. This choice is justified by the fine mesh in the region of interest and the lower computational cost. An analytically reduced chemical scheme which was already used in [36] consisting of 33 species, 513 reactions and 41 QSS was developed. This scheme contains excited species such as N^+, O^+, H^-. Chemistry timescales were activated to restrict the time step, resulting in a time step of the order of 1 ns.

All particles have spherical shape and are uniformly spaced. A two-way coupling is considered between the disperse and the liquid phase, employing the Schiller-Naummann model [122]. Abramzon-Sirignano [4] evaporation model is used and each particle is tracked individually.

The ignition model in [37] is exactly retained with the parameters reproduced in Table 7.1 and equations written in Eqs. 7.1. The model is based on the energy deposition model [64] in which a source of energy is deposited in a small region of the domain around the igniter location, here a cylindrical region between the electrodes gap. This model distinguishes two phases of ignition which were discussed in chapter 2: the breakdown and the glow phase. The breakdown duration ($t_{breakdown}$) is fixed to 20 ns following [66], while the rest of the time (2.6 ms) the electrodes work in the glow regime. On the other hand, an efficiency of 95% (breakdown) and 30% (glow) for the electrode conversion of electricity to thermal energy in the kernel was used in accordance with [77]. Finally, a 5% of the total energy was assumed to be applied during the breakdown as in [37]. Figure 7-3 contains a graphical description of the geometrical parameters used in the energy deposition model. The region where energy is deposited is a cylinder whose length is 2.4 mm and diameter is 150 μm.
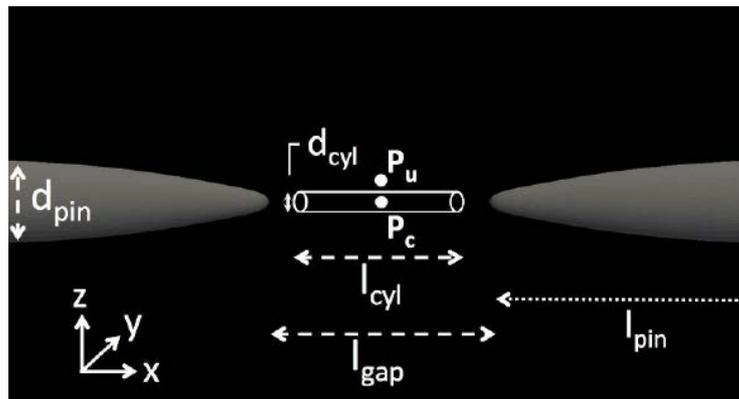
Figure 7-3: Zoom over the energy deposition parameters for the CORIA pin-pin experiment [36]

Table 7.1: Energy deposition model parameters used in the simulations of the pin-pin CORIA experiment. $E_{breakdown}$, $t_{breakdown}$, $\eta_{breakdown}$ correspond to the energy, the time duration and the electrical to thermal efficiency the breakdown phase. The subscript "glow" refers to equivalent parameters for the glow phase

$E_{breakdown}$	$t_{breakdown}$	$\eta_{breakdown}$	E_{glow}	t_{glow}	η_{glow}
5.0 mJ	20 ns	95%	85.0 mJ	2.6 ms	30%

$$For\ 0 < t < t_{breakdown} \quad \frac{dE}{dt} = \frac{\eta_{breakdown} E_{breakdown}}{t_{breakdown}} \tag{7.1}$$

$$For\ t_{breakdown} < t < t_{glow} \quad \frac{dE}{dt} = \frac{2\eta_{glow} E_{glow}}{t_{glow}^2}(t_{glow} - t) \tag{7.2}$$

The mesh is refined near the electrodes. The details of the mesh are:

$$\Delta x = \begin{cases} 25\mu m \text{ if inside deposition cylinder} \\ 50\mu m \text{ if r<3 mm} \\ \text{linear variation from } 50\mu m \text{ at r=3 mm to } 0.2mm \text{ at r=7.5 mm} \\ \text{linear variation from } 0.2mm \text{ at r=7.5 mm to } 0.8mm \text{ at r=24 mm} \\ \text{linear variation from } 0.8mm \text{ at r=24 mm to } 1mm \text{ at r=100 mm} \end{cases} \tag{7.3}$$

Cases

Different conditions were tested, which are indicated in Table 7.2, in order to assess the effect of:

1. Liquid content (change of liquid equivalence ratio $\phi_l = {}^{(m_{f,l}/m_{O_2})}/{(m_{f,l}/m_{O_2}|_{stoch})}$ where $m_{f,l}$ is the mass of liquid fuel and m_{O_2} is the mass of oxygen)

2. Pre-vaporized fuel (change of initial gaseous equivalence ratio)

3. Droplet size

179

4. Droplet distribution (monodisperse or polidisperse)

The air is initially at rest at a temperature of 293 K and 1 atm and, except for the cases with pre-evaporation, is composed only of oxygen and nitrogen. On the other hand, the whole fluid volume is occupied by droplets, and are initially at a temperature of 293 K. Figure 7-4 and 7-5 contain an example of a calculation. The back rectangle in Fig. 7-5 indicates the domain that will be shown for the display of variables in the next sections.
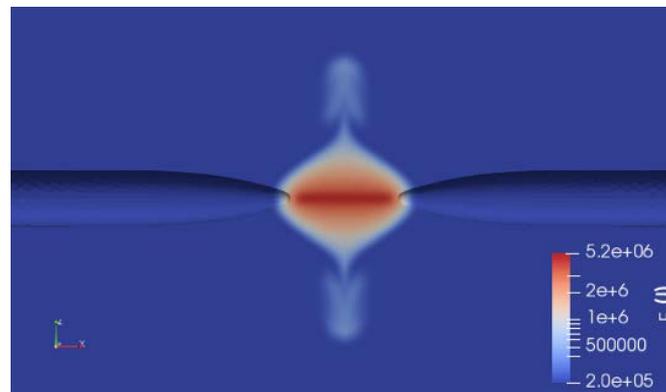
Figure 7-4: View of contours of energy for the DNS of pin-pin at t=500 μs after the breakdown
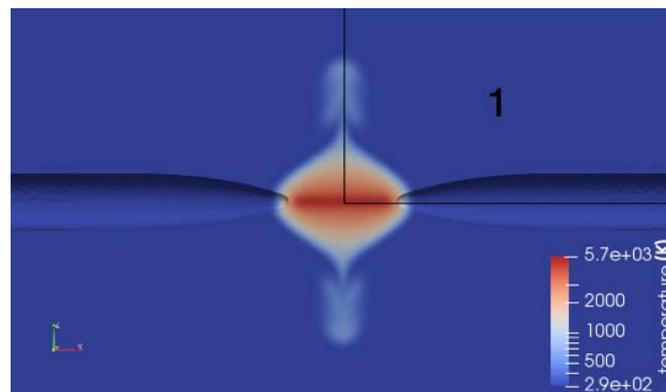
Figure 7-5: View of contours of temperature for the DNS of pin-pin μs after the breakdown. The black rectangle indicates the sector of the domain that will be used as a base for the display of results

Table 7.2: Summary of cases for the pin-pin CORIA configuration

Case number	ϕ_g	ϕ_l	ϕ_{tot}	D_{drop} (μm)	Size distribution
1	0.5	0.125	0.625	15	Monodisperse
2	0	0.625	0.625	15	Monodisperse
3	0	10	10	100	Monodisperse
4	0	10	10	50	Monodisperse
5	0	10	10	15	Monodisperse
6	0	10	10	50	Polydisperse
7	0.25	10	10.25	50	Monodisperse

Cases 1 and 2 had the objective of showing the flame features at low to moderate liquid content and both feature small droplets of 15 microns in diameter and the same overall equivalence ratio ($\phi_{tot} = 0.625$). Cases 3 to 5 were chosen to simulate the behavior in engine starting conditions in which the fuel does not evaporate and accumulates ($\phi_l = 10$). Case 6 shows the effect of a polydisperse distribution of droplet diameter size. The size distribution has a Gaussian profile with mean diameter of 50 μm and a mean standard deviation of 14.4 μm. The choice of a Gaussian distribution is based on the fact that its PDF is defined by two parameters only: the average and the standard deviation. The change in diameter accounts for the several atomisation qualities found during engine start in which the fuel pressure evolves progressively. The average SMD was chosen to be equal to the monodisperse cases. On the other hand, the standard deviation could be calculated as a result so as to ensure that the same quantity of fuel is added with respect to monodisperse cases. Finally, case 7 shows the effect of fuel pre-evaporation ($\phi_{g,0} = 0.25$). The value of ϕ_g in case 7 corresponds to the lower flammability limit for n-heptane at ambient conditions.

7.2.1 Results and Discussion

This section is organized as follows. First, a qualitative description of the DNS of each case is presented with a few additional diagnostics. Following to that there is a

quantitative comparison of the temporal evolution of parameters in the reaction zone: total heat release, number droplet density, gaseous equivalence ratio, mean Takeno index (TI, defined in Eq. 7.4) and surface-to-volume ratio.

$$TI = \frac{\nabla Y_{fuel} \cdot \nabla Y_{O_2}}{|\nabla Y_{fuel} \cdot \nabla Y_{O_2}|} \tag{7.4}$$

Figure 7-6 shows the flame evolution for case 1 (ϕ_g=0.5 ϕ_l=0.125 $D_{droplet}$=15 μm). The dashed line indicates the position of the electrode. The flame remains compact and is predominantly premixed as indicated by the regions of positive Takeno index. The flame engulfs droplets inside its envelope, and there is widespread evaporation indicated by the presence of droplets with 50% or higher evaporated volume.

Figure 7-7 shows the flame evolution for case 2 (ϕ_g=0 ϕ_l=0.625 $D_{droplet}$=15 μm). This case is similar to case 1, where the flame remains compact and is predominantly premixed. The droplets remain inside the flame envelope, and have enough time for widespread evaporation. Case 2 represents a successful ignition.

Figure 7-8 displays the flame evolution for case 3 (ϕ_g=0 ϕ_l=10 $D_{droplet}$=100 μm). The main differences of case 3 with respect to the previous cases is its higher liquid content (ϕ_l=10) and bigger droplets ($D_{droplet}$=100 μm). Contrary to case 1 and 2, the flame structure appears to be broken and features both premixed and diffusion zones. This case features the biggest droplets, therefore it requires the longest time to evaporate them and mixing and thus the diffusion zones. For t>2 ms the flame seems not to be able to engulf droplets and recedes. The flame in case 3 eventually quenches.

Figure 7-9 displays the flame evolution for case 4 (ϕ_g=0 ϕ_l=10 $D_{droplet}$=50 μm). The main differences of case 4 with respect to 3 is a reduction in the droplet diameter from 100 to 50 μm. The flame in case 4 has similar characteristics to case 3: For this droplet diameter, the flame features a broken structure and has both premixed and diffusion zones (although less diffusion zones than in case 3 as quantified in Fig. 7-21).
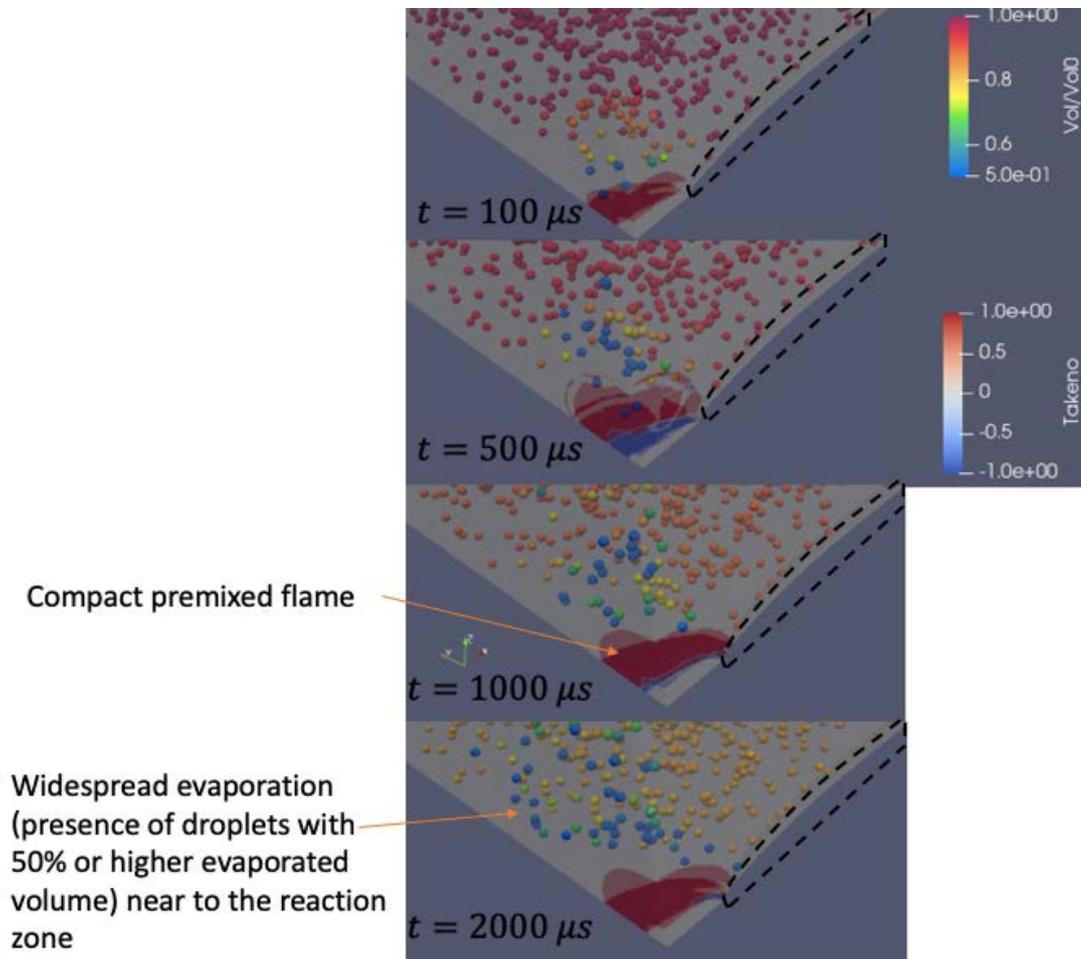
Figure 7-6: Flame evolution colored by Takeno and droplets colored by volume evaporated for case 1 (ϕ_g=0.5 ϕ_l=0.125 $D_{droplet}$=15 μm). The hollow space on the right part of image corresponds to the igniter and there is symmetry with respect to the three planes (left, right and bottom)

At t=2 ms the flame has not been able to retain a substantial amount of evaporated fuel inside the reaction zone. The droplets progressively move away from the flame and the hot igniter region due to the bulk flow expansion. This leads to the flame not being able to find fuel sources and the flame eventually quenches.

Figure 7-10 displays the flame evolution for case 5 (ϕ_g=0 ϕ_l=10 $D_{droplet}$=15 μm). The main differences of case 5 with respect to 3 and 4 is a further reduction in the droplet diameter to $D_{droplet}$ equal to 15 μm. The flame behavior is markedly

183
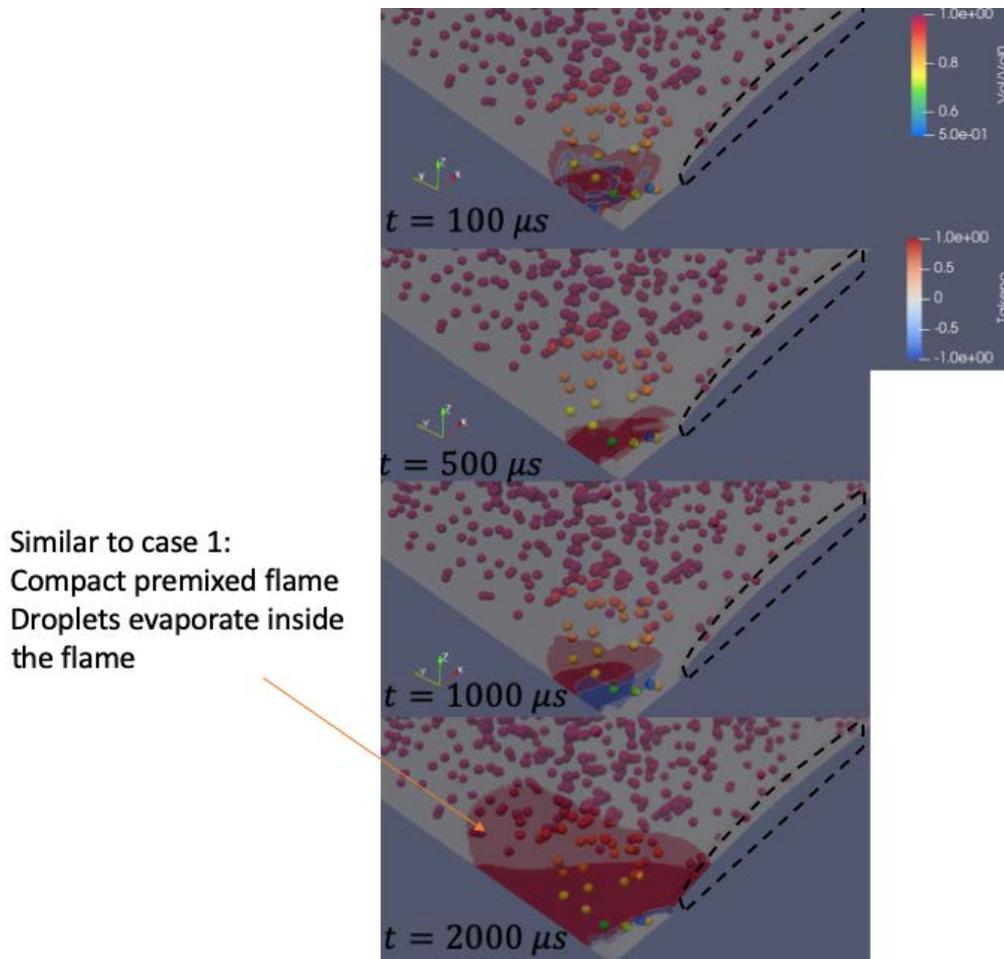
Figure 7-7: Flame evolution colored by Takeno and droplets colored by volume evaporated for case 2 (Successful ignition) (ϕ_g=0 ϕ_l=0.625 $D_{droplet}$=15 μm)

different to cases 3 and 4. For this droplet diameter, the flame features a compact structure. There is widespread evaporation, as indicated by the high percentage of droplets evaporated. At t=2 ms, droplets are near to the reaction zone and evaporate readily, which allows the flame to continue propagating. Case 5 represents a successful ignition.

Figure 7-11 shows the flame evolution for case 6 (ϕ_g=0 ϕ_l=10 $D_{droplet}$=50 μm with a polydisperse distribution, $\mu = 50$ microns, σ=14.4 microns). The main differences of case 6 with respect to the rest of cases is its polydisperse size distribution. The

"Broken" flame structure featuring both premixed and diffusion zones due to large droplets ($D_{drop} = 100\,\mu m$)

The flame does not manage to engulf droplets, and eventually quenches
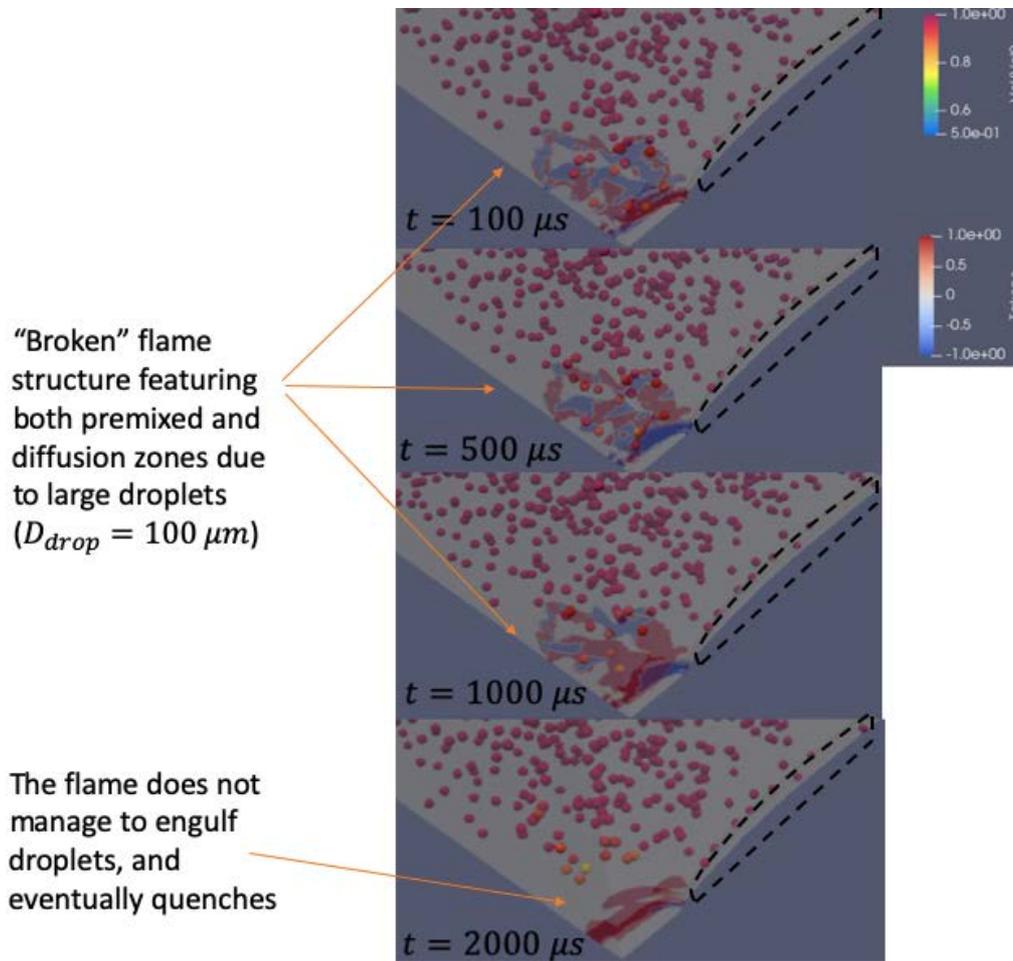
Figure 7-8: Flame evolution colored by Takeno and droplets colored by volume evaporated for case 3 (Failed ignition) (ϕ_g=0 ϕ_l=10 $D_{droplet}$=100 μm)

flame behavior combines features from case 4 (monodisperse, $D_{droplet}$=50 μm) and case 5 (monodisperse, $D_{droplet}$=15 μm). The flame initially has a broken structure (as case 4), possibly due to the presence of large droplets which inhibit certain regions for combustion, but eventually evolves to a compact structure (as in case 5). In addition to that, it features premixed and diffusion zones during the initial instants as in case 4, but evolves to an almost complete premixed regime at t=2 ms. There is widespread evaporation as indicated by the high percentage of droplets evaporated (those of with the smaller diameters). At t=2 ms, the flame has managed to engulf

"Broken" flame structure featuring both premixed and diffusion zones due to large droplets ($D_{drop} = 50\ \mu m$)

Droplets have been pushed away from the reaction region due to "bulk expansion"

The flame eventually quenches

$t = 100\ \mu s$

$t = 500\ \mu s$

$t = 1000\ \mu s$

$t = 2000\ \mu s$

$t = 3000\ \mu s$
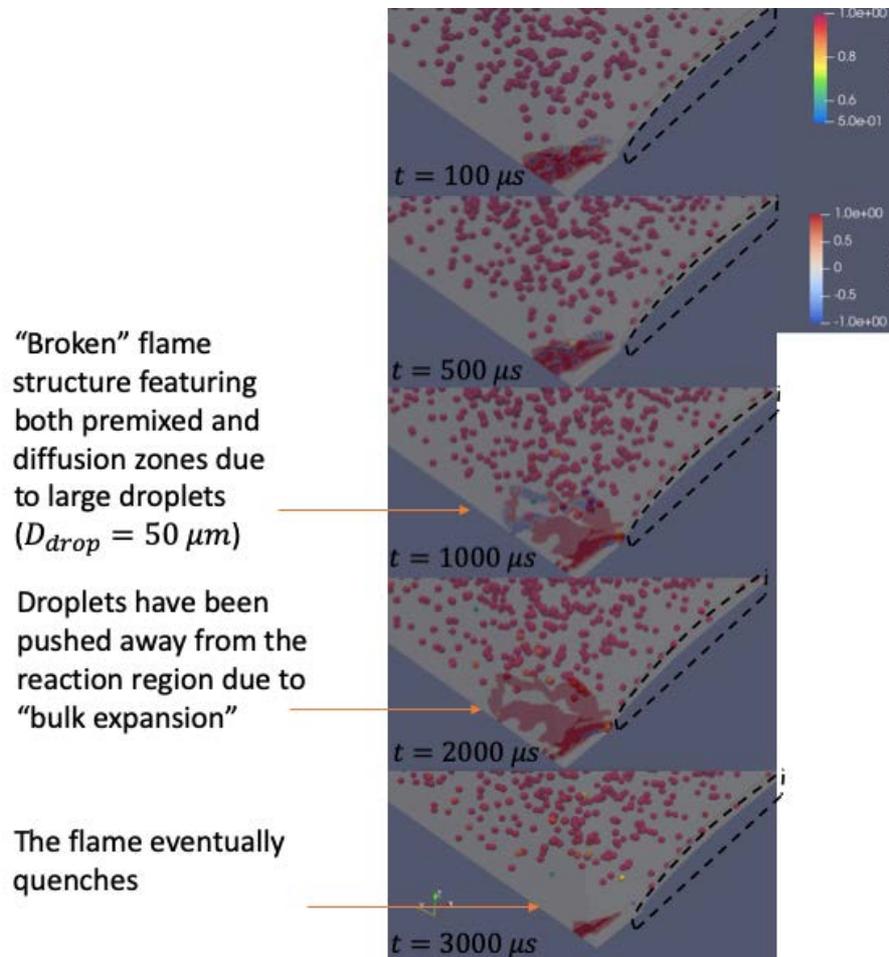
Figure 7-9: Flame evolution colored by Takeno and droplets colored by volume evaporated for case 4 (Failed ignition) (ϕ_g=0 ϕ_l=10 $D_{droplet}$=50 μm)

a large quantity of droplets of several sizes and can continue propagating. Case 6 is a successful ignition.

Figure 7-12 exhibits the flame evolution for case 7 (ϕ_g=0.25 ϕ_l=10 $D_{droplet}$=50 μm). The main differences of case 7 with all cases (except case 1) is the presence of pre-evaporated fuel $\phi_{g,0}$=0.25. The pre-evaporated fuel leads to a compact flame structure, reacting mostly at a premixed regime. On the other hand, the droplets color indicate a weak evaporation. Furthermore, the droplets move away from the flame due to the bulk expansion. Eventually, the flame consumes all the available

186
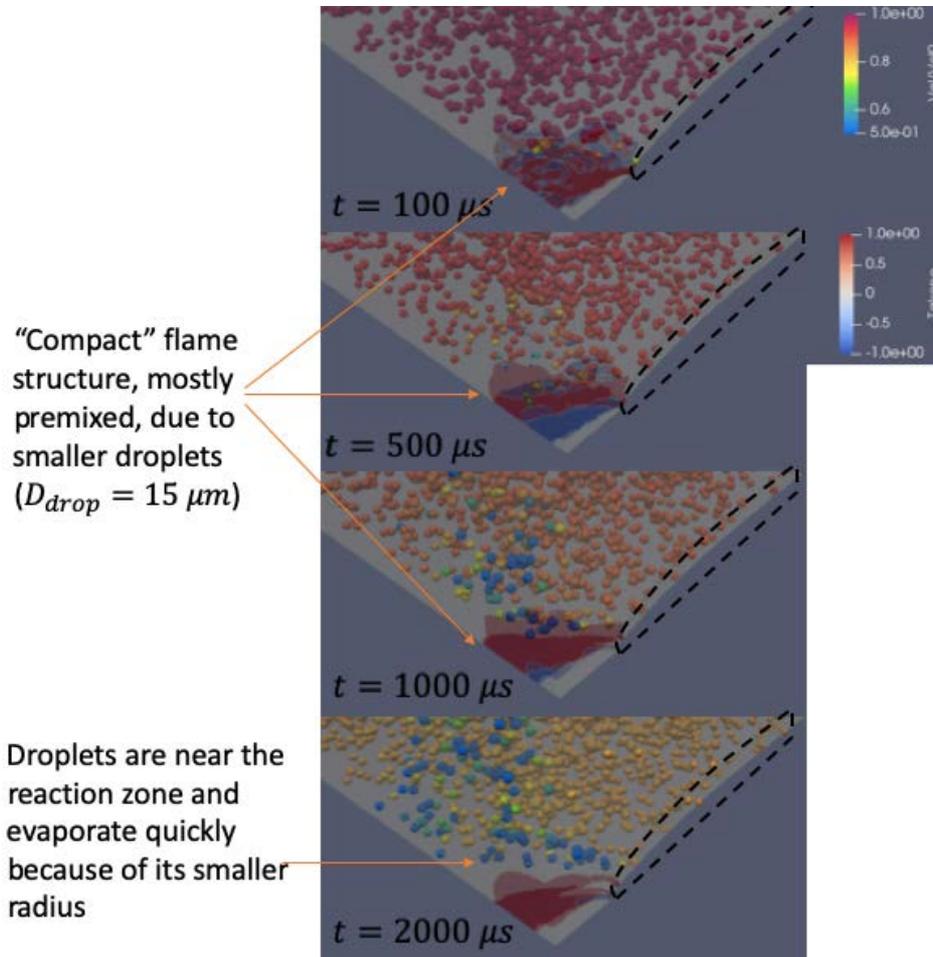
Figure 7-10: Flame evolution colored by Takeno and droplets colored by volume evaporated for case 5 (Successful ignition) (ϕ_g=0 ϕ_l=10 $D_{droplet}$=15 μm)

gaseous fuel near the igniter and does not manage to engulf more droplets. Finally, the flame runs out of fuel and eventually quenches.

Figures 7-13 to 7-15 contain the droplet temperature probability density function for cases 3, 4 and 5 ($D_{droplet} = 100, 50, 15 \, \mu m$).

Figure 7-16 contains a comparison of the temporal evolution of heat release and mass evaporation terms. The terms have been made non-dimensional by their value at t=100 μs for ease of comparison. In addition to that, Fig. 7-17 contains the temporal evolution of the non-dimensional ratio $\Xi = hr * V_{flame}/(\dot{m}_{evap} * \Delta H_r)$ where the flame
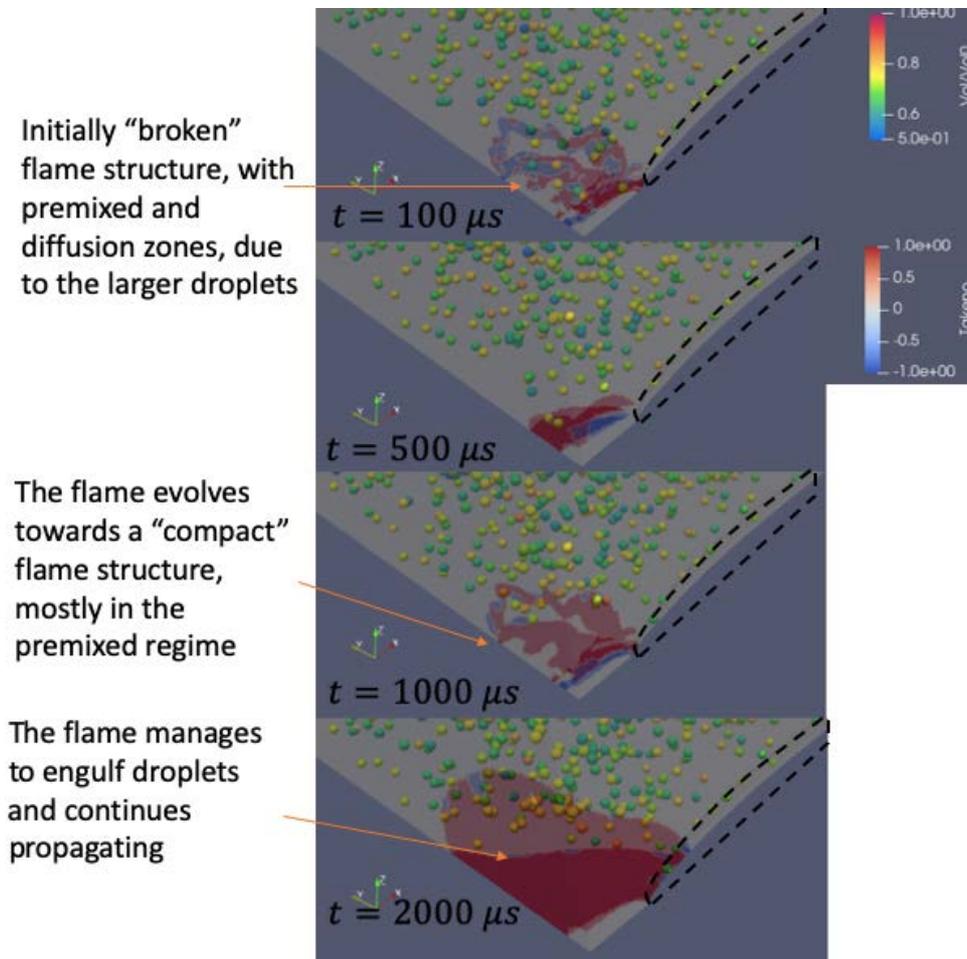
Figure 7-11: Flame evolution colored by Takeno and droplets colored by volume evaporated for case 6 (Successful ignition) (ϕ_g=0 ϕ_l=10 $D_{droplet}$=50 μm)

has been identified as the region with hr>1e5 W/m^3. From these figures we can derive that heat release decays faster than the evaporation term. Thus, evaporation is not missing in the failed ignition cases but, in the failed cases, droplets have been pushed away from the flame due to the bulk flow expansion and the flame cannot reach the areas where the newly gaseous fuel is located. This phenomenon will be explained in more detail in the next section.
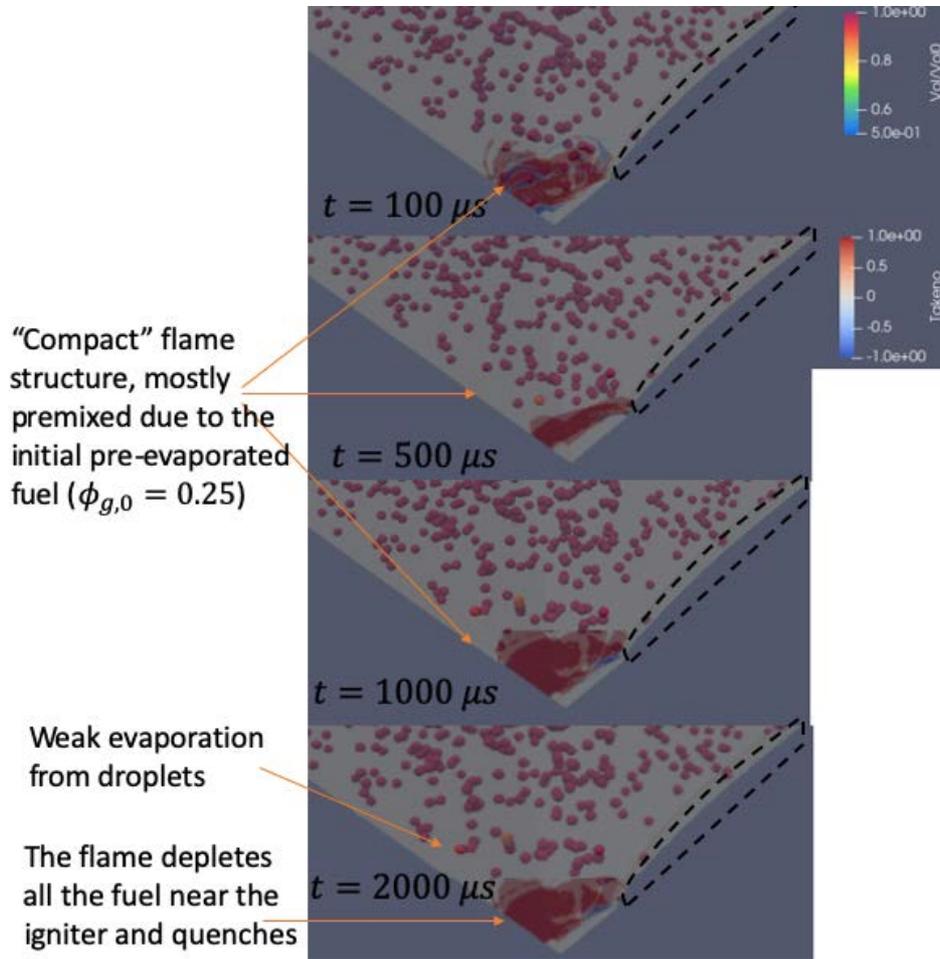
Figure 7-12: Flame evolution colored by Takeno and droplets colored by volume evaporated for case 7 (Failed ignition) (ϕ_g=0.25 ϕ_l=10 $D_{droplet}$=50 μm)

7.3 Detailed Analysis of the Kernel Propagation

By comparing cases 4 (monodisperse) and 6 (polydisperse) we can observe the effect of the size distribution. For early times (t<1 ms), in both cases the flame behaves similarly and the effect polydispersity is not visible. Both flames feature broken structures as they face big enough droplets which create local quenching. The effect of polydispersity becomes visible at times of the order of the evaporation of the mean droplet diameter (in this study $t_{Evap,D=50\mu m}$=1.6 ms). At t=2 ms, case 6 shows a higher flame propagation since it has managed to completely evaporate the
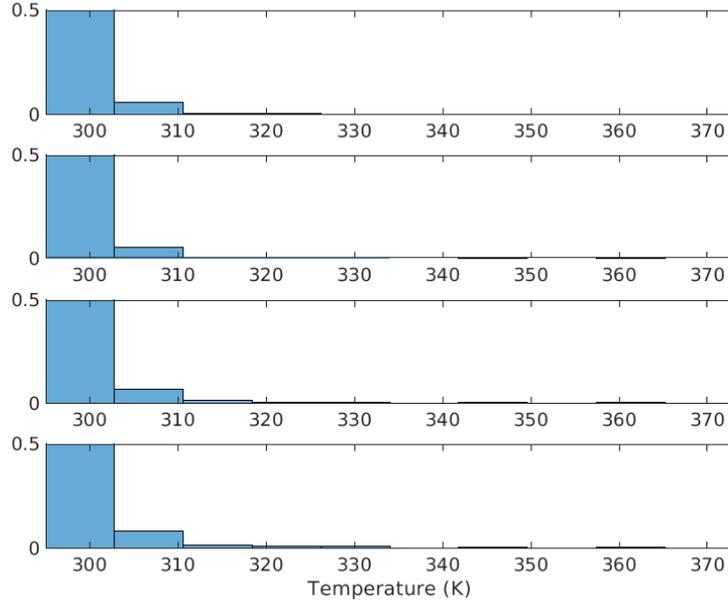
Figure 7-13: PDF of droplet temperature at t=100, 500, 1000 and 2000 μs after spark for case 3 (ϕ_l=10 $D_{droplet}$=100 μm)

smaller droplets of the size distribution. On the other hand, in the monodisperse case, evaporation is weaker and the flame does not manage to engulf droplets. In the meantime, it maintains a broken structure and eventually recedes and quenches.

The comparison of case 7 (with pre-evaporation, $\phi_g = 0.25$) and case 4 (no pre-evaporation, $\phi_g = 0$) show the effect of fuel volatility. The presence of pre-evaporation allows for the creation of a compact flame structure. However, in both cases, the size of the droplets (D=50 μm) is the governing characteristic to determine ignition success since the droplets take too long to evaporate and the flame does not have enough fuel to continue propagation. In the end, neither of the cases manage to obtain a self-propagating flame.

Cases 4 ($D_{droplet}$=50 μm) and 5 ($D_{droplet}$=15 μm) give us understanding of the effect of the droplet size. For the case with smaller droplets, the smaller evaporation time leads to the flame propagating in a similar mode as in a premixed, gaseous
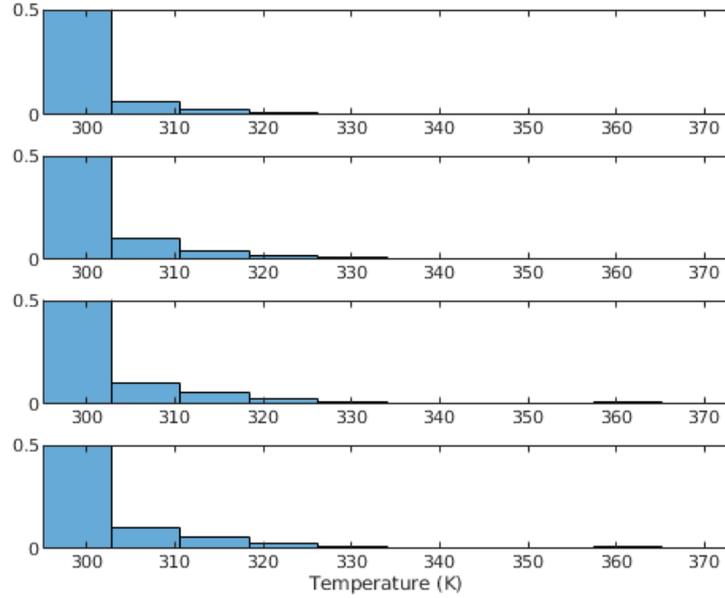
Figure 7-14: PDF of droplet temperature at t=100, 500, 1000 and 2000 μs after spark for case 4 (ϕ_l=10 $D_{droplet}$=50 μm)

environment. On the other hand, the case with bigger droplets features a broken flame structure, typical of flames under biphasic environments due to local quenching. In addition to that, the shorter evaporation times in case 5 leads to constant availability of gaseous fuel at the reaction region and the possibility for flame propagation. On the other hand, in case 4, droplets take longer to evaporate and the flame exhausts all the available gaseous fuel before receding and quenching.

By comparing cases 2 ($\phi_l = 0.625$, $D_{droplet}$=15 μm) and 5 ($\phi_l = 10$, $D_{droplet}$=15 μm), it is possible to extract the effect of liquid content. The main effect of higher liquid fuel content is a slower flame propagation. The higher fuel content involves that a substantial amount of the heat from the flame is used for droplet evaporation. On the other hand, the case with smaller liquid content has more fraction of its heat release available to diffuse upstream and thus the flame is able to propagate at a greater speed.
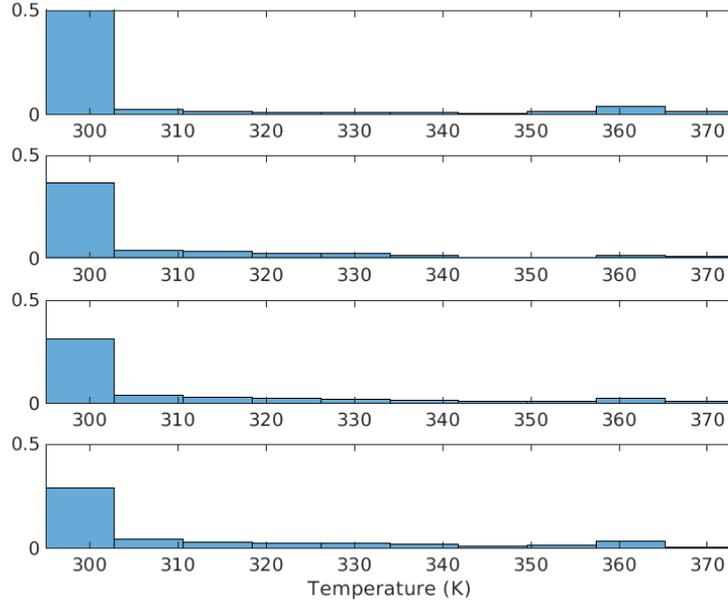
Figure 7-15: PDF of droplet temperature at t=100, 500, 1000 and 2000 μs after spark for case 5 (ϕ_l=10 $D_{droplet}$=15 μm)

7.3.1 Quantitative Analysis

A series of figures show a quantitative analysis of the ignition processes. Figure 7-18 shows the heat release evolution with time. All cases display some degree of heat release decrease as the high energy effect of the breakdown phase gives way to the lower energy phase of the glow. However, cases 1, 2, 5 and 6 manage to stabilize/maintain a higher heat release. These cases correspond to those whose images show an expanding flame. On the other hand, the heat release in cases 3,4 and 7 decays faster and these cases correspond to those whose images in the previous section show a receding flame. The cases with asterisks indicate failed flame propagation. The circles indicate successful flame propagation.

Figure 7-19 displays the temporal evolution of the number of droplets which remain inside the flame volume. The flame volume is defined as the spatial region with $c = 0.65 \pm 0.15$ as in [81] ($c = (T - T_0)/(T_{max} - T_0)$). Nearly all successful
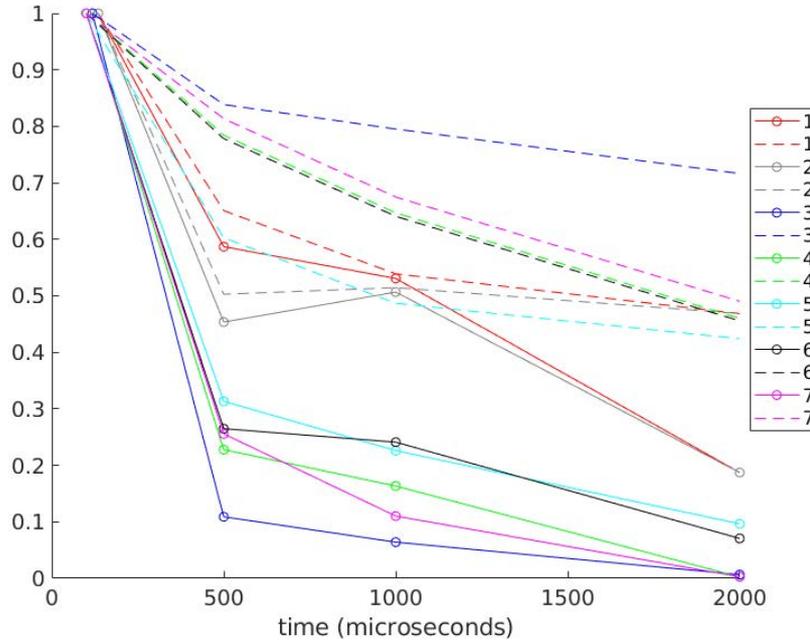
Figure 7-16: Temporal evolution of heat release (solid line) and mass evaporation terms (dashed line). Each variable for each case is made non-dimensional with the value at t=100 μs

cases (1, 2, 5) are characterized by the flame retaining a large number of droplets per unit of volume in the reaction region. On the other hand, the failed cases feature lower droplet number density. Finally, the flame in case 6 (polydisperse diameter distribution) shows a peculiar behavior at t=2 ms, being able to successfully propagate while having the lowest droplet number density. This is due to the fact that very small droplets (D<15 μm) have already disappeared due to full evaporation. On the other hand, the abundant presence of (larger) droplets can be verified in the bottom part of Fig. 7-11.

Figure 7-20 exhibits the mean gaseous equivalence ratio inside the flame volume. Again, nearly all successful cases (1, 5, 6) feature a gaseous equivalence ratio stabilizing near 0.1. On the other hand, case 2 (successful, $\phi_l = 0.625$ $D_{droplet}$=15 μm) has an almost zero value of gas content. This is explained by the fact that all the

193
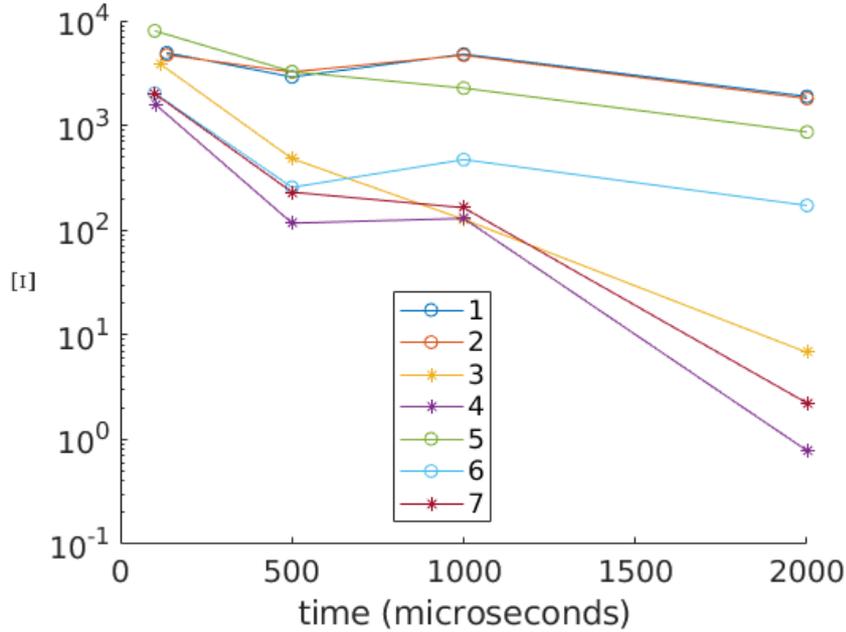
Figure 7-17: Temporal evolution of non-dimensional ratio of heat release by mass evaporation term $\Xi = hr * V_{flame}/(\dot{m}_{evap} * \Delta H_r)$ Circles mark successful ignition, while asterisks mark failures

fuel that is evaporated from the droplets is immediately consumed and it is therefore not recorded in the postprocess. Case 7 (with pre-evaporation $\phi_{g,0} = 0.25$) has the highest value of ϕ_g during the early instants, but exhibits a monotonously decreasing value and had depleted all the available gaseous fuel for t=2 ms.

Figure 7-21 displays the fraction of reaction zone reacting in the diffusion regime (negative Takeno number). Cases with larger diffusion zones correspond to those with highest liquid content (3, 4, 5, 6) and/or larger droplets (3, 4, 6). On the other hand, all cases tend to burn in the premix regime at later instants (t>2 ms). Therefore, for this configuration, the fraction of flame in the diffusion regime is not a characterizing factor indicating the flame propagation success.

Figure 7-22 shows the ratio of surface to volume in the reaction region ($c = 0.65 \pm 0.15$). All the failed cases (3, 4, 7) exhibit larger values of S/V. This is linked to the aforementioned local quenching of the flames due to the liquid content, which

194
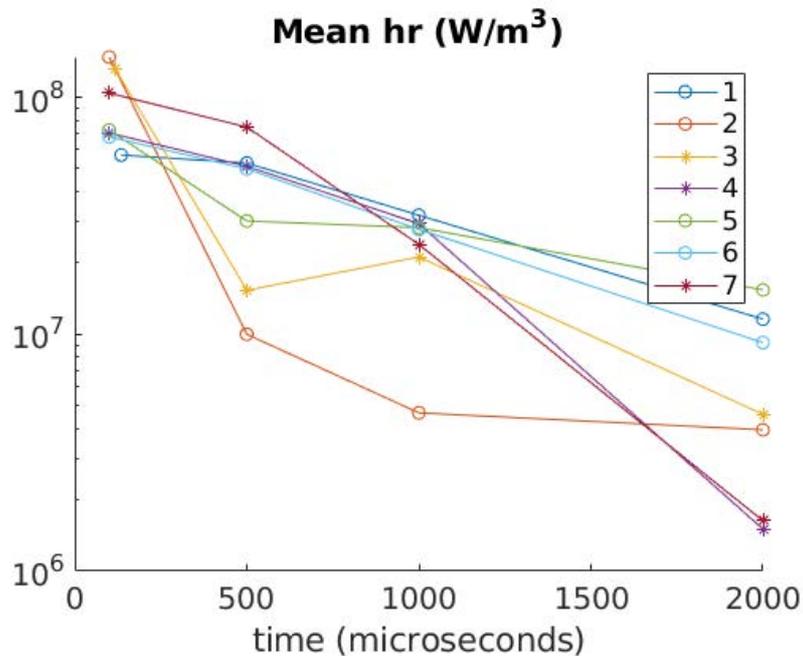
Figure 7-18: Heat release evolution with time. The cases with circles indicate successful flame propagation. The asterisks indicate failed flame propagation

creates the broken structures. For these cases, the high value of surface leads to higher heat losses and, eventually, quenching. On the other hand, the successful cases (1, 2, 5, 6) exhibit lower values of S/V and all display compact flame regions after the initial instants.

In summary, for this configuration, successful flame propagation is attained when the flame engulfs a high number of droplets, maintain a gaseous equivalence ratio in the reaction region higher or equal to ϕ_g=0.08. In addition to that, the reaction region has to be able to surmount heat losses by featuring a moderate to low surface-to-volume ratio.

7.3.2 Theoretical Analysis

An effort was made to provide a theoretical explanation to the distinct success behavior of the flames in this configuration based on non-dimensional parameters.
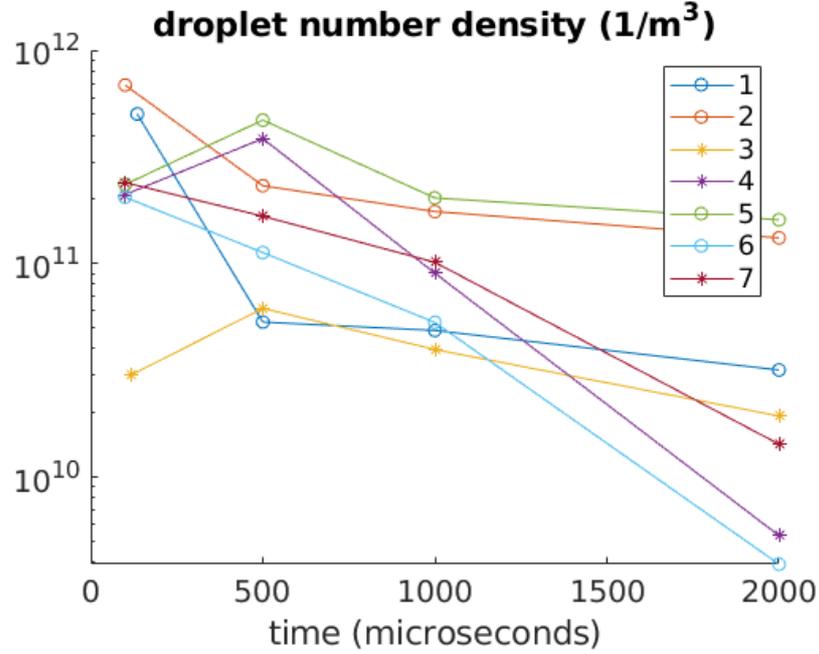
Figure 7-19: Droplet number density inside reaction zone $c = 0.65 \pm 0.15$. The circles indicate successful flame propagation, asterisks unsuccessful

Figures 7-6 to 7-12 indicate that droplets evaporate while being pushed away from the igniter region due to bulk flow expansion. Droplets have a characteristic relaxation time to adapt to the flow velocity indicated in Eq. 7.5. On the other hand, the droplet evaporation time is described by Eq. 7.6.

$$\tau_{drag} = \frac{\rho_l d_p^2}{18\mu_g(1 + 0.15Re_p^{0.687})} \tag{7.5}$$

$$\tau_{evap} = \frac{\rho_l d_{p,0}^2}{8\rho_g D_F \ln(B_M + 1)} \tag{7.6}$$

Table 7.3 contains each case characteristics and the value of the ratio τ_{Drag}/τ_{Evap}. The cases where successful propagation occurs correspond to those with $\tau_{Drag}/\tau_{Evap} > 0.2$ while the failed ignition fall have a ratio less than 0.2.

A high τ_{Drag}/τ_{Evap} indicates that droplets evaporate more before being pushed

196
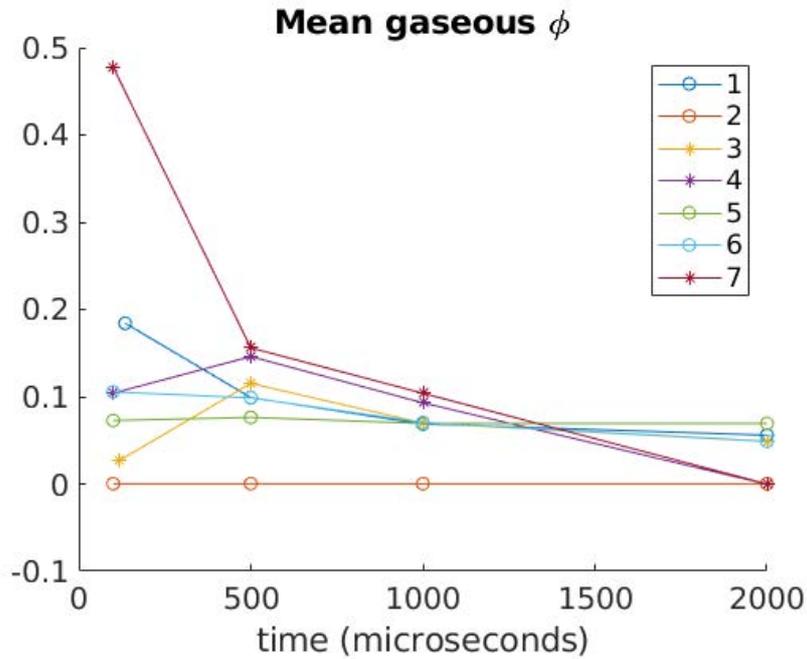
Figure 7-20: Mean ϕ_g inside the reaction region ($c = 0.65 \pm 0.15$). The circles indicate successful flame propagation, asterisks unsuccessful

away by the bulk flow. Therefore, the flame is able to engulf the droplets before they move away. On the other hand, a low τ_{Drag}/τ_{Evap} indicates that droplets have a weak evaporation and are moved away by the flow very rapidly. Ignition cases with this characteristics will lead to flames that deplete the available fuel in gaseous phase while not having been able to engulf the necessary number of droplets. Eventually, there is no more fuel in the reaction region and the droplets have been pushed too far away to provide a substantial amount of fuel source to the flame.

Figure 7-23 indicates the evolution of the ratio of drag to evaporation time scales with droplet diameter.

In addition to that, if we use a droplet group number definition given in [12]:

$$G = \frac{m_l}{4\pi r^2 R_c \rho_l} \tag{7.7}$$

197
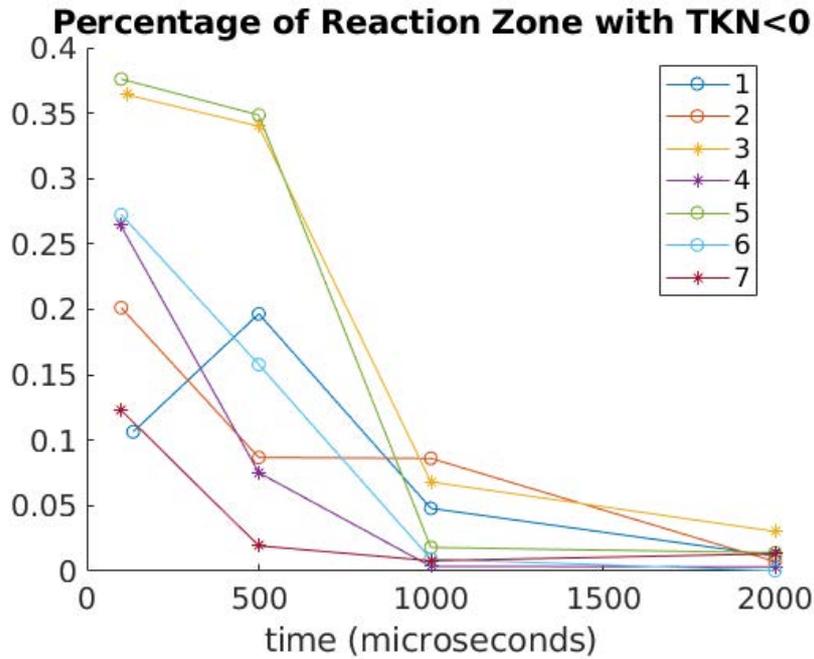
Figure 7-21: Fraction of reaction zone ($c = 0.65\pm0.15$) with negative Takeno (indicating diffusion combustion regime). The circles indicate successful flame propagation, asterisks unsuccessful

where m_l is the total liquid mass, r the droplet radius, R_c the characteristic length of the size of the droplet cloud and ρ_l is the density of the liquid fuel, we can obtain that the droplet group number for all cases varies is much greater than 1. In particular it varies between 73 (case 1) and 5800 (case 5). Due to $G >> 1$, all the cases under study feature a close packaging of droplets, and a flame covering a large group of droplets is the predominant combustion mode.

The validity of this theoretical analysis is restricted to this specific pin-pin geometry with its corresponding temporal power supply and droplet group number.
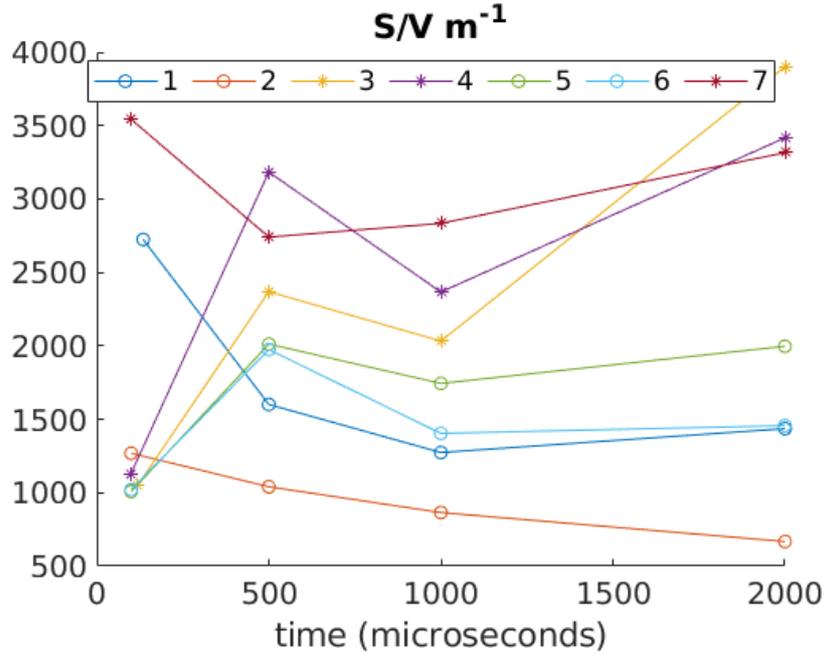
Figure 7-22: Fraction of surface over volume in the reaction region ($c = 0.65 \pm 0.15$)

7.4   Conclusion

A DNS study of ignition with a pin-pin electrode in two-phase flow conditions is presented for several conditions changing the liquid content, the initial gaseous equivalent ratio, the droplet diameter and the droplet size distribution. In the early instants, the flame burns at a combination of premixed and diffusion regimes, but all cases eventually burn predominantly in the premixed regime for $t > 1$ ms. For this electrode geometry, where the energy is deposited in a thin channel resembling the electric arc and there is no turbulence which pushes the droplets towards the electric arc, the droplets are gradually pushed away from the electrode region by the bulk flow. Therefore, only the cases in which the flame propagates faster (in the absolute frame) than the velocity at which droplets are pushed away due to bulk expansion provide successfully ignition. In summary, for this configuration, successful flame propagation is obtained when the flame engulfs a high number of droplets, maintains a gaseous equivalence ratio in the reaction region with $\phi_g >= 0.08$ and has a surface

Table 7.3: Summary of cases for CORIA pin-pin configuration with the corresponding ratio of drag relaxation time to evaporation time. The "*" in case 6 indicates that this value corresponds to the average droplet diameter of the distribution

Case number	ϕ_g	ϕ_l	D_{drop} (μm)	Size	τ_{Drag}/τ_{Evap}	Behavior
1	0.5	0.125	15	Monodisperse	**0.40**	**Success**
2	0	0.625	15	Monodisperse	**0.40**	**Success**
3	0	10	100	Monodisperse	0.12	Failure
4	0	10	50	Monodisperse	0.19	Failure
5	0	10	15	Monodisperse	**0.40**	**Success**
6	0	10	50	Polydisperse	**0.40***	**Success**
7	0.25	10	50	Monodisperse	0.19	Failure
8	0.5	10	50	Monodisperse	0.19	Failure
9	0.25	5	50	Monodisperse	0.19	Failure
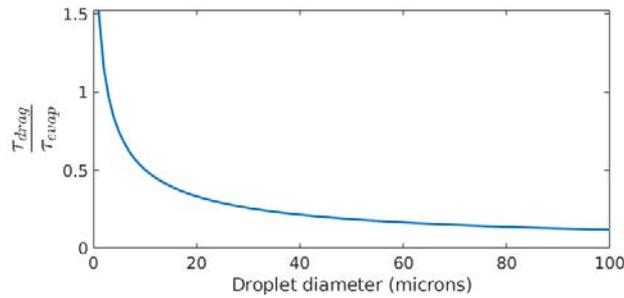
Figure 7-23: Evolution of the ratio τ_{Drag}/τ_{Evap}

to volume ratio equal or lower than 2000 m^{-1}. This behavior is limited to this pin-pin geometry, its electrical characteristics and the range of conditions studied. In particular, aeronautical igniters create a bigger area of high temperature in a shorter time ($t_{depos,aero} \approx 0.1 \cdot t_{depos,pin-pin}$), and the turbulent flow in the combustor provides a continuous influx of fresh mixture.

Chapter 8

LES of kernel formation and annular propagation in the Safran-NTNU Spinning Combustion Test Bed

Contents

This chapter covers the simulations performed with NTNU bench equipped with the spinning combustion technology. The experimental setup consists of an annular rig which emulates a small helicopter engine combustion chamber in which injectors are oriented so as to create the same level of azimuthal flow as seen in Safran spinning combustion engines. This test bed was jointly developed by Safran Helicopter Engines and NTNU within the Marie Sklodowska-Curie Actions Initial Training Network Annulight [8].

8.1   Experimental Setup

Figure 8-1 contains an overview of the rig. A premixed air-methane mixture is introduced into the plenum chamber and then passes through straight injector tubes to the injectors. The injectors consists of elbow-like tubes fitted with a swirler at the injector exit with a geometrical swirl number of 1.22 [143]. Figure 8-2 shows a detailed view of the injector arrangement. The injectors can be rotated both in the yaw and pitch angles as indicated in Fig. 8-3 although for this study the β angle was fixed to 0 (swirler axis parallel to backplane).

The combustion chamber inner diameter is 127 mm and outer diameter is 212 mm. For this study, the height of the inner and outer combustor walls is 200 mm. The outer wall is made of quartz to have optical access, while the inner wall employed in this study is made of steel. The igniter is composed of a single electrode which is introduced into the chamber by a hole perforated in the inner wall at a height of 18 mm above the backplane. Fig. 8-4(Left) indicates the igniter position, and it protrudes 10 mm into the chamber.

The igniter is a Danfoss EBI4 1P model, a unit designed for intermittent ignition of medium-size burners. It provides a nominal voltage output of 12 kV and a (rms)
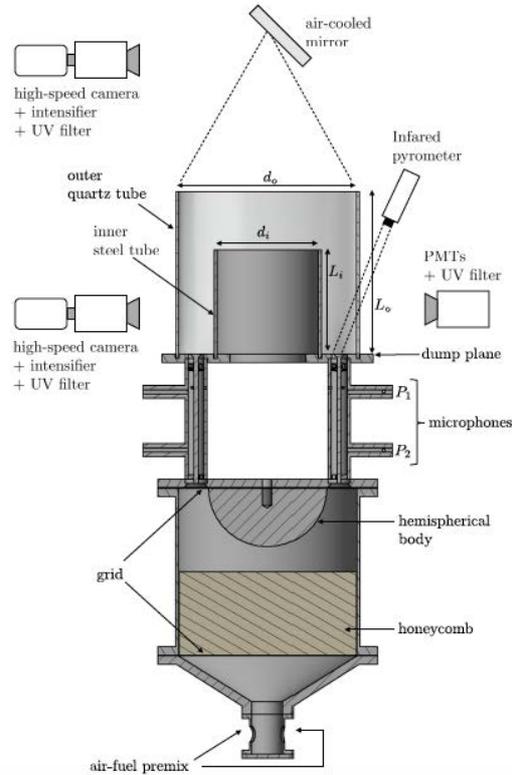
Figure 8-1: NTNU spinning combustion rig (courtesy of Yi-Hao Kwah (NTNU))

current of 40 mA. However, the circuit was modified so as to provide a temporally periodic deposition of energy with a frequency of 50 Hz. Each cycle consists of 20 ms. For each cycle, during 0<t<7.5 ms, the igniter provides an almost constant amount of power, and does not provide any power for the rest of the cycle (7.5<t<20 ms) as shown in Fig. 8-5. This evolution repeats during the whole duration of one run, which means that runs whose light-around lasts for more than 20 ms undergo more than one energy deposition period. The spark is established between the igniter tip and the inner combustion wall. Its low amperage indicates that the igniter works mostly in the glow regime [77]. The nomenclature for the position of each injector is shown in Fig. 8-4(Left).

For ignition, the set of diagnostics is composed of the following items:
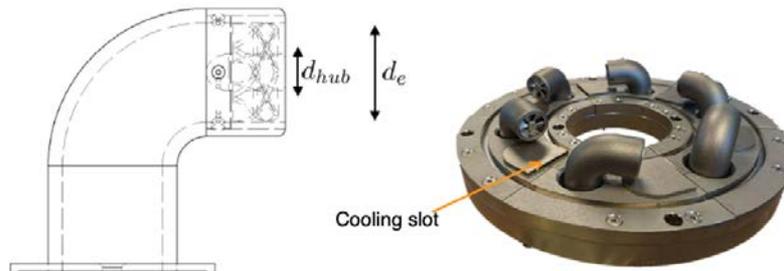
Figure 8-2: (Left) Detailed view of an injector ($d_e = 19$ mm, $d_{hub} = 7$ mm). (Right) Arrangement in NTNU SCT bench. The cooling slots did not provide any outflow during the ignition experiments to improve repeatability
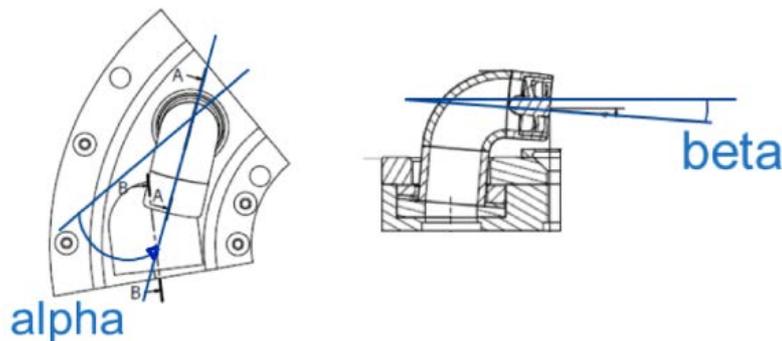
Figure 8-3: Angle definition for NTNU SCT injectors. β fixed to 0 in this study. Two settings for α: 0 (pointing towards outer wall) and 23 degrees (outlet closer to inner wall)

1. Photomultiplier (PMT) with OH* filter and CH* filter at each injector position.

2. Thermocouples at several positions at the backplane.

3. An infrared thermometer (Pyrometer).

4. A fast-camera capturing direct visualization of the light-around from a top view.

Each injector has a photomultiplier for flame detection at a height of 30 mm over the dump plane. Fig. 8-4(Right) shows an example of the field of view in each of the injectors. The camera records direct visualization images at a frequency of 20 kHz.
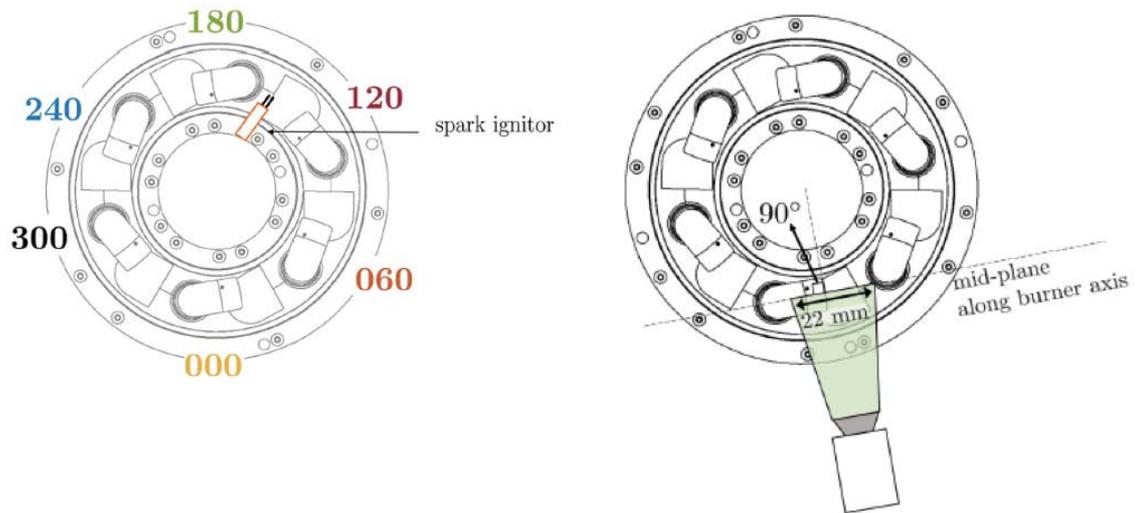
Figure 8-4: Left: Igniter position for NTNU SCT marked in orange and injector position nomenclature, Right: representation of the field of view for each injector (courtesy of Yi-Hao Kwah(NTNU))

The air and fuel flow rates are regulated by Alicat mass flow controllers (MFCs) which have an accuracy of 1%.

Prior to the ignition tests, the non-reactive velocity flow profile at the fuel injector exit has been characterised using hot-wire anemometry [8].

The ignition procedure follows a "spark first, fuel later" approach. This means that the igniter is activated and only when the electrical functioning has been verified in search of shortcircuits, the fuel is introduced. As a result of that, the relative time difference between the igniter start and the start of the filling of the chamber was not recorded.

In order to control the effect of the wall temperature and ensure repeatability, each run procedure starts just after the backplane temperature measurement from the pyrometer reaches a value of 150 degrees Celsius. The sequence is the following:

1. Air (only) is introduced into the combustion chamber.
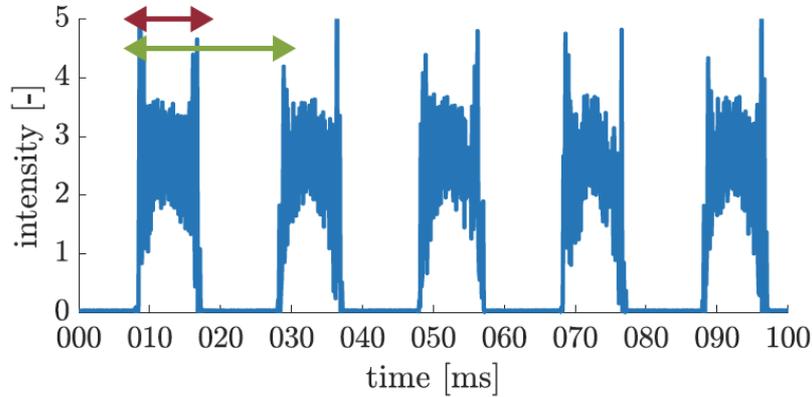
Figure 8-5: Temporal evolution of the igniter spark intensity. Each cycle lasts for 20 ms, which is indicated by the green arrow. For each cycle, during the first 7.5 ms energy is deposited and it is indicated by a red arrow. It is to be noted that this repeats during the whole duration of each of the runs (There may be more than one spark per run). (Courtesy of Yi-Hao Kwah (NTNU)).

2. Once the temperature measurement of the backplane is 150 °C by means of the pyrometer, the ignition system is triggered.

3. Once the absence of short-circuit has been verified, the mixture of fuel and air is introduced. Meanwhile, the igniter remains providing energy with a period of 20 ms.

8.2 Numerical Setup

The AVBP V7 solver was used, with the same settings which were validated in the radius chamber study (See chapter 6). Notably, the same chemical scheme for methane consisting of 19 species and 184 reactions is retained, the same subgrid models for turbulence and turbulence-chemistry interaction and sensor with the same choice of parameters are kept. With the sole objective of reducing the computational time, two modifications with respect to the radius chamber study were introduced. Firstly, the calculation of the β parameter of the dynamic formulation of the wrinkling

206

factor was restricted (as in [111,135]) to a frequency of once to every 0.1 ms, which is smaller than the integral scale eddy turn-over time. In addition to that, the frequency of calculation of the generic sensor [118] to detect the flame region was set to once every 1 μs, choosing not to reduce the frequency to a lower value due to the iterative process in the inner workings of the generic sensor.

The computational simulations replicate the same procedure as in the experiments. First, the domain is filled with air, in this case until the turbulent kinetic energy reaches a stable value. This segment of the calculation is done with a single sector of the chamber (60°) with a typical cell size of 0.4 mm, which consists of 14M cells. In order to save computational time and with the knowledge that sparking at the early instants will not be successful due to the low equivalence ratio, the chamber is left to be filled with fuel for at least a duration of 40 ms (2 igniter periods) before sparking. In practice, a filling time between 60 and 180 ms was necessary to manage successful ignition, ignition failing before due to not enough fuel content.

During the energy deposition phase, a mesh made up by 3 copies of the 60° sector (making a total of a 180° section) was used. In addition to that, this mesh was refined in the energy deposition region so as to directly describe the flame in the vicinity of the igniter without using the thickened flame model. The mesh resolution in this zone is 100 μm, and it is 0.35 mm in the rest of the chamber. A detailed view of the energy deposition refinement in a 60° sector can be seen in Fig. 8-6. This mesh consists of 150M cells.

For t=3 ms after the igniter start and after verifying that the kernel is far from the periodic boundaries yet and the periodic setting does not affect the solution, the solution is interpolated to a 360 degree mesh (the 360 degree solution has been initialized to the same level of swirl as at t=0 and by means of the HIP tool [92], the 180 degree solution with energy deposition partially overwrites the 360 degree solution). The 360 degree mesh is a duplication of the 180 degree mesh in which the
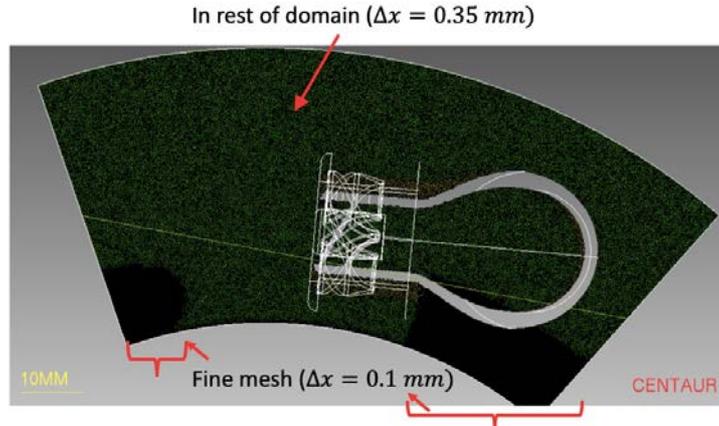
Figure 8-6: Detailed view of the mesh refinement near the igniter for NTNU SCT energy deposition instants

circumferential extent of refinement region is smaller and the immediate vicinity of the injector exit is refined to a cell size of 0.25 mm to properly describe the mixing between the jet and the environment. This mesh consists of 275M cells. As a brief note, the computational cost of each case entails an approximate amount of 5 million CPU-hours.

The boundary conditions are indicated in Fig. 8-7. The fuel tube inlet (cyan) was modelled with NSCBC (Navier-Stokes Characteristic Boundary Condition [104]) inlet boundary in which the velocity, temperature and species are specified. The outlet (green) is modelled with NSCBC in which the static pressure is specified. The solid boundaries are modelled as isothermal no-slip walls. The temperature of the walls are set to the values predicted by a conjugated heat transfer calculation performed before these computations. These conjugated heat transfer equations follow the same procedure as in experiments. First, a stable flame is calculated. Then, the flame is extinguished and the domain is left to cool down by introducing air through the inlet tube only. When the temperature of the backplane decreases to 150 °C, (instant at which experiments would start a new run) the temperature of the walls is recorded. Since the light-around cases have a duration of a few tens of milliseconds,
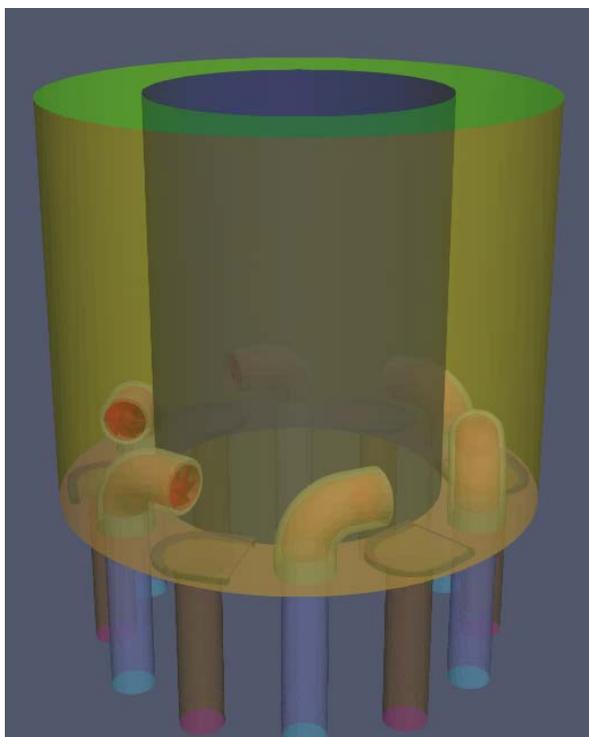
Figure 8-7: Mesh for NTNU SCT showing the different boundaries in different colors

the temperature at the walls is assumed to remain constant. The mesh used in the conjugated heat studies is shown in Fig. 8-8 and its results in Fig. 8-9.

Since there are two geometric configurations (α=0 and 23°), a different set of values is used for each configuration. These values are shown in table 8.1.

Table 8.1: Wall temperature at the solid boundaries for the case α=0, 23°

Wall temperature in K	α=23°	α=0°
Backplane	423	423
Inner radius	370	300
Outer radius	300	370
Fuel injector	323	323
Internal and external		
Fuel tube	293	293

In order to model ignition, the energy deposition model used for the Radius chamber and CORIA pin-pin studies is used. Contrary to the radius chamber and pin-pin
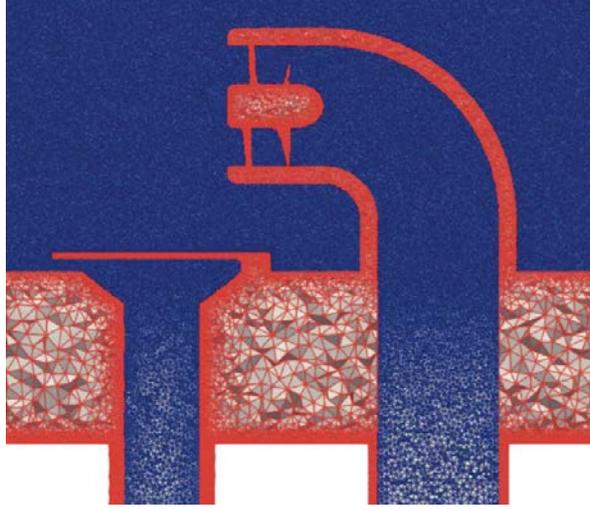
Figure 8-8: Mesh for NTNU SCT conjugated heat transfer study showing meshing both in the fluid and solid domains [7]

cases, no detailed temporal evolution of power with time was available and a modification to provide an intermittent sparking of 50 Hz was made. To calculate the resulting energy profile, the following rationale was followed: First, from the igniter manufacturer characteristics, the igniter provides a RMS power of 480 W with a frequency 20 kHz. Assuming no power is lost in the electronics, and introducing the electrical to thermal efficiency at glow ($\eta = 0.3$) the conversion of the profile to the one indicated in Fig. 8-5 results in a the following input to the energy equation:

$$\dot{Q} = \begin{cases} 347 \text{ W for } 0 < t < 7.5 \text{ ms in each cycle of 20 ms} \\ 0 \text{ W for } 12.5 < t < 20 \text{ ms in each cycle of 20 ms} \end{cases} \tag{8.1}$$

Finally, as a posteriori check, the size of the energy deposition has to be chosen so that the temperature in the zone is near to 3000 K [77] (since the igniter works in the glow regime). In order to adjust the size of the energy deposition, the large deposition time (7.5 ms) has to be taken into account as it may cause the energy channel to be altered by the flow movement, and the energy channel will preferentially be established in the electrode wake. Taking everything into account, a hollow
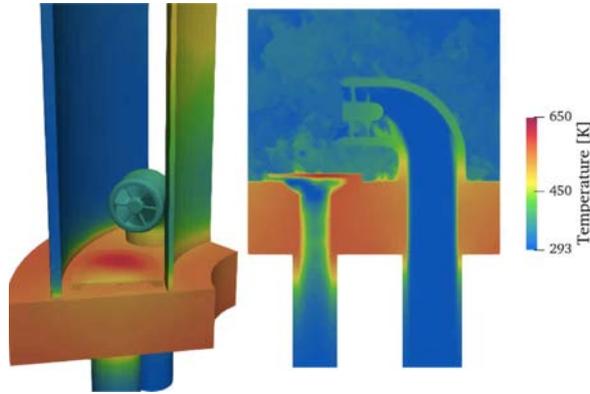
Figure 8-9: Wall temperature at the end of the cooling procedure for the NTNU SCT conjugated heat transfer study [7]

semisphere with $D_{out} = 10$ mm (equal to the igniter protrusion into the chamber) and $D_{in} = 9.6$ mm situated downstream the igniter was adjusted as an average representative geometrical region occupied by the energy channel. This region can be seen in Fig. 8-10. The choice of these dimensions ensured the temperature in the deposition zone is approximately 3000 K.
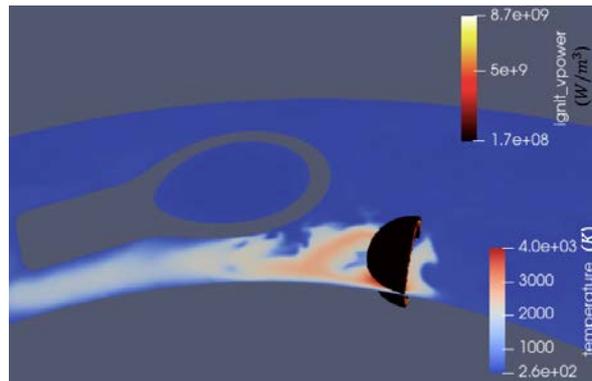
Figure 8-10: View of the semispheric hollow region adopted as a representative location of the energy channel from the igniter and a planar cut of the annular chamber showing that the fluid which as traversed through the deposition zone acquires a temperature of approximately 3000 K

8.2.1 Cases under Study

Table 8.2 contains the cases under study. They consist of two different injector orientations and two different equivalence ratios. It is to be noted that all cases feature the same thermal power. For that reason, the cases with lower equivalence ratio ($\phi = 0.7$) feature a higher inlet velocity than those at $\phi = 1$. The inlet mixture is considered to be at 273 K and atmospheric pressure.

Table 8.2: Summary of cases for NTNU SCT configuration

Case number	α	ϕ	v_{inlet} (m/s)
231	23	1	15.6
237	23	0.7	21.6
07	0	0.7	21.6

The experimental data in case 231 shows successful ignition in the mean azimuthal direction (anticlockwise), as it is indicated in Fig. 8-11. On the other hand, the experimental images of case 237 display a successful flame propagation both in favour and against the mean azimuthal flow (See Fig. 8-12). Finally, case 07 is a particular example of ignition in which the flame is not stabilized and forms a kernel that rotates in the direction of the mean azimuthal flow (See Fig. 8-13).
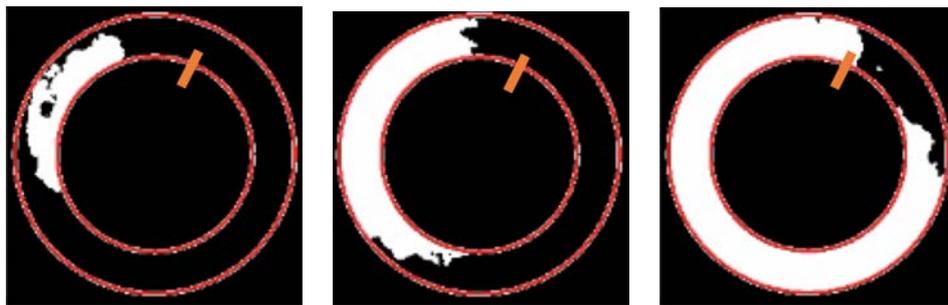
Figure 8-11: Direct visualization images of case 231 at several instants (Igniter position marked in orange)

Figure 8-14 shows the velocity profiles at a location 2.5 mm downstream the injector (following the injector axis). This location is highlighted in Fig. 8-15. All
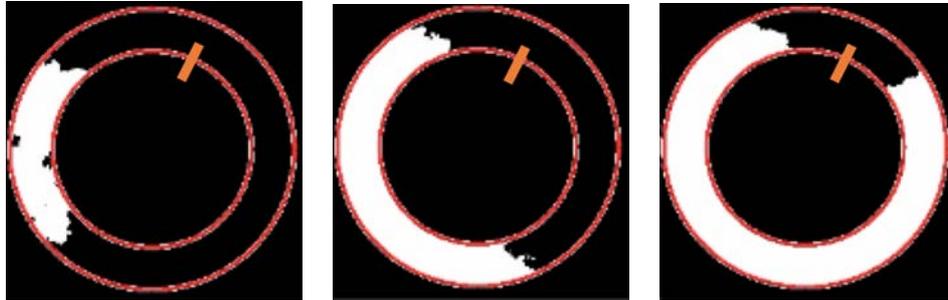
Figure 8-12: Experimental images of case 237 at several instants (Igniter position marked in orange)
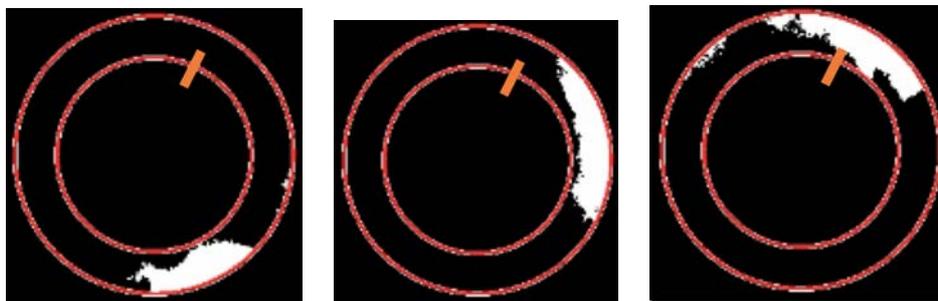
Figure 8-13: Experimental images of case 07 at several instants (Igniter position marked in orange)

cases indicate two peaks coinciding with the injector diameter. The cases with $\phi = 0.7$ have higher absolute values. Finally, a recirculation zone where $u_x < 0$ is visible for all cases for $-0.75 < x/R_{inj} < 0.75$.
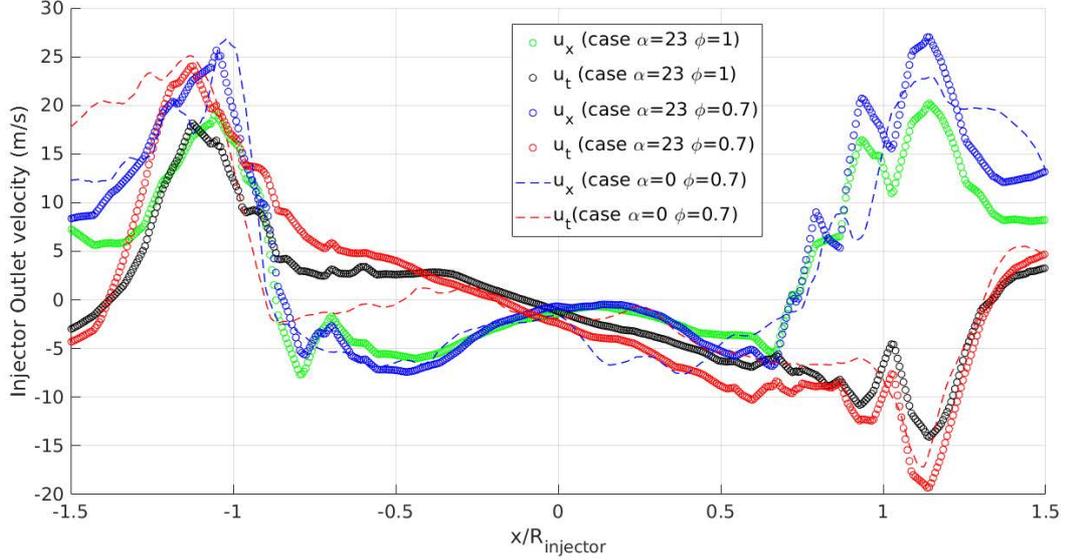
Figure 8-14: Averaged velocity profiles at 2.5 mm (0.26 R_{inj}) downstream the injector face from LES calculations. The axial component is normal to the injector face, while the transversal component is perpendicular to the normal and parallel to the annulus axis

8.3   Results

8.3.1   Case 231

Experimental Results

This case is characterized by a moderate injector jet exit velocity ($v_{ax,jet-exit} \approx 18$ m/s), and the highest reactivity $\phi = 1$. The injector is oriented towards the inner combustor radius $\alpha = 23°$. With $\alpha = 23°$, the axis of the injector swirler is oriented towards the inner annulus radius surface of the injector downstream (See Fig. 8-4). The flame has a space of 2.7 injector diameters between the injector and the next solid boundary. With $\alpha = 23°$, the region between the inner radius and the injector forms a convergent section (See Fig. 8-16) that will affect the light-around process.

The experiment shows a successful light-around which starts at the injector imme-

214
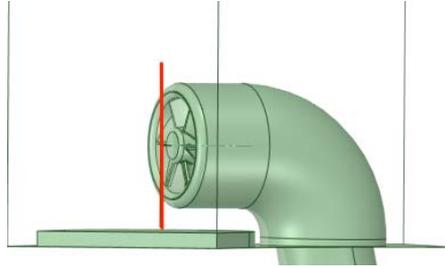
Figure 8-15: Station where velocity profiles are measured (2.5 mm (0.26 R_{inj}) down-stream the injector face). The axial component is normal to the injector face, while the transversal component is perpendicular to the normal and parallel to the annulus axis
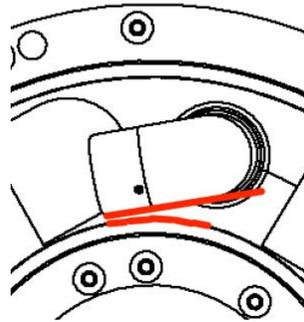
Figure 8-16: Geometric detail of the converging section between the injector and the inner radius wall for case with $\alpha = 23°$

diately downstream of the igniter (180) and proceeds in a sequence that follows the net azimuthal flow generated by the injectors (anti-clockwise direction) as indicated in Fig. 8-17. Assuming that the total light-around time follows a normal distribution function, the data of the 21 experimental runs realized indicate a mean of 15 ms and a standard deviation of 2.6 ms (17% of the mean).

Numerical Results

Since the starting time of the igniter with respect to the filling of the chamber was not recorded in the experiment, several attempts were made to initiate the light around after having filled the chamber at different instants after the igniter start since
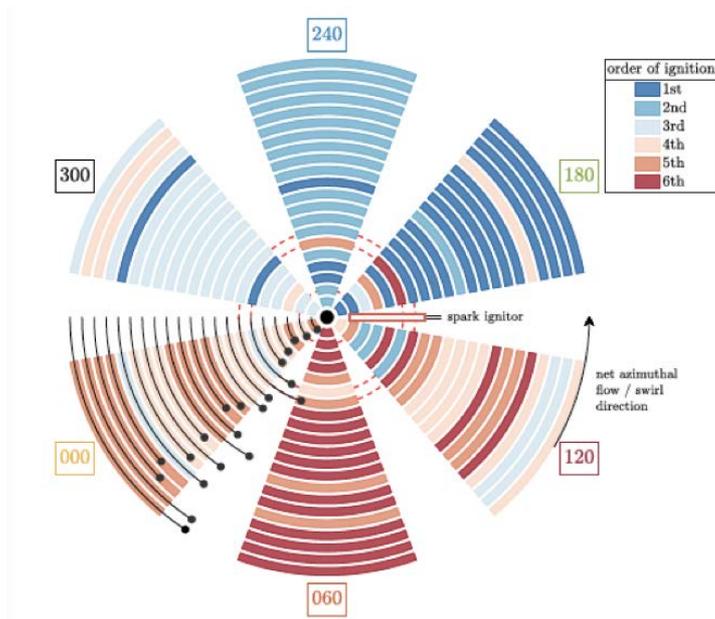
Figure 8-17: Experimental data for case 231 courtesy of Yi-Hao Kwah (NTNU). The sectors are labelled with numbers (e.g. 120, 180, 240...) and the colors represent the order of ignition (from dark blue for the first sector to ignite to dark red, which is the last). Each ring consists of one run (There are 21 experiment runs vs 1 simulation of this case in total). The length of the black lines near sector 0 represent the duration of the light-around for each run. For this case, the flame propagation follows the net azimuthal flow which is indicated by the arrow near the external radius in sector 120.

the igniter provides energy every 20 ms (See Fig. 8-5). It was found that ignition was not successful until 60 ms after the start of the filling of the chamber with fuel. The equivalence ratio field at t=60 ms is shown in Fig. 8-18 and indicates a stratified mixture which falls inside the flammable region ($\phi > 0.52$) of a height of $3D_{injector}$ above the backplane, where the majority of the region has $\phi > 0.7$ (as indicated by the contour lines).

Figure 8-19 shows a graphical comparison of the top images for both experiments and LES computations. The temporal flame evolution is closely matched in LES, and both LES and experiments show a flame front that propagates faster along the annulus inner radius.
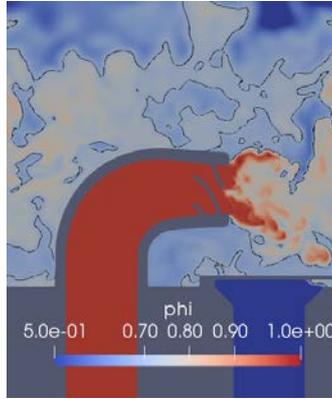
Figure 8-18: Meridional view of the equivalence ratio with a contour line for $\phi = 0.7$ at the igniter start (t=0)

The LES calculation indicates that the flame originated from the igniter is immediately able to propagate downstream along the inner radius towards the injector downstream (injector 180). At t=3 ms after the igniter start, the leading point of the propagating flame reaches the outlet of injector 180. For 3<t<4 ms, the flame branch in contact with the injector jet exit is quenched due to the jet exit velocity, as indicated in the top image of Fig. 8-20. The bottom image of Fig. 8-20 shows that for t=5 ms the flame has managed to propagate vertically downwards towards the backplane, reaching the injector recirculation zone, and producing the complete ignition of the injector 180 .

The following downstream injectors (240, 300 and 0) undergo ignition by a different mechanism. For these injectors, the bulk flow expansion originated from the ignition of the injector upstream accelerates the flame propagation (see Fig. 8-21) which allows the flame to propagate across the jet exit (the flame does not need to travel downstream to find the recirculation region and be able to ignite the injector), as it can maintain its chemical activity across the jet exit jet, as shown in Fig. 8-22.

Lastly, the injector immediately upstream the igniter (injector 120) ignites in a different mode from the remaining injectors. For this injector, its recirculation zone is close to the igniter energy deposit. Therefore, some eddies are able to bring energy

| 5 ms | 7.5 ms | 10 ms |

| 12.5 ms | 13.5 ms | 15 ms |
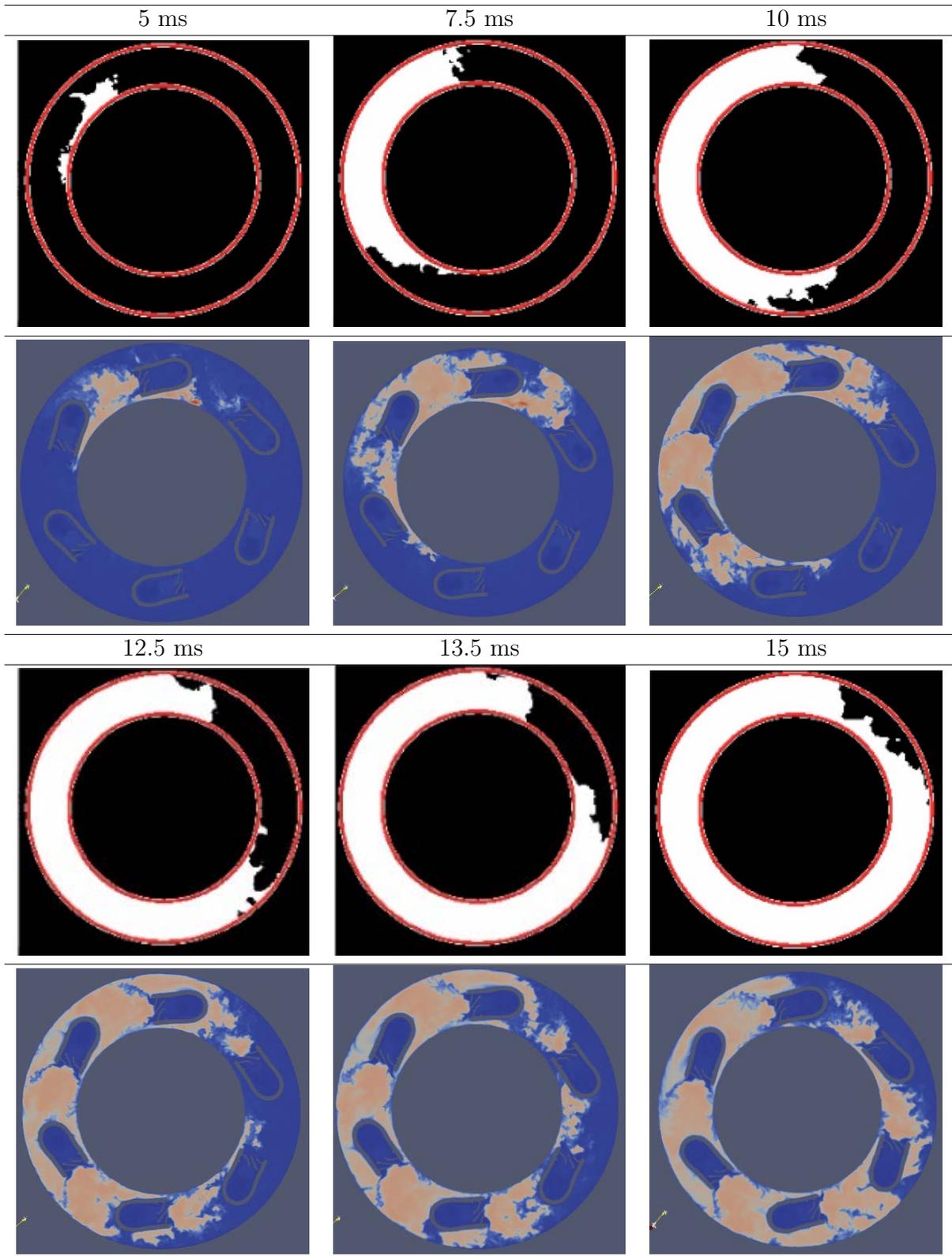
Figure 8-19: Comparison of experimental edge-detection images with temperature fields at plane $x = 1.16 D_{inj}$ (parallel to backplane) for case 231 ($\alpha = 23°$, $\phi = 1$) at various times after spark.

The leading point of the flame is approaching the region of low velocities (blue) as seen on the left of the top image

At t=5 ms the flame has completed ignition of the injector 180 by propagating upstream across the recirculation zone.
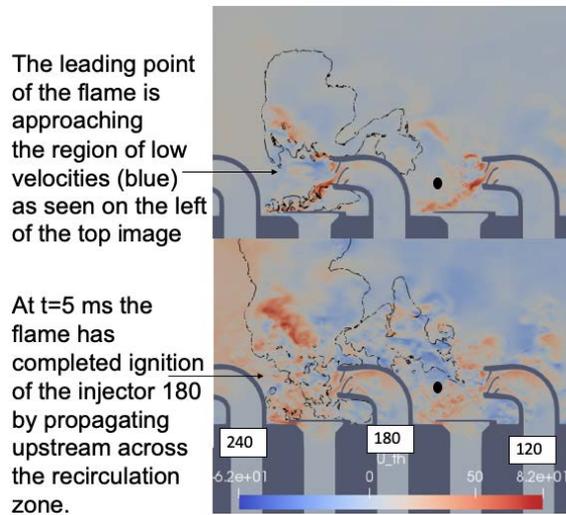
Figure 8-20: Planar projection of annular cut at r=85 mm (mid-radius) for case $\alpha = 23°$ and $\phi = 1$ at t=4 ms (Top) and t=5 ms (Bottom) after igniter start showing the tangential velocity (m/s) and a heat release contour at 5e6 W/m^3. The injector numbers are indicated in the inlet tubes.
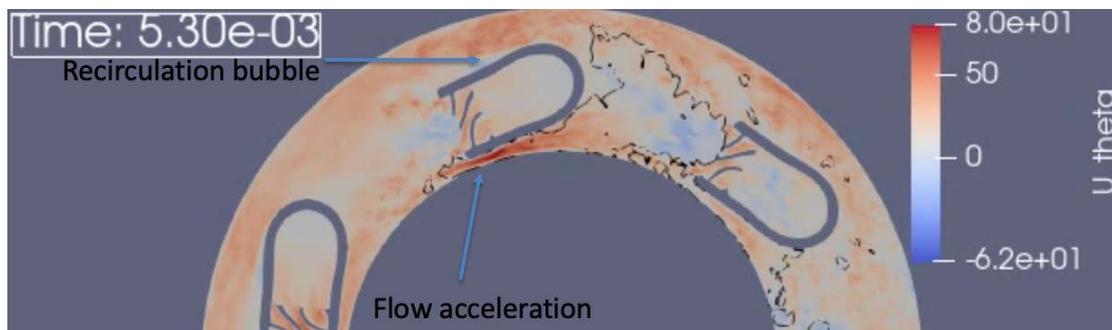
Figure 8-21: Planar cut at injector showing tangential velocity field (m/s) for case $\alpha = 23°$ and $\phi = 1$ at t=5.3 ms after igniter start with a contour of heat release at 5e6 W/m^3 showing flame propagation acceleration.

upstream (against the net azimuthal flow) towards the injector. This effect can be seen in the top image of Fig. 8-23. In addition to that, the ignition of injector 180 downstream affects the ignition of injector 120 upstream. After the injector 180 is ignited, a flame front is generated that, due to the bulk flow expansion, propagates against the net azimuthal flow and travels towards the injector 120. This effect can be seen in the bottom image of Fig. 8-24. Both these effects work simultaneously

219

The flame propagation in the radial direction across the jet exit (top image) precedes the flame propagation from the overarching flame (bottom image).
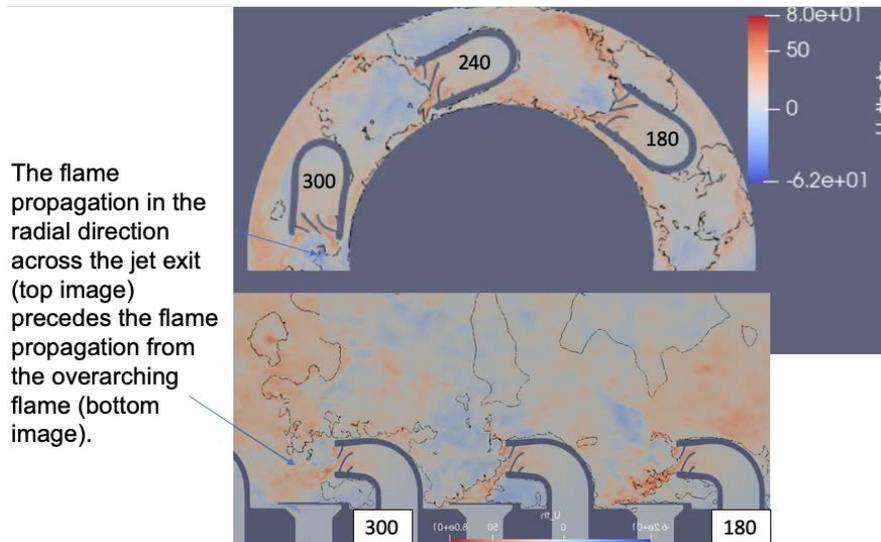
Figure 8-22: (Top) Planar cut at injector showing tangential velocity field (m/s) for case $\alpha = 23°$ and $\phi = 1$ at t=8.3 ms with a contour of heat release at 5e6 W/m^3. (Bottom) Projection of annular cut at r=85 mm (mid-radius location).

to increase the temperature at the injector 120 face, which experiments a progressive ignition process which is completed at t=13 ms.
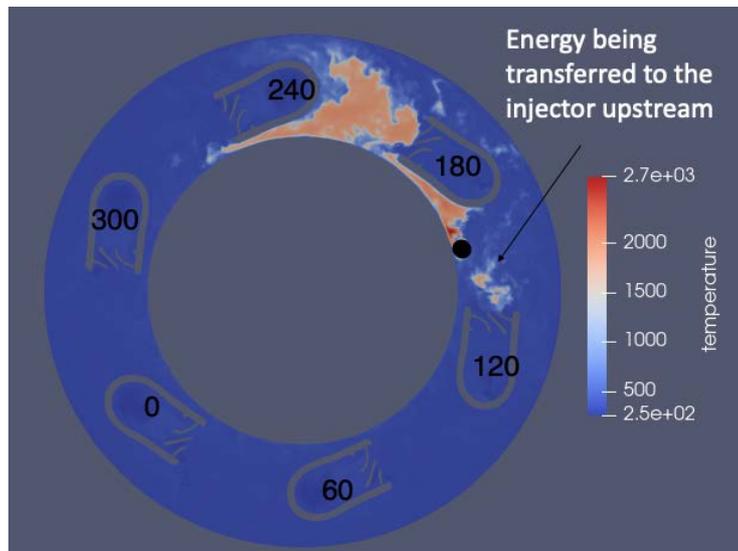
Figure 8-23: Planar cut at injector showing temperature field in Kelvin for case $\alpha = 23°$ and $\phi = 1$ at t=5.6 ms after igniter start. The location of the igniter is indicated by a black point.
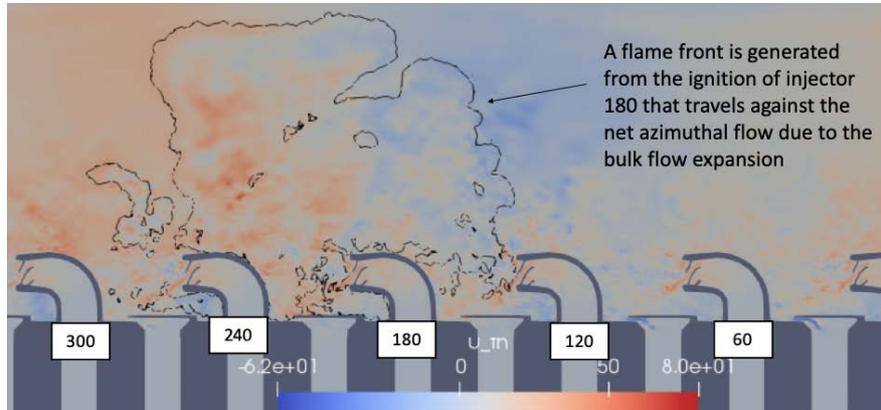
Figure 8-24: Projection of annular cut at r=85 mm (mid-radius) at t=6.3 ms after igniter start showing tangential velocity in m/s.

The flame leading point trajectory, defined as the point of the flame isosurface with $q = 0.8$ (q being the progress variable based on temperature) and the highest azimuth (igniter is $\theta = 0$) is shown in Fig. 8-25. The flame propagates predominantly along the inner radius, which is promoted by the acceleration due to the contraction seen in Fig. 8-16. In addition to that, for the outer radius trajectory, the flame faces a longer distance and the recirculation bubbles at the injector surface (as indicated in Fig. 8-21), which hinders this propagation mode.

The experiment and LES ignition times are identical except for a maximum deviation of 1 ms occurring for the injector 120. This injector is located immediately upstream of the igniter and it is ignited by a combination of the anti-clockwise propagating flame and eddies bringing energy upstream from the igniter. As a result of that, it is subjected to a greater level of stochasticity. It is to be noted that the ignition of the first injector (180) occurs 2 ms after the flame leading edge reaches the injector exit. On the other hand, the ignition of injectors 240, 300, 0 and 60 is faster and take place at a regular interval of 2.5 ms. Table 8.3 contains a comparison of the injector ignition times from the experiment and the LES computation.

Figure 8-26 contains the temporal evolution of the total heat release in the domain. There is a linear increase during the first instants of the light around process
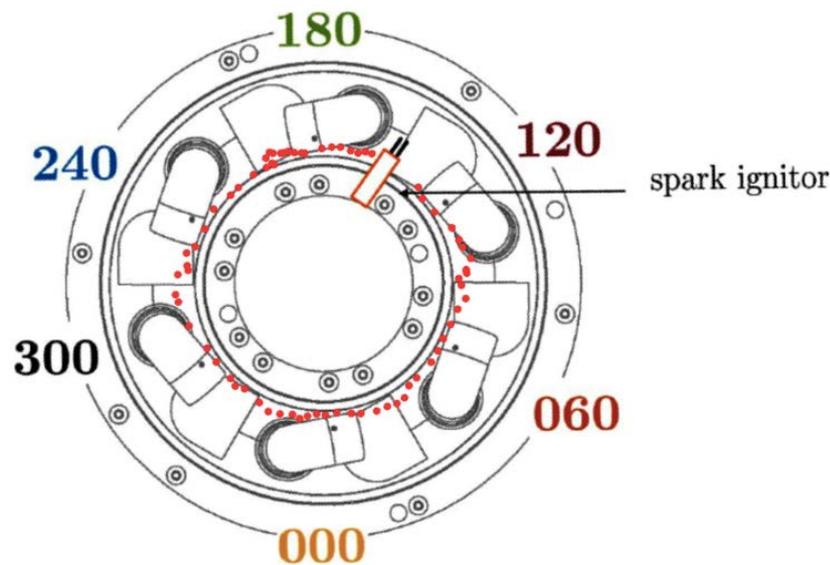
Figure 8-25: Leading point trajectory for case $\alpha = 23°$ and $\phi = 1$. Each point represents a 0.2 ms increment.

Table 8.3: Sector (indicated by its angle) ignition times in ms after igniter start for case $\alpha = 23°$ and $\phi = 1$

	180	240	300	0	60	120
Experiment	5	7.5	10	12.5	13.5	15
LES	5	7.6	10	12.5	15	13

(2<t<8 ms). For t>8 ms, the figure is not significant since the slope decay is caused by the flame reaching the top part and the burnt gases leaving the domain.

For case 231, the "thrust-effect" (as denominated by [68]) plays a major role in accelerating the flame propagation and, consequently, allowing the flame to propagate across zones of high strain (the jet exit from the injector). This contribution can be observed in Fig. 8-27.
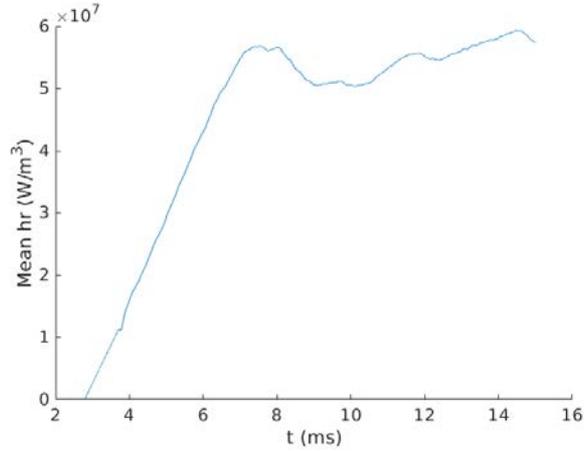
Figure 8-26: Temporal evolution of the total heat release in the domain for case $\alpha = 23°$ and $\phi = 1$. For t>8 ms, the slope decay is caused by the burnt gases leaving the domain through the outlet
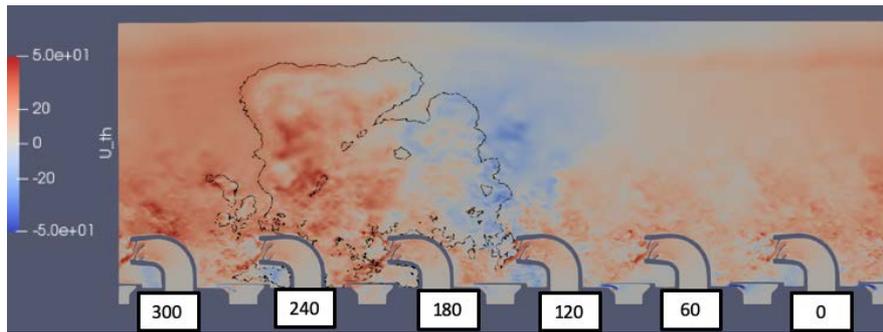
Figure 8-27: . Projection of annular cut at mid-radius for case $\alpha = 23°$ and $\phi = 1$ at t=6 ms showing tangential velocity in m/s. The reddish zone on the right of the image indicates enhanced azimuthal velocity, while the bluish part represents the contrary sense of azimuthal motion

8.3.2   Case 237

Experimental Results

This case is characterized by a high injector jet exit velocity ($v_{ax,jet-exit} \approx 25$ m/s), and a moderate reactivity $\phi = 0.7$. The same geometry from case 231 is kept ($\alpha = 23°$), so the injector is oriented towards the inner combustor radius. As seen for case 231, for this geometry the flame has a space of 2.7 $D_{injector}$ between the injector

face and the closest solid boundary.

The experiment shows a successful light-around which skips the injector immediately downstream the igniter (injector 180) and starts near the second injector downstream (240) as indicated in Fig. 8-28. Then, injectors 300 and injector 0 ignite (following the net azimuthal motion, anticlockwise direction). At the same time and in a progressive fashion, the injector 180 is ignited, which gives the appearance that the light-around progresses in both favour and against the net azimuthal motion. Finally, the branch from igniter 240, 300 and 0 continues its progress following the net azimuthal motion and ignites injectors 60 and 120. This can be seen in Fig. 8-29. Assuming that the total light-around time follows a normal distribution function, the data of the 20 experiment runs realized indicate a mean of 25.8 ms and a standard deviation of 4.5 ms (17% of the mean).
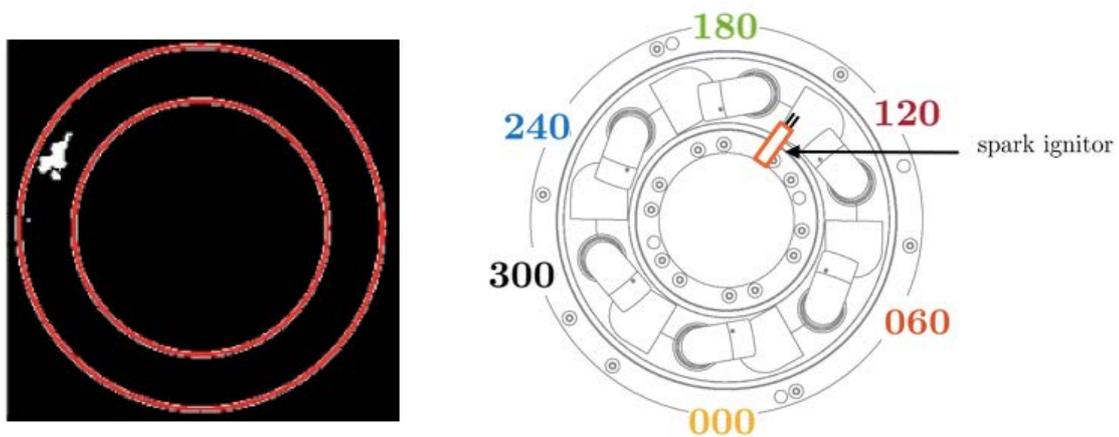
Figure 8-28: First instants of flame propagation in case 237, the first signal of luminescence captured by the camera is near injector 240, indicating the flame kernel has skipped the injector closest to the igniter (180)

Numerical Results

Figure 8-30 shows a graphical comparison of the top images for both experiments and LES computations. The temporal flame evolution is closely matched in LES,
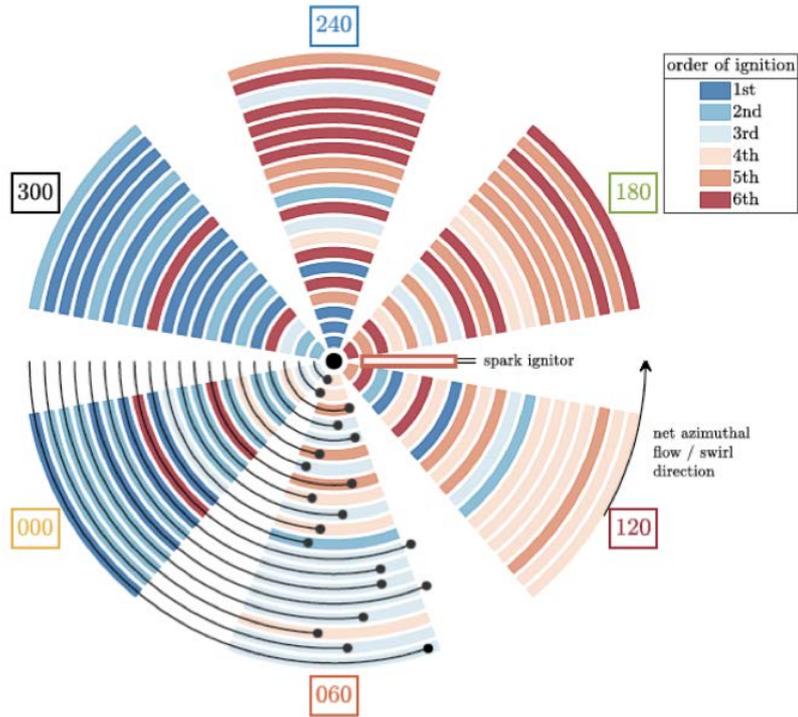
Figure 8-29: Top representation of the light-around of case $\alpha = 23°$ and $\phi = 0.7$ (Courtesy of Yi-Hao Kwah (NTNU)). Each ring consists of one run (There are 20 experiment runs of this case in total)

and both LES and experiments show an increase of the duration of the light-around progress with respect to the previous case with $\phi = 1$.

To perform the LES computation and similarly to case 231, several attempts were made to initiate the light around after having filled the chamber with fuel for different periods of time. For this case, a chamber filling time greater than 180 ms is needed to ensure light-around, which is three times larger than that of case 231 and results in a more homogeneous initial mixture at spark than the conditions of case 231. The equivalence ratio field at t=180 ms is shown in Fig. 8-31 and indicates an homogeneous mixture with $\phi = 0.7$, showing the need for a uniform mixture at the nominal equivalence ratio $\phi = 0.7$ over most of the domain unlike case 231.

7 ms	9 ms	14 ms

16 ms	18.5 ms	23 ms
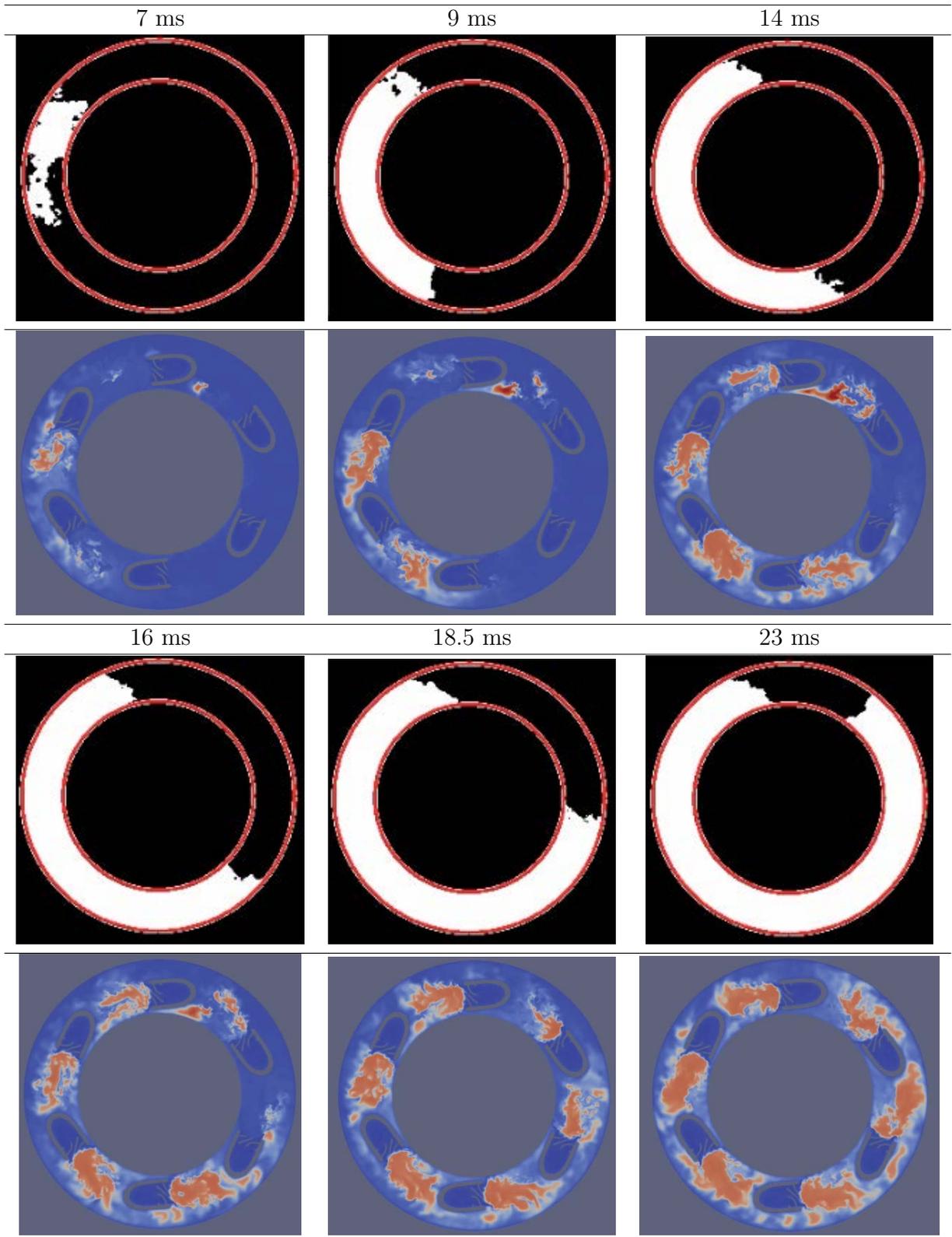
Figure 8-30: Comparison of experimental edge-detection images with temperature fields at plane $x = 1.58D_{inj}$ (parallel to backplane) for case 237 ($\alpha = 23°$, $\phi = 0.7$) at various times after spark.
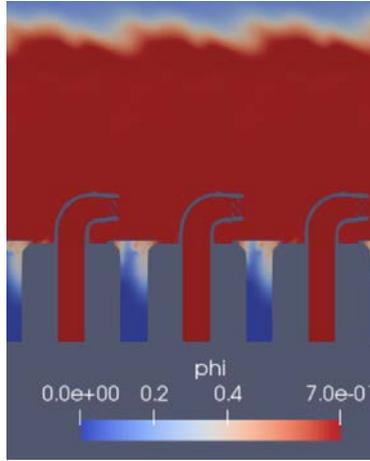
Figure 8-31: Meridional view of the equivalence ratio at the igniter start of the first successful ignition (chamber filled with fuel for 180 ms) for case 237 ($\alpha = 23°$ and $\phi = 0.7$)

The LES calculation indicates that the flame originated from the igniter propagates downstream along the inner radius towards the injector downstream (injector 180) but, differently to case 231, the kernel does not manage to ignite injector 180 but survives and keeps developing in the circumferential and vertical directions. This behavior can be observed in Fig. 8-32. For 16<t<21.3 ms, the flame continues growing in the circumferential direction and vertically towards the combustor outlet (See Fig. 8-33). Despite the flame front having reached injector 240 at t=16 ms, it takes until 21.3 ms for the flame front to propagate to injector 240's recirculation zone and upstream to reach stable combustion. At t=23.5 ms, approximately two milliseconds after injector 240 ignites and due to the advancement made by the flame in the circumferential direction, injector 300 ignites. Its ignition mode is similar to injector 240: The flame reaches its recirculation zone and travels upstream to anchor itself at the injector face.

From t=24 ms, we can distinguish two processes. Firstly, mainly due to the reactivation of the injector for its second cycle of operation, injector 180 follows an ignition process that finishes at t=29 ms. This can be seen in Fig. 8-34. The ignition
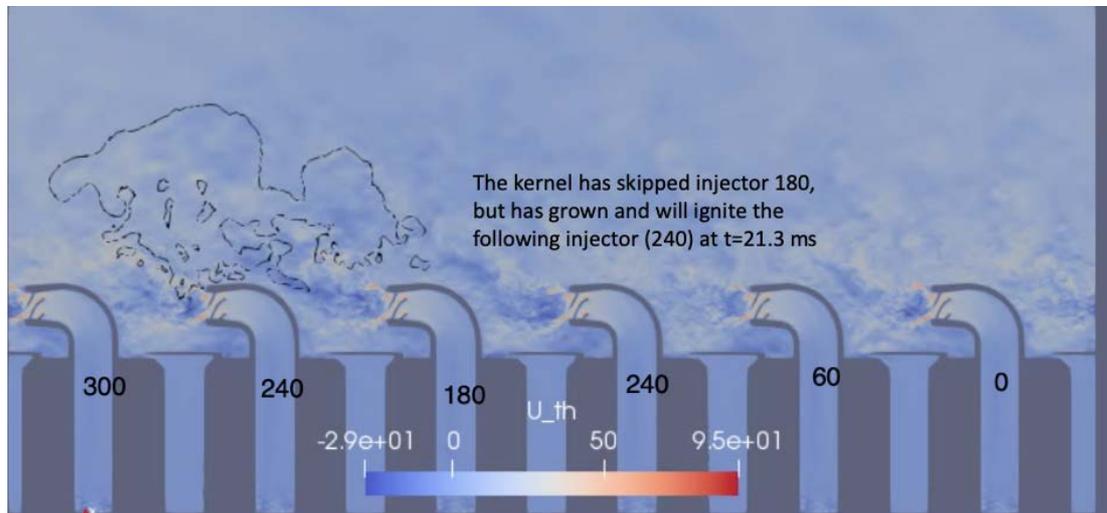
Figure 8-32: Planar projection of annular cut at r=85 mm for case $\alpha = 23°$ and $\phi = 0.7$ at t=16 ms after igniter start showing the tangential velocity (m/s) and a heat release contour at 1e6 W/m^3.
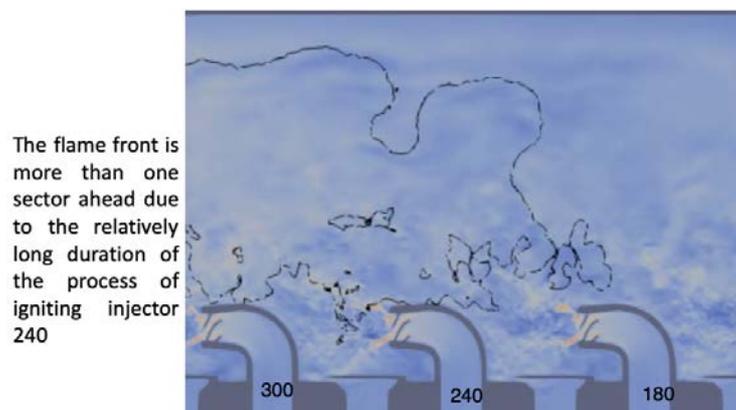
Figure 8-33: Planar projection of annular cut at r=85 mm for case $\alpha = 23°$ and $\phi = 0.7$ at t=20 ms after igniter start showing the tangential velocity (m/s) and a heat release contour at 1e6 W/m^3.

of injector 180 goes against the net azimuthal flow, and gives the appearance that the light-around progresses both in the counterclockwise (in favor of net azimuthal flow) and clockwise (against) directions. Meanwhile, the flame branch propagating in the direction of the net azimuthal flow continues its progress and manages ignition of injectors 0, 60 and 120 at times t=28, 31.5 and 36 ms respectively.

228
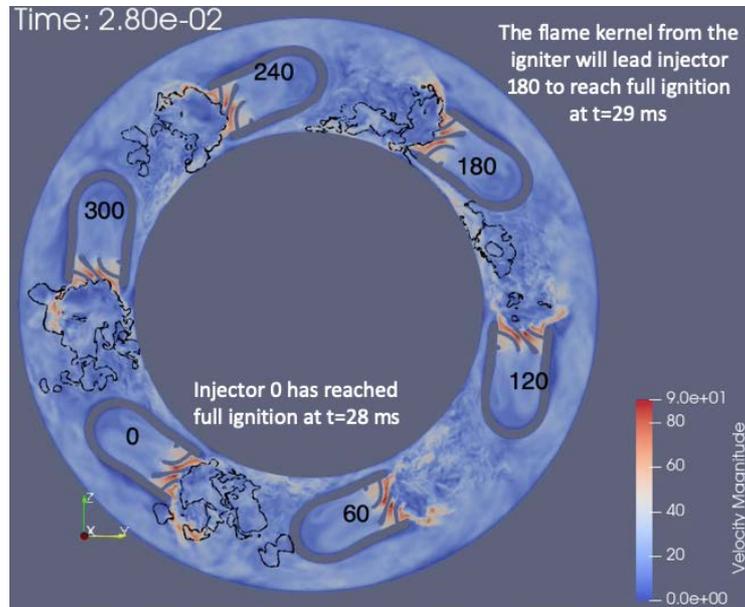
Figure 8-34: Planar cut at swirler axis for case $\alpha = 23°$ and $\phi = 0.7$ at t=28 ms after igniter start showing the velocity magnitude (m/s) and a heat release contour at 1e6 W/m^3.

For case 237 and contrary to case 231, the flame propagation is preferentially vertical (upwards towards the outlet), which is indicated in Fig. 8-35. This may be due to the comparatively higher jet exit velocity for the case of lower equivalence ratio. As a result of that, the flame does not display a preferential propagation along the inner radius (as in case 231).

For this case, the bulk expansion following each injector ignition does not have a noticeable effect on the flame propagation. As indicated in Fig. 8-33, due to the prolonged time period necessary to ignite each injector, the leading flame front is more than one sector ahead of the injector which is undergoing ignition. As a result of this distance, this effect is diminished and no noticeable acceleration of the flame front is observed due to the "thrust effect".

The experiment and LES ignition total duration and processes are similar. In the experiment, the kernel from the igniter skips injectors 180 and ignites 240 first at
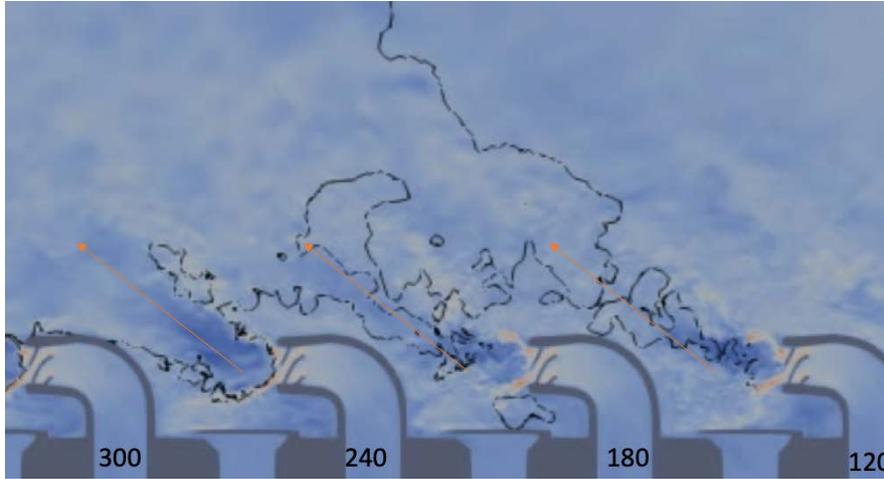
Figure 8-35: Planar projection of annular cut at r=85 mm for case $\alpha = 23°$ and $\phi = 0.7$ at t=26 ms after igniter start showing the tangential velocity (m/s) and a heat release contour at 1e6 W/m^3. The burnt gases trajectory is indicated by arrows

t=9.8 ms. On the other hand, in LES, the first injector to be ignited is 240 after a process lasting for approximately 7 ms. Afterwards, both LES and experiments show similar speeds in the anti- and clockwise flame propagation. The flame branch advancing in favor of the net azimuthal flow manages ignition of each sector at an approximately constant interval of 5 ms, which is twice as much as the case with $\phi = 1$. The total duration for the experiment is 23 ms, while the LES simulation is 21.7 ms. Table 8.4 contains a comparison of the injector ignition times from the experiment and the LES computation.

Table 8.4: Ignition times in ms for case $\alpha = 23°$ and $\phi = 0.7$, the injector number is between brackets. Note: the origin of time for LES is the same as in the experiment i.e. t=0 is the instant when a 10% value of the maximum chemical activity is reached in any injector

Experiment	(240) 9.8	(300) 12.8	(180) 15.9	(0) 17.3	(60) 19.4	(120) 22.6
LES	(240) 7	(300) 9.2	(0) 13.7	(180) 14.7	(60) 17.2	(120) 21.7

230

8.3.3 Case 07

Experimental Results

This case is characterized by a high injector jet exit velocity ($v_{ax,jet-exit} \approx 25$ m/s), and the moderate reactivity $\phi = 0.7$ with an orientation of the injectors ($\alpha = 0°$) towards the outer wall (See Fig. 8-36). For this geometry setting, the flame has a reduced space of 1.25 $D_{injector}$ to propagate downstream the injector face (The case with $\alpha = 23°$ had more than twice that distance, 2.7 $D_{injector}$) before being obstructed by a solid boundary and the flame formation is constrained by the solid boundaries.
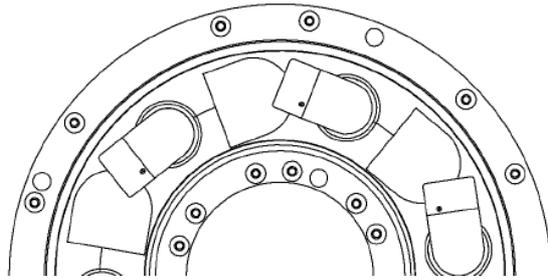
Figure 8-36: Geometric detail of the configuration with $\alpha = 0°$

The experiment shows an "intermittent" behavior of the light-around process. A kernel is formed at one injector (See top-left image of Fig. 8-38). This kernel propagates both in the direction of the net azimuthal flow and, albeit slowly, in counter-rotation with respect to the mean flow (See top-right image of Fig. 8-38). The chemical activity is weaker than the case with $\alpha = 23°$, as indicated in Fig. 8-39. As a result of this, the flame front propagating in counter-rotation decreases its chemical activity and begins to recede while the one in favour manages to advance (See middle-left image of Fig. 8-38). This behavior gives the impression of a flame kernel that rotates in the direction of the net azimuthal flow. Eventually, the flame front in favour of the net azimuthal flow completes the circumference and seems to occupy the full annulus (See middle-right image of Fig. 8-38). However, shortly after, some regions cease to have chemical activity (See bottom-left image of Fig. 8-38).

The quenching continues progressively in a process that lasts for $t \approx 45$ ms (which is equivalent to the residence time of a full turn) until only a small residual kernel remains (See bottom-right image of Fig. 8-38). Fig. 8-37 contains temperature contours from the LES calculations indicating correspondence between experiments and computations.

Figure 8-40 indicates that this process repeats several times, with a low-chemical activity time which varies largely between the periods of activity and that differs from the period of the igniter energy deposition.

Numerical Results

The equivalence ratio field at various instants of the filling of the chamber is shown in Fig. 8-41.

In the LES calculation, after 40 ms of the chamber being filled with fuel and coinciding with a new period of activity of the igniter, a kernel is formed at the igniter location which travels in the direction of the mean azimuthal flow (Red dots in Fig. 8-42). This kernel is not able to ignite the injector downstream (injector 180) due to the high jet exit velocity from the injector and instead deviates towards the inner radius wall as seen in Fig. 8-43. After travelling downstream a distance of approximately $3D_{injector}$, this leading branch quenches and retrocedes (Red arrow towards the blue points in Fig. 8-42). During a period of 2.5 ms, the flame does not manage to advance and stays approximately at the same location. Due to progressive heating, a reaction zone finally appears in the recirculation zone of injector 180 (indicated by a hollow green point in Fig. 8-42). At t=59 ms, this front which reached the recirculation zone of injector 180 manages to obtain ignition in this injector. For 59<t<66 ms the flame front advances downstream, first towards the inner radius, later trying a trajectory around the outer radius, but being blocked by the stagnation flow generated by the collision of the jet exit into the outer wall. This instant is depicted in Fig. 8-44. The
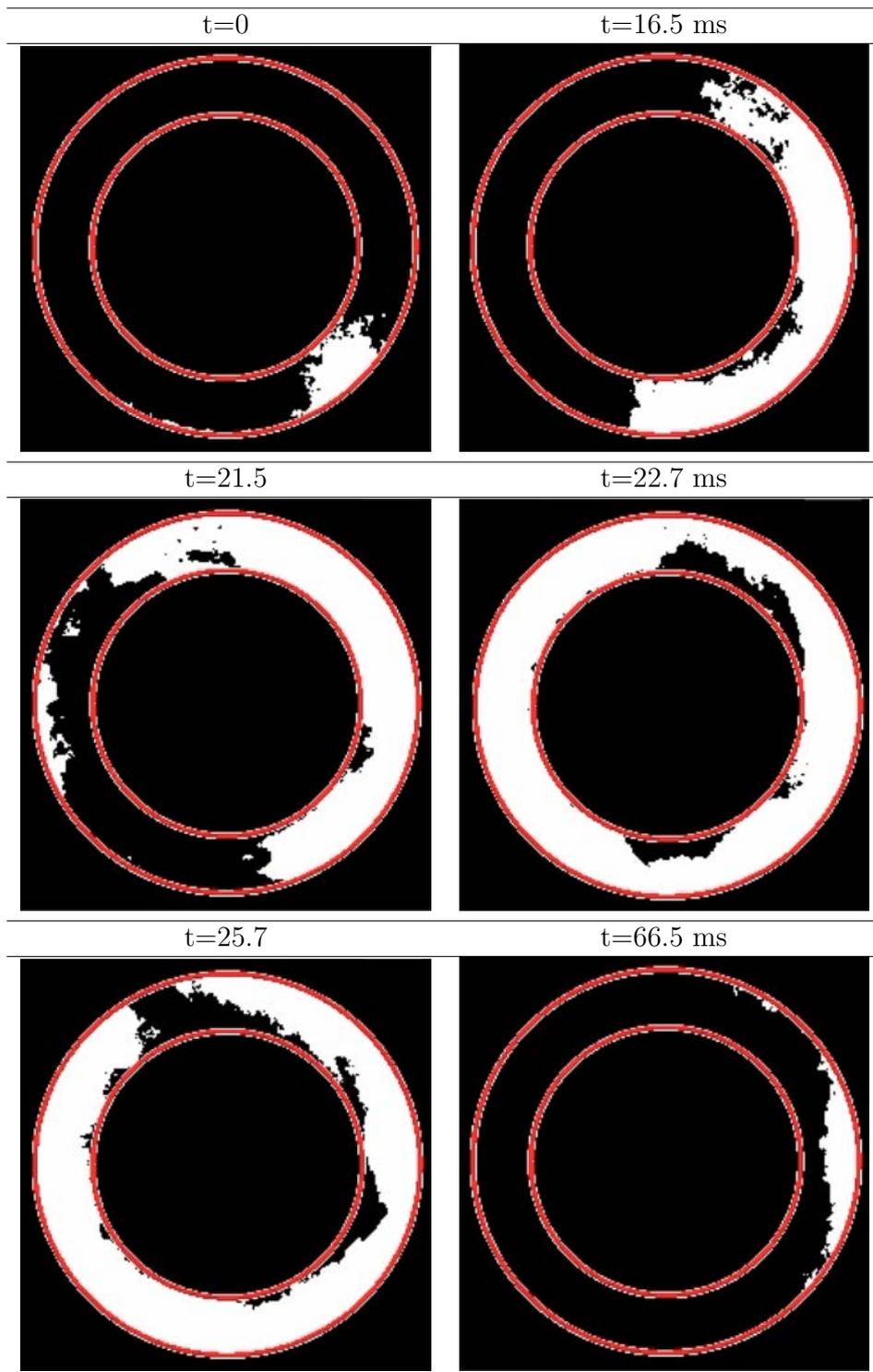
Figure 8-37: Direct visualization images after a binary edge detection process for case $\alpha = 0° \; \phi = 0.7$ (Courtesy of Yi-Hao Kwah (NTNU))
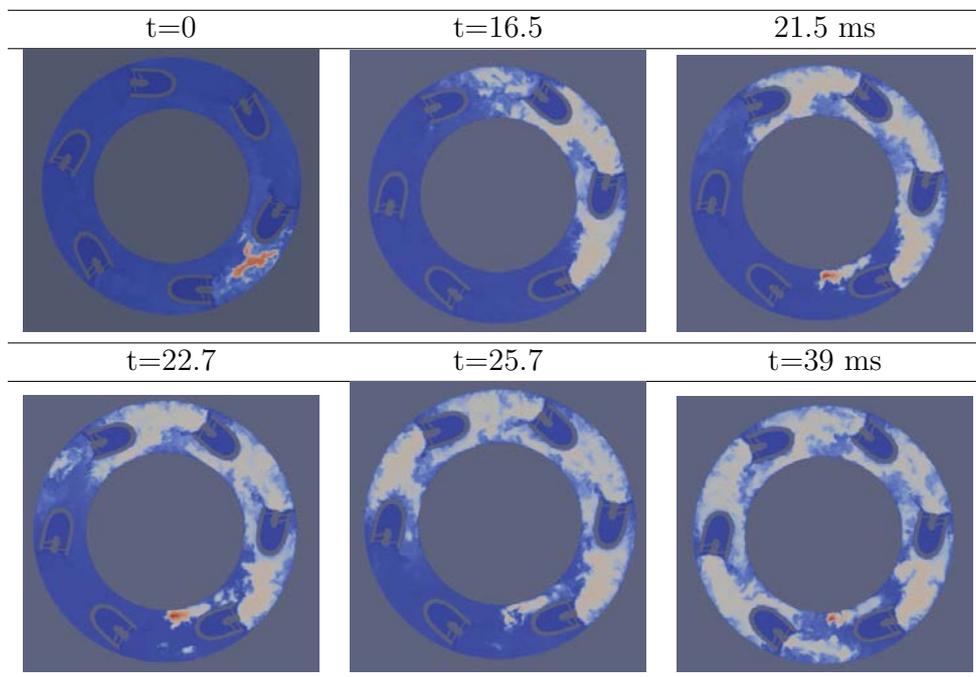
Figure 8-38: Planar cut at swirler axis with temperature contours for case $\alpha = 0°$ $\phi = 0.7$
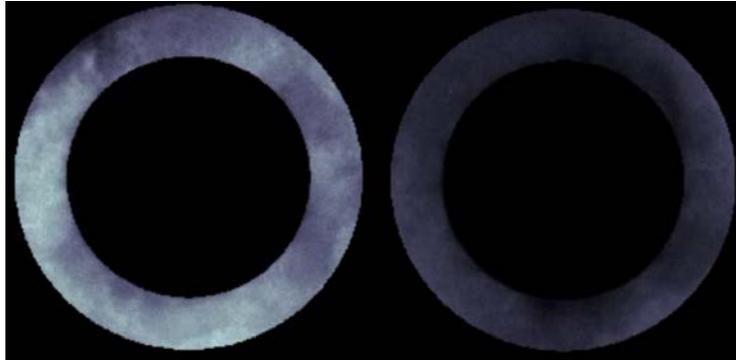
Figure 8-39: (Left) Direct visualization image for case $\alpha = 23°$ and $\phi = 0.7$. (Right) Direct visualization image for case $\alpha = 0°$ and $\phi = 0.7$. Both images taken at the instant of maximum luminosity, the weaker luminosity in the case $\alpha = 0°$ indicates weaker chemical activity (Courtesy of Yi-Hao Kwah (NTNU))
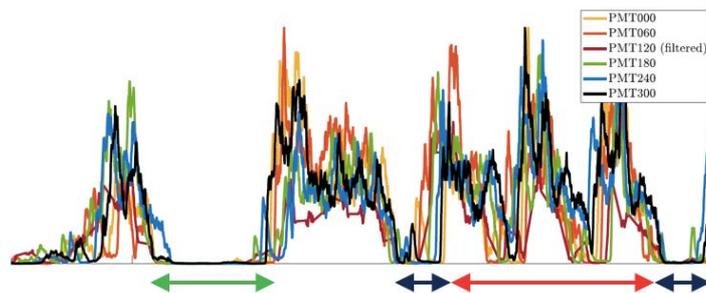
Figure 8-40: Photomultiplier signals for case $\alpha = 0°$ and $\phi = 0.7$ showing oscillating light-around behavior and arrows indicating dissimilar duration of periods of low chemical activity (Courtesy of Yi-Hao Kwah (NTNU))

flame is finally able to propagate downstream along the inner radius (Green arrow that points to the yellow points in Fig. 8-42) helped by the effect of a new hot kernel originated from the igniter due to the third cycle of igniter ($t = 60ms$ which is the start of the third deposition of energy from the igniter).

The flame front continues its propagation in favour of the azimuthal flow (yellow points in Fig. 8-42). This time (after the ignition of injector 180) the flame can propagate radially across the injector exit and reach a region of low velocity marked as the hollow yellow point in Fig. 8-42. Similarly to the previous injector (180), the

235
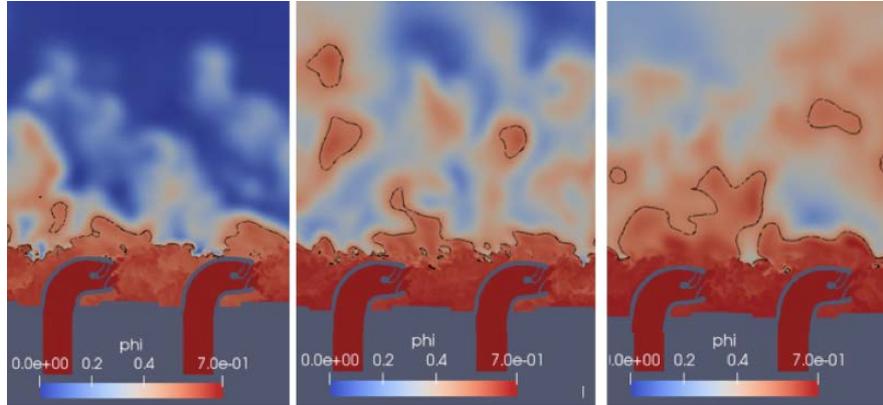
Figure 8-41: Case $\alpha = 0°$ and $\phi = 0.7$ meridional view of the equivalence ratio with a contour line for $\phi = 0.52$ (lower flammability limit) after filling for t=62, 80 and 99 ms. The last image coincides with the first successful injector ignition (injector 180)

flame will manage to propagate upstream through the recirculation zone and ignite the injector 240 at t=67.5 ms. The ensuing flame propagation will be obstructed by the elbow of injector 300, and the leading branch will pass from the external radius to the inner radius twice before continuing its propagation along the inner radius as shown in Fig. 8-45. The chemical activity of this front will not be strong enough to survive the strain effects at the injector 300 exit, and the flame front will retrocede (Yellow arrow towards the purple points in Fig. 8-42). Eventually, the flame regains its propagation along the inner radius and advances downstream reaching the recirculation zone of the previous injector and obtaining its ignition at t=76 ms as shown in Fig. 8-46. Figure 8-47 shows an image at the end of the simulation in which the flame has propagated across all injectors.

This mechanism replicates for the ignition of all injectors: The leading flame front chemical activity is impeded by the strain originated from the high velocity of the injector jet exit and stops its advance. During this time, the temperature of the recirculation zone increases progressively until a reaction zone is formed in the recirculation zone downstream the injector. This reaction zone extends upstream to anchor itself to the injector and the injector is ignited. The resulting flame attempts
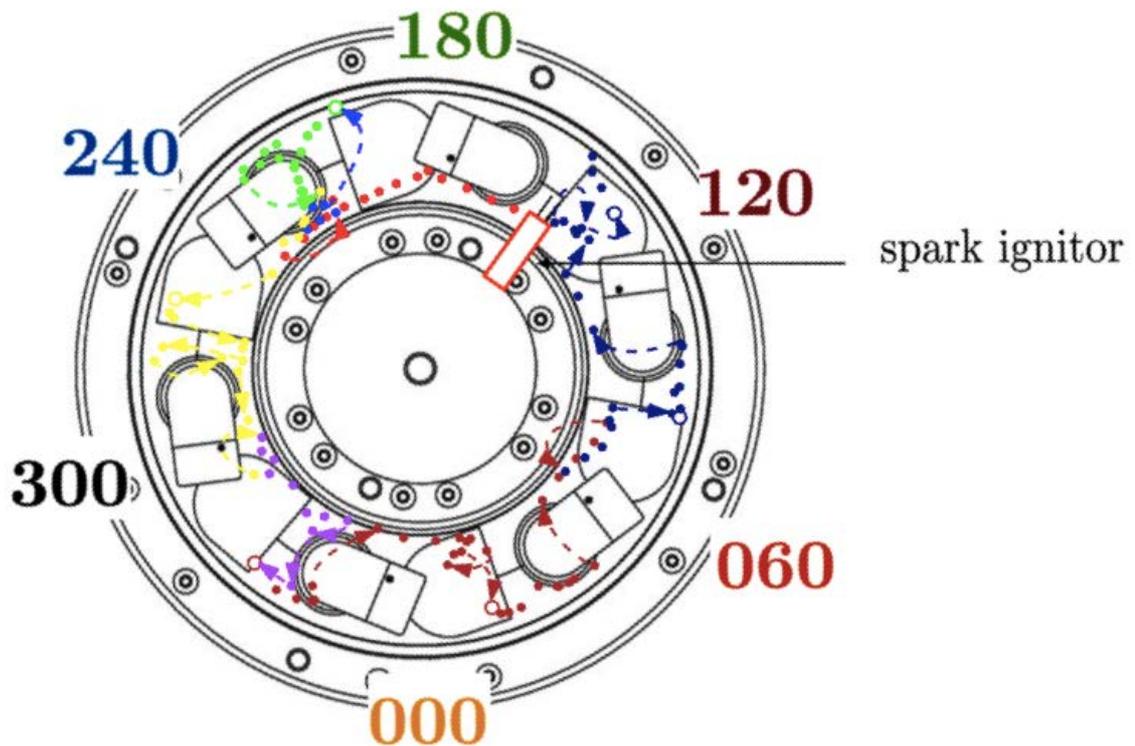
Figure 8-42: Leading point trajectory for case $\alpha = 0°$ and $\phi = 0.7$. Each point represents a 0.5 ms increment. Different colors were introduced to facilitate the understanding of the trajectory and go in this order: red, blue, green, yellow, purple, brown and navy (The arrows usually serve to follow the change of color). The hollow dots represent the location where the flame reaches the recirculation zone of each injector and manages each injector's ignition

to continue growing along the outer radius, but it is obstructed by the stagnation flow from the collision of the jet into the nearby outer wall, and ends up propagating along the inner radius to the next injector. Supporting evidence for the similarity on the ignition at all injectors for case 07 is the fact that the time between ignition of a pair of successive injectors is approximately constant and equal to 10 ms.

The experiment and LES time for the annulus to be covered by reaction zones is identical (≈ 50 ms) and is approximately equal to the residence time of a particle doing one full rotation along the middle radius location (48 ms). For this case a comparison

Figure 8-43: Planar cut at the swirler axis for case $\alpha = 0°$ and $\phi = 0.7$ at t=47.4 ms showing the tangential velocity (m/s) and a heat release contour at 1e6 W/m^3. Injector location marked with numbers and igniter with an arrow.

of sector ignition times is not possible since the signal from the photomultipliers in the experiments implies that the ignition is not stable and a reliable ignition time cannot be identified. Therefore only the LES sector ignition times are reported in Table 8.5.

Table 8.5: Sector (indicated by its angle) ignition times in ms for case $\alpha = 0°$ and $\phi = 0.7$ t=0 is the start of the fuel filling into the chamber

	180	240	300	0	60	120
LES	61	67.6	76	87	97	107

Figure 8-48 contains the temporal heat release evolution. For 0<t<60 ms there are three unsuccessful sparking processes whose longevity increases as the chamber is filled with more fuel. For 61<t<73 ms there is a linear increase in heat release which coincides with the ignition of injectors 180 and 240. For 73<t<76 ms, the heat release ceases to increase, which may be due to the difficulties in igniting injector 300. After injector 300 is ignited, the heat release regains its positive slope, slowing down slightly near the time for ignition of injector 0. Between the ignition of injector 0 and 60 the heat release decreases slightly, again due to the local flame quenching due to the jet exit from injector 60. Once the injector 60 ignites the heat release resumes its ascent until injector 180 ignites.

238

Figure 8-44: Planar cut at the swirler axis for case $\alpha = 0°$ and $\phi = 0.7$ at t=64.5 ms showing the tangential velocity (m/s) and a heat release contour at 1e6 W/m^3. Injector location marked with numbers and igniter with the black dot.

For case 07, the "thrust-effect" originated from the successful ignition of an injector has a small effect in the acceleration of the propagation of the following flames. This may be due to the already mentioned fact that, for the case $\alpha = 0$ geometry, the flame growth from one injector is obstructed by the next injector elbow. However, a small increase in tangential velocity which affects the region above the injectors can be observed in Fig. 8-49.

8.4   Analysis of Flame Speed Terms Contribution

An analysis following that of [111] was introduced to study the evolution of the terms which compose the flame speed. As shown in the derivation by [102], the flame absolute velocity averaged over the resolved surface by LES $\{S_a\}_{res}$ can generally be written as:

$$\{S_a\}_{res} = \underbrace{\frac{\rho_u}{\rho_b} S_c^\Delta}_{\text{Term A}} - \underbrace{\frac{\dot{m}_b^{out}}{\rho_b A_{res}}}_{\text{Term B}} \tag{8.2}$$

239
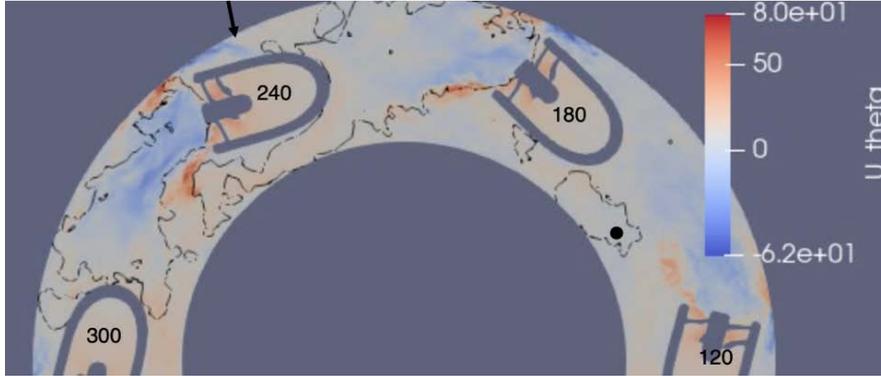
Figure 8-45: Planar cut at the swirler axis for case $\alpha = 0°$ and $\phi = 0.7$ at t=72.4 ms showing the tangential velocity (m/s) and a heat release contour at 1e6 W/m^3. Injector location marked with numbers and igniter with the black dot.

$$A_{res} = \int_{V_{cc}} |\nabla \tilde{c}| dV \qquad (8.3)$$

where ρ_u is the density of the fresh gases, ρ_b the density of the burnt gases, S_c^Δ is the consumption speed obtained in LES, $\dot{m}_b^{out}$ are the portion of mass flow composed of burnt gases exiting the chamber, and c is the progress variable based on the fuel species ($c = 1 - Y/Y_{max}$). It is to be noted that, in this thesis, the resolved surface is calculated in Eq. 8.3 while [111] uses a reference surface equal to a meridional section of the chamber.

The results are plotted in Fig. 8-50 and show that the term A (consumption) rises faster than term B (evacuation of gases at the outlet). This is in correspondence with experiments, where a flame develops in a spiral trajectory along the annulus, igniting all the injectors and thus consuming the mixture without producing a substantial amount of burnt gases at the outlet. This is shown graphically in Fig. 8-51 and 8-52. Consequently, in the NTNU SCT bench, the absolute velocity S_a computed as the difference between term A and B, increases during light-around phase and a constant velocity is not reached. On the other hand, the MICCA-spray calculations in [111],

The flame front which had been quenched by the injector 300 exit jet has managed to reach the recirculation zone of this injector and propagates upstream igniting injector 300 at t=76 ms
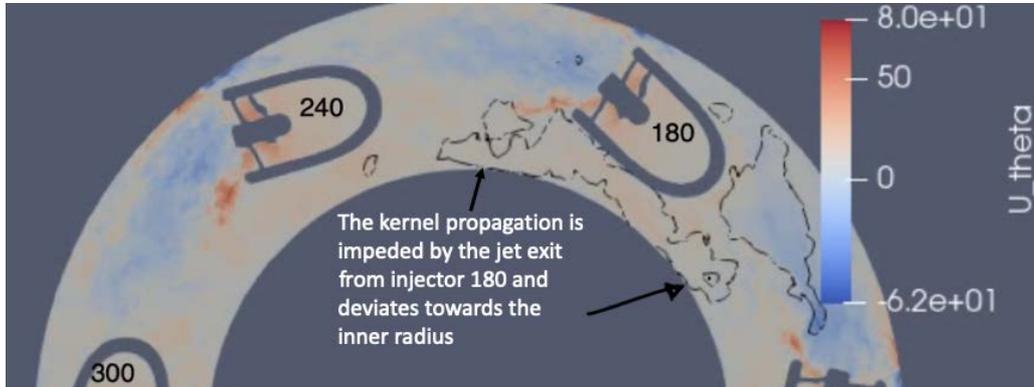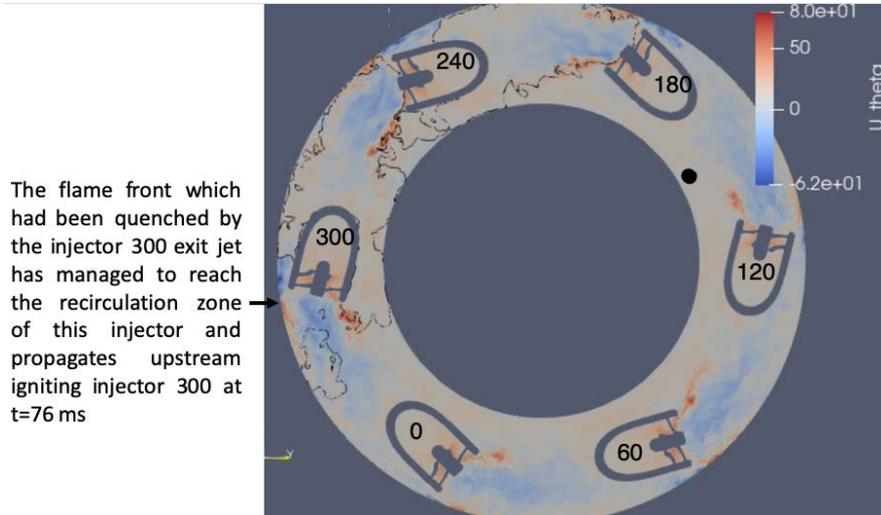
Figure 8-46: Planar cut at the swirler axis for case $\alpha = 0°$ and $\phi = 0.7$ at t=75.7 ms showing the tangential velocity (m/s) and a heat release contour at 1e6 W/m^3. Injector location marked with numbers and igniter with the black dot.

which features a longer light-around process (two to three times that of NTNU SCT), the greater duration of the light-around process permits that the consumption term (term A) and outlet flux (term B) reach a balance and a constant value of absolute velocity is reached in the later stages of the light-around process. The magnitude of S_a obtained from this analysis coincides with the experimental observation: case A features an absolute flame speed of ≈ 2 m/s ($t_{light-around} \approx 15$ ms). On the other hand, case B features $S_a \approx 1$ m/s ($t_{light-around} \approx 25$ ms) and, lastly, case C with $S_a \approx 0.5$ m/s.

This study shows that, in this SCT combustor for the $\alpha = 23$ degrees configuration, the flame kernel is convected rapidly and ignites all the injectors before the flame fully grows downstream each injector. This is different from traditional combustors where the flame first stabilizes downstream each injector before propagating to a neighbouring injector.
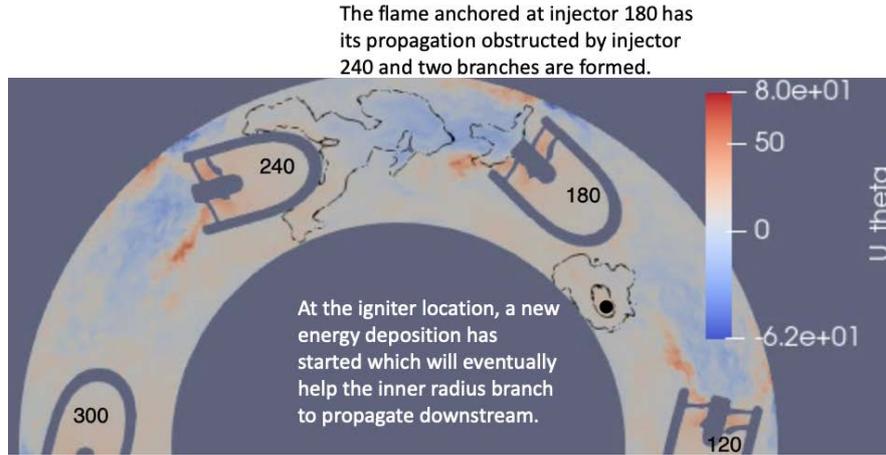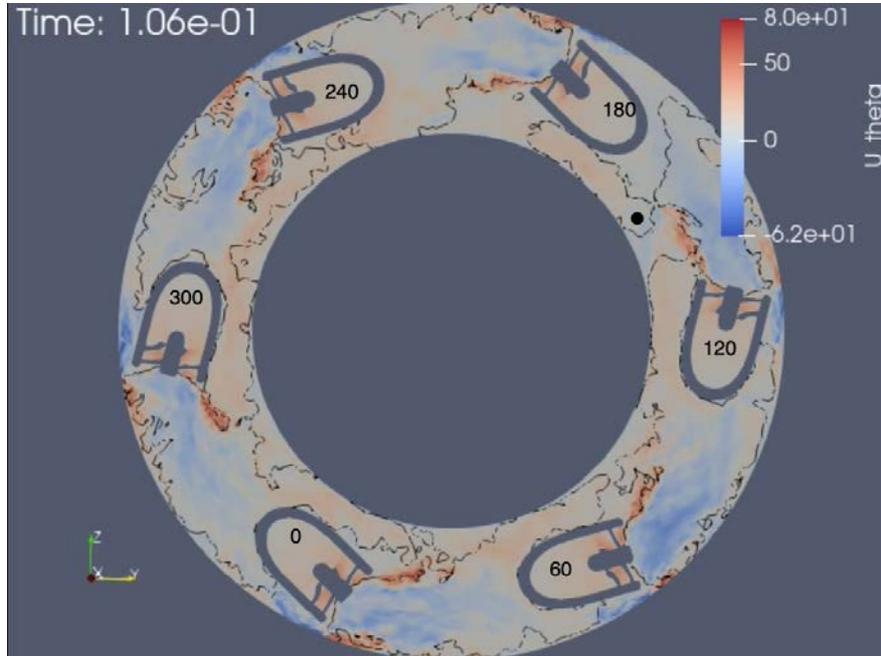
Figure 8-47: Planar cut at the swirler axis for case $\alpha = 0°$ and $\phi = 0.7$ at t=106 ms showing the tangential velocity (m/s) and a heat release contour at 1e6 W/m^3. Injector location marked with numbers and igniter with the black dot.

8.5   Conclusion

This chapter includes the first presentation of experiments and LES for ignition in the NTNU bench equipped with spinning combustion technology. The computational results have shown that the LES computations using the energy deposition model, the dynamic formulation of efficiency in [31] with the model values tested and verified in the Radius chamber experiment simulation (chapter 6) and the analytically reduced chemistry in [76] are able to reproduce the main features observed in the experiments. In particular, the computation of case with $\alpha = 23°$ and $\phi = 1$ shows the preferential trajectory along the inner radius and the shortest time for light-around. On the other hand, the computation of case $\alpha = 23°$ and $\phi = 0.7$ display light-around advancing in clockwise and anti-clockwise directions, and a longer time for light-around that the case with $\phi = 1$. Finally, the computations of case $\alpha = 0°$ and $\phi = 0.7$ exhibit the
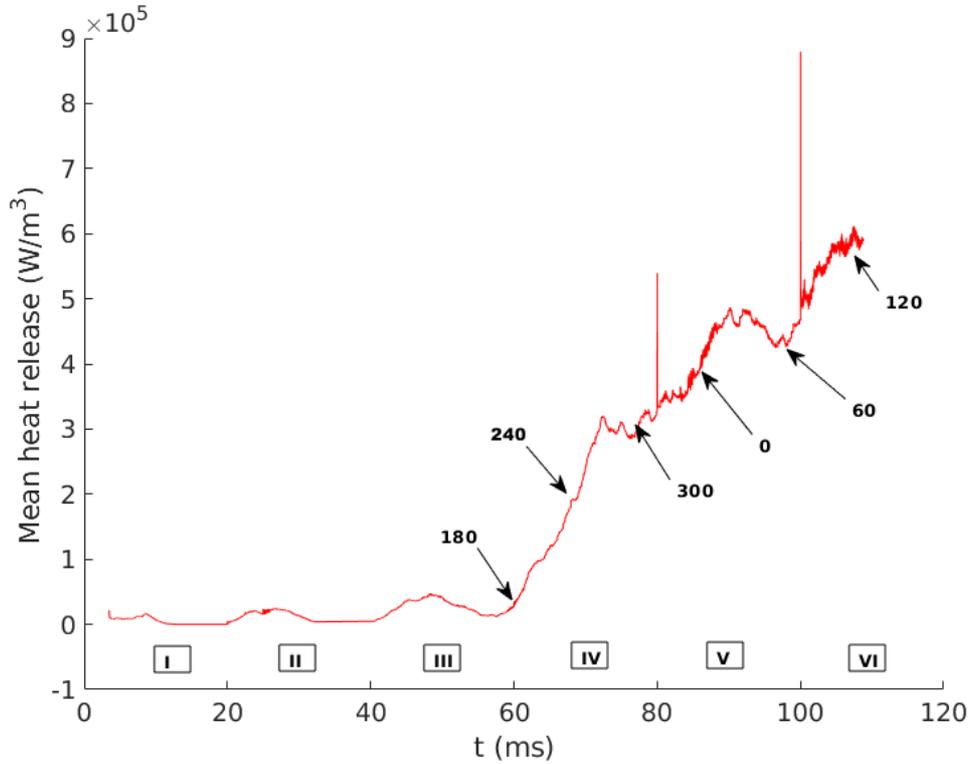
Figure 8-48: Temporal heat release evolution for case $\alpha = 0°$ and $\phi = 0.7$. The arrows indicate the instant for injector ignition. The time origin coincides with the first sparking from the igniter, which follows a cycle of period 20 ms as marked by the roman numbers along the x-axis. The spikes at t=80 and 100 ms are caused by the igniter spark start of periods V and VI

slowest flame propagation. The different computations constitute only one instance of the conditions encountered in the experiments and, ideally, several instances of each LES also varying the fuel content in the chamber at the start of the spark should be included.
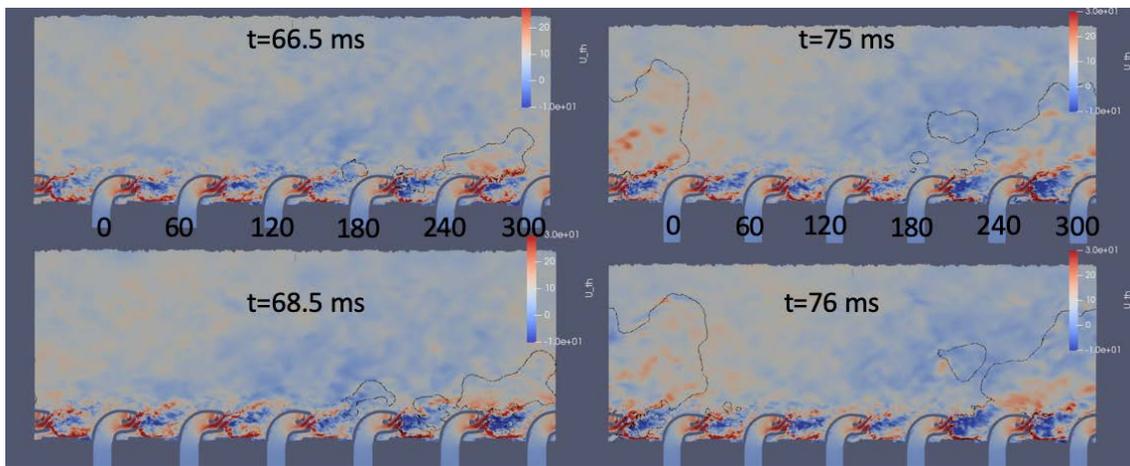
Figure 8-49: . Projection of annular cut at r=85 mm (mid-radius) for case $\alpha = 0°$ and $\phi = 0.7$ showing tangential velocity (m/s). The instants correspond to the ignition of injector 240 (left) and injector 300 (right) and show a weak contribution of the bulk flow expansion for case 07
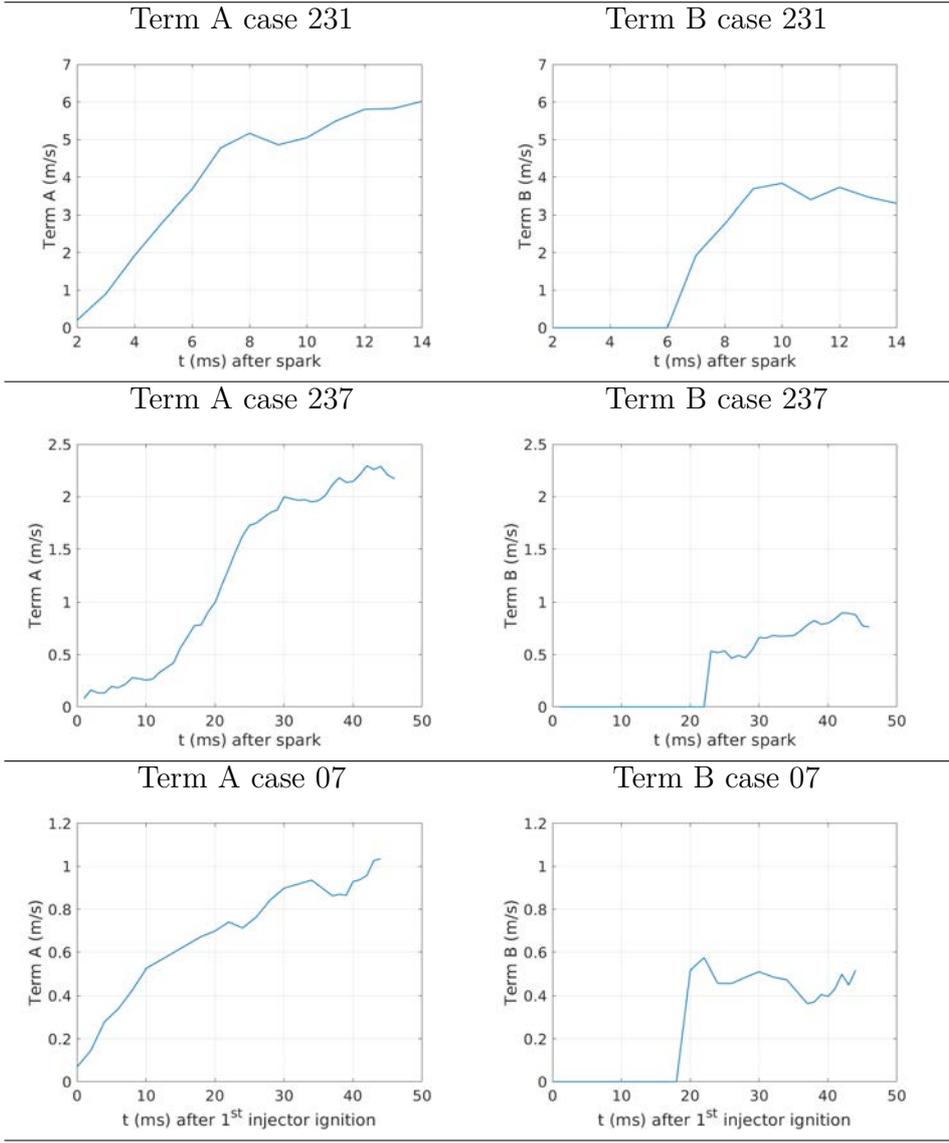
Figure 8-50: Comparison of term contribution
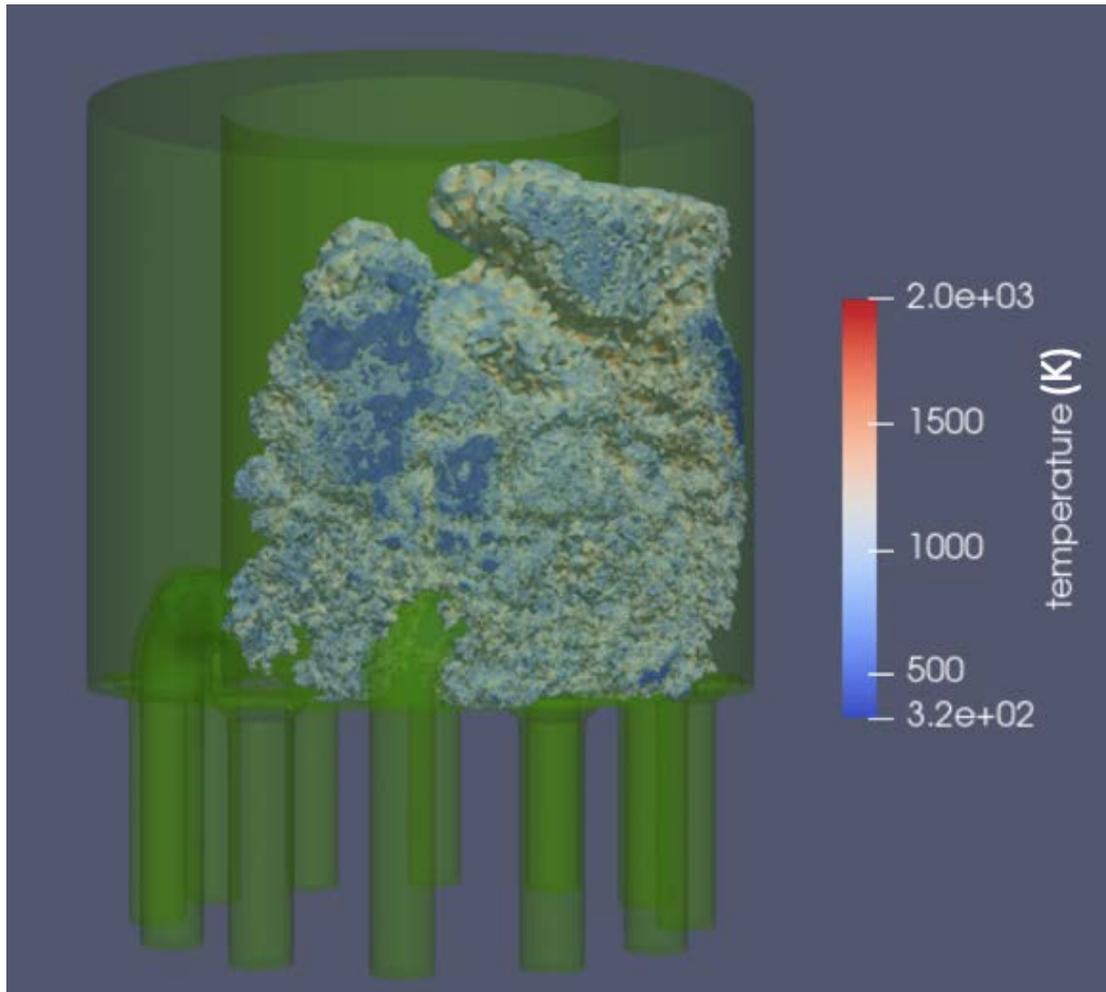
Figure 8-51: Isosurface of heat release at 5e6 W/m^3 for case $\alpha = 23°$ and $\phi = 1$ (Case 231). The surface of the consuming reactants covers three injectors while the burnt gases have not arrived to the outlet yet.
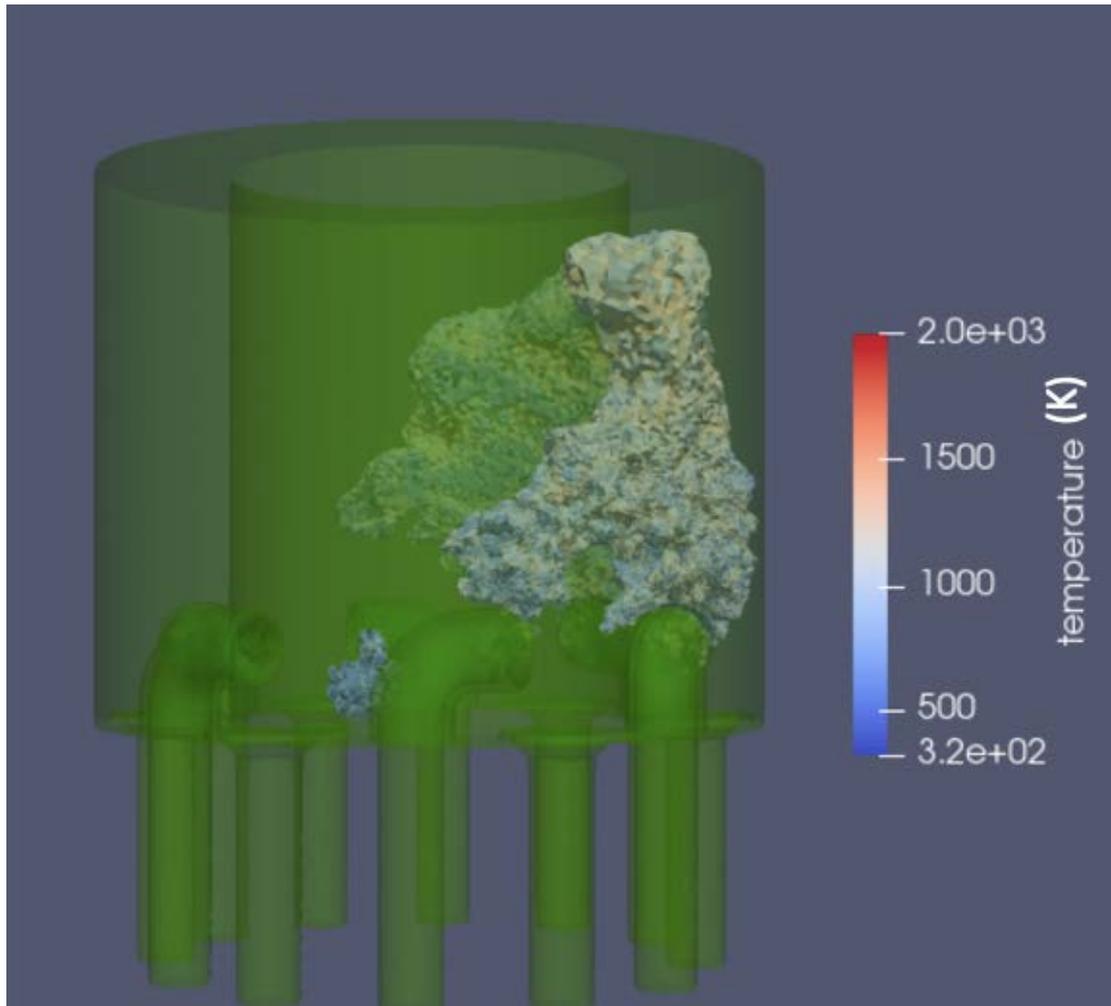
Figure 8-52: Isosurface of heat release at 5e6 W/m^3 for case $\alpha = 23°$ and $\phi = 0.7$ (Case 237). As for the case 231, the surface of the consuming reactants covers three injectors while the burnt gases have not arrived to the outlet yet highlighting the difference between terms A and B in the absolute velocity contribution analysis.

Chapter 9

General Conclusions and Future Perspectives

This work has introduced numerical simulations of experimental setups which emulate the physical processes in spinning combustion technology engines and actual aeronautical igniters. Firstly, computations in a calorimetry chamber were made and compared to Schlieren images to evaluate several techniques to model the effect of the igniter on the fluid during the time of energy deposition. The model presented has the novelty of incorporating detailed temporal power measurements of the igniter. The chosen ignition model was applied to a cylindrical chamber setup (Radius chamber) which permitted the comparison of LES predictions to temporal pressure signals and Schlieren images of the flame kernel growth process towards a fully developed flame. This study demonstrated the ability of the dynamic formulation of the wrinkling factor [31] to model transient effects. In order to study the design space of ignition using liquid fuel, an academic configuration consisting of a pin-pin electrode was analyzed under a numerous variation of liquid fuel characteristics (equivalence ratio, droplet size, size distribution and preevaporation content). Successful ignition cases corresponded to the ones in which the flame was able to remain compact to minimize

heat losses and envelop a large number of droplets. It was determined that there was a correspondence between the ignition success in this setup and a non-dimensional number composed of the ratio of the droplet evaporation time to the drag relaxation. Finally, a 360° annular configuration which features the same level of azimuthal mean flow as engines equipped with spinning combustion technology (NTNU SCT bench) was modelled using the same models as the ones in the Radius Chamber case. The results showed that the time for ignition was well captured for a range of operating conditions and injector configurations.

The main outcomes of this thesis are:

1. The energy deposition model using a static deposition zone can be used to model the energy release of aeronautical igniters for times after the breakdown phase until the full kernel formation.

2. The generic sensor for the thickened flame model recently developed by Rochette [118] is able to detect a propagating flame and can therefore be used in ignition studies.

3. For the case of ignition at three operating conditions representative of actual aeronautical combustors, the use of the dynamic formulation of the wrinkling factor [31] has shown that its exponent is different and lower than the value assumed for the static version of the wrinkling factor [32].

4. Analytically reduced chemistry, and more particularly the 19 species methane-air chemistry model utilized, is an effective approach to study ignition processes. In order to suppress numerical oscillations of species associated to small time scales, an implicitation procedure as detailed in section 6.2.4 may be necessary in some cases.

Future work would benefit of joint experimental-numerical studies on simplified configurations featuring chamber cooling by multi-perforated plates, liquid fuels and

aeronautical igniters. These three factors are envisaged to modify the trajectory and survivability of flame kernels and would increase the resemblance with Safran Helicopter products. Detailed experimental measurements of the shape of the energy deposition zone during the sparking phase as well as the temporal power profile and the delay between the fuel injection and sparking start would benefit future ignition studies.

Appendix A
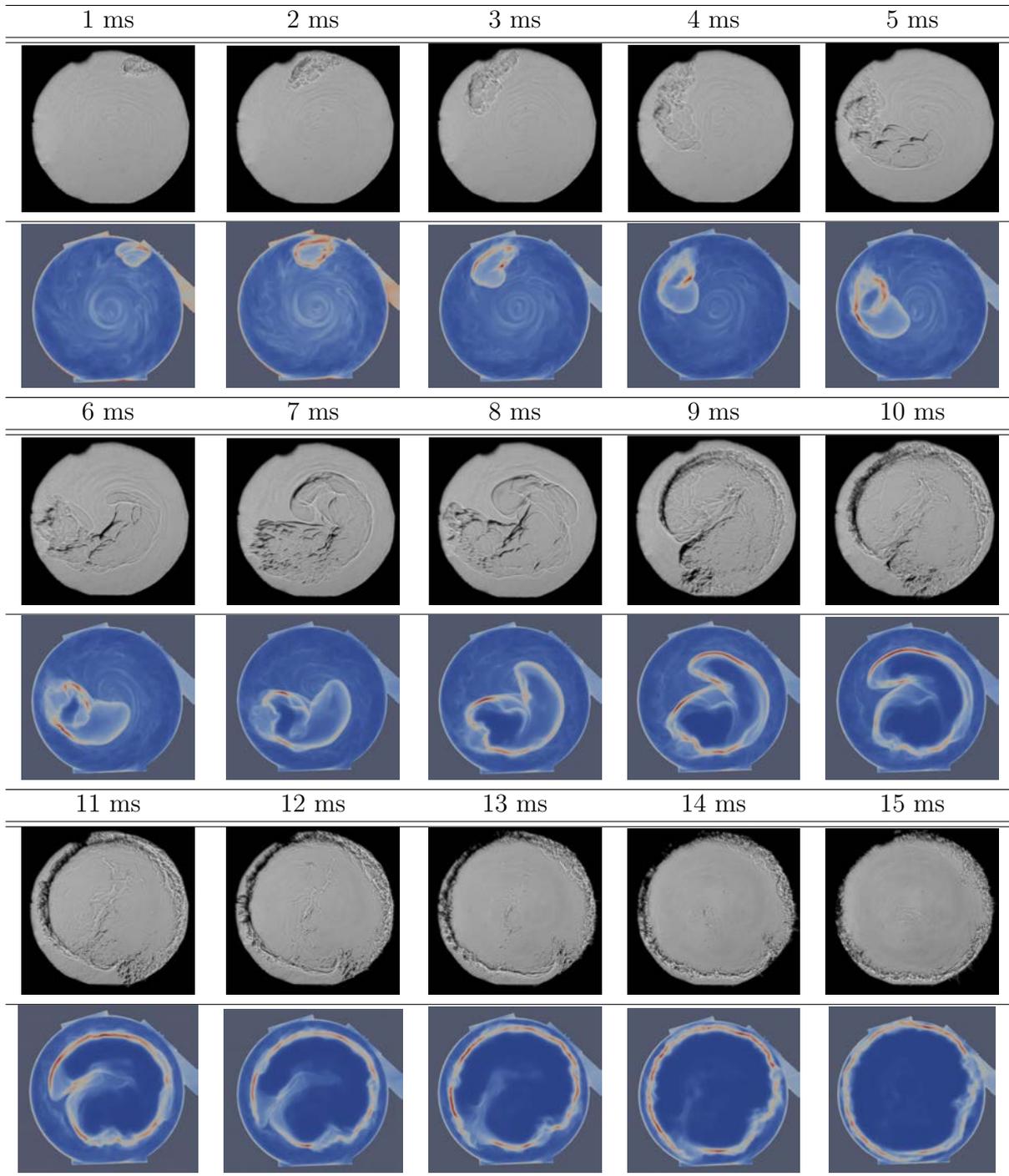
Figure A-1: Comparison of images with LOS integrated density gradient images from LES for case A ($p_{ini} = 1bar$, $t_{delay} = 5ms$) at various times after spark. Dynamic efficiency formulation

| 1 ms | 2 ms | 3 ms | 4 ms | 5 ms |

| 6 ms | 7 ms | 8 ms | 9 ms | 10 ms |

| 11 ms | 12 ms | 13 ms | 14 ms | 15 ms |
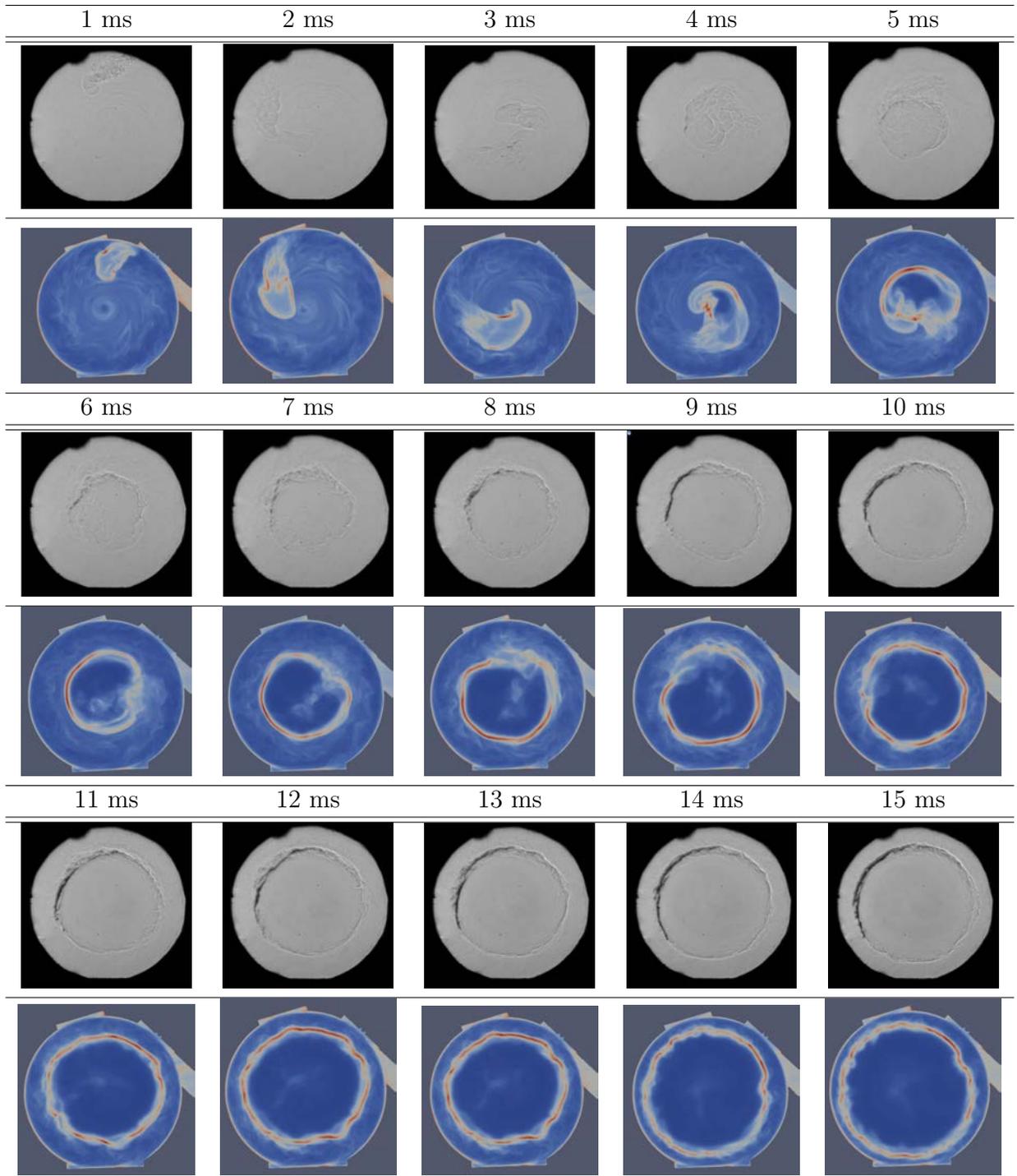
Figure A-2: Comparison of images with LOS integrated density gradient images from LES for case B ($p_{ini} = 0.5bar$, $t_{delay} = 5ms$) at various times after spark. Dynamic efficiency formulation
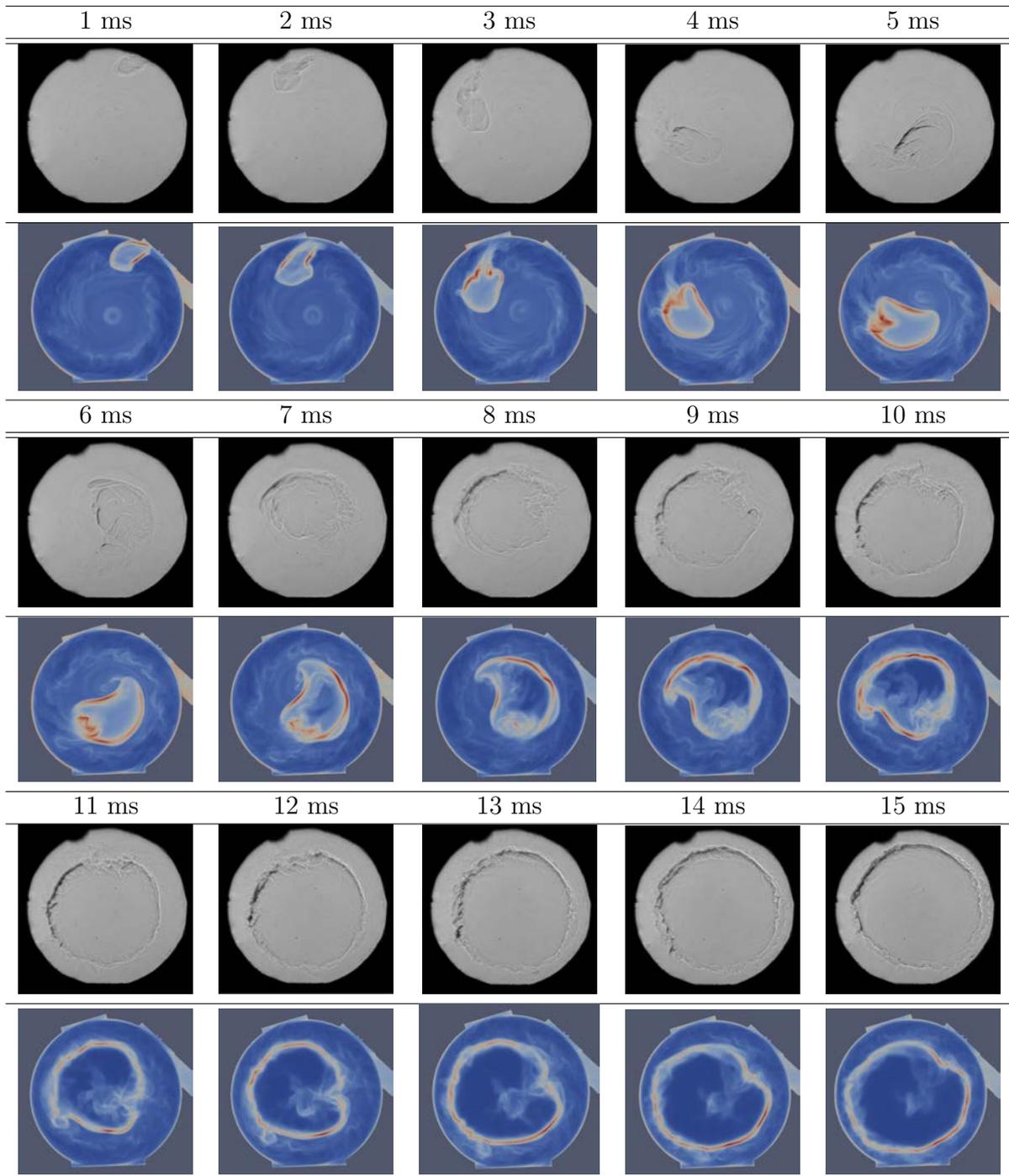
Figure A-3: Comparison of images with LOS integrated density gradient images from LES for case C ($p_{ini} = 0.5bar$, $t_{delay} = 30ms$) at various times after spark. Dynamic efficiency formulation
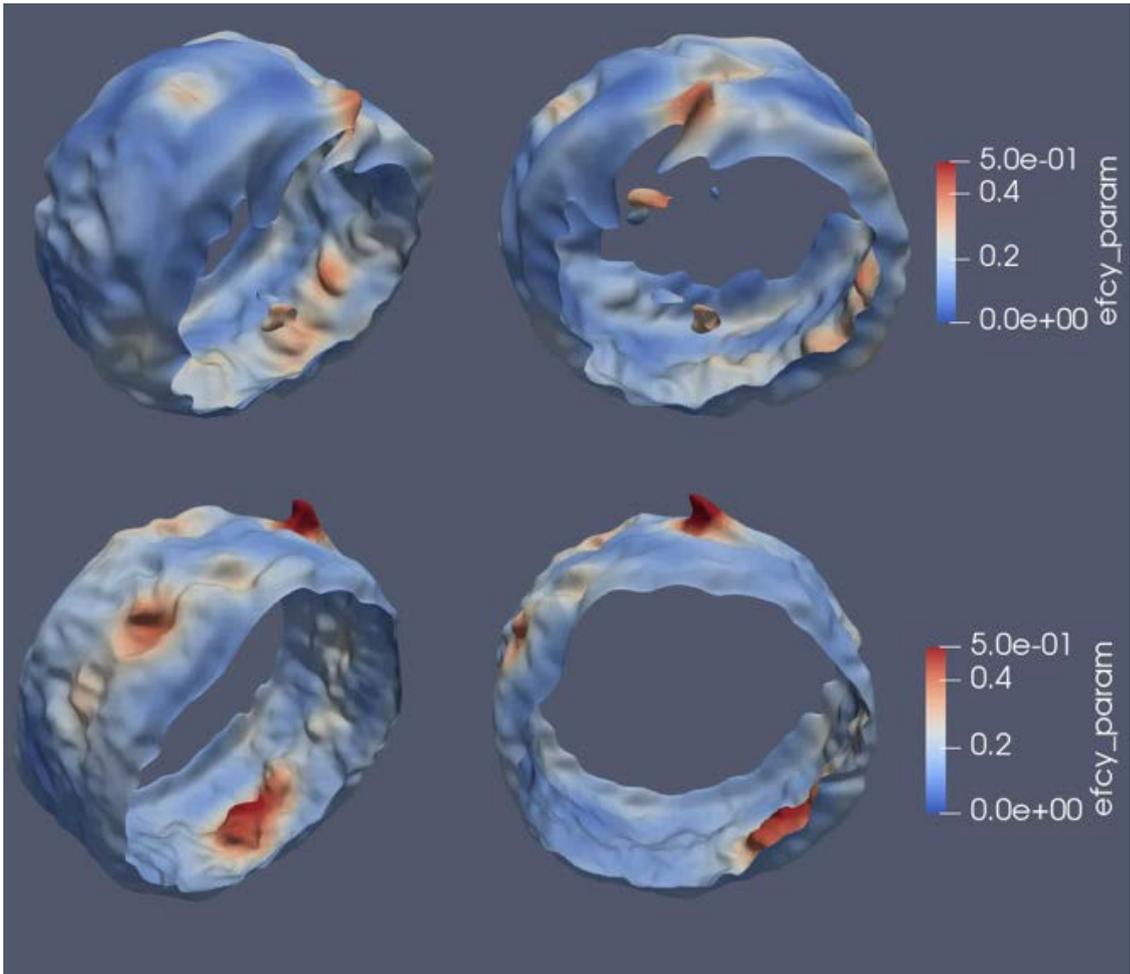
Figure A-4: Case B lateral and frontal views of β for an isosurface of q=0.5 at t=15 ms (up) and t=20 ms after spark (bottom) showing that, on average, $\beta < 0.5$ for these conditions

Figure A-5: Evolution of β PDF for an isosurface of q=0.5, Case A ($p_{ini} = 1bar$, $t_{delay} = 5ms$) for various times after spark
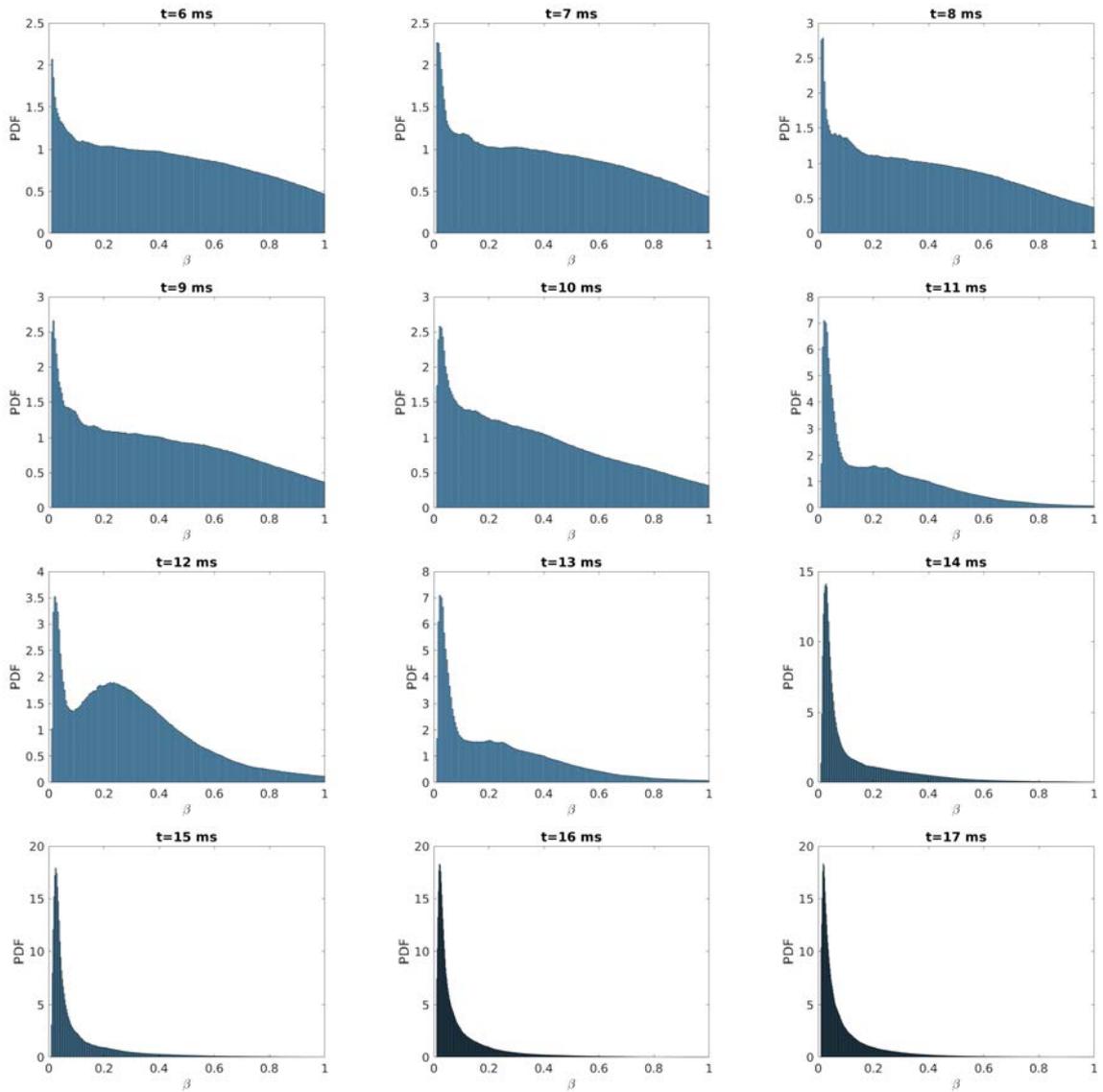
Figure A-6: Evolution of β PDF for an isosurface of q=0.5, Case B ($p_{ini} = 0.5bar$, $t_{delay} = 5ms$) for various times after spark
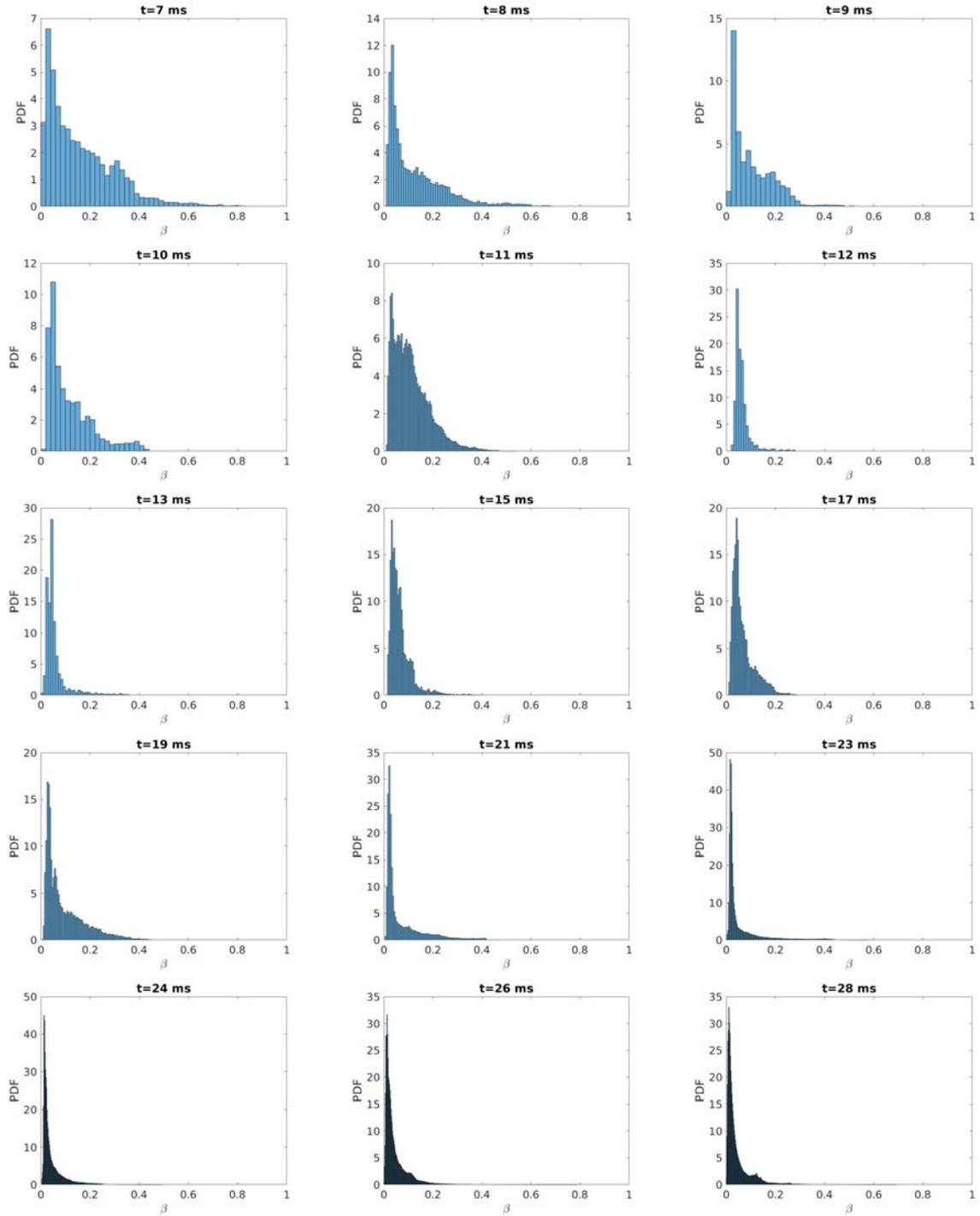
Figure A-7: Evolution of β PDF for an isosurface of q=0.5, Case C ($p_{ini} = 0.5bar$, $t_{delay} = 30ms$) for various times after spark
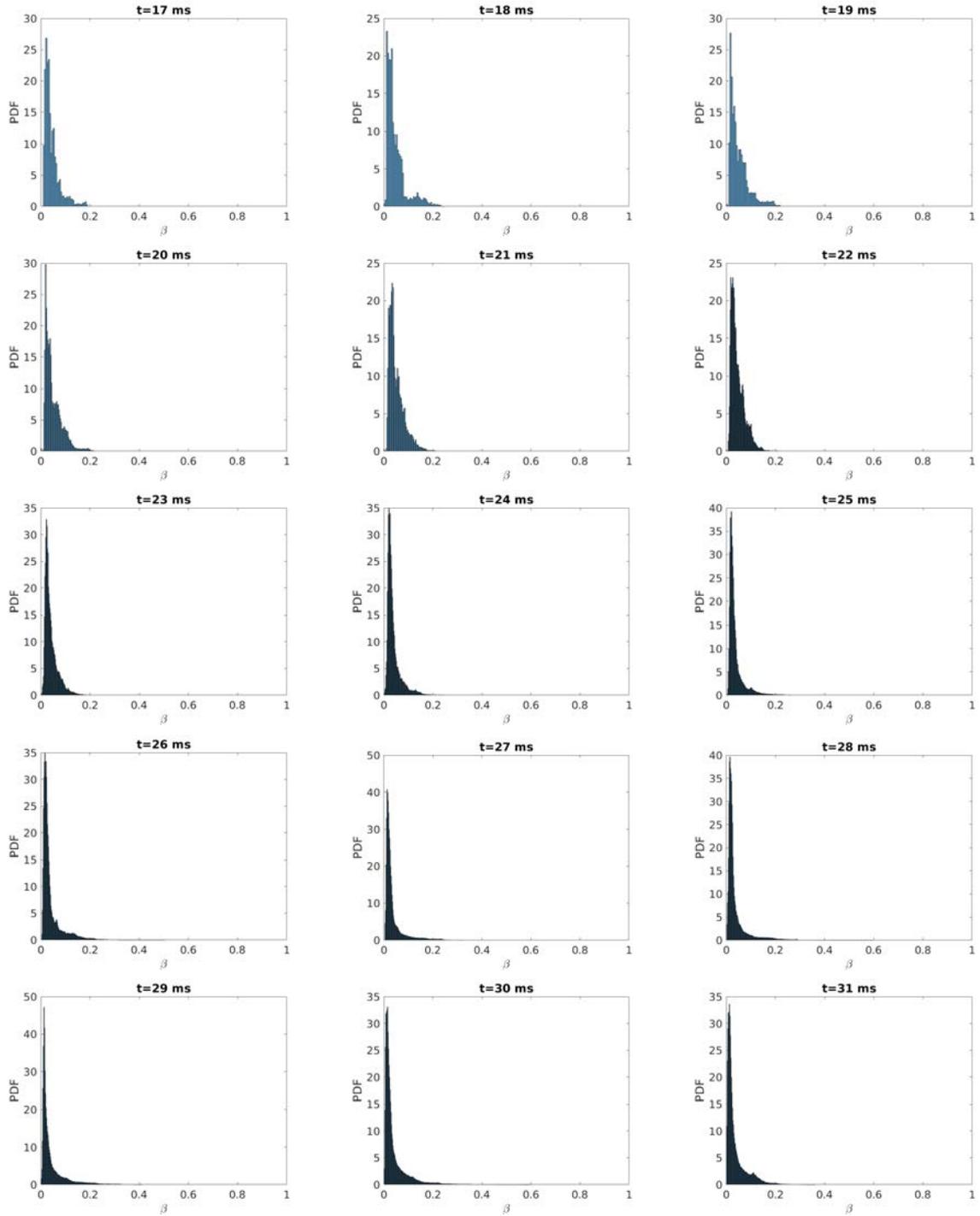
Bibliography

[1] Helicopter: hybrid propulsion in all its forms. `https://www.safran-group.com/news/helicopter-hybrid-propulsion-all-its-forms-2021-12-07`. Accessed: 2021-12-27.

[2] Spark plugs. Technical Report December, Popular Mechanics, 1965.

[3] J. Abraham and H. Reddy. Influence of turbulence–kernel interactions on flame development in lean methane/air mixtures under natural gas-fueled engine conditions. *Fuel*, 103, 2013.

[4] B. Abramzon and W. A. Sirignano. Droplet vaporisation model for spray combustion calculations. *Int. J. Heat and Mass Transfer*, 9:1605–1618, 1989.

[5] S. K. Aggarwal. Review of spray ignition phenomena: present status and future research. *Prog. Energy Combust. Sci.*, 24, 1998.

[6] S. K. Aggarwal and A. Sirignano. Ignition of fuel sprays: deterministic calculations for idealized droplet arrays. *Proc. Combust. Inst.*, (20):1771–1780, 1984.

[7] P. W. Agostinelli. *Assessment of Large Eddy Simulation in the Conjugate Heat Transfer context for engine operability : application to Hydrogen enrichment and Spinning Combustion Technology.* PhD thesis, Université de Toulouse, France - MeGeP Dynamique des Fluides, 2022. phd.

[8] P. W. Agostinelli, Y. H. Kwah, S. Richard, G. Exilard, J. R. Dawson, L. Gicquel, and T. Poinsot. Numerical and experimental flame stabilization analysis in the new spinning combustion technology framework. In *ASME Turbo Expo*, London, UK, 2020.

[9] S. F. Ahmed, R. Balachandran, T. Marchione, and E. Mastorakos. Spark ignition of turbulent nonpremixed bluff-body flames. *Combust. Flame*, 151:366–385, 2007.

[10] S.F Ahmed and E. Mastorakos. Spark ignition of lifted turbulent jet flames. *Combust. Flame*, 146:215–231, 2006.

[11] S.F. Ahmed and E. Mastorakos. Correlation of spark ignition with the local instantaneous mixture fraction in a turbulent nonpremixed methane jet. *Combust. Sci. Technol.* , 182, 2010.

[12] K. Annamalai and W. Ryan. Interactive processes in gasification and combustion. part I: liquid drop arrays and clouds. *Prog. Energy Combust. Sci.* , 18(2):221–295, 1992.

[13] D. R. Ballal and A. H. Lefebvre. The influence of flow parameters on minimum ignition energy and quenching distance. *Proc. Combust. Inst.* , 15:1473–1481, 1974.

[14] D. R. Ballal and A. H. Lefebvre. Ignition and flame quenching in flowing gaseous mixtures. *Proc. R. Soc. Lond. A* , 357:163–181, 1977.

[15] D. R. Ballal and A. H. Lefebvre. Ignition and flame quenching of flowing heterogeneous fuel-air mixtures. *Combust. Flame*, 35:155–168, 1979.

[16] D. R. Ballal and A. H. Lefebvre. Flame propagation in heterogeneous mixtures of fuel droplets, fuel vapor and air. *Proc. Combust. Inst.* , 18:321–327, 1981.

[17] D. R. Ballal and A. H. Lefebvre. A general model of spark ignition for gaseous and liquid fuel-air mixtures. In *Eighteenth Symposium (International) on Combustion*, pages 1737–1747, 1981.

[18] D. Barre. *Numerical simulation of ignition in aeronautical combustion chambers.* PhD thesis, Institut National Polytechnique de Toulouse, 2014.

[19] D. Barre, L. Esclapez, M. Cordier, E. Riber, B. Cuenot, G. Staffelbach, B. Renou, A. Vandel, L.Y.M. Gicquel, and G. Cabot. Flame propagation in aeronautical swirled multi-burners: Experimental and numerical investigation. *Combust. Flame*, 161(9):2387 – 2405, 2014.

[20] C. J. Benito-Parejo. *Experimental characterization of electrical discharges and formation of the ignition kernel. Application to the study of performances of aeronautical igniters.* PhD thesis, Ecole Nationale Superieure De Mecanique et d'Aerotechnique, 2019.

[21] R. W. Bilger, S. H. Starner, and R. J. Kee. On reduced mechanisms for methane-air combustion in nonpremixed flames. *Combust. Flame*, 80:135–149, 1990.

[22] A. D. Birch, D. R. Brown, and M. G. Dodson. Ignition probabilities in turbulent mixing flows. In *18th Symposium (Int.) on Combustion*, pages 1775–1780. The Combustion Institute, Pittsburgh, 1981.

[23] M. Boileau. *Simulation aux grandes échelles de l'allumage diphasique des foyers aéronautiques.* PhD thesis, INP Toulouse, 2007.

262

[24] K. N. C. Bray and J. B. Moss. A closure model for the turbulent premixed flame with sequential chemistry. *Combust. Flame*, 30:125–131, 1977.

[25] J. Buckmaster and G. Ludford. *Theory of laminar flames.* Cambridge University Press, 1982.

[26] W. Bush and F. Fendell. Asymptotic analysis of laminar flame propagation for general lewis numbers. *Combust. Sci. Technol.* , 1:421, 1970.

[27] S. M. Candel and T. Poinsot. Flame stretch and the balance equation for the flame surface area. *Combust. Sci. Technol.* , 70:1–15, 1990.

[28] J. Carmona. *Modelisation des phenomenes diphasiques dans des injecteurs aeronautiques de type Airblast.* PhD thesis, Institut National Polytechnique de Toulouse, 2021.

[29] N. Chakraborty and E. Mastorakos. Direct numerical simulations of localised forced ignition in turbulent mixing layers: The effects of mixture fraction and its gradient. *Flow, Turb. and Combustion* , 80, 2008.

[30] N. Chakraborty, E. Mastorakos, and R. S. Cant. Effects of turbulence on spark ignition in inhomogeneous mixtures: A direct numerical simulation(DNS) study. *Combust. Sci. Technol.* , 179(1-3):293–317, 2007.

[31] F. Charlette, D. Veynante, and C. Meneveau. A power-law flame wrinkling model for les of premixed turbulent combustion part II: Dynamic formulation. *Combust. Flame*, 131:181–197, 2002.

[32] F. Charlette, D. Veynante, and C. Meneveau. A power-law wrinkling model for LES of premixed turbulent combustion: Part I - non-dynamic formulation and initial tests. *Combust. Flame*, 131:159–180, 2002.

[33] H. H. Chiu, H. Y. Kim, and E. J. Croke. Internal group combustion of liquid droplets. In *19th Symp. (Int.) on Combustion*, pages 971–980. The Combustion Institute, Pittsburgh, 1982.

[34] P. Clavin and F. A. Williams. Effects of molecular diffusion and of thermal expansion on the structure and dynamics of premixed flames in turbulent flows of large scales and low intensity. *J. Fluid Mech.* , 116:251–282, 1982.

[35] O. Colin, F. Ducros, D. Veynante, and T. Poinsot. A thickened flame model for large eddy simulations of turbulent premixed combustion. *Phys. Fluids* , 12(7):1843–1863, 2000.

[36] F. Collin-Bastiani. *Modeling and Large Eddy Simulation of Two-Phase Ignition in Gas Turbines.* PhD thesis, Institut National Polytechnique de Toulouse, 2019.

[37] F. Collin-Bastiani, O. Vermorel, C. Lacour, B. Lecordier, and B. Cuenot. DNS of spark ignition using Analytically Reduced Chemistry including plasma kinetics. *Proc. Combust. Inst.* , 37(4):5057–5064, 2019.

[38] M. Cordier, A. Vandel, G. Cabot, B. Renou, and A. M. Boukhalfa. Laser-induced spark ignition of premixed confined swirled flames. *Combust. Sci. Technol.* , 185, 2012.

[39] C. Crowe, M. Sommerfeld, and Y. Tsuji. *Multiphase Flows with Droplets and Particles.* 1998.

[40] B. Cuenot and T. Poinsot. Effects of curvature and unsteadiness in diffusion flames. implications for turbulent diffusion flames. *Proc. Combust. Inst.* , 25:1383–1390, 1994.

[41] A. M. Danis, I. Namer, and N. P. Cernansky. Droplet size and equivalence ratio effects on spark ignition of monodisperse n-heptane and methanol sprays. *Combust. Flame*, 74, 1988.

[42] P. M. de Oliveira. *Ignition and propagation mechanisms of spray flames.* PhD thesis, University of Cambridge, 2019.

[43] P. M. de Oliveira and E. Mastorakos. Mechanisms of flame propagation in jet fuel sprays as revealed by OH/fuel planar laser-induced fluorescence and OH * chemiluminescence. *Combust. Flame*, 206:308–321, 2019.

[44] O. Delabroy, F. Lacas, B. Labegorre, and J.-M. Samaniego. Paramètres de similitude pour la combustion diphasique. *Rev. Gén. Therm.*, (37):934–953, 1998.

[45] F. Ducros, F. Nicoud, and T. Poinsot. Wall-adapating local eddy-viscosity models for simulations in complex geometries. In *ICFD*, pages 293–300. Baines M. J., 1998.

[46] L. Esclapez. *Numerical study of ignition and inter-sector flame propagation in gas turbines.* PhD thesis, Institut National Polytechnique de Toulouse, 2015.

[47] L. Esclapez, E. Riber, and B. Cuenot. Ignition probability of a partially premixed burner using LES. *Proc. Combust. Inst.* , 35(3):3133 – 3141, 2015.

[48] B. Fiorina, R. Vicquelin, P. Auzillon, N. Darabiha, O. Gicquel, and D. Veynante. A filtered tabulated chemistry model for LES of premixed combustion. *Combust. Flame*, 157:465–475, 2010.

[49] B. Franzelli. *Impact of the chemical description on direct numerical simulations and large eddy simulations of turbulent combustion in industrial aero-engines.* PhD thesis, Institut National Polytechnique de Toulouse, 2011.

[50] B. Franzelli, E. Riber, M. Sanjosé, and T. Poinsot. A two-step chemical scheme for Large-Eddy Simulation of kerosene-air flames. *Combust. Flame*, 157(7):1364–1373, 2010.

[51] M. Germano, U. Piomelli, P. Moin, and W. Cabot. A dynamic subgrid-scale eddy viscosity model. *Phys. Fluids* , 3(7):1760–1765, 1991.

[52] C. B. Graves, Y. L. Tang, and J. G. Skifstad. Ignition of a fuel spray by a hot surface. *AIAA Journal*, 24, 1986.

[53] A. Haselbacher, F. M. Najjar, and J. P. Ferry. An efficient and robust particle-localization algorithm for unstructured grids. *J. Comput. Phys.* , 225(2):2198–2213, 2007.

[54] S. Hayashi, S. Kumagai, and T. Sakai. Propagation velocity and structure of flames in droplet-vapor-air mixtures. *Combust. Sci. Technol.* , 15:169–177, 1976.

[55] CC. Huang, SS. Shy, CC. Liu, and YY. Yan. A transition on minimum ignition energy for lean turbulent methane combustion in flamelet and distributed regimes. *Proc. Combust. Inst.* , 31, 2007.

[56] T. Jaravel. *Prediction of pollutants in gas turbines using Large Eddy Simulation.* PhD thesis, Institut National Polytechnique de Toulouse, 2016.

[57] W. P. Jones and V. N. Prasad. LES-pdf simulation of a spark ignited turbulent methane jet. *Proc. Combust. Inst.* , 33(1):1355–1363, 2011.

[58] W. P. Jones and V. N. Prasad. Large Eddy Simulation of the Sandia Flame Series (D-F) using the Eulerian stochastic field method. *Combust. Flame*, 157:1621–1636, 2019.

[59] S. Kerkemeier, C.E. Frouzakis, A.G. Tomboulides, E. Mastorakos, and K. Boulouchos. Autoignition of a diluted hydrogen jet in a heated 2-D turbulent air flow. In *Conference on DNS and LES of reacting flows, 22–24 October, Technische Universiteit Eindhoven, The Netherlands*, 2008.

[60] A. R. Kerstein, W. Ashurst, and F. A. Williams. Field equation for interface propagation in an unsteady homogeneous flow field. *Phys. Rev. A*, 37(7):2728–2731, 1988.

[61] T. Kravchik and E. Sher. Numerical modeling of spark ignition and flame initiation in a quiescent methane-air mixture. *Combust. Flame*, 99:635–643, 1994.

[62] T. Kravchik, E. Sher, and J. B. Heywood. From spark ignition to flame initiation. *Combust. Sci. Technol.* , 108, 1995.

[63] K. K. Kuo. *Principles of Combustion*. John Wiley, New York, 1986.

[64] G. Lacaze, B. Cuenot, T. J. Poinsot, and M. Oschwald. Large eddy simulation of laser ignition and compressible reacting flow in a rocket-like configuration. *Combust. Flame*, 156(6):1166–1180, 2009.

[65] G. Lacaze, E. Richardson, and T. J. Poinsot. Large eddy simulation of spark ignition in a turbulent methane jet. *Combust. Flame*, 156(6):1993–2009, 2009.

[66] C. Lacour, A. Lo, J. Marrero, F. Lefebvre, P. Vervisch, A. Cessou, and B. Lecordier. Characterisation of electric discharge in laminar flow with optical diagnostics. In *18th International Symposium on the Application of Laser and Imaging Techniques to Fluid Mechanics*, Lisbon, Portugal, 2016.

[67] N. Lamarque. *Schémas numériques et conditions limites pour la simulation aux grandes échelles de la combustion diphasique dans les foyers d'hélicoptère*. Phd thesis, INP Toulouse, 2007.

[68] T. Lancien. *Etude numérique de l'allumage diphasique de foyers annulaires multi-brûleurs*. PhD thesis, Université Paris-Saclay, 2018.

[69] K.P. Lee, S.H. Wang, and S.C. Wong. Spark ignition characteristics of monodisperse multicomponent fuel sprays. *Combust. Sci. Technol.* , 113, 1996.

[70] A.H. Lefebvre. *Gas turbine combustion*. Taylor & Francis, 1998.

[71] C. Letty, E. Mastorakos, A. R. Masri, M. Juddoo, and W. O'Loughlin. Structure of igniting ethanol and n-heptane spray flames with and without swirl. *Experimental Thermal and Fluid Science*, 43, 2012.

[72] M. T. Lim, R. W. Anderson, and V.S. Arpaci. Prediction of spark kernel development in constant volume combustion. *Combust. Flame*, 69:303–316, 1987.

[73] W. Lochte-Holtgreven and H. Maecker. Temperaturbestimmung an frei brennenden kohlelichtbögen mit hilfe der cn-banden. *Zeitschrift für Physik volume 105*, 1937.

[74] T. Lovas, D. Nilsson, and F. Mauss. Automatic reduction procedure for chemical mechanisms applied to premixed methane/air flames. *Proc. Combust. Inst.* , 28:1809–1815, 2000.

[75] T. Lu and C.K. Law. Systematic approach to obtain analytic solutions of quasi steady state species in reduced mechanisms. *J. Phys. Chem.*, 110, 2006.

[76] T. Lu and C.K. Law. A criterion based on computational singular perturbation for the identification of quasi steady state species. *Combust. Flame*, 154:763–774, 2008.

[77] R. Maly. *Fuel economy*, chapter 3. Springer Science+Business Media New York, 1984.

[78] R. Maly and M. Vogel. Initiation and propagation of flame fronts in lean CH4-air mixtures by the three modes of the ignition spark. *Proc. Combust. Inst.* , 1979.

[79] T Marchione, S F Ahmed, and E Mastorakos. Ignition of turbulent swirling n-heptane spray flames using single and multiple sparks. *Combust. Flame*, 156(1):166–180, January 2009.

[80] J. Marrero-Santiago. *Experimental study of lean aeronautical ignition. Impact of critical parameters on the mechanisms acting along the different ignition phases.* PhD thesis, INSA Rouen, 2018.

[81] J. Marrero-Santiago, F. Collin-Bastiani, E. Riber, G. Cabotand, B. Cuenot, and B. Renou. On the mechanisms of flame kernel extinction or survival during aeronautical ignition sequences. Experimental and numerical analysis. *Combust. Flame*, 222, 2020.

[82] E. Mastorakos. Forced ignition of turbulent spray flames. *Proc. Combust. Inst.* , 36:2367–2383, 2017.

[83] A. Matino, J. Sotton, M. Bellenoue, C. Viguier, and S. Richard. Simultaneous characterization of discharge kernel properties induced by an helicopter engine igniter. WIPP. 39th Symposium on Combustion, 2022.

[84] B.J. McBride, S. Gordon, and M.A. Reno. Technical Report TM-4513, NASA, 1994.

[85] G. Meyer and A. Wimmer. A thermodynamic model for the plasma kernel volume and temperature resulting from spark discharge at high pressures. *Journal of Thermal Analysis and Calorimetry*, 133(2), 2008.

[86] X. Mi, C. Zhang, X. Hui, and Y. Lin. Ignition failure modes during ignition kernel propagation in swirl spray flames. In *Proceedings of Global Power and Propulsion Society ISSN-Nr: 2504-4400 Beijing Conference 2019 16th–18th September*, 2019.

[87] Q. Michalski, C. J. Benito-Parejo, A. Claverie, J. Sotton, and M. Bellenoue. An application of speckle-based background oriented schlieren for optical calorimetry. *Experimental Thermal and Fluid Science*, 91:470–478, 2018.

[88] Y. Mizutani and A. Nakajima. Combustion of fuel vapor-drop-air systems: Part I-open burner flames. *Combust. Flame*, 20, 1973.

[89] Y. Mizutani and A. Nakajima. Combustion of fuel vapor-drop-air systems: Part II—spherical flames in a vessel. *Combust. Flame*, 20, 1973.

[90] V. Moureau, P. Domingo, and L. Vervisch. From large-eddy simulation to direct numerical simulation of a lean premixed swirl flame: Filtered laminar flame-pdf modeling. *Combust. Flame*, 158(7):1340–1357, 2011.

[91] V. Moureau, G. Lartigue, Y. Sommerer, C. Angelberger, O. Colin, and T. Poinsot. Numerical methods for unsteady compressible multi-component reacting flows on fixed and moving grids. *J. Comput. Phys.* , 202(2):710–736, 2005.

[92] J.-D. Müller. *A User's guide to hip*. CERFACS, Toulouse, France, 2020. (version 20.04).

[93] S. Nakaya, K. Hatori, M. Tsue, M. Kono, D. Segawa, and T. Kadota. Numerical analysis on flame kernel in spark ignition methane/air mixtures. *J. Prop. Power* , 27, 2011.

[94] A. Neophytou and E. Mastorakos. Simulations of laminar flame propagation in droplet mists. *Combust. Flame*, 156(8):1627–1640, 2009.

[95] A. Neophytou, E. Mastorakos, and R. S. Cant. DNS of spark ignition and edge flame propagation in turbulent droplet-laden mixing layers. *Combust. Flame*, 157, 2010.

[96] A. Neophytou, E. Mastorakos, and R. S. Cant. The internal structure of igniting turbulent sprays as revealed by complex chemistry DNS. *Combust. Flame*, 159, 2012.

[97] F. Nicoud, H.B. Toda, O. Cabrit, S. Bose, and J. Lee. Using singular values to build a subgrid-scale model for large eddy simulations. *Phys. Fluids*, 8(23), 2011.

[98] D. Paulhiac. *Modelisation de la combustion d'un spray dans un bruleur aero-nautique*. PhD thesis, Institut National Polytechnique de Toulouse, 2015.

[99] P. Pelce and P. Clavin. Influence of hydrodynamics and diffusion upon stability limits of laminar premixed flames. *J. Fluid Mech.* , 124:219, 1982.

[100] P. Pepiot and H. Pitsch. An efficient error-propagation-based reduction method for large chemical kinetic mechanisms. *Combust. Flame*, 154:67 – 81, 2008.

[101] N. Peters. *Turbulent combustion*. Cambridge University Press, 2001.

[102] M. Philip. *Dynamique de l'allumage circulaire dans les foyers annulaires multi-injecteurs.* PhD thesis, Université Paris-Saclay, 2016.

[103] T. Poinsot, T. Echekki, and M. G. Mungal. A study of the laminar flame tip and implications for premixed turbulent combustion. *Combust. Sci. Technol.* , 81(1-3):45–73, 1992.

[104] T. Poinsot and S. Lele. Boundary conditions for direct simulations of compressible viscous flows. *J. Comput. Phys.* , 101(1):104–129, 1992.

[105] T. Poinsot and D. Veynante. *Theoretical and Numerical Combustion.* Third Edition (www.cerfacs.fr/elearning), 2011.

[106] C.E. Polymeropoulos and S. Das. The effect of droplet size on the burning velocity of kerosine-air sprays. *Combust. Flame*, 25, 1975.

[107] S. B. Pope. Lagrangian PDF methods for turbulent flows. *Ann. Rev. Fluid Mech.* , pages 23–63, 1994.

[108] S. B. Pope. *Turbulent flows.* Cambridge University Press, 2000.

[109] H. Poritsky and C. G. Suits. The determination of arc temperature from sound velocity measurements. II. *Physics*, 6, 1935.

[110] P. Pouech, F. Duchaine, and T.Poinsot. Premixed flame ignition in high-speed flows over a backward facing step. *Combust. Flame*, 229, 2021.

[111] S. Puggelli, D. Veynante, and R. Vicquelin. Impact of dynamic modelling of the flame subgrid scale wrinkling in large-eddy simulation of light-round in an annular combustor. *Combust. Flame*, 230:166–178, 2021.

[112] E Ranzi, A Frassoldati, R Grana, A Cuoci, T Faravelli, A P Kelley, and C K Law. Hierarchical and comparative kinetic modeling of laminar flame speeds of hydrocarbon and oxygenated fuels. *Prog. Energy Combust. Sci.* , 38(4):468–501, August 2012.

[113] S.A. Rashkovsky. Spark ignition of ill-mixed gases. In *First Mediterranean Combustion Symposium, Antalya, Turkey*, 1999.

[114] S. Refael and E. Sher. A theoretical study of the ignition of a reactive medium by means of an electrical discharge. *Combust. Flame*, 59:17–30, 1985.

[115] J. Réveillon and L. Vervisch. Analysis of weakly turbulent diluted-spray flames and spray combustion regimes. *J. Fluid Mech.* , 537:317–347, 2005.

[116] E. S. Richardson and E. Mastorakos. Numerical investigation of forced ignition in laminar counterflow non-premixed methane-air flames. *Combust. Sci. Technol.* , 179, 2007.

[117] B. Rochette. *Modelisation et simulation de la combustion turbulente diphasique dans les moteurs aeronautiques.* PhD thesis, Institut National Polytechnique de Toulouse, 2019.

[118] B. Rochette, B. Cuenot, E. Riber, and O. Vermorel. A generic and self-adapting method for flame detection and thickening in the thickened flame model. *Combust. Flame*, 212:448–458, 2019.

[119] E. Rochette, B. Riber and B. Cuenot. Effect of non-zero relative velocity on the flame speed of two-phase laminar flames. *Proc. Combust. Inst.* , 32, 2018.

[120] M. Rudgyard. Integrated preprocessing tools for unstructured parallel CFD applications. Technical Report TR/CFD/95/08, CERFACS, 1995.

[121] N. Savary and G. Taliercio. The Safran helicopter engine spinning flame combustor concept to meet customer needs. In *42nd European Rotorcraft Forum September 5-8, 2016*, Lille, France, 2016.

[122] L. Schiller and A. Nauman. A drag coefficient correlation. *VDI Zeitung*, 77:318–320, 1935.

[123] D. Sepulveda and E.E. Striebel. Starting means for a gas turbine, 1983. Patent 4,417,439.

[124] B. Sforzo, A. Lambert, J. Kim, J. Jagoda, S. Menon, and J. Seitzman. Post discharge evolution of a spark igniter kernel. *Combust. Flame*, 162:181–190, 2015.

[125] F. Shum-Kivan. *Simulation aux Grandes Echelles de flammes de spray et modelisation de la combustion non-premelangees.* PhD thesis, Institut National Polytechnique de Toulouse, 2017.

[126] A. K. Singh and C. E. Polymeropoulos. Spark ignition of aerosols. *Proc. Combust. Inst.* , 21, 1988.

[127] D. B. Spalding. The combustion of liquid fuels. In *4th Symp. (Int.) on Combustion*, pages 847–864. The Combustion Institute, Pittsburgh, 1953.

[128] S. Subramaniam. Lagrangian-Eulerian methods for multiphase flows. *Prog. Energy Combust. Sci.* , 39:215–245, 2013.

[129] M. Thielle, S. Selle, U. Riedel, J. Warnatz, and U. Maas. Numerical simulation of spark ignition including ionization. In *Twenty-Eighth Symposium (International) on Combustion*, pages 1177–1185, 2000.

[130] M. Thielle, J. Warnatz, and U. Maas. Geometrical study of spark ignition in two dimensions. *Combust. Theor. Model.* , 4:413–434, 2000.

[131] T. Turanyi, A. S. Tomlin, and M. J. Pilling. On the error of the quasi-steady-state approximation. *The Journal of Physical Chemistry*, 97:163–172, 1993.

[132] A. Umemura and S. Takamori. Percolation theory for flame propagation in non- or less volatile fuel spray : A conceptual analysis to group combustion excitation mechanism. *Combust. Flame*, 141:336–349, 2005.

[133] L. Valino. Field monte carlo formulation for calculating the probability density function of a single scalar in a turbulent flow. *Flow, Turb. and Combustion* , 60:157–172, 1998.

[134] D. Veynante and V. Moureau. Analysis of dynamic models for large eddy simulations of turbulent premixed combustion. *Combust. Flame*, 162:4622–4642, 2015.

[135] P S Volpiani, T Schmitt, and D Veynante. A posteriori tests of a dynamic thickened flame model for large eddy simulations of turbulent premixed combustion. , 174(C):166–178, December 2016.

[136] A. von Engle and M. Steenbeck. Uber die temperatur in des gassaule eines lichtbogens. *Wiss. Veroff. Siemens-Konz. Bd 10*, 1931.

[137] A. von Engle and M. Steenbeck. *Elektrische Gasentladungen.* Springer Berlin, 1932.

[138] A. P. Wandel, N. Chakraborty, and E. Mastorakos. Direct numerical simulations of turbulent flame expansion in fine sprays. *Proc. Combust. Inst.* , 32(2):2283–2290, 2009.

[139] G. Wang, M. Boileau, and D. Veynante. Implementation of a dynamic thickened flame model for large eddy simulations of turbulent premixed combustion. *Combust. Flame*, 158(11):2199 – 2213, 2011.

[140] G. Wang, M. Boileau, D. Veynante, and K. Truffin. Large eddy simulation of a growing turbulent premixed flame kernel using a dynamic flame surface density model. *Combust. Flame*, 159(8):2742 – 2754, 2012.

[141] F. A. Williams. *Combustion Theory.* Benjamin Cummings, Menlo Park, CA, 1985.

271

[142] A. Wood, W. Hwang, and J. Eaton. Preferential concentration of particles in homogeneous and isotropic turbulence. *International journal of multiphase flow*, 31:1220–1230, 2005.

[143] N.A. Worth and J.R. Dawson. Modal dynamics of self-excited azimuthal instabilities in an annular combustion chamber. *Combust. Flame*, 160(11):2476–2489, 2013.